DEVELOPMENT OF BIODEGRADABLE SOLID POLYMER ELECTROLYTES INCORPORATING DIFFERENT NANOPARTICLES FOR ELECTRIC DOUBLE LAYER CAPACITOR

CHONG MEE YOKE

FACULTY OF SCIENCE
UNIVERSITY OF MALAYA
KUALA LUMPUR

2017

DEVELOPMENT OF BIODEGRADABLE SOLID POLYMER ELECTROLYTES INCORPORATING DIFFERENT NANOPARTICLES FOR ELECTRIC DOUBLE LAYER CAPACITOR

CHONG MEE YOKE

THESIS SUBMITTED IN FULFILMENT OF THE REQUIREMENTS FOR THE DEGREE OF DOCTOR OF PHILOSOPHY

DEPARTMENT OF PHYSICS
FACULTY OF SCIENCE
UNIVERSITY OF MALAYA
KUALA LUMPUR

2017

UNIVERSITY OF MALAYA

ORIGINAL LITERARY WORK DECLARATION

Name of Candidate: **CHONG MEE YOKE**

Registration/Matric No: **SHC130028**

Name of Degree: **DOCTOR OF PHILOSOPHY**

Title of Thesis:

DEVELOPMENT OF BIODEGRADABLE SOLID POLYMER ELECTROLYTES INCORPORATING DIFFERENT NANOPARTICLES FOR ELECTRIC DOUBLE LAYER CAPACITOR

Field of Study: **EXPERIMENTAL PHYSICS**

I do solemnly and sincerely declare that:

(1) I am the sole author/writer of this Work;
(2) This Work is original;
(3) Any use of any work in which copyright exists was done by way of fair dealing and for permitted purposes and any excerpt or extract from, or reference to or reproduction of any copyright work has been disclosed expressly and sufficiently and the title of the Work and its authorship have been acknowledged in this Work;
(4) I do not have any actual knowledge nor do I ought reasonably to know that the making of this work constitutes an infringement of any copyright work;
(5) I hereby assign all and every rights in the copyright to this Work to the University of Malaya ("UM"), who henceforth shall be owner of the copyright in this Work and that any reproduction or use in any form or by any means whatsoever is prohibited without the written consent of UM having been first had and obtained;
(6) I am fully aware that if in the course of making this Work I have infringed any copyright whether intentionally or otherwise, I may be subject to legal action or any other action as may be determined by UM.

Candidate's Signature   Date:

Subscribed and solemnly declared before,

Witness's Signature   Date:

Name:

Designation:

ABSTRACT

The increasing demand, rapid consumption of fossil fuels and undesirable consequences of environmental pollution are the alarming concerns from the last few decades. Therefore, much effort has been made to develop biodegradable solid polymer electrolyte (SPE) using natural polymer as host polymer for energy storage and energy conversion devices. The choice of natural polymers as host polymer for the preparation of SPE are hydroxylpropylmethyl cellulose (HPMC) and hydroxylethyl cellulose (HEC). As a result, HEC has been chosen in this study because it has huge amount of hydroxyl groups compared to cellulose and its derivatives. Consequently, it assists in the adsorption of charge carriers, which results in the improvement of charge storage capacity. However, preparation of biodegradable SPE by using solution casting technique exhibits low ionic conductivity. Thus, green ionic liquid (1-ethyl-3-methylimidazolium trifluoromethane-sulfonate (EMIMTf)) and nanoparticles (fumed silica (fumed SiO_2), copper(II) oxide (CuO) and yttrium(III) oxide (Y_2O_3)) have been incorporated into the biodegradable SPE along with magnesium trifluoromethanesulfonate ($MgTf_2$) salt as mobile charge carriers to improve its ionic conductivity for electric double layer capacitor (EDLC). Electric double layer capacitor has been chosen over batteries owing to their good thermal and chemical stability, higher potential window (which leads to high energy density) and longer cycling stability. Based on the findings, cell fabricated by inclusion of 2 wt. % of CuO nanoparticles obtained the highest specific capacitance (36.7 F/g) at scan rate of 5 mV/s along with the lowest charge transfer resistance (25.0 Ω) whereas cell fabricated by 2 wt. % of Y_2O_3 nanoparticles achieved the highest capacitance retention of 91.3 % over 3,000 cycles at current density of 0.4 A/g.

ABSTRAK

Sejak beberapa dekad yang lalu, permintaan dan kadar pengunaan bahan api fosil yang tinggi serta kesan pencemaran yang tidak diingini amat membimbangkan. Oleh yang demikian, pelbagai usaha telah dikaji untuk membangunkan polimer elektrolit pepejal (SPE) biodegradasi dengan menggunakan polimer semulajadi sebagai polimer tuan rumah. Polimer semulajadi yang menjadi pilihan sebagai polimer tuan rumah adalah selulosa hidroksilpropilmetil (HPMC) dan selulosa hidroksiletil (HEC). Secara kesimpulannya, HEC telah dipilih dalam kajian ini kerana ia mempunyai sejumlah besar kumpulan hidroksil berbanding dengan selulosa lain serta terbitannya. Kumpulan hidroksil pada selulosa hidroksiletil berupaya membantu dalam penjerapan pembawa cas yang seterusnya meningkatkan keupayaan untuk menyimpan cas. Walau bagaimanapun, penyediaan SPE biodegradasi dengan menggunakan teknik pelarutan mempamerkan kekonduksian ionik yang rendah. Oleh itu, cecair ionik (1-etil-3-metilimidazolium triflorometansulfonat (EMIMTf)) dan nanopartikel (silika wasap (fumed SiO_2), kuprum(II) oksida (CuO) dan yttrium(III) oksida (Y_2O_3)) yang hijau telah diperbadankan ke dalam SPE biodegradasi berserta dengan garam magnesium triflorometansulfonat ($MgTf_2$) selaku pembawa cas mudah alih untuk meningkatkan kekonduksian ionik dalam penggunaan sebagai kapasitor elektrik dwilapis (EDLC). Kapasitor elektrik dwilapis telah dipilih dalam kajian ini berbanding bateri kerana EDLC mempunyai kestabilan kimia dan haba yang baik, julat keupayaan voltan yang tinggi (yang seterusnya membawa kepada ketumpatan tenaga yang tinggi) dan kestabilan kitaran yang tinggi. Berdasarkan kepada hasil kajian, sel yang telah difabrikasi dengan menggunakan 2 % jisim CuO nanopartikel memberikan kemuatan tertentu yang tertinggi (36.7 F/g) pada kadar imbasan sebanyak 5 mV/s beserta dengan rintangan pemindahan caj yang terendah (25.0 Ω) manakala sel yang difabrikasi dengan menggunakan 2 % jisim Y_2O_3 nanopartikel mencapai kemuatan retensi

yang tertinggi sebanyak 91.3 % pada ketumpatan arus sebanyak 0.4 A/g selama 3,000 kitaran.

ACKNOWLEDGEMENTS

First, I would like to take this opportunity to express my profound gratitude to Prof Dr Ramesh T. Subramaniam and Assoc Prof Dr Ramesh Kasi, for accepting me as a student into their research group. Also, I felt so grateful to have them as supervisors because they never give up on any students, will always be there to help and guide us with their valuable advice and ideas patiently. Without their support and encouragement, I could not have completed my study and this thesis.

I extend my heartfelt appreciation to my laboratory members and Kolej Kediaman 12 friends who have helped me throughout the whole PhD program especially Numan Arshid. I cherish the moments that we coped with the difficulties and challenges. Besides, I would like to thank all laboratory officers and block C laboratory members who have helped me to accomplish this dissertation. Their cooperation and assistance make it easier for me to finish the research work in time.

I would like to express my greatest appreciation to my family who have been with me all the time through the difficulties.

TABLE OF CONTENTS

LIST OF FIGURES

LIST OF TABLES

LIST OF SYMBOLS AND ABBREVIATIONS

A	:	Area of the electrodes connected to the sample
A	:	Integral area of the cyclic voltammogram loop
BMIMTf	:	1-Butyl-3-Methylimidazolium Trifluoromethanesulfonate
C	:	Capacitance value in the Hemholtz double layer
C_o	:	Vacuum capacitance
C_p	:	Frequency dependent values of capacitance
C_{sp}	:	Specific capacitance
C_{total}	:	Overall capacitance
CuO	:	Copper(II) oxide
CE	:	Consumer Equipment
CV	:	Cyclic Voltammetry
d	:	Spacing between layers of atoms
d	:	Thickness of EDL
DMSO	:	Dimethylsulfoxide
DSSC	:	Dye-Sensitized Solar Cell
ε'	:	Dielectric permittivity
ε''	:	Dielectric loss
$\varepsilon^*_r(\omega)$	:	Relative permittivity
ε_0		Permittivity of free space
E_a	:	Activation energy
E&E	:	Electrical and Electronic
EDL	:	Electric Double Layer
EDLC	:	Electrochemical Double Layer Capacitor
EIS	:	Electrochemical Impedance Spectroscopy

EMIMTf	:	1-Ethyl-3-Methylimidazolium Trifluoromethanesulfonate
ESR	:	Equivalence Series Resistance
FTIR	:	Fourier Transform Infrared Spectroscopy
GCD	:	Galvanostatic Charge-Discharge
GPE	:	Gel Polymer Electrolyte
HA	:	Household Appliances
HEC	:	Hydroxylethyl Cellulose
HPMC	:	Hydroxylpropylmethyl Cellulose
I	:	Discharge current
ICT	:	Information Technology and Telecommunication
IL	:	Ionic Liquid
j	:	Constant
k	:	Boltzmann constant
k		Dielectric constant of the electrolyte
l	:	Thickness of the film
LPE	:	Liquid Polymer Electrolyte
m	:	Total mass of the electrode materials on both electrodes
M'	:	Real part modulus
M''	:	Imaginary part modulus
MgTf$_2$	:	Magnesium Trifluoromethanesulfonate
N	:	Integer (whole number)
NMP	:	N-Methyl-2-Pyrrolidone
θ	:	Angle between the incident rays and the surface of the crystal
PAN	:	Poly(acrylonitrile)
PEG	:	Poly(ethylene glycol)
PEO	:	Poly(ethylene oxide)

PMMA	:	Poly(methyl metaacrylate)
PTFE	:	Poly(tetrafluoroethylene)
PVA	:	Poly(vinyl alcohol)
PVC	:	Poly(vinyl chloride)
PVP	:	Poly(vinyl pyrrolidone)
PVdF	:	Poly(vinylidene fluoride)
PVdF-HFP	:	Poly(vinylidene fluoride-*co*-hexafluoropropylene)
R	:	Residual group
R_b	:	Bulk resistance
R_{ct}	:	Charge transfer resistance
R_p	:	Parallel resistance
SiO_2	:	Silica
SPE	:	Solid Polymer Electrolyte
Δt	:	Discharged time after IR drop
T	:	Absolute temperature
T_g	:	Transition glass temperature
TGA	:	Thermogravimetry Analysis
v	:	Scan rate
ΔV	:	Potential window
XRD	:	X-Ray Diffraction
Y_2O_3	:	Yttrium(III) oxide
Z'	:	Real impedance
Z''	:	Imaginary impedance
Z*	:	Complex impedance
σ	:	Ionic conductivity
σ_o	:	Pre-exponential factor

| ω | : | Angular frequency |
| λ | : | Wavelength of the rays |

CHAPTER 1: INTRODUCTION

1.1   Research Background

In this modern society, the demand of electronic and electrical equipment (cell phones, thumb drive, monitors, television, refrigerators, etc.) are increasing rapidly. The electronic and electrical waste (e-waste) generated by these equipment is increasing dramatically every year (Orlins & Guan, 2016; Zhang et al., 2016). According to European Union directive, the e-waste can be classified into eight categories (large household appliances (large HA), small household appliances (small HA), Information Technology and Telecommunication (ICT) equipment, consumer equipment (CE), lightning equipment, electrical and electronic tools (E&E tools), toys equipment and medical devices).

Among these e-waste, large HA are the highest contributor to the total e-waste which was then followed by ICT equipment (used mobile phones and used monitors). However, the e-waste from ICT equipment possesses less hazardous materials than the large HA due to the heavy metals (i.e. copper, aluminium, chromium, lead, mercury, etc.), flame retardants plastic casing and energy storage devices (i.e. batteries and supercapacitor) used (Nnorom & Osibanjo, 2009; Suja et al., 2014).

Thus, managing (disposals from landfill and incineration) e-waste from ICT equipment is a challenging task owing to their huge volume, short life-span of the equipment and the release of numerous hazardous materials (flame retardants and heavy metals) which may pose a threat to the environment and human health (Heacock et al., 2016; Herat & Agamuthu, 2012; Sthiannopkao & Wong, 2013). Therefore, materials recovery especially heavy metals from the flame retardants plastic casing through

smelting, pyrometallurgical and hydrometallurgical methods have been adopted to reduce the discharge of harmful wastes to the environment (Sun et al., 2015; Sun et al., 2015). In addition, biodegradable energy storage devices are critically needed as an alternative solution to the increase usage of ICT equipment resulted in the reduction of space for dumping (Herat & Agamuthu, 2012).

Energy storage device is an apparatus used for storing electric energy when needed and releasing it when required. The commonly used energy storage devices in the ICT equipment are batteries and supercapacitors. Between these energy storage devices, supercapacitors (electrochemical capacitors or ultracapacitors) attracted huge attention from researchers since 1800 owing to its higher power and energy densities than batteries and conventional capacitors. Supercapacitors are divided into pseudocapacitors and electrochemical double layer capacitors (EDLCs). The electrodes in pseudocapacitors undergo Faradaic process whereas the electrodes in EDLCs undergo non-Faradaic process. An EDLC has more prominent advantages such as larger specific capacitance, higher specific power and longer life cycle than a pseudocapacitor (Lim et al., 2014a). On top of that, EDLC will have an additional feature that is environmental friendly by using biodegradable host polymers such as natural and synthetic polymers.

1.2   Scope of the Research

The aim of this research is to prepare biodegradable solid polymer electrolytes (SPEs) for EDLC in order to mitigate the environmental problem created by dumping of hazardous materials from e-waste. Hydroxylethyl cellulose (HEC) has been chosen in this study as the host polymer for SPE because it has additional three oxygen atoms per monomer compared to cellulose which provides more absorption space for mobile carriers. The HEC is non-conducting in nature, therefore to enhance the ionic conductivity, magnesium trifluoromethanesulfonate ($MgTf_2$) salt has been incorporated

into the host polymer to provide mobile carriers. Magnesium trifluoromethanesulfonate was used due to its high theoretical capacity as lithium (both are located diagonally in the periodic table with similar physical and chemical properties). The ionic conductivity of SPE can be boosted by adding ionic liquid (IL). Ionic liquid serves as charge carriers as well as a plasticizer which increases the flexibility of the host polymer. Here, 1-ethyl-3-methylimidazolium trifluoromethanesulfonate (EMIMTf) which has easier dissociation properties than its counterparts due to its weaker Lewis base property was used in this research. In addition to that, metal oxide nanoparticles has been incorporated into the polymer electrolyte in order to further improve the ionic conductivity of the SPE. Three types of metal oxides nanoparticles namely fumed silica (fumed SiO_2), copper(II) oxide (CuO) and yttrium(III) oxide (Y_2O_3) are chosen in this study. The preparation of SPEs by CuO and Y_2O_3 nanoparticles for EDLC have never been reported by any researchers and their performances were compared with commonly used fumed SiO_2 in this research work.

1.3 Objectives of the Research

The aims of the research are as follows:

1. To prepare and optimize the SPE by incorporating with nanofillers.

2. To characterize the prepared SPE based on fumed silica (SiO_2), copper(II) oxide (CuO) and yttrium(III) oxide (Y_2O_3) nanoparticles.

3. To investigate the EDLC performances of the prepared SPE based on fumed silica (SiO_2), copper(II) oxide (CuO) and yttrium(III) oxide (Y_2O_3) nanoparticles.

1.4 Outline of Thesis

The structure of this thesis can be summarized as follows:

Chapter 1 presents the current problems created by electronic wastes, consequences and the methods to overcome it by developing a biodegradable supercapacitors. The research objectives and materials used in this study were discussed.

Chapter 2 describes the literature review on the principles and types of supercapacitors. The latter part of chapter 2 is to discuss the types of polymer electrolyte for EDLC and the methods to improve the ionic conductivity of the prepared polymer electrolyte.

Chapter 3 presents the methods to prepare SPE (with and without nanoparticles), preparation of carbon electrodes and fabrication of EDLC. Characterization analyses such as electrochemical impedance spectroscopy (EIS), Fourier transform infrared spectroscopy (FTIR), X-ray diffraction (XRD) and thermogravimetry analysis (TGA) on SPEs are described. In addition, performance studies including cyclic voltammetry (CV), galvanostatic charge-discharge (GCD) and EIS on the EDLC are illustrated.

Chapter 4 focuses on characterization of the prepared SPEs based on the three types of nanoparticles. Also, the performance studies of the EDLCs fabricated by the SPEs are discussed.

Chapter 5 describes the comparison of the EDLC performances from the three systems.

Chapter 6 concludes the thesis by highlighting the relationship between the SPE characterizations and EDLC performances from each system. Possible future research

recommended for the enhancement of supercapacitor performances are proposed at the end of this chapter.

CHAPTER 2: LITERATURE REVIEW

2.1   Introduction

This chapter divided into four major parts. The first part describes the types of supercapacitor and their evolution as an energy storage device. Following this, the charge storage mechanism and the components used in the fabrication of EDLC are discussed. Subsequently, the third part of this chapter discusses the types of polymer electrolytes used in the fabrication of a supercapacitor. The methods to improve the ionic conductivity of polymer electrolytes in order to enhance the performance of a supercapacitor were discussed in the last part of this chapter.

2.2   Supercapacitor

The imminent consumption of fossil fuels and undesirable consequences of environmental pollution emerging drastically. The World Energy Outlook 2014 claimed that global energy demands will grow by 37 % by 2040 (World Energy Outlook, 2014) and nearly 80% of today's global energy demands are meet by the fossil fuels, including oil, gas and coal which are the significant contributor of CO_2 and other harmful gases. This give motivation to the development of green, sustainable and highly efficient electrochemical energy conversion and storage devices. Electrochemical energy storage also known as energy storage devices consists of batteries and capacitors. Capacitors are fundamental electrical circuit elements that have two main applications. One of its function is to charge or discharge electricity in the order of microfarads. The other function is to block the flow of direct current by extracting required frequencies characteristics. There are three types of capacitors namely electrostatic, electrolytic and electrochemical (Jayalakshmi & Balasubramanian, 2008).

2.2.1 Electrostatic capacitor

Electrostatic capacitor is the first generation capacitor that is build-up of two parallel metal electrodes separated by a dielectric. When a voltage is applied to a capacitor, opposite charges accumulate on the surfaces of each electrode. The charges are kept separate by the dielectric, thus producing an electric field that allows the capacitor to store energy. The operating voltage of the capacitor depends upon the strength of the dielectric material that is measured in volts per meter. The dielectric strength is the maximum electric field, which can exist in a dielectric without electrical breakdown. This is illustrated in Figure 2.1. Conventional capacitors have relatively high power densities, but relatively low energy densities because the stored electrical energy can be discharged rapidly to produce a lot of power.
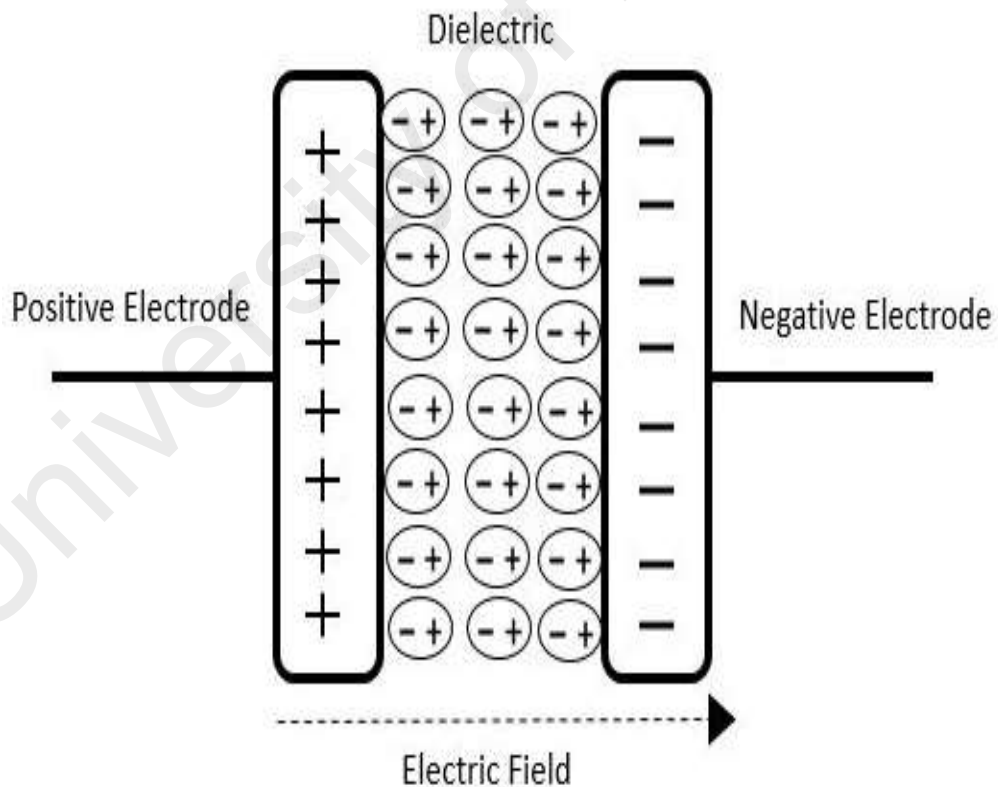
Figure 2.1: Schematic diagram of an electrostatic capacitor

2.2.2 Electrolytic capacitor

Electrolytic capacitor is the second generation capacitor. They are similar to batteries in cell construction. Figure 2.2 illustrates the schematic diagram of an electrolytic capacitor. An electrolytic capacitor is made up of two metal electrodes and paper (separator) that are immersed into a conductive electrolyte salt. One of the metal electrodes is coated with an insulating oxide layer serves as a dielectric and the opposite electrode is coated with an air oxide layer. The electrolytic capacitors are classified into three categories depending on the dielectric materials including aluminium, tantalum and ceramic.
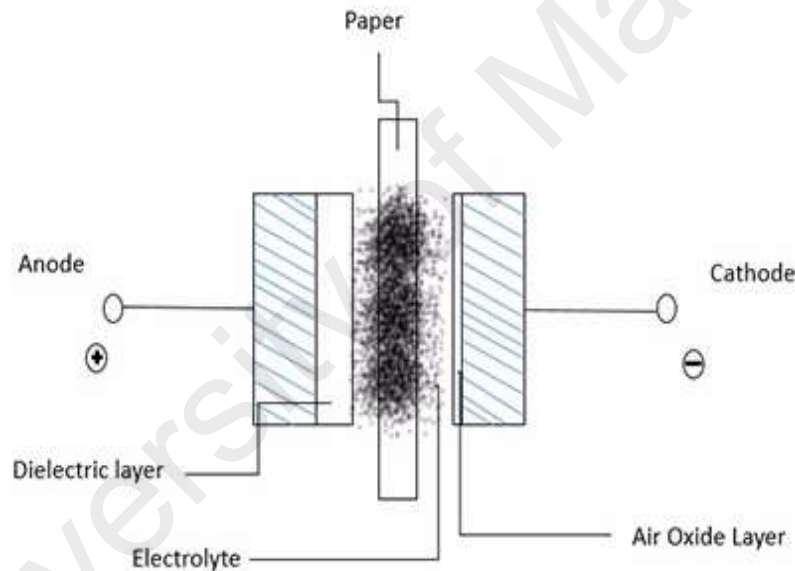
Figure 2.2: Schematic diagram of an electrolytic capacitor

2.2.2.1 Aluminium electrolytic capacitors

The anode of a typical aluminum electrolytic capacitor consists of aluminium foil and a dielectric film. The dielectric film is prepared by anodizing high purity aluminium in boric acid solutions. On the other hand, the cathode consists of aluminium foil and its surface is exposed to the air to form an insulating oxide layer. A treated cathode foil is opposed to the dielectric film of the anode foil and a separator interposed between them to make up a lamination. The laminated cell is dipped completely in an electrolyte and it

is housed in a metallic sheathed package in cylindrical form with a closed-end equipped with a releaser. This type of electrolytic capacitors are mainly used as power supplies for automobiles, aircraft, space vehicles, computers, monitors, motherboards of personal computers and other electronics (Nagata, 1983).

In order to broaden its applications, researchers tried to reduce the electrostatic resistance in the aluminium electrolytic capacitors by modifying the electrodes, electrolyte and dielectric materials. In terms of anode electrode, researchers utilized etched aluminium foil and alloy foils (Al-Ti, Al-Zr, Al-Si, Al-Nb and Al-Ta composite oxide films) (Masuda et al., 1986; Park & Lee, 2004; Watanabe et al., 1999; Xu, 2004; Yamamoto et al., 1999). In addition to that, researchers used polyaniline/polypyrrole, aluminium oxide and EC as cathode, dielectric and electrolyte, respectively (Monta & Matsuda, 1996; Ue et al., 1996; Yamamoto et al., 1996).

2.2.2.2 Tantalum electrolytic capacitors

A tantalum capacitor uses tantalum metal and its oxide as an anode and dielectric, respectively. There are two types of tantalum capacitors commercially available in the market namely wet electrolytic capacitors which use sulfuric acid as the electrolyte and solid electrolytic capacitors which use MnO_2 as the solid electrolyte. The tantalum capacitor produces similar capacitance (in the range of 0.1–10 F with a working voltage of 25–50 V) to aluminium capacitor with greater thermal stability (Nishino, 1996).

2.2.2.3 Ceramic electrolytic capacitors

Historically, a ceramic capacitor is a two-terminal non-polar device which is also known as disc capacitor. It was used extensively in electronic equipment, providing high capacity and small size at low price. A disc capacitor has evolved into a newer version of ceramic capacitor. The electrodes for the newer version of ceramic capacitor are

constructed by alternating layers of metal (Mn, Ca, Pd, Ag) and ceramic whereas the dielectric is made up of ceramic materials ($CaZrO_3$, $MgTiO_3$, $SrTiO_3$). These ceramic capacitors produce higher capacitance (in the range of 10 F) than aluminium and tantalum electrolytic capacitors. Therefore, they are highly useful in high frequency applications (Sakabe, 1997).

2.2.3   Electrochemical capacitor

Electrochemical capacitor is the third generation capacitor. An electrochemical capacitor also known as supercapacitor or ultracapacitor due to its trade name. It is constructed by two high surface-area porous electrodes ($1000–2000$ m^2/cm^3) separated by an electrolyte. Supercapacitor gained its fame over batteries and conventional capacitors because it has extremely high power density, rapid charge-discharge dynamics, excellent cyclic retention, good energy density, minimum charge separation and safety (Inagaki et al., 2010). The important characteristics of electrochemical capacitor over conventional capacitor and battery have been reported by Pandolfo & Hollenkamp (2006) and summarized in Table 2.1. Hence, in the late 1800s, supercapacitor evolved owing to its aforementioned ubiquitous features and promising future market to compete and replace batteries in several applications.

In 1746, the first double-layer supercapacitor (also known as Leyden jar) was discovered at Leyden in the Netherlands. A typical design of the Leyden jar consisted of a glass vial, containing acidic electrolyte as a conductor and which was contacted by an immersed metal electrode. The glass medium is used as a dielectric between the conducting metal coating on the inner and outer surfaces. The outer and inner surfaces store equal but opposite charge and this double layer charging occurs due to the presence of the acidic electrolyte. Charging of the Leyden jars were usually carried out using electrostatic generators such as the Hawkesbee machine. In the early twentieth century,

an improved version of the Leyden jar called the electrophorus was invented by Volta. An ebonite (a hard plastic) is used as the dielectric material instead of glass and sandwiched between two metal electrodes.

Table 2.1: Comparisons of important characteristics for conventional capacitor electrochemical capacitor and battery

Characteristics	Conventional capacitor	Electrochemical capacitor	Battery
Specific energy (Wh/kg)	<0.1	1–10	10–100
Specific power (W/kg)	>>10,000	500–10,000	<1,000
Discharging time	10^{-6} to 10^{-3} s	s to min	0.3 – 3 hrs
Charging time	10^{-6} to 10^{-3} s	s to min	1 – 5 hrs
Charge/discharge efficiency (%)	~100	85–98	70–85
Cycle-life (cycles)	Infinite	>500,000	~1,000
Maximum voltage determinants	Dielectric thickness and strength	Electrode and electrolyte stability window	Thermodynamics of phase reactions
Charge stored determinants	Electrode area and dielectric	Electrode microstructure and electrolyte	Active mass and thermodynamics

Following this, in year 1957, H. I. Becker of General Electric (U.S. Patent 2,800,616) invented an electrical device resembles an electrolytic cell (consists of two high surface area carbon electrodes immersed into a beaker of electrolyte) but his attempt failed because the design was impractical (Peng et al., 2008). Later on, in year 1962, a group of researchers from the Standard Oil Company of Ohio (SOHIO) led by Robert A. Rightmire

and Donald A. Boos improved the work done by Becker by figuring out a more reliable capacitor for commercialization.

Finally in 1970, supercapacitor engineered by SOHIO using double layer capacitance of high surface area carbon materials and tetraalkylammonium salt as a non-aqueous electrolyte was commercialized successfully owing to its higher operating voltage (3.4–4.0 V) and larger specific energy storage. Therefore, it has been widely used in small power applications (i.e. back-up power devices for volatile clock chips, complementary metal-oxide semiconductor computer memories and engine starting) which is then extended to intermediate and large scale applications (i.e. hybrid electric vehicles, power generation systems, industrial actuator power sources and high-efficiency energy storage for electric vehicles). All in all, disregarding to its application, supercapacitors are divided into two broad categories according to the process occurred at its electrode namely Faradaic and non-Faradaic process supercapacitors.

2.2.3.1 Faradaic Process Supercapacitor

A supercapacitor that undergoes Faradaic process at its electrode is also known as pseudocapacitor. The first pseudocapacitor was developed using RuO_2 as new electrode material in 1971 by Conway and co-workers (Miller, 2007; Trasatti & Buzzanca, 1971). Generally, there are two types of Faradaic process occurred at the electrodes of the pseudocapacitor because the electrodes are fabricated commonly by the composites of conducting polymers (i.e. polyaniline, polypyrrole, and poly[3,4-ethylenedioxy-thiophene]) and transition metal oxides (i.e. RuO_2, Co_3O_4, NiO and MnO_2) (Ghosh & Lee, 2012; Peng et al., 2008). The electrodes fabricated using conducting polymers involve bulk process and less dependent on its surface area although a relatively high surface area is useful in the distribution of electrolyte ions to and from the electrodes in a cell (Burke, 2000). In addition to that, this type of pseudocapacitor experiences the

doping and de-doping of active conducting polymer material in the electrode. Conversely, the electrodes fabricated by transition metal oxides engage to the surface mechanism and it is highly dependent on the surface area of the electrode material. Also, it experiences redox reaction at the transition metal oxide's surface with ions from the electrolyte. In all cases, the electrodes must have high electronic conductivity to distribute and collect the electron current. Figures 2.3(a) and (b) illustrate the mechanism of pseudocapacitor fabricated using conducting polymer and transition metal oxides, respectively.
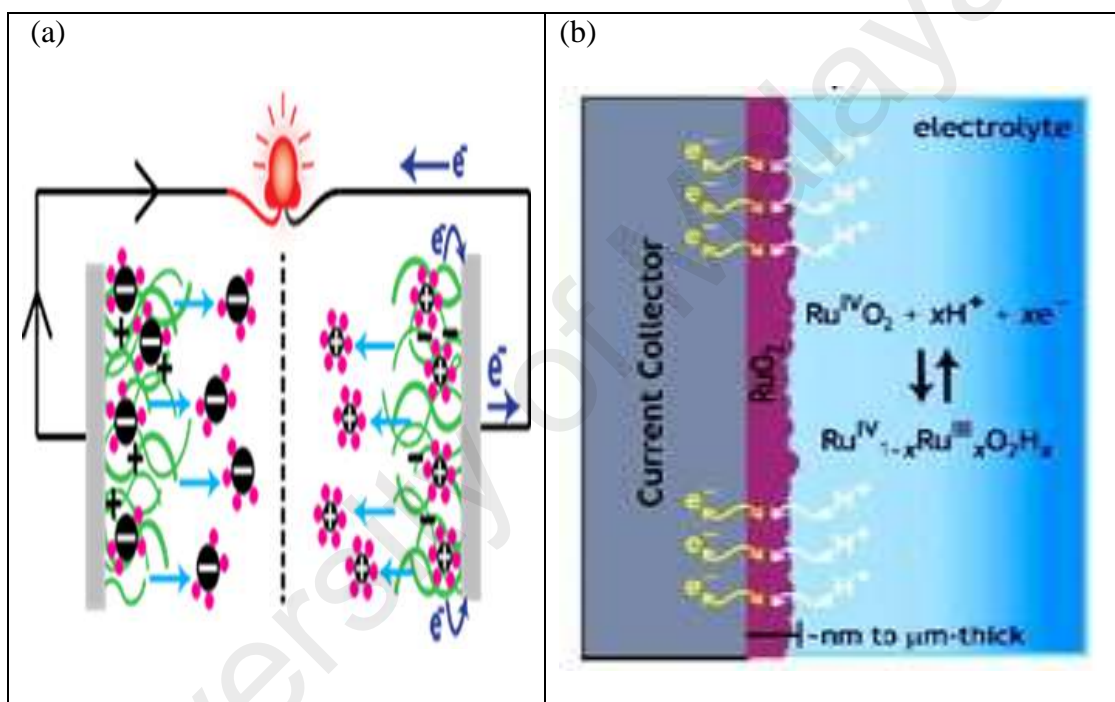
Figure 2.3: The mechanism of pseudocapacitor fabricated using (a) conducting polymer (Source: D'Arcy Research Lab) and (b) transition metal oxides (Nithya & Arul, 2016)

2.2.3.2 Non-Faradaic Process Supercapacitor

A supercapacitor that undergoes non-Faradaic process at its electrode is also known as EDLC. In short, the fabrication of EDLC has been a choice of application in this research because it possesses excellent advantages over Faradaic-type supercapacitor as tabulated in Table 2.2 (Inagaki et al., 2010; Pell & Conway, 2004; Zhang et al., 2009). On the other hand, Figure 2.4 summarizes the taxonomy of energy storage devices

discussed earlier and the basic components to fabricate an EDLC and its charge storage

mechanism will be discussed in details in Section 2.3.

Table 2.2: Comparisons of Faradaic and non-Faradaic process supercapacitors

Properties	Faradaic	Non-Faradaic
Power density	Low	High
Energy density	High	Low
Cycle-life	Short	Long
Thermal stability	Not consistent because it involves different activation energies and degradation processes	Consistent
Reversibility	Partially reversible because some residual electrode materials remained, which led to the loss of active materials, hence it limits the intrinsic electrode kinetic-rate	Highly reversible because it exhibits instantaneous electrostatic responses, hence it is kinetically stable and does not involve any phase changes
Working voltage	Lower than non-Faradaic process electrodes and electrolytic capacitor	Higher than Faradaic process electrodes but lower than electrolytic capacitor
Voltammogram shape	Exhibits mirror image with redox peak	Exhibits mirror image with redox peak (only if redox mediator has been added)
Cost	High (due to expensive materials such as conducting polymer, lithium metal and transition metal oxides)	Low
Safety	Poisonous (due to the use of transition metal oxide)	Environmental friendly
Fabrication	Electrode material and supercapacitor cell fabrication involves complicated steps	Fabrication of supercapacitor cell is facile
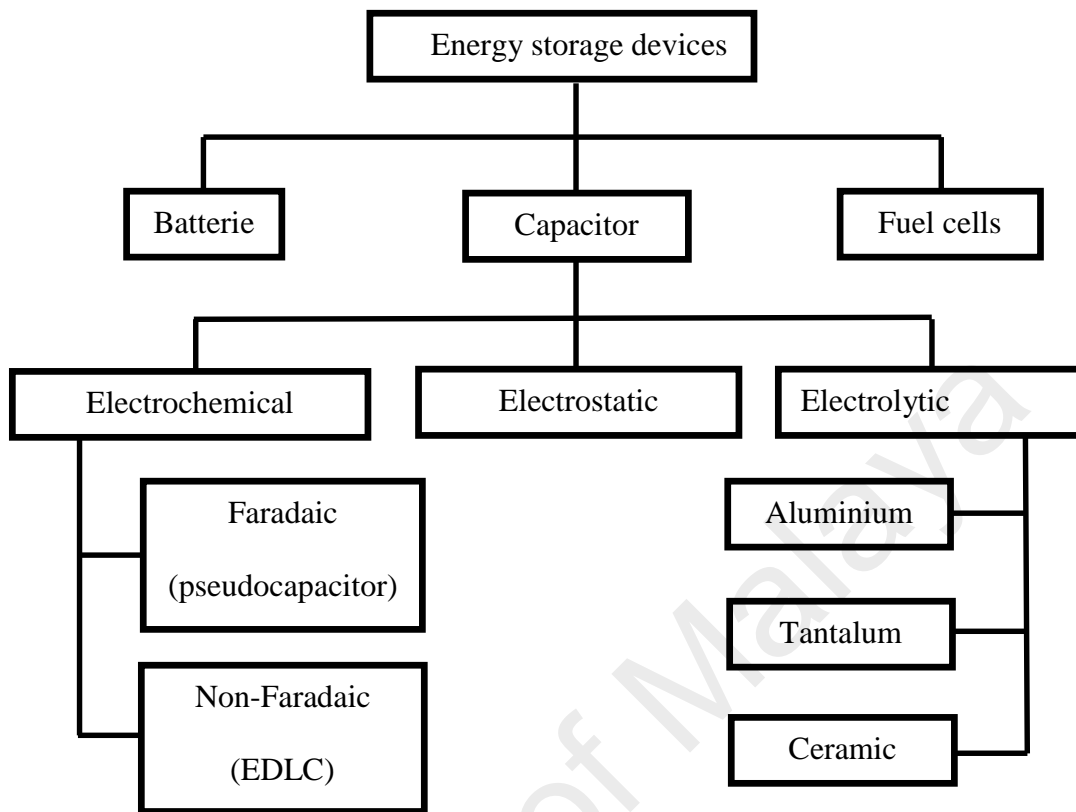
Figure 2.4: Taxonomy of energy storage devices

2.3   Electric Double Layer Capacitor

2.3.1   The charge storage mechanism of EDLC

The basic concept of charge storage mechanism in a supercapacitor is proposed by a German physicist, Hermann von Helmholtz (1879) based on an electrolytic capacitor. Figure 2.5(a) depicts the charge storage mechanism based on Gouy model. When voltage is applied, an electrode will be positively charged, hence the negatively charged ions from the electrolyte will be induced to its surface and adsorb strongly through chemical affinities. As a result, an electric double layer (EDL) (also known as inner Helmholtz plane) is formed at the solid electrode/electrolyte interface to store the electrical charge electrostatically. The electric potential drops linearly as the ions are going further from

the surface of the electrode. The capacitance value in the Hemholtz double layer (*C*) can be calculated by using Equation 2.1 (Zhang & Zhao, 2009):

$$C = k \frac{\varepsilon_0 A}{d}$$ Equation 2.1

where ε_0 is the permittivity of free space (8.854×10^{-12} F/m), k is the dielectric constant of the electrolyte, *A* is the surface area of the electrode (m^2) and *d* is the thickness of EDL (m) depending on the size of ions and the concentration of electrolyte.

However, after the Helmholtz model was proposed, it became realized that the electrolyte ions in the double layer would not remain static in a compact array but instead will be subjected to the effects of thermal fluctuation of the electrolyte ions (Namisnyk, 2003). By taking into account the effects of thermal fluctuation and the continuous distribution of the electrolyte ions, Gouy and Chapman modified Helmholtz's representation of a double layer. According to Gouy and Chapman model, "diffuse" double-layer (also known as outer Helmholtz plane layer) is formed due to the conjugation of counterions to the electrode as shown in Figure 2.5(b). At this point, the solvated counterions were assumed to be point charges with the electrolyte having a net charge density equal and opposite to the electrode surface. However, the attempt made by Gouy and Chapman was unsuccessful because it is not suitable to explain highly charged double layer.

Finally, in 1924, Otto Stern come up with his model (Stern model) as shown in figure 2.5(c) by combining both Hemholtz and Gouy-Chapman models. The Stern's model comprises of the inner and outer Helmholtz layers to explain the formation of EDL and its overall capacitance (C_{total}) can be calculated by Equation 2.2 (Frackowiak & Beguin, 2001; Sharma & Bhatti, 2010; Winter & Brodd, 2004):

$$C_{total} = \frac{1}{C_{(at\ inner\ Hemholtzlayer)}} + \frac{1}{C_{(at\ outer\ Hemholtzlayer)}} \qquad \text{Equation 2.2}$$

The Stern model of double layer remained as a good basis for general interpretation of the electrode/electrolyte interface phenomena until the detailed work of Grahame in the 1947 on the double layer capacitance.
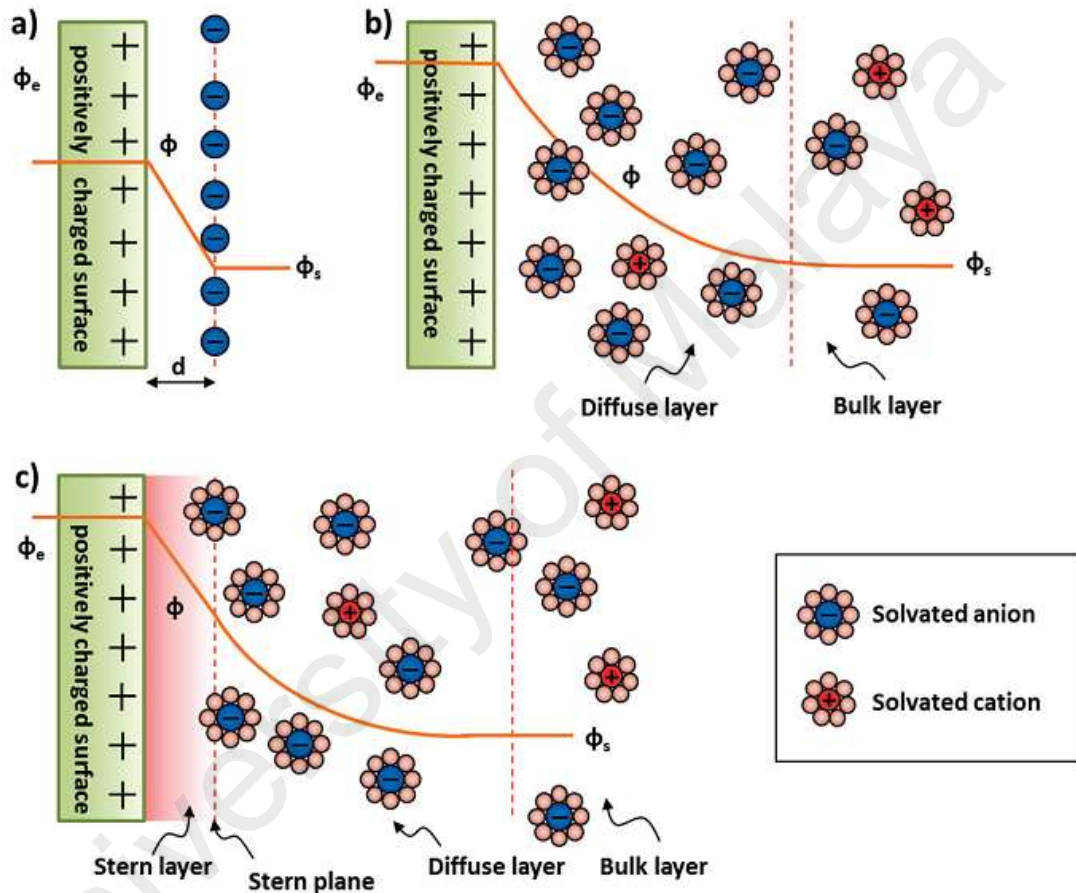
Figure 2.5: The charge storage mechanism in supercapacitor based on (a) Hemholtz model (b) Gouy-Chapman model and (c) Stern model (Frackowiak & Beguin, 2001)

2.3.2 Components for fabrication of EDLC
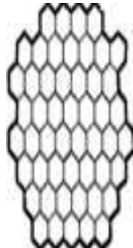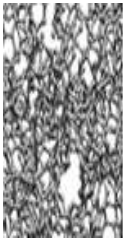
2.3.2.1 Electrode

Electrode play an important role in the construction of an EDLC because the storing capacity of an EDLC is partially influenced by the pore size of the electrode. Carbon has been the pioneer choice of electrode material to fabricate an EDLC owing to its stability (good corrosion resistance and able to withstand high temperature), abundance in nature,

inexhaustibility, high conductivity and enhanced electrochemical surface area (~1 to >2000 m^2/g) (Adhyapak et al., 2002; Pandolfo & Hollenkamp, 2006). Many approaches has been implemented for the fabrication of electrode by using novel carbon-based electrode materials. Recently highly conductive carbons such as activated carbon, carbon foams, carbon aerogels, carbon fibers, graphene and carbon nanotubes have been choices of electrode materials in order to enhance its electrochemical surface area. Also, modifications in the carbonaceous materials such as activation of carbon materials, incorporation of metal oxides and synthesize of tangled network with open central network has been conducted to tailor the desired pore size of the carbon electrodes for better entrapment of charge carriers. Table 2.3 shows the properties of different structure of carbonaceous materials used as electrode in EDLC (Simon & Gogotsi, 2012).

Table 2.3: Properties of different structures of carbonaceous materials used as electrode in EDLC

Material	Carbon onions	Carbon nanotubes	Graphene	Activated carbon	Carbide derived carbon	Template carbon
Dimension	0-D	1-D	2-D	3-D	3-D	3-D
Conductivity	High	High	High	Low	Moderate	Low
Volumetric capacitance	Low	Low	Moderate	High	High	Low
Cost	High	High	Moderate	Low	Moderate	High
Structure						

2.3.2.2 Separator

The mediator in the construction of an EDLC is a separator. It is located between the two electrodes which is not only to prevent the occurrence of electrical contact between them but also it provides medium for ion transportation. The specific requirements of a separator are low electrical resistance for ion transfer within the electrolyte while having a strong electronic insulating capability, high chemical and electrochemical stabilities in the electrolyte, good mechanical strength to provide device durability and low thickness (Schneuwly & Gallay, 2000; Zhong et al., 2015). Therefore, separators are usually made from thin and highly porous films or membranes. Commonly used separator materials in EDLC are cellulose, polymer membranes, glass fibre, paper, ceramic and polymer electrolyte.

As generally realized, the choice of separator materials depends on the type of electrode, working temperature and cell voltage (Bittner et al., 2012). Furthermore, the separator's properties such as chemical composition, thickness, porosity, pore size distribution and surface morphology were found to have a noticeable influence on several EDLC performance indicators including polarizability limits, specific capacitance, equivalent series resistance, specific energy and power densities (Tõnurist et al., 2012; Zhang et al., 2009)

2.3.2.3 Electrolyte

Nevertheless, the architecture of an EDLC is incomplete without an electrolyte because it controls the working voltage of the cell. Generally, two types of conventional electrolytes have been employed since the development of EDLC that are organic and aqueous electrolyte. The comparisons and examples of these conventional electrolytes have been summarized in Table 2.4 (Hall et al., 2010; Tanahashi et al., 1990; Xu, 2004). As a result, the shortcomings of the classical electrolytes (organic and aqueous) can be

overcome by adopting polymer electrolyte in the application of energy storage devices, which will be further elaborate in Section 2.4 (Hallinan Jr & Balsara, 2013).

Table 2.4: Comparisons and examples of conventional electrolytes

Properties	Conventional electrolytes	
	Organic	**Aqueous**
Potential window range	Wide (~ 3 V)	Narrow (~ 1.3 V) which is due to electrolysis of water
Ionic conductivity	Low	High
Electrical resistance	High	Low
Power density	Low	High
Energy density	High	Low
Viscosity	High	Low
Cost	High	Low and easy to manufacture
Risk and safety	Toxic, volatile and flammable	Nontoxic, nonvolatile and nonflammable
Examples	$[NH_4(C_2H_5)_4][BF_4]$, $[NH_4(C_2H_5)_4][CF_3SO_3]$, $[NH_4(C_4H_9)_4][BF_4]$, etc.	H_2SO_4, KOH, NaCl, etc.

2.4   Polymer Electrolyte

Polymer electrolyte was discovered in 1973 by Fenton et al. and he found out that alkali salts are soluble in polyethylene oxide. According to Nawaz et al. (2016), polymer electrolytes are conducting macromolecules upon doping of ionic salts into it. The polymer electrolytes gain its popularity among the researchers because they have potential in overwrite the role of classical electrolytes owing to its prominent features (easy to process, wide electrochemical window, capable to form thin film, etc.) (Sa'adun et al., 2014; Susan et al., 2005).

Polymer electrolytes will be categorized into five classes as below (Gray, 1997):

a) **Single phase polymer electrolyte** – a system (either solid or liquid) contains salt and polymer without any solvent.

b) **Gel polymer electrolyte** – is also known as dual phase system that is prepared by two steps. The first step is to prepare a conducting solution by dissolving salt and solvent (either polar or ionic liquid). The second step is to adjust the mechanical strength of the conducting solution by adding inert polymer.

c) **Plasticized polymer electrolyte** – is a system formed by adding either high dielectric constant solvent or ionic liquid to the other classes of polymer electrolyte.

d) **Ionic rubber polymer electrolyte** – is a system formed by adding small amount of high molecular weight polymer to a low temperature liquid mixture.

e) **Ion conducting polyelectrolytes** – is also known as single-ion conductors. It involves chemical interactions between ionic groups and the backbone of the host polymers.

Unfortunately, the polymer electrolytes suffer from low ionic conductivity which limits its wide usage in energy storage devices (batteries, fuel cells and supercapacitors), electrochromic devices, sensors and dye-sensitized solar cells. The best solution to this problem is to incorporate the innovative materials such as ionic liquids and inorganic fillers into the host polymer in order to assist the polymer electrolyte to fulfill its role in the aforementioned applications that will be discussed thoroughly in Sections 2.5.1 and 2.5.4, respectively. Prior to the application of a device, polymer electrolyte must fulfill three basic requirements concurrently that are:

a) Performance – the polymer electrolyte used must have good performance in terms of high ionic conductivity and wide potential window, which led to higher power output from the device (Quartarone & Mustarelli, 2011; Simon & Gogotsi, 2008).

b) Durability – the polymer electrolyte must possesses optimum mechanical strength and achieves highest compatibility with the electrodes to sustain its performance when it is subjected under operating conditions (i.e. operating temperature and electrochemical potential) (Wang, 2009).

c) Safety – the choice of polymer electrolyte and methods to be used for the application of devices have to be taken into account to prevent harm such as leakage, internal short circuit, use of corrosive solvent and production of hazardous gases (Scrosati, 1993).

In general, the polymer electrolytes for EDLCs can be classified to the types of host polymers used and its physical state.

2.4.1   Classifications based on Types of Host Polymer

The word 'polymer' comes from the Greek words *poly* (meaning 'many') and *meros* (meaning 'parts'). Polymers are very large molecules made when hundreds of monomers join together to form long chain. Monomers are small individual repeating units/molecules. Basically, the polymers used as the host polymer in preparing the polymer electrolytes for supercapacitor can be classified into two broad categories that are natural and synthetic polymers. Natural polymers are isolated from natural materials whereas synthetic polymers are the polymers synthesized from low molecular compounds. Mostly, all the natural polymers are biodegradable and on the other hand, synthetic polymers comprised of both biodegradable and non-biodegradable type of polymers. Figure 2.6 summarized the categories of polymer and its relevant examples.

Biopolymers from biomass:

Starch, Cellulose and its derivatives, Fibres, Chitin and chitosan, Gums, Agarose, corn, wheat and gluten, soyprotein, collagen and gelatin, casein and caseinates, whey proteins, cross-linked lipids

Biopolymers modified naturally or genetically organisms:

Poly(hydroxyalkanoates), poly-(3-hydroxybutyrate), poly(hydroxybutyrate-hydroxyvalerate), poly-(ε-caprolactone), bacterial cellulose, poly(lactic acid), poly(glycolic acid)

Poly(ethylene), poly(propylene), poly(urethane), poly(carbonate), poly(vinyl chloride) (PVC), poly(methyl metacrylate) (PMMA), poly(tetrafluoroethylene) (PTFE), poly(ethylene oxide) (PEO), poly(acrylonitrile) (PAN), poly(ethylene glycol) (PEG)

Poly(vinyl alcohol) (PVA), poly(vinyl acetate), poly(glycolic acid), poly(lactic acid) and their copolymers, poly(caprolactone), poly(butylene succinate), poly(succinate adipate)

Polymer → Natural → Biodegradable

Polymer → Synthetic → Non-biodegradable

Polymer → Synthetic → Biodegradable

Figure 2.6: Classifications of polymers and its relevant examples

2.4.1.1 Synthetic Polymer

Non-biodegradable synthetic polymers played their role as host polymer in the preparation of polymer electrolyte for EDLCs by virtue of their durability and highly resistant to all forms of degradation (Swift, 1993).

The most durable EDLC fabricated using PAN-*b*-PEG-*b*-PAN copolymer as polymer electrolyte demonstrated excellent stability of 30,000 cycles at current density of 12.5 A/g and working voltage of 2 V with negligible loss of capacitance retention. It achieved specific capacitance, energy density and power density of 101 F/g, 11.5 Wh/kg and 10 kW/kg, respectively at current density of 0.125 A/g (Huang et al., 2012). Despite, various non-biodegradable synthetic polymers has been utilized as the host polymer for EDLC such as PEO, PMMA, polyacrylamide, succinonitrile, poly(vinyl pyrrolidone)(PVP), poly(vinylidene fluoride-*co*-hexafluoropropylene) (PVdF-HFP), poly(2-hydroxylethyl methacrylate-*co*-methyl methacrylate), blend polymer of perfluorosulphonic acid and PTFE, etc. (Asmara et al., 2011; Kumar et al., 2012; Łatoszyńska et al., 2015; Rodríguez et al., 2013; Singh et al., 2015; Stepniak & Ciszewski, 2011; Subramaniam et al., 2011; Verma et al., 2014).

In order to reduce the environment problem and to maintain the superior performance of EDLC simultaneously, some researchers prepared polymer electrolyte by blending non-biodegradable and biodegradable polymers. However, the approach was unsuccessful because the specific capacitance and life cycle of blended polymer was very low. In the case of EDLC based on PEO/chitosan blend, the specific capacitance achieved was 106.5 mF/g with total 140 cycles at current density of 0.021 mA/cm^2 with potential window of 0 to 1 V (Shukur et al., Ithnin, 2013). The result obtained is lower than a previous work by Kumar & Bhat (2009b), in which they obtained specific capacitance of

40 F/g at 5 mV/s and 1,000 cycles at current density of 2 mA/cm^2 using blend polymer of PVA/polysulphonic acid.

Nonetheless, the use of non-biodegradable polymers create major disposal problem, expensive and severe depletion of petroleum resources incurs (Salleh et al., 2016; Swift, 1993). As a consequence, there is a need to switch to the use of biodegradable polymer in the preparing polymer electrolyte for EDLC.

2.4.1.2 Biodegradable Polymer

According to Swift (1993), biodegradable polymer are the polymers that are broken down partially or completely by enzymatic process into biologically acceptable molecules that will not hamper the environment and ecology system. Biodegradable polymers arise from natural polymers (also known as biopolymer) and synthetic polymers. They have been a promising candidate as the host polymer for EDLC because they are cheap (easily accessible and renewable source), environmental friendly by releasing minimum hazardous products and biocompatibility (Ramesh et al., 2012; Rozali et al., 2012; Stepniak et al., 2016).

Among the natural polymers, chitosan and starch gained the most popularity as host polymer for EDLC because they are capable to form a mechanically stable thin film and good solubility and electrolytic properties (Arof et al., 2010; Liew & Ramesh, 2015; Pawlicka et al., 2008; Stepniak et al., 2016; Yusof et al., 2014). Chitosan is a natural amino polysaccharide, which consists of β-(1→4)2-amino-2-deoxy-Ɖ-glucose-(Ɖ-glucosamine) repeating units, whereas starch is a mixture of amylose (poly-α-1,4-Ɖ-glucopyranoside) and branched amylopectin (poly-α-1,4-Ɖ-glucopyranoside and α-1,6-Ɖ-glucopyranoside). Chitosan has an extra eminent feature compare to starch because it can be modified through crosslinking and grafting owing to its amine and hydroxyl groups (Ngah et al., 2011). As a result, in early 2016, the most outperform green EDLC

is fabricated by using blend polymer of chitosan and chitin sponge. The EDLC can endure 10,000 cycles without any change in capacitance which is in line with high specific capacitance, energy and power densities of 97 F/g, 8.91 Wh/kg and 563 W/kg, respectively at constant current of 5 mA and working voltage of 0.8 V (Stepniak et al., 2016). The success of this EDLC is due to previous works on other natural polymers as host namely agarose (polysaccharides derived from seaweed), iota(ι)-carrageenan (sulfated polysaccharides derived from red edible seaweed), xanthan gum (polysaccharides secreted by the bacterium *Xanthomonas campestris*) and cellulose derivatives (hydroxylethyl cellulose, cellulose acetate and methyl cellulose) (Arof et al., 2010; Moon et al., 2015; Selvakumar & Bhat, 2008; Shuhaimi et al., 2012; Sudhakar et al., 2015a, 2015b).

On the other hand, PVA is the most attractive host polymer for EDLC among biodegradable synthetic polymers due to its water solubility and good mechanical property (Huang et al., 2014; Liew et al., 2015, 2016). According to the work by Fan et al. (2014), polymer electrolyte prepared by PVA with the presence of redox mediator (combination of KI and $VOSO_4$) attained the highest specific capacitance (1232.8 F/g) at current density of 0.5 A/g. The optimum energy density, power density and cycles achieved by this EDLC at 0.5 A/g were 25.4 Wh/kg, 190 W/kg and 3,000 cycles with 93.7 % capacitance retention, respectively.

In conclusion, the use of biodegradable polymer to prepare polymer electrolyte for EDLC is still new as not many biopolymers has been explored for energy storage application (i.e. poly(hydroxyalkanoates), lipids, poly(lactic acid), poly(glycolic acid), etc.). Also, there are plenty of room for improvement to overcome its limitations to create a benign environment. Thus, I continued my research in the exploration and improvement of cellulose derivatives (HPMC and HEC) as host polymer for EDLC which was

influenced by the great success of chitosan/chitin sponge polymer electrolyte. Both chitosan and chitin have many electron-donating atoms (oxygen and nitrogen) that provide spaces for adsorption of charge carriers. The unique property in both chitosan and chitin is found in the cellulose derivatives chosen. Hence, one of the most important criteria (high ionic conductivity) of polymer electrolyte will be fulfilled. Likewise, PEO became the primordial polymer electrolyte in view of its charge carrier adsorption area that is ether group (C–O–C) (Karan et al., 2008; Zhang et al., 2008). Figure 2.7 depicts the structure of chitosan, chitin, HPMC and HEC.
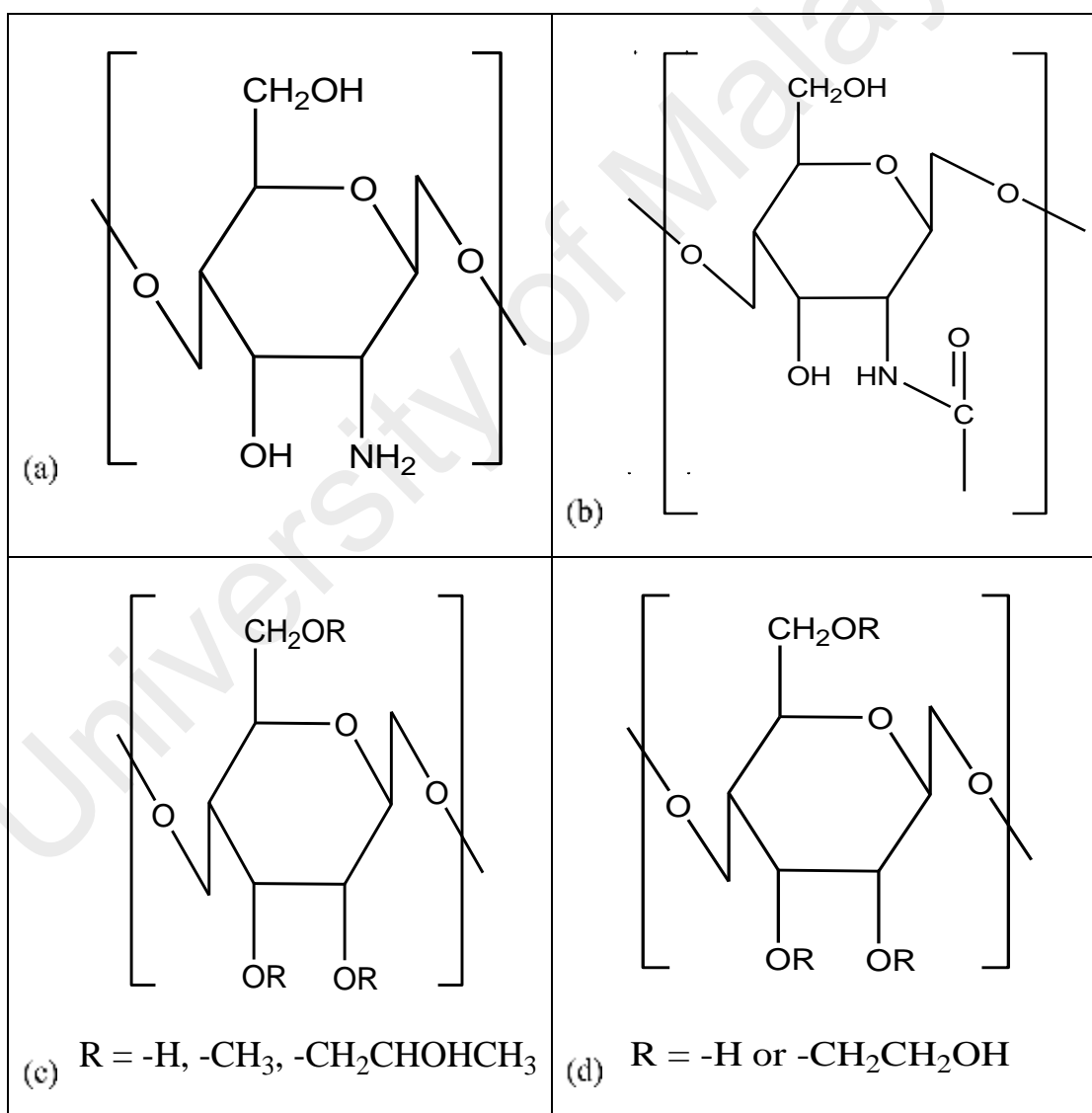
Figure 2.7: Structure of (a) chitosan (b) chitin (c) HPMC and (d) HEC

(a) Hydroxylpropylmethyl Cellulose (HPMC)

Hyroxylpropylmethyl cellulose is one of the cellulose derivatives derived from the structure of natural cellulose by substituting the −OH group with −OR group (R is the residual group) in the cellulose. The HPMC (termed as hypromellose) is obtained by chemically linking hydroxypropyl and methyl groups to the β-1,4-D-glucan cellulosic backbone as the R group. The R group in HPMC polymer is 2-hydroxypropyl, in which it can be classified as secondary alcohol due to the position of hydroxyl group and it exhibits greater steric hindrance due to the presence of two methyl groups. Additionally, the amphiphillic properties of HPMC can be manipulated by adjusting the ratio of propyl to methyl during chemical linking and by changing the temperature (Chen et al., 2009; Hager & Arendt, 2013). It is an important asset for HPMC as it broadens the choice of utilizing environmental friendly solvents for dissolution (Vila et al., 2007). Furthermore, the presence of hydroxylpropyl and methyl groups on the cellulose chains enhance its surface activity, which leads to good adsorption of ions on the polymer (Chen et al., 2009). On top of that, HPMC is a very versatile material as it is available in a wide range of molecular weight, non-toxicity, and cost-effectiveness (AlKhatib et al., 2008; Goodwin et al., 2011; Pani & Nath, 2014; Seyedlar et al., 2014). Hence, it has been widely used in pharmaceutical film coating mainly for esthetic and protective reasons, hydrophilic matrix drug delivery systems, and the preparation of edible films in food industry (Cespi et al., 2011; Goodwin et al., 2011; Jiménez et al., 2010; Pani & Nath, 2014; Seyedlar et al., 2014).

(b) Hydroxylethyl Cellulose (HEC)

Hydroxylethyl cellulose is one of the cellulose derivatives, in which the H atom in the cellulose is replaced by 2-hydroxylethyl as the R group. Thus, HEC possesses unique physicochemical properties due to the large amount of hydroxyl groups compared to cellulose and its derivatives. Consequently, it assists in the adsorption of charge carriers

through ion-dipole interaction, which results in the improvement of charge storage capacity (Li et al., 2014). These distinct features due to unique structure and environmental friendly nature makes it suitable candidate for energy storage applications. On top of that, HEC is a versatile polymer owing to its prominent features like green material with excellent biocompatibility and solubility in water, easy availability and low cost (Zulkifli et al., 2013). Due to its influential properties, it is widely used in pharmaceutical and food industry, zinc–carbon battery (as an organic inhibitor), proton conducting EDLC, composite for relative humidity sensor and polymer light-emitting diodes (Deyab, 2015; Lokman et al., 2015; Sudhakar et al., 2015b; Taghizadeh & Seifi-Aghjekohal, 2015; Wu & Chen, 2015).

2.4.2 Classifications based on Types of Physical State

The polymer electrolyte used in EDLC can be categorized into three types of physical state namely liquid, gel and solid polymer electrolyte.

2.4.2.1 Liquid Polymer Electrolyte (LPE)

The glory of SPE and GPE in any field is fueled by the fundamental studies using LPE. The fundamental studies are designed to support the mechanism of ion-conduction and the interactions between ion-ion and ion-polymer. The behavior of LPE depends on the molecular structure, transition glass temperature (T_g) and its dynamics. At any temperature above T_g, a low molecular weight polymer exhibits a viscous liquid. On the other hand, a high molecular weight polymer becomes rubbery at temperature greater than T_g. The effects arise from the chain entanglement. LPE is unattractive in EDLC because it suffered from leakage, although it exhibits extreme high ionic conductivity (Raghavan et al., 2010; Ye et al., 2013).

2.4.2.2 Gel Polymer Electrolyte (GPE)

Gel polymer electrolyte (GPE) also known as plasticized polymer electrolyte gained its fame in order to overcome the flaws in SPE for EDLC. It was first introduced in 1975 by Feuillade and Perche by virtue of its prominent features over SPE and liquid polymer electrolyte (LPE) (Feuillade & Perche, 1975). A GPE exhibits high ionic conductivity at room temperature and good adhesive properties over SPE, still it enhances safety by preventing leakage problem in LPE (Kim et al., 2003; Kumar & Bhat, 2009a).

A GPE is prepared by entrapping a liquid electrolyte (an ionic or organic salt is dissolves into either a polar or nonpolar solvent) in a host polymer network with the help of incorporating either high dielectric constant plasticizer or ionic liquid through solution casting technique and swelling (Asmara et al., 2011; Pandey & Hashmi, 2013b; Yang et al., 2014). Both plasticizer and ionic liquid act as a lubricant by reducing the rigidity of the polymer chain (Chupp et al., 2015; Kumar et al., 2012). The commonly used plasticizers are mixture of EC/PC, mixture of EC/DEC, dibutyl phthalate and glycerol whereas the use of ionic liquids depends on the nature of host polymer, salt used and its applications (Asmara et al., 2011; Kumar & Bhat, 2009a; Ramesh et al., 2013; Sudhakar et al., 2015a; Yamagata et al., 2013).

The GPE prepared by xanthan gum incorporated with $Li_2B_4O_7$ and glycerol as plasticizers exhibits the highest ionic conductivity at ambient temperature (2.2×10^{-2} S/cm). It was then used to fabricate EDLC and achieved specific capacitance of 82 F/g at scan rate of 5 mV/s. Another example of good performance EDLC based on GPE reported by Pandey et al. (2010a) achieved the cycling stability greater than 50,000 cycles at current density of 1.0 mA/cm^2 and working potential of 2.0 V. Also, it achieved high ionic conductivity at room temperature (8.0×10^{-3} S/cm), high energy density (17 Wh/kg) and high power density (13 kW/kg). Recently, a new technique known as

electrodeposition has been developed to enhance the performance of EDLC and to overcome the poor mechanical strength of GPE caused by impregnation of plasticizer or ionic liquid (Kim et al., 2008; Zhang et al., 2011). In this technique, the ionic salt and host polymer are electrodeposited on the electrode directly. Hence, it saves energy and materials because it can reduce the cumbersome of incorporation plasticizer or ionic liquid. As a result, the GPE prepared fulfills the criterions of EDLC, that are good specific capacitance and cycling stability of 65.9 F/g at 0.1 A/g and 10,000 cycles with 90 % capacitance retention at 1 A/g (Jiang et al., 2016).

2.4.2.3 Solid Polymer Electrolyte (SPE)

The first solid polymer electrolyte also known as "dry solid" polymer electrolyte by Fenton et al. was discovered in 1973 as mentioned earlier. The commonly used method to prepare SPE for EDLC is solution casting technique. The word solution casting indicates that this technique consists of two steps. The first step is to prepare a miscible solution by adding appropriate amount of salt and polymer into solvent. Then, the mixture is stirred magnetically until a homogeneous solution is formed. Subsequently, the well stirred solution is poured into a Petri dish and sufficient drying time is given for the development of a thin film.

Despite, researchers are trying to create a better interfacial contact between the SPE and electrodes and thereby hot-press (extrusion) technique has been introduced and innovated aside from solution casting technique (Gray et al., 1986; Pandey et al., 2008). Basically, hot-press technique consists of two steps. The first step involves physical mixing of appropriate amount of salt and polymer prior to melt the mixture at the melting point of polymer. The slurry obtained is pressed between two cold metal blocks to form a uniform thin film. The advantages of hot-press technique are cheap, less hassle, fast, uniform thickness of thin film, solvent free and a completely dry technique. However, the

attempt to prepare SPE for EDLC by using hot-press method needs to be polished because it achieves low specific capacitance. It was proven from the work reported by Verma et al. (2014) using PEO, AgI and activated carbon for the fabrication of EDLC. As a result, the EDLC obtained low specific capacitance of 5 F/g with high ionic conductivity at room temperature (1.92×10^{-3} S/cm).

Various SPEs have been prepared for EDLC owing to its unique properties such as light in weight, easy to handle, flexible, leak-proof, excellent dimensional and electrochemical, good safety performances and long cycle life (Adebahr et al., 2003; Liew & Ramesh, 2014, 2015; Nicotera et al., 2006; Pandey et al., 2011; Yusof et al., 2014). However, SPE suffered from poor ionic conductivity (10^{-8} and 10^{-7} S/cm) and thereby many efforts have been implemented to curb the problems which will be discussed in details in Section 2.5 (Arof et al., 2010). Consequently, the ionic conductivity of SPEs at room temperature improved to 10^{-4} and 10^{-3} S/cm and they are suitable for EDLC and other energy storage devices (Murata et al., 2000).

The biodegradable SPE prepared by Kumar & Bhat (2009b) obtained the highest ionic conductivity of 2.0×10^{-2} S/cm at room temperature using PVA/polystyrene sulphonic acid blend and it was followed by the biodegradable SPE prepared by Liew et al. (2015) using PVA and ammonium acetate ionic conductivity of 9.3×10^{-3} S/cm at room temperature. On the contrary, the SPE prepared by non-biodegradable PEO and 1-ethyl-3-methylimidazolium hydrogensulfate achieved ionic conductivity of 2.2×10^{-3} S/cm at room temperature (Ketabi & Lian, 2013). In summary, biodegradable polymers are found to be more suitable in preparing high ionic conductivity SPE for EDLC rather than non-biodegradable polymers. Similarly, improvement need to be taken into considerations for the sake of the energy and power densities with a remarkable cycling stability.

2.5   Methods to Improve Ionic Conductivity

As aforesaid in Section 2.4.2.1, there is a need to improve the ionic conductivity of SPE for EDLC. Hence, various methods has been implemented by the researchers such as incorporation of ionic liquid, preparation of blend polymer and copolymer and incorporation of nanoparticles.

2.5.1   Incorporation of Ionic Liquids

Ionic liquids also known as room temperature ionic liquids because some of the salts have melting temperature at room temperature and below $100\degree C$. The ILs have been widely used as reaction media for organic synthesis and biochemical processes, extraction solvent for chelate and metal, polymer electrolytes for energy storage devices and dye-sensitized solar cell (DSSC), biological applications (i.e. drug delivery and activating agent for enzymes) and biomass processing applications (i.e. conversion of biomass for biofuel and bio-oil) by virtue of their marvelous properties such as large electrochemical potential window, negligible vapor pressure, high thermal stability and high ionic conductivity (Armand et al., 2009; Ma et al., 2016; Patel & Lee, 2012).

Figure 2.8 represents the classification of IL based on types of cation. Generally, the cations in ILs are predominantly nitrogen heterocycles and it can be categorized into pyrrolidinium, imidazolium, and piperidinium types of cation. Pyrrolidinium and piperidinium are saturated alicyclic whereas imidazolium is unsaturated alicyclic. Both pyrrolidinium and piperidinium are stronger Lewis base than imidazolium. As a result, pyrrolidinium and piperidinium create stronger interaction with its counter ion than imidazolium. Thus, the dissociation of imidazolium from its counter ion is easier which is in accordance to Osada et al. (2016) as depicted in Figure 2.9. Consequently, imidazolium type of ILs (1-butyl-3-methylimidazolium trifluoromethanesulfonate (BMIMTf) and 1-ethyl-3-methylimidazolium trifluoromethanesulfonate (EMIMTf))

have been a choice of IL in this research because it is believed to improve the ionic conductivity of the polymer electrolyte for EDLC. The choice made was corroborated from the reported works upon doping of imidazolium type of ILs on polymer electrolyte for EDLC (Chupp et al., 2015; Kumar et al., 2012; Liew & Ramesh, 2014, 2015; Liew et al., 2014; Liew et al., 2016; Pandey et al., 2010a; Pandey et al., 2010b; Ramesh et al., 2013). The structures of BMIMTf and EMIMTf ionic liquids are shown in Figure 2.10.

The highest ionic conductivity at ambient temperature (1.6×10^{-2} S/cm) was achieved by Yamagata et al. (2013) upon incorporation of EMIMBF$_4$ into chitosan-based EDLC. Nevertheless, it obtained specific capacitance (131 F/g) with 2.5 V working voltage at current density of 2.5 mA/cm^2 and 5,000 cycles with 99.9 % coulombic efficiency at 12.5 mA/cm^2. In conclusion, ILs act as a plasticizer in the preparation of polymer electrolyte for energy storage devices and DSSC. As a result, it increases the flexibility of the host polymer, hence the ionic conductivity at room temperature improves (Yang et al., 2014).
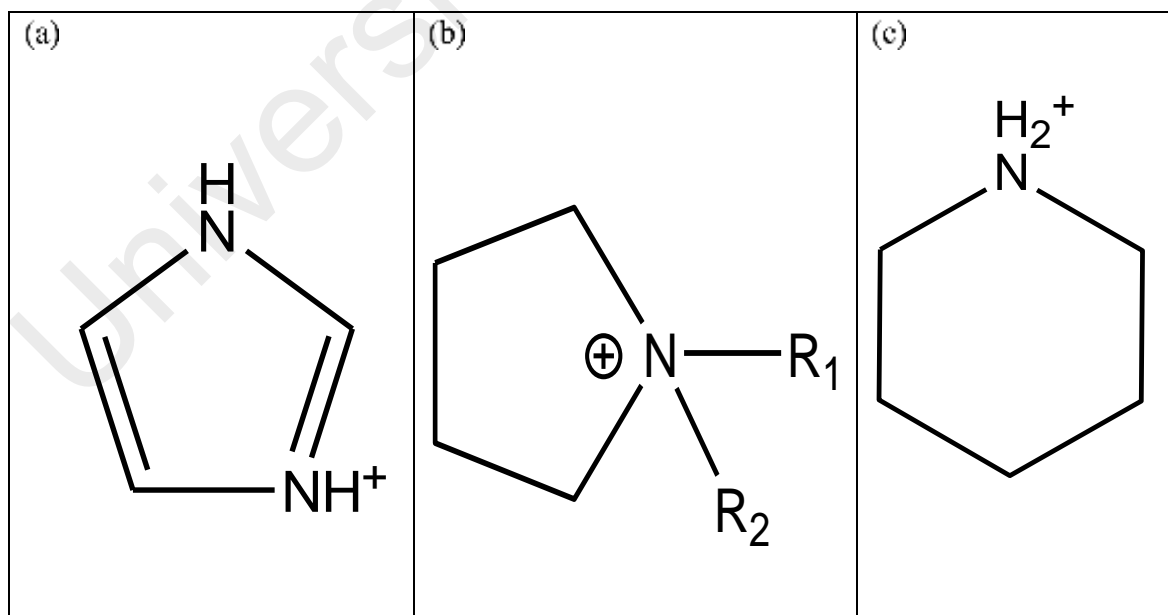
Figure 2.8: The structure of (a) imidazolium (b) pyrrolidinium and (c) piperidinium
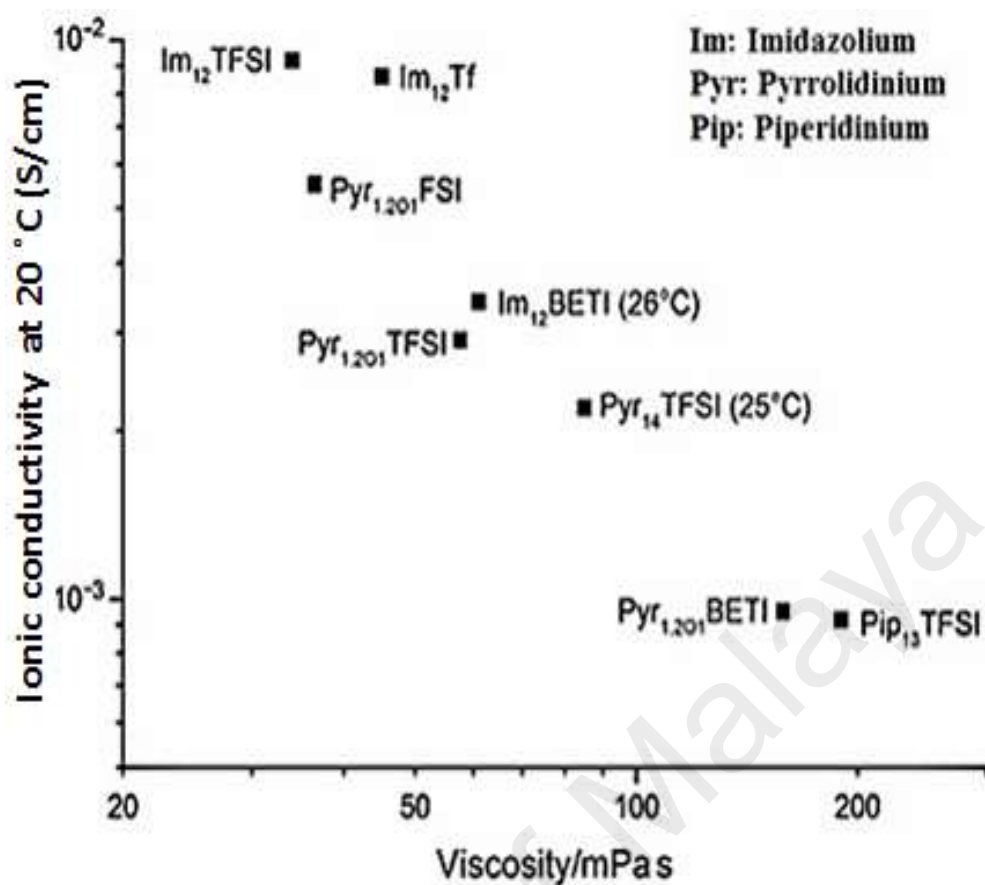
Figure 2.9: Relationship between ionic conductivity and viscosity of imidazolium, pyrrolidinium and piperidinium ILs (Osada et al., 2016)
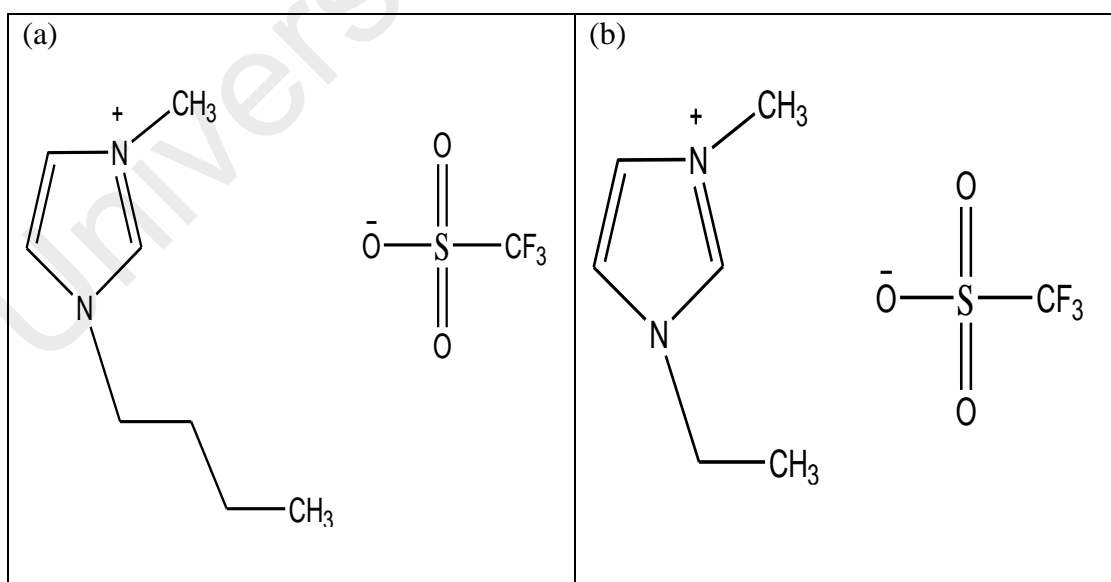
Figure 2.10: Structure of (a) BMIMTf and (b) EMIMTf ionic liquids

2.5.2   Polymer blends

Polymer blending is a process to modify new class of polymers through physical mixing of two or more polymers. The first polymer blend between natural rubber and gutta-percha was patented in 1846 by Parkes (Utracki & Wilkie, 2002). The selection of polymers for blending depends on the desired application. Polymer blends can be classified into 4 categories as follows:

a) **Immiscible Polymer Blends** – The blends exhibit phase separation between them with various amount of T_g values. The number of T_g values are directly proportionate to the number of polymers used for blending.

b) **Miscible Polymer Blends** – The blends exhibit single-phase (homogeneous) structure with one T_g value.

c) **Compatible Polymer Blends** – The immiscible blends exhibit macroscopic uniform physical properties caused by strong interface interactions between the polymers.

d) **Compatibilized Polymer Blends** – The immiscible blends exhibit microscopic uniform physical properties caused by adding compatibilizers (surface-active species) which influences various morphological processes (i.e. deformation, breakup and coalescence of droplets).

The benefit of polymer blends is to create materials with combinations of better mechanical, chemical and versatile properties than the individual polymer. Moreover, it is cheaper to modify the existing polymer rather than invent a new monomer or polymer (Kadir & Arof, 2011; Parameswaranpillai et al., 2014).

Hence, it motivates the researchers to look into this method to improve the ionic conductivity of SPEs for EDLCs instead of all aforementioned advantages. In polymer blends, the amount of spaces for absorption of charge carriers increases which result in

the enhancement of ionic conductivities (Kumar & Bhat, 2009b). In addition to this, there are assorted polymer blends developed by the researchers for EDLCs such as chitosan/PVA, chitosan/PEO, chitosan/κ-carrageenan, chitosan/iota (ʟ)-carrageenan, chitosan/starch, chitosan/sponge chitin, PVA/polystyrene sulphonic acid, PVdF-HFP/PVP, perfluorosulphonic acid/PTFE, polyethylene glycol diacrylate/PVdF/PMMA, PVC/PMMA, PVC/PEO, etc. (Arof et al., 2010; Kadir & Arof, 2011; Kumar & Bhat, 2009b; Ramesh et al., 2007; Ramesh et al., 2007; Shuhaimi et al., 2008; Shukur et al., 2013; Shukur & Kadir, 2015; Stepniak et al., 2016; Subramaniam et al., 2011; Sudhakar & Selvakumar, 2012; Syahidah & Majid, 2013; Yang et al., 2005; Yusof et al., 2014). The most outstanding polymer blends is chitosan/sponge chitin, in which chitin has been reinforced into chitosan in order to troubleshoot the mechanical instability of chitosan upon swelling. As a result, EDLC based on polymer blends exhibits a preferable performances (high ionic conductivity, specific capacitance, energy density, power density and excellent cycling stability) over EDLC based on single polymer.

2.5.3   Copolymerization

Copolymerization is a method to form a copolymers, which is formed when two or more monomers combined chemically. According to Mayo & Walling (1950), the reaction of copolymerization was first described in 1914 by Klatte using vinyl esters as monomer. The advantages of copolymers are similar to polymer blends as mentioned in Section 2.5.2. Copolymers can be classified into 6 categories as follows (Ring et al., 1985):

a) Unspecified arrangement of monomeric unit copolymers – the polymers that has unspecified sequence arrangement of monomers.

-A-B-A-B-A-B-A-A-A-B-B-B-A-B-B-A-

b) Statistical or random copolymers – polymers that has sequential distribution of monomers based on statistical laws. It was prepared by simultaneous polymerization of two or more monomers randomly.

-A-A-B-B-B-A-A-B-

c) Alternating copolymers – polymers that has alternating sequential distribution of two or more monomers regularly.

-A-B-A-B-A-B-A-B-A-B-A-B-A-B-

d) Periodic copolymers – polymers that has ordered sequential distribution of two or more monomers periodically.

-AAB-AAB-AAB-AAB-AAB-AAB-
-AB-AB-AB-AB-AB-AB-AB-AB-
-ABAC-ABAC-ABAC-ABAC-ABAC-

e) Block copolymers – polymers that has linear arrangement of blocks.

-AAAAAA-BBBBBB-AAAAAA-BBBBBB-

-ABABBB-AAAAAA-BBBBBB-AAAAAA-

f) Graft polymers – polymers that has one or more species of block (side chains) connected to the main chain. Both side and main chains have different features from each other.

```
-AAAAXAAA-AAAAXAAA-AAAAXAAA-
        |           |           |
        B           B           B
        B           B           B
        B           B           B
        B           B           B
        B           B           B
        |           |           |
```
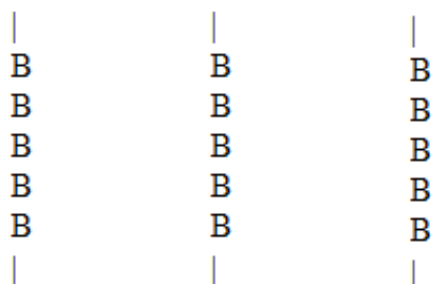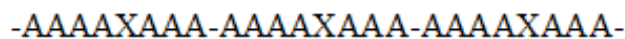
g) Condensed polymers – polymers formed through condensation of two or more monomers with different functional groups by elimination of molecules (either water or ammonia). A condensed polymers also can be formed through a single monomer with two different functional groups in it.

$$-CO-R-CONH-R'-NH-CO-R-CONH-R'-NH-$$

The most frequently used copolymer as polymer electrolyte for EDLC is PVdF-HFP because it has mediocre properties of crystalline and amorphous from PVdF and HFP, respectively (Fattah et al., 2016; Kumar et al., 2012; Pandey & Hashmi, 2013a, 2013b; Pandey et al., 2010a, 2010b; Ramesh & Lu, 2012). The use of PVdF-HFP as host polymer in polymer electrolyte has been widespread because it contains seven fluorine atoms per monomer for adsorption of charge carriers, which is believed to improve the ionic conductivity, large porosity, low T_g (–62 $^{\circ}$C) and high dielectric constant (~8.4) (Baskaran et al., 2006; Mishra et al., 2013; Sim et al., 2016). The GPE prepared by PVdF-HFP and 1-ethyl-3-methylimidazolium tetracyanoborate exhibits the highest ionic conductivity of 9.0×10^{-3} S/cm at room temperature. However, the GPE suffered from poor performance in cycling stability. In another case, the GPE prepared using PVdF-HFP, LiTf, EMIMTf and a mixture of EC/PC plasticizer was fabricated for EDLC. The cycling stability of the GPE improved to 50,000 cycles at 1 mA/cm^2 with working voltage of 2.0 V. Nevertheless, the best performed EDLC was attained by using copolymer of PAN-*b*-PEG-*b*-PAN as discussed in Section 2.4.1.1.

2.5.4   Incorporation of Nanoparticles

Embedding numerous types of nanoparticles into polymer electrolyte for energy storage devices (fuel cells, lithium ion batteries and proton conducting secondary batteries) is not new (Agrawal & Pandey, 2008; Croce et al., 1998). It starts gaining interests among the researchers as one of the methods to boost ionic conductivity and

mechanical strength of polymer electrolyte at room temperature by maintaining the porous network of the host polymer (Mishra et al., 2013). The porous networks assist polymer electrolyte in trapping the ions that lead to the enhancement of electrolyte uptake. Besides boosting the ionic conductivities of the polymer electrolyte, the mechanical strength, thermal, electrochemical and interfacial stability between electrode and electrolyte improved concurrently upon incorporation of nanoparticles (Calebrese et al., 2011; Jian-hua et al., 2008; Kim et al., 2002; Krawiec et al., 1995; Tang et al., 2012). The nanoparticles successfully increase the ionic conductivity at room temperature of the polymer electrolyte can be categorized into:

a) Inert nanoparticles (SiO_2, Al_2O_3 and TiO_2) − the filler particles behave like solid plasticizers, in which it reduces the crystallinity of the host polymer (Croce et al., 1999; Kumar & Rodrigues, 2001; Shin & Passerini, 2004).

b) Functionalized ceramic filler super-acid sulfated-zirconia (SO_4^{2-}–ZrO_2) − the filler has specific surface state condition that creates pathway for the migration of cations (Croce et al., 2006).

c) Ferroelectric nanoparticles ($BaTiO_3$, $PbTiO_3$ and $LiNBO_3$) − the filler has been used widely in the electronics industry for transducers and actuators because of high dielectric constant (Matsui, 2005; Sun et al., 2000; Sun et al., 1999).

d) High dielectric constant nanoparticles (ZrO_2 and TiO_2) − the filler decrease the viscosity of the polymer electrolyte and limit the interactions between cation and anion of the salt (Kumar et al., 2012; Morita et al., 2001).

e) Carbon-based nanoparticles (graphene sheets, carbon black, carbon nanotubes and carbon nanofibers) − the surface of the filler are functionalized to adsorb more charge carriers. In addition, they are highly conducting (Kuilla et al., 2010).

However, the development of integration of nanoparticles into the polymer electrolyte for EDLC is still new because it was investigated by a handful researchers. Up until now, the nanoparticles that has been incorporated into the polymer electrolyte for EDLC are fumed SiO_2, TiO_2 and Sb_2O_3 (Ketabi & Lian, 2013; Lim et al., 2014a; Lim et al., 2014b; Teoh et al., 2015). The merit of fumed SiO_2 was unworkable without PEO (host polymer) and [EMIM][HSO$_4$] (charge carriers) and thereby the highest ionic conductivity achieved at room temperature was 2.2×10^{-2} S/cm. Also, the EDLC was stable at high scan rate of 1,000 mV/s in which it maintained its rectangular shape of CV with specific capacitance of 2.0×10^{-3} F/cm^2 from the 1st cycle to the 5,000th cycles (Ketabi & Lian, 2013). In another case, the energy density and power density of EDLC based on PVA, LiClO$_4$ and TiO_2 nanoparticles were 1.56 Wh/kg and 198.7 W/kg, respectively at 1 mA/cm^2. It is stable up to 1,000 cycles with 90 % of coulombic efficiency. Although, both the EDLCs incorporated with fumed SiO_2 and TiO_2 nanoparticles performed lower than the other EDLCs, still, it has many room for improvement because only few metal oxides nanofillers has been explored in this field. As a result, three inorganic nanoparticles, namely fumed SiO_2, CuO and Y_2O_3 from group 14 (*p*-block), group 11 (*d*-block) and group 3 (*d*-block also known as rare-earth), respectively have been studied in this research.

2.5.4.1 Fumed Silica (Fumed SiO₂)

Figure 2.11 illustrates the classifications of silica based on its processes (Merget et al., 2002). Fumed SiO_2 nanoparticles is an amorphous silica without any impurities (crystalline silica) (Rahman & Padavettan, 2012). It is a hydrophilic metal oxide because the reactive silanol group (Si–OH) on its surface forms hydrogen bonding (Kim et al., 2015; Osińska et al., 2009). Additionally, it has large surface contact area which improves the ionic conductivity of the polymer electrolyte. Thus, it led to the superior interfacial stability (Ramesh & Liew, 2012; Tang et al., 2007).
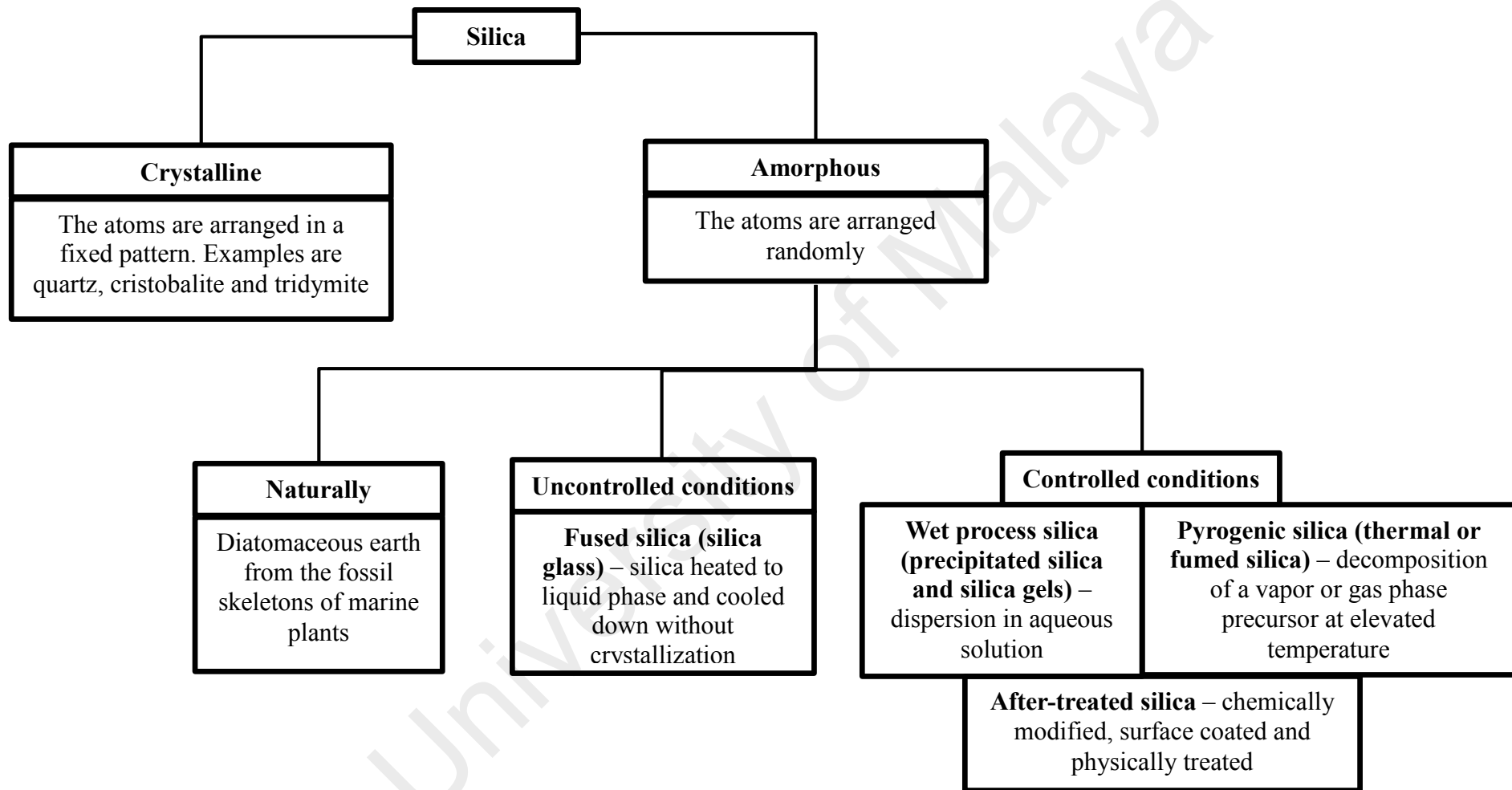
Figure 2.11: Classifications of silica based on its processes

Therefore, fumed SiO$_2$ has been widely used as reinforcing filler for silicon rubber, high and low temperature resistant elastomer (in wires, cables and automotive components) and thermal insulation materials, thickening and anti-setting agents in liquid systems (coatings, adhesives, printing inks, cosmetics, foods and fire extinguisher powders) (Ng et al., 2013).

2.5.4.2 Copper(II) Oxide (CuO)

Copper is a d-block element with electronic configuration of [Ar]3d^{10}4s^1. It is a p-type semiconductor which has ability to promote the transfer of electrons that leads to the improvement in electrochemical activity and thus it performs better in non-enzymatic glucose sensing, catalytic activities, solar cells and electrodes for lithium batteries (Carnes & Klabunde, 2003; Frietsch et al., 2000; Sau et al., 2010; Song et al., 2013). The merit of CuO nanoparticles in the aforesaid applications is owing to their greatest achievement as a cheap and effective antimicrobial agent since prehistoric time (Ingle et al., 2014). Additionally, the utilization of CuO nanoparticles in optical properties and nanofluids are due to its thermal dependence of magnetic properties (Yu & Xie, 2012). Figure 2.12 summarizes the field of application of CuO nanoparticles based on the publications indexed by Thomson Reuters ISI Web of Science in March 2013 (Bondarenko et al., 2013).

2.5.4.3 Yttrium(III) Oxide (Y$_2$O$_3$)

Yttrium is a rare-earth element that has electronic configuration of [Kr]4d^{1}5s^2. It has similar chemical properties as lanthanide elements such as excellent chemical and physical properties, high refractive index, exceptionally high melting point (~2430 °C), excellent mechanical properties and exhibit good ionic conductivity (Cheng et al., 2006; Juying et al., 2011; Shon et al., 2012). According to Langjahr et al. (2001), Y$_2$O$_3$ nanoparticles stabilized with zirconia films is well-known for its application as thermal

barrier coatings for gas turbine parts. Despite, it has been used as antireflective coatings for large area chemical vapor deposition diamond optical components and cathode materials for lithium batteries owing to its high mechanical durability (Aghazadeh et al., 2013; Mollart & Lewis, 2001). The chemical properties in their $4f$ electrons makes it suitable candidate as host lattice for the luminescence materials and as superior phosphors (Feng et al., 2010; Jia et al., 2008).
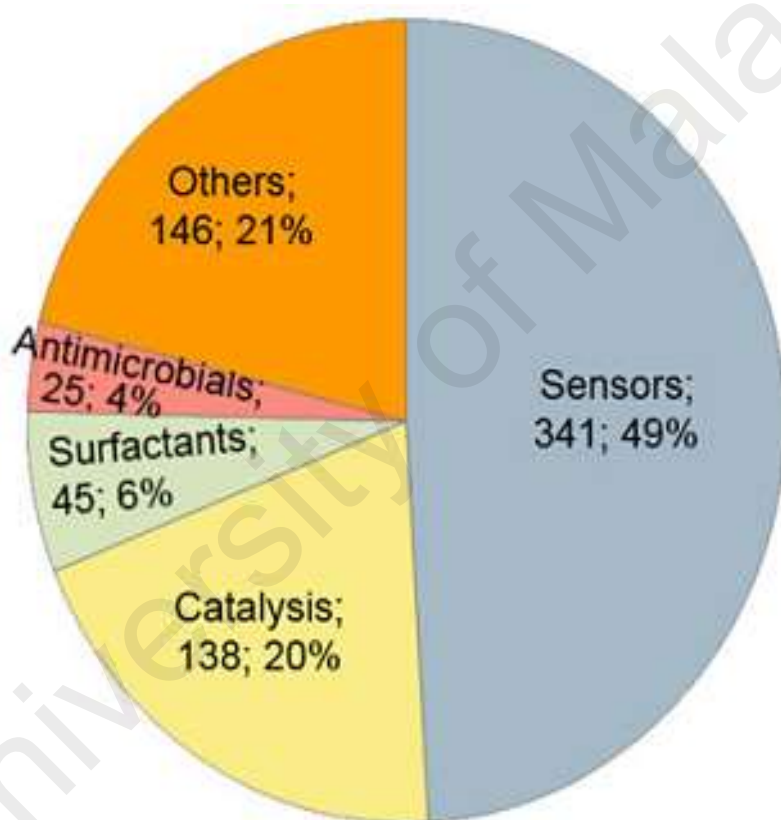
Figure 2.12: Field of application of CuO nanoparticles based on the publications indexed by Thomson Reuters ISI Web of Science in March 2013 (Bondarenko et al., 2013)

CHAPTER 3: METHODOLOGY

3.1   Introduction

This chapter is divided into three parts. The first part consists of the brief introduction of all the materials used in this study whereas the second part describes the preparation of solid polymer electrolyte and its characterization techniques (EIS, XRD, FTIR and TGA). The methods to fabricate EDLC and its performance studies (CV, EIS and GCD) are covered in the last part of this chapter.

3.2   Materials

Table 3.1 depicts the list of materials used in the preparation of SPE and fabrication of EDLC.

3.3   Research Outline

The research outline consists of three parts. The first part of the research outline describes the way to select best host polymer. After that, it was followed by the brief illustration on the way to choose IL using best host polymer. The last part explained the preparation, characterization and performance studies of the SPE prepared using best host polymer, $MgTf_2$, best IL and three types of nanoparticles.

3.3.1   Selection of host polymer

The research begins with the selection of host polymer (between HPMC and HEC) using $MgTf_2$ as the mobile carriers. The method to select the best host polymer is divided into two steps. The first step is to measure the ionic conductivity at room temperature of SPEs for the HPMC-pMgTf$_2$ (p: 0, 10, 20, 30 and 40 wt. %) complexes. Once, the most optimum conducting SPE in the HPMC-MgTf$_2$ complexes were obtained, it was further incorporated with various wt. % of BMIMTf for EIS measurement. The two steps

optimization method was repeated by replacing HPMC with HEC as host polymer. After that, the most conducting SPE from HPMC-MgTf$_2$-qBMIMTf (q: 10, 20, 30 and 40 wt. %) and HEC-MgTf$_2$-rBMIMTf (r: 10, 20, 30 and 40 wt. %) complexes were compared. Subsequently, the SPE that achieved the highest ionic conductivity at room temperature was chosen as the best host polymer.

Table 3.1: List of materials used in the preparation of SPE and fabrication of EDLC

Materials used during the preparation of solid polymer electrolyte		
Materials	**Role**	**Source**
Hydroxylpropylmethyl cellulose (HPMC)	Host polymer	Sigma-Aldrich
Hydroxylethyl cellulose (HEC)		
Magnesium trifluoromethanesulfonate (MgTf$_2$)	Inorganic salt	
1-Butyl-3-methylimidazolium trifluoromethanesulfonate (BMIMTf)	Ionic liquids	
1-Ethyl-3-methylimidazolium trifluoromethanesulfonate (EMIMTf)		
Fumed silica	Nanoparticles	
Copper(II) oxide		
Yttrium(III) oxide		
Dimethylsulfoxide (DMSO)	Solvents	
Deionized water		NIL
Materials used during the preparation of carbon electrode		
Materials	**Role**	**Source**
Activated carbon (BP20)	Active materials	Sigma-Aldrich
Carbon black (Super P)		
Poly(vinylidene fluoride) (PVdF)	Binder	Kuraray Chemical Co. Ltd.
N-Methyl-2-pyrrolidone (NMP)	Solvent	Merck

3.3.2 Selection and characterization of ionic liquid using the best host polymer

The EIS measurement was conducted on the SPE prepared by the best host polymer at various wt. % of EMIMTf. The most conducting SPE from best polymer-MgTf$_2$-*s*BMIMTf (*s*: 10, 20, 30 and 40 wt. %) and best polymer-MgTf$_2$-*t*EMIMTf (*t*: 10, 20, 30 and 40 wt. %) complexes were compared. Consequently, the best IL was chosen from the SPE that achieved the highest ionic conductivity at room temperature. After that, the SPEs prepared by using best host polymer, MgTf$_2$ and various wt. % of optimized IL were characterized by using EIS, XRD and FTIR.

3.3.3 Preparation, characterizations and performance studies of best host polymer-MgTf$_2$-best ionic liquid-nanoparticles

Nevertheless, the enhancement of ionic conductivity for best host polymer-MgTf$_2$-best IL complex was carried out through three systems by doping three types of nanoparticles (fumed SiO$_2$, CuO and Y$_2$O$_3$) at various wt. %. The SPEs prepared for the three systems were characterized by using EIS, XRD, FTIR and TGA. Subsequently, all the SPEs from each system were fabricated for EDLC and experienced the performance studies (CV, EIS and GCD). The overall research outline is summarized in Figure 3.1.

3.4 Preparation of Solid Polymer Electrolyte

3.4.1 HPMC-based SPE

HPMC and MgTf$_2$ were pre-heated at 100 °C for 1 hour in order to eliminate trace amounts of water presented into these materials. HPMC, MgTf$_2$ and BMIMTf were added into DMSO according to the compositions along with appropriate designations as shown in Table 3.2. The solution was stirred continuously for 48 hours at room temperature. After that, the as prepared solution was casted on an aluminum foil coated with Teflon and allowed to evaporate in an oven for 72 hours at 80 °C. A transparent thin film was obtained after drying process. The technique to prepare SPE is illustrated in Figure 3.2.

The ionic conductivity of the prepared SPEs at room temperature was measured using EIS techniques.
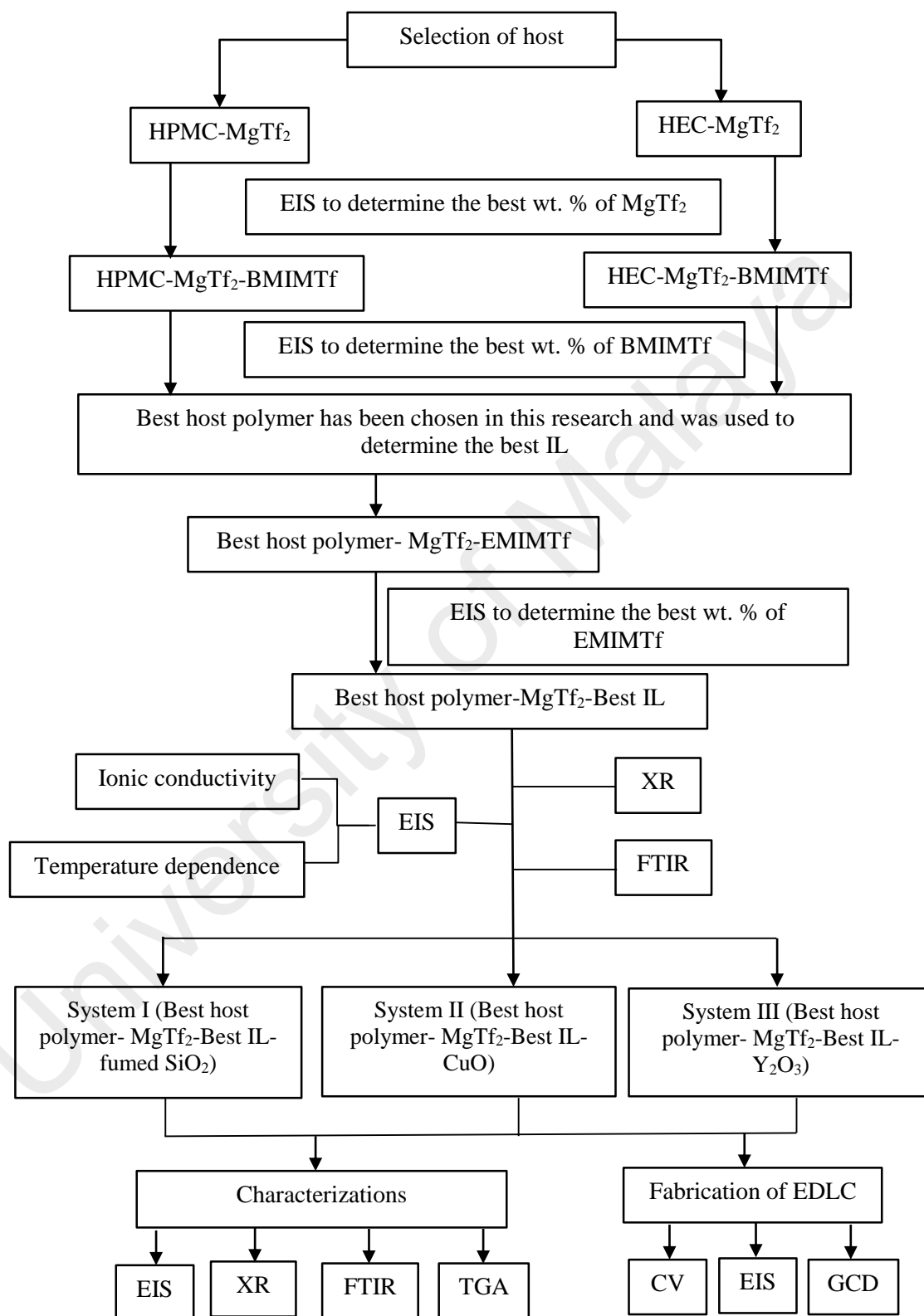
Figure 3.1: Summary of research outline

3.4.2 HEC-based SPE

HEC and MgTf$_2$ were heated at 100 ˚C for 1 hour prior to mixing with BMIMTf in deionized water using solution casting technique. The materials were mixed and labeled appropriately according to the compositions as depicted in Table 3.2. The mixture was stirred continuously for 24 hours and it was allowed to evaporate in an oven for 24 hours at 70 °C after being cast on an aluminum foil coated with Teflon. A transparent thin film was obtained after drying process. The steps were repeated by replacing BMIMTf with EMIMTf. The prepared SPEs upon optimization of addition ionic liquid were characterize using EIS, XRD and FTIR to measure its conduction mechanism, structural and interactions among the host polymer, salt and IL.

Table 3.2: Compositions and designations of HPMC and HEC based SPEs

Compositions (wt. %)	Designations	
Host polymer: MgTf$_2$: BMIMTf	HPMC	HEC
100: 0: 0	M0	H0
90: 10: 0	M10	H10
80: 20: 0	M20	H20
70: 30: 0	M30	H30
60: 40: 0	M40	H40
54: 36: 10	MB10	HB10
48: 32: 20	MB20	HB20
42: 28: 30	MB30	HB30
36: 24: 40	MB40	HB40
Compositions (wt. %)	Designations	
Host polymer: MgTf$_2$: EMIMTf		
54: 36: 10	HE10	
48: 32: 20	HE20	
42: 28: 30	HE30	
36: 24: 40	HE40	
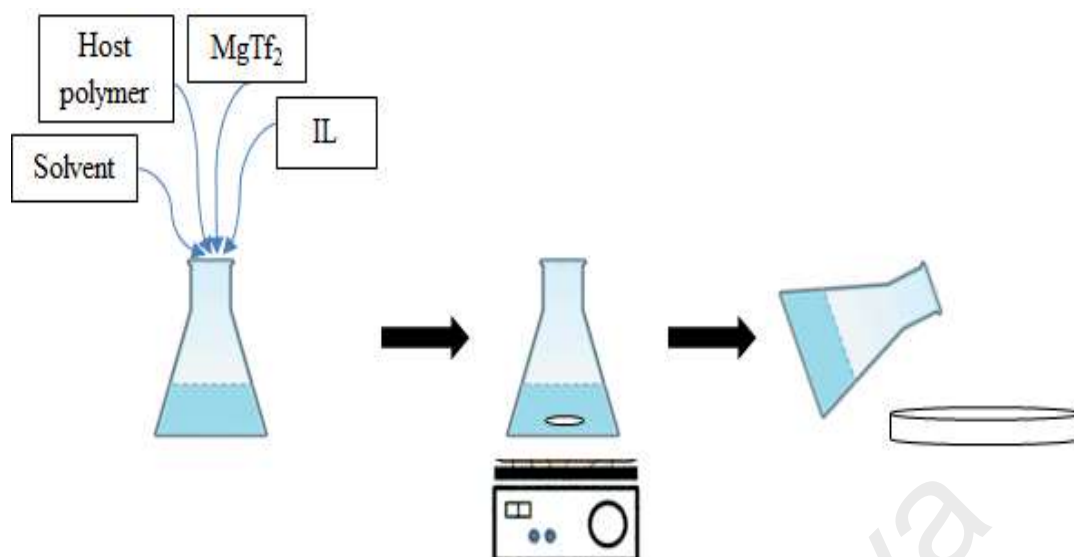
Figure 3.2: Solution casting technique to prepare SPE

3.4.3   Activation of Nanoparticles

The nanoparticles (fumed SiO_2, CuO and Y_2O_3) were pre-heated at 450 ˚C for 2 hours. The nanoparticles were cooled down and dispersed in the deionized water. In order to segregate these nanoparticles, the solution was treated with sonication for 30 minutes prior to dry.

3.4.4   HEC-based SPE with Nanoparticles

HEC, $MgTf_2$ and activated fumed SiO_2 nanoparticles were pre-heated for 1 hour at 100 ˚C. After that, the dried HEC, $MgTf_2$, various wt. % of activated fumed SiO_2 nanoparticles and EMIMTf were mixed in deionized water (as shown in Table 3.3) using solution casting technique. The viscous homogeneous mixture was sonicated for 30 minutes prior to continuous stirring for 24 hours at room temperature. It was cast on a Teflon coated aluminum foil and allowed to evaporate at 70 °C for 24 hours. A thin solid film was obtained after the drying process. The same steps were repeated by substituting fumed SiO_2 nanoparticles with CuO and Y_2O_3 nanoparticles. The color of the prepared thin films depends upon the color of the nanoparticles used, i.e. colorless, opaque brown and white upon doping with fumed SiO_2, CuO and Y_2O_3 nanoparticles, respectively (as

illustrated in Figure 3.3). The ionic conductivity (at room temperature and from 30–120 ˚C), dielectric studies, structural, interactions and thermal stability were analyzed using EIS, XRD, FTIR and TGA, respectively.

Table 3.3: Compositions and designations for HEC: MgTf$_2$: EMIMTf: Nanoparticles complexes

Compositions (wt. %)	Designations		
HEC: MgTf$_2$: EMIMTf: Nanoparticles	Fumed SiO$_2$	CuO	Y$_2$O$_3$
47.2: 11.8: 40: 1	HS1	HC1	HY1
46.4: 11.6: 40: 2	HS2	HC2	HY2
45.6: 11.4: 40: 3	HS3	HC3	HY3
44.8: 11.2: 40: 4	HS4	HC4	HY4
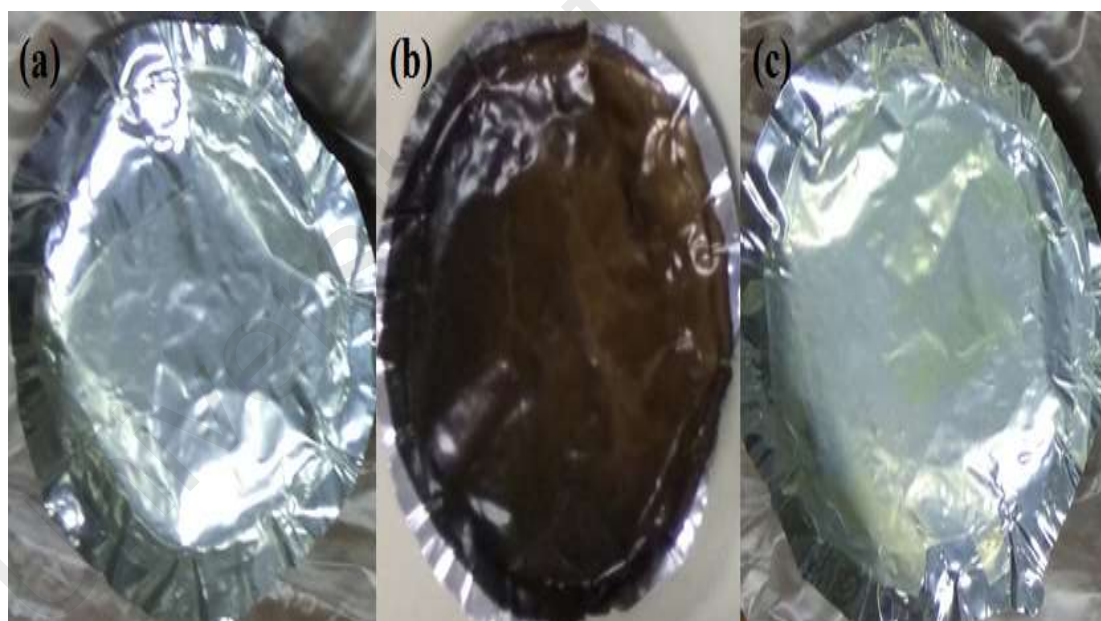
Figure 3.3: The color of thin films prepared with doping of (a) fumed SiO$_2$ (b) CuO and (c) Y$_2$O$_3$ nanoparticles

3.5 Characterizations of Solid Polymer Electrolyte

3.5.1 Electrochemical Impedance Spectroscopy (EIS)

The electrochemical impedance spectroscopy is a technique to characterize the electrochemical system in a broad range of frequencies at a given applied potential. It is

a fundamental approach of all impedance methods. The electrochemical impedance spectroscopy was performed using a HIOKI 3532-50 LCR Hi-Tester bridge interface with a computer in order to study the electrochemical properties of SPEs. The SPE was sandwiched between two stainless steel electrodes which act as blocking electrodes for the ions. Measurements were made over a frequency of 50 Hz to 1,000,000 Hz at room temperature.

At each frequency, sets of complex impedance, Z^*, real impedance, Z' and imaginary impedance, Z'' values were obtained. The relationships between Z^*, Z' and Z'' are based on Equation 3.1.

$$Z^* = Z' - jZ'' \qquad\qquad \text{Equation 3.1}$$

where $Z' = |Z|\,\omega\cos\theta$, $Z'' = |Z|\,\omega\sin\theta$ and j is constant.

After obtaining all the readings from the instrument, the complex impedance curves were plotted. The complex impedance plots are also known as Cole-Cole plots or Nyquist plots, having imaginary impedance component, Z'' plotted against the real impedance component, Z' at each excitation frequency. Figure 3.4 represents typical Cole-Cole plot. The intersection of the arc on the Z' yield the bulk resistance value (R_b) which is very important component to be used to calculate the ionic conductivity. The formula used to determine the ionic conductivity is based on Equation 3.2:

$$\sigma = \frac{l}{R_b A} \qquad\qquad \text{Equation 3.2}$$

where σ is the ionic conductivity (S/cm), l is the thickness of the film (cm), R_b is the bulk resistance (Ω) and A is the area of the electrodes connected to the sample (cm^2).
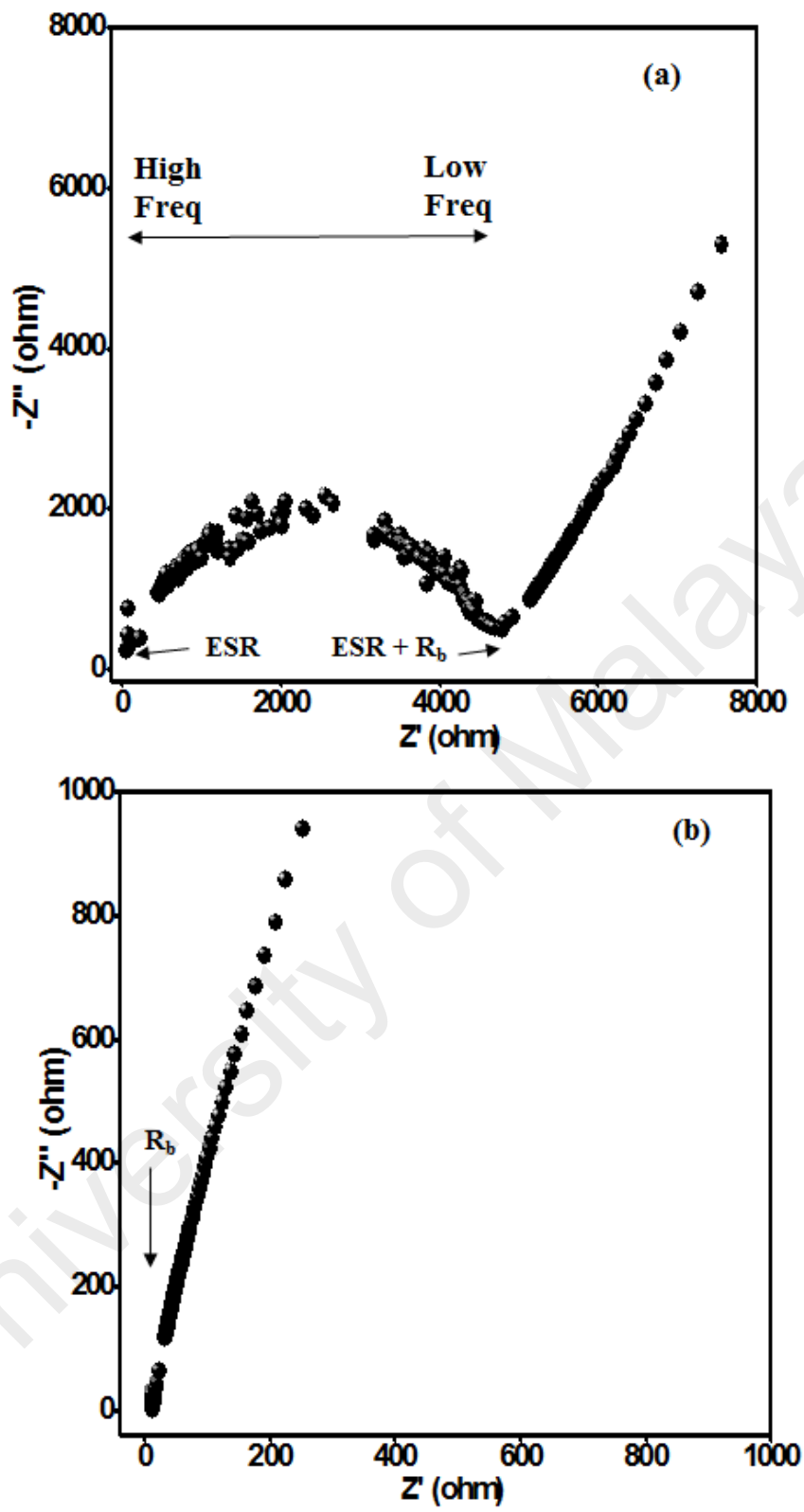
Figure 3.4: Nyquist plot for (a) low ionic conductivity (H20) and (b) high ionic conductivity (HY2) polymer electrolytes

3.5.1.1 Temperature Dependence–Ionic Conductivity Studies

The temperature dependence–ionic conductivity studies of all the SPEs were also carried out using a computer controlled HIOKI 3532-50 LCR Hi-Tester over the linear frequency range from 50 Hz to 1,000,000 Hz from 30–120 ˚C. The conductivity-temperature relationship of the SPEs can follow Arrhenius behavior. The Arrhenius equation can be represented as:

$$\sigma = \sigma_o \exp\left(\frac{-E_a}{kT}\right) \qquad \qquad \text{Equation 3.3}$$

where σ is the ionic conductivity at any absolute temperature, σ_o is the pre-exponential factor (S/cm), E_a is the activation energy (eV), k is the Boltzmann constant (8.617×10^{-5} eV/K) and T is the absolute temperature (K).

According to Arrhenius model ionic conduction, when a graph of log σ versus 1000/T is plotted, a linear relationship is observed. It indicates that the mobile charge carriers does not depends on the existence of free volume. In addition, it can be used to calculate the activation energy of the SPE. Activation energy is the energy required for the ion to detach from its initial site. The energy can be obtained from its' environment or through heat supplied. Consequently, as E_a decreases, the conductivity of sample increases indicating that the ions in highly conducting samples require lower energy for migration.

3.5.1.2 Dielectric Studies

The dielectric properties of all the SPEs were also carried out using a computer controlled HIOKI 3532-50 LCR Hi-Tester over the linear frequency range from 50 Hz to 1,000,000 Hz at room temperature. Frequency dependent values of capacitance (C_p) and parallel resistance (R_p) of the sample holder loaded with SPE samples were measured in parallel mode for the determination of the dielectric/electrical functions of the SPE

samples. The frequency dependent real part, Z' and imaginary part, Z" of complex impedance, Z*(ω) of the electrolyte films were evaluated by the following equation:

$$Z*(\omega) = Z' - jZ'' = \frac{R_p}{(1 + (\omega C_p R_p)^2)} - \frac{j[(\omega C_p R_p)^2]}{(1 + (\omega C_p R_p)^2)}$$

Equation 3.4

(a) *Dielectric Relaxation Studies*

The study of the relative permittivity ($\varepsilon*_r (\omega)$) of the SPEs samples were done to understand the polarization effect took place at the electrode and electrolytes interface and the correlation between the ionic relaxation time with the ionic conductivity. The relative permittivity is the dimensionless ratio of the permittivity ($\varepsilon_r(\omega)$) over the permittivity of free space (ε_0). It is also shown as a function of angular frequency where it has the real and imaginary component. The formula is shown as below:

$$\varepsilon*_r (\omega) = \frac{\varepsilon_r(\omega)}{\varepsilon_0} = \varepsilon'(\omega) - j\varepsilon''(\omega)$$

Equation 3.5

where $\varepsilon_0 = 8.854 \times 10^{-12}$ F/m, ε' is the dielectric constant, ε'' is the dielectric loss and $j = \sqrt{-1}$. The dielectric constant is the relative permittivity of a dielectric material. It is an important parameter to characterize the electrical charges capacity of a dielectric material that could be attained and stored. Dielectric loss measures a dielectric material's inherent dissipation of electromagnetic energy into the movement of ions and the alignment of dipoles when the polarity of the energy field reserves rapidly. It is associated with the electrical conductivity of the materials. The dielectric constant (ε') and dielectric loss (ε") can be calculated by following formula:

$$\varepsilon' = \frac{(Z'')^2}{\omega C_o ((Z')^2 + (Z'')^2)}$$

Equation 3.6

$$\varepsilon'' = \frac{(Z')^2}{\omega C_o((Z')^2 + (Z'')^2)}$$

Equation 3.7

where C_o is the vacuum capacitance and ω is angular frequency $(2\pi f)$

(b) *Modulus Studies*

An abrupt increase in ε' and ε'' values at lower frequency side in the dielectric spectra can be observed and it is actually due to large electrode polarization effect. This phenomenon always causes the ionic conduction relaxation to be misjudged. In order to overcome the misjudgments, modulus studies have been used and it is widely used to analyze the different relaxation phenomenon in the polymeric system and to assist in the electrolyte. Electric modulus can be defined as the reciprocal of complex relative permittivity and the inversion process able to suppress the electrode polarization effect at denominator to the second power in the loss function. The relationship between electric modulus, relative permittivity and impedance are given in the equations below:

$$M^* = M' + jM'' = \frac{1}{\varepsilon^*_r} = \frac{1}{\varepsilon' - j\varepsilon''} = \frac{\varepsilon'}{(\varepsilon')^2 + (\varepsilon'')^2} + \frac{\varepsilon''}{(\varepsilon')^2 + (\varepsilon'')^2}$$

Equation 3.8

$$M^* = j\omega C_0 Z^* = \omega C_0 Z'' + j\omega C_0 Z'$$

Equation 3.9

where M' is real modulus and M'' is imaginary modulus.

3.5.2 Fourier Transform Infrared Spectroscopy (FTIR)

The FTIR is a technique employed to identify the types of chemical bonds (functional groups) in a molecule by producing an infrared absorption spectrum. The basic vibration of the polymer electrolytes were studies using FTIR spectroscopy in the wavenumber region between 4000 and 650 cm^{-1} at a resolution of 4 cm^{-1} using Thermo Scientific Nicolet iSIO Smart ITR machine. Figure 3.5 illustrates the Thermo Scientific Nicolet

iSIO Smart ITR machine and its working principle. The FTIR spectrum of a sample is collected when a beam of infrared light passed through the sample. The transmitted light could reveals how much energy was absorbed at each wavenumber. The FTIR spectrometer could assist in measuring all the wavenumbers at once. The transmittance and absorbance spectrum can be produced by the machine. These analysis on the absorption characteristics could reveal the details about the molecular structures of a sample.
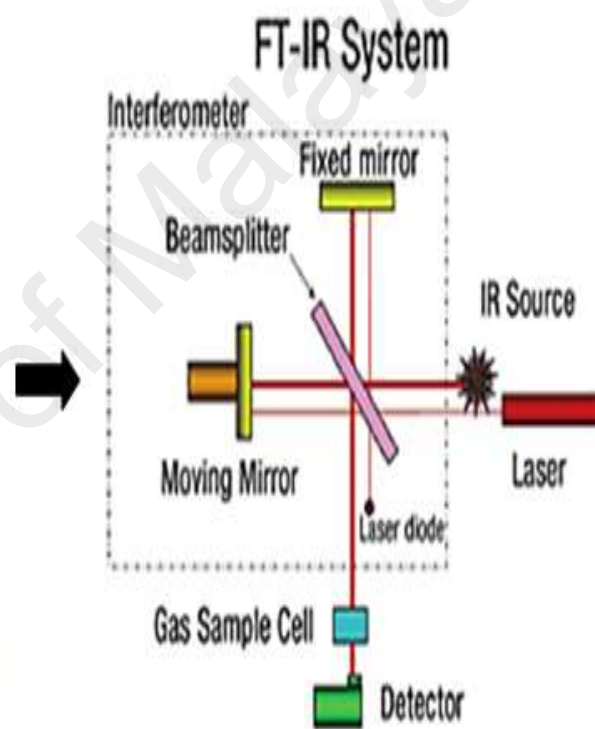
Figure 3.5: The FTIR machine and working principle (Source: Research And Development Indian Institute of Technology Kanpur)

3.5.3 X-Ray Diffraction Spectroscopy (XRD)

X-Ray diffraction is a rapid analytical technique usually used to identify the phase of the crystalline material and provides information about dimensions of the cell unit. It could be used to identify unknown substances, by comparing diffraction data against a database which is maintained by the International Centre for Diffraction Data. Max von

Laue was the person responsible in the discovery of XRD as he discovered that the crystalline substances actually act as three-dimensional diffraction grating for the X-Ray wavenumbers is similar to the spacing of the planes in a crystal lattice.

Figure 3.6 shows the working principle of XRD and its relation to Bragg's law. The fundamental principles of XRD is actually not very complicated, XRD is basically based on the constructive interference of the monochromatic X-Rays and crystalline samples. A cathode ray tube is used to generate the X-Rays and then the X-Rays are filtered to produce monochromatic radiation and then collimated to concentrate before directed towards the samples. The interaction of the X-Rays with the sample could produce constructive interferences and also a diffracted ray when it has the conditions which could satisfy the Bragg's Law as shown in Equation 3.10:

$$n\lambda = 2d \sin \theta$$
Equation 3.10

where n is an integer (whole number), λ is the wavelength of the rays (m), d is the spacing between layers of atoms (m) and θ is the angle between the incident rays and the surface of the crystal ($^{\circ}$).

Bragg's Law relates the wavenumber of the electromagnetic radiation to the diffraction angle and the lattice spacing in the crystalline sample. Then, they would be detected, processed and studied. All sample would be scanned at a range of 2θ angles so all possible diffraction directions of the lattice could be attained because of the natural random orientation of the powdered material. XRD can also be used to characterize the heterogeneous mixture to determine the relative abundance of the crystalline compounds.
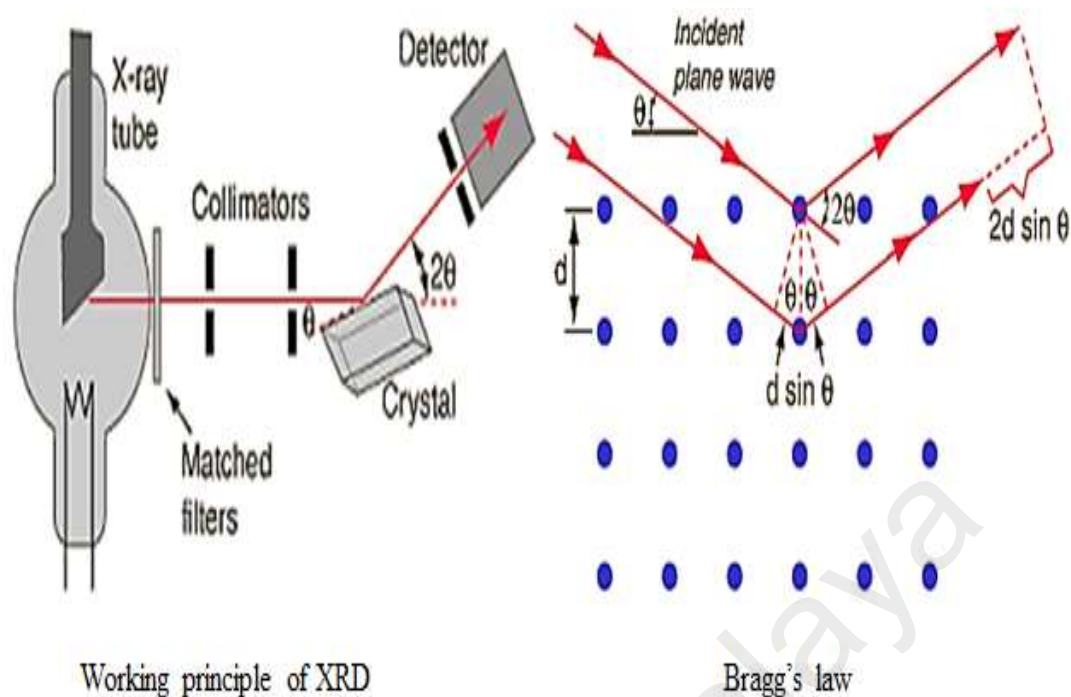
Figure 3.6: The working principle of XRD and Bragg's law (Source: Hyperphysics, Department of Physics and Astronomy, Georgia State University)

3.5.4 Thermogravimetric Analysis (TGA)

Thermogravimetric analysis is a thermal analysis technique which is mainly used to measure the changes in the weight of a sample as a function of temperature or time. In polymer electrolytes, TGA is commonly used to determine the degradation temperature, residual solvent levels, absorbed moisture content and the amount of inorganic filler in the samples.

In this study, the sample is placed into a TGA sample pan holder/crucible which is made from silica. The sample pan holder was then placed on a sensitive balance and then into the high temperature chamber. The balance can measure the initial sample weight at room temperature and then continuously monitor the changes in the sample weight as heat is gradually applied to the sample. The TGA studies were carried out on a TA Instrument Universal Analyzer 2000 with Universal V4.7A software. The sample was heated from 30°C to 750 °C at a heating rate of 40 °C/min in a nitrogen atmosphere with a flow rate of 60 mL/min. Typical TGA curve provides information concerning the

thermal stability of the initial sample, intermediate compounds and the residue if there were any of them. In addition to thermal stability, the weight losses observed in TGA can be quantified to predict the pathway of degradation or to obtain information.

3.6 Preparation of Carbon Electrodes

An 80 wt. % of activated carbon, 10 wt. % of carbon black and 10 wt. % of PVdF binder were mixed in NMP solvent under ultrasonication to prepare carbon slurry prior to fabrication of the working electrode. The slurry was stirred overnight at ambient temperature until it attained homogeneity. It was subsequently coated on the 10 mm diameter coin-shaped stainless steel current collectors and dried in an oven for 8 hours at 70 °C. Finally, these electrodes were spin-coated 8 times with the prepared polymer electrolyte solution to ensure the surface of the carbon electrodes were well dispersed with the polymer electrolyte.

3.7 Fabrication of Electric Double Layer Capacitor (EDLC)

The non-aqueous symmetric EDLC cell was fabricated by sandwiching the SPE between two activated carbon electrodes as portrayed in Figure 3.7. The mass of two activated carbon electrodes used for each cell is 6.7 mg. Thereafter, the cell was pressed by hydraulic hand pump at 0.7 MPa to ensure good contact between the electrode and electrolyte. Next, the EDLC cell configuration was eventually placed in a cell kit for further electrochemical analyses.

3.8 Performance Studies of Fabricated EDLC

Figure 3.8 depicts the Gamry Interface 1000 instrument and the electrodes used to study the CV, EIS and GCD performances of the fabricated EDLC.

The SPE is sandwiched
between the carbon
electrodes (EDLC)

EDLC has been placed in the cell kit
for electrochemical analysis

Figure 3.7: Fabricated EDLC and the cell kit for electrochemical analysis

Gamry Interface 1000 instrument

**The electrodes for Gamry
Interface 1000 instrument**

Figure 3.8: Gamry Interface 1000 instrument and the electrodes

3.8.1 Cyclic Voltammetry (CV)

The CV measurements of EDLC were performed at different scan rates of 5, 10, 20, 30, 40, 50 and 100 mV/s in the potential window between -1 to 1 V. The specific capacitance (C_{sp}) of EDLC calculated by CV using equation as follows:

$$C_{sp(CV)} = \frac{A}{\Delta V \times v \times m}$$

Equation 3.11

where A is the integral area of the cyclic voltammogram loop (AV), ΔV is the potential window (V), v is the scan rate (V/s), m is the total mass of the electrode materials on both electrodes (g).

3.8.2 Electrochemical Impedance Spectroscopy (EIS)

The electrochemical impedance spectroscopy also can be used to determine the equivalence series resistance (ESR) and charge transfer resistance (R_{ct}) of the device (as illustrated in Figure 3.9). The ESR arises from the electronic resistance of the electrode material, interfacial resistance between the electrode and the current-collector, ionic diffusion (resistance) of ions to the small pores and electrolyte resistance (Pandolfo & Hollenkamp, 2006). The EIS measurement was done in the frequency range of 0.001 Hz to 100,000 Hz using Gamry Interface 1000 instrument.

3.8.3 Galvanostatic Charge-Discharge (GCD)

The GCD was performed at different current densities such as 30, 40, 60, 80 and 100 mA/g. The specific capacitance (C_{sp}) of EDLC calculated by GCD using equation as follows:

$$C_{sp(GCD)} = \frac{I \times \Delta t}{\Delta V \times m} \times 2$$

Equation 3.12

where ΔV is the potential window (V), m is the total mass of the electrode materials on both electrodes (g), I is the discharge current (A) and Δt is the discharged time after IR drop (s). Factor 2 was used in Equation 3.12 because the series capacitance was formed in a two-electrode system.
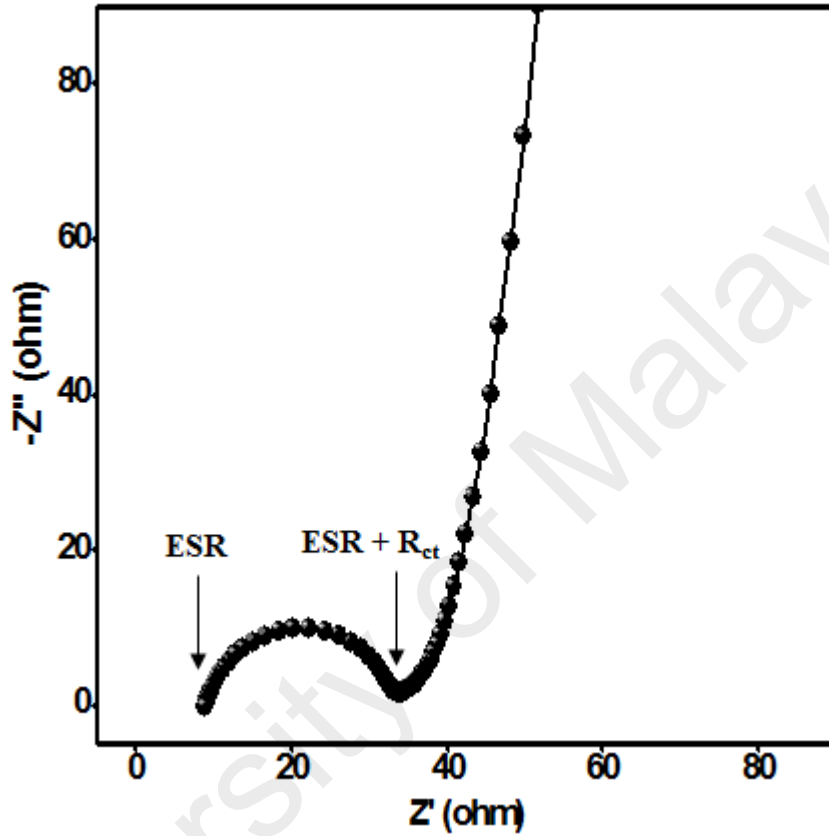
Figure 3.9: Nyquist plot for HC2-based EDLC

4.1 Introduction of the Chapter

This chapter is divided into three parts. The first part of this chapter illustrates the optimization of host polymer by using EIS. The second part describes the optimization of the IL in the host polymer selected from the first part by measuring their ionic conductivities at room temperature. In addition to that, the characterization of the optimized SPEs by XRD and FTIR are briefly explained. The characterizations (EIS, XRD, FTIR and TGA) of the optimized SPEs incorporated with three types of nanofillers (fumed SiO_2, CuO and Y_2O_3) are elaborated in the third part of this chapter. On top of that, the electrochemical studies (CV, EIS, GCD and life cycle) of the EDLCs fabricated by using the optimized SPEs incorporated with three types of nanofillers (fumed SiO_2, CuO and Y_2O_3) were discussed.

4.2 Ionic Conductivity Studies and Optimization of Host Polymers for SPEs

4.2.1 Introduction

Two types of cellulose derivatives (HPMC and HEC) has been used to prepare the SPEs. The optimization of the prepared SPEs was done using EIS by measuring their ionic conductivities at room temperature.

4.2.2 HPMC-MgTf₂ SPEs

Figure 4.1 depicts the variation of ionic conductivity at room temperature as a function of $MgTf_2$ salt contents for HPMC-$MgTf_2$ SPEs. When 10, 20 and 30 wt. % of $MgTf_2$ were added into M0, the ionic conductivity at ambient temperature increased to 4.69×10^{-9} S/cm, 5.69×10^{-9} S/cm and 6.76×10^{-9} S/cm, respectively compared to M0 at 3.95×10^{-9} S/cm. It was found that M40 experienced the highest ionic conductivity at

room temperature of 4.08×10^{-8} S/cm compared to M0. As a result, the ionic conductivities at room temperature increased because there was greater mobility of charge carriers caused by the high concentration of mobile carriers (Kido et al., 2015). Thus, it led to the increased of the amount of charge carriers that can participate in the conduction process (Klongkan & Pumchusak, 2015). Nonetheless, the incorporation of 50 wt. % of salt was discontinued for the entire research because the aim of this study is to prepare a conventional polymer electrolyte (salt in polymer) in which the wt. % of polymer must be greater than salt (Suo et al., 2013).
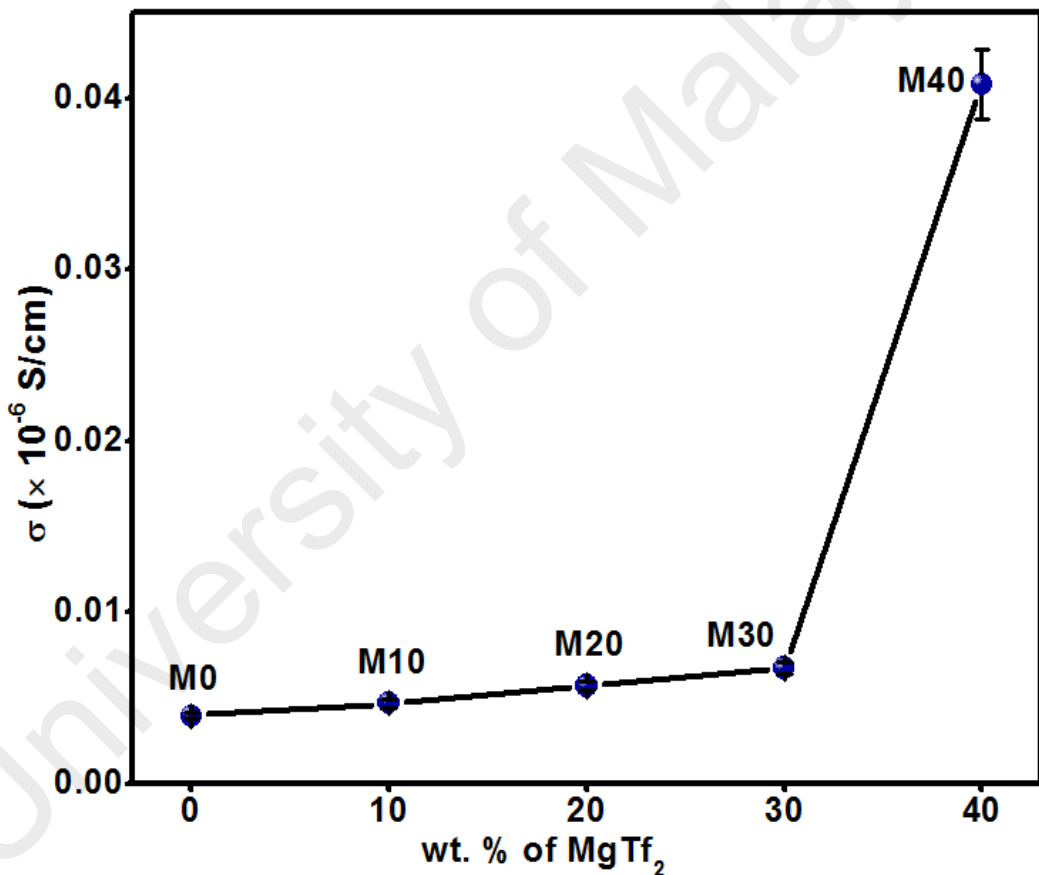
Figure 4.1: Variation of ionic conductivity as a function of salt contents for HPMC-MgTf$_2$ SPEs at room temperature

4.2.3   HPMC-MgTf$_2$-BMIMTf SPEs

Figure 4.2 shows the variation of ionic conductivity at room temperature as a function of BMIMTf contents for HPMC-MgTf$_2$-BMIMTf SPEs. Analogous to salt, the ionic

conductivity at room temperature was also increased at elevated concentrations of IL. The ionic conductivity at room temperature increased consistently to 9.52×10^{-7} S/cm, 9.36×10^{-6} S/cm, 4.35×10^{-5} S/cm and 2.36×10^{-4} S/cm when 10, 20, 30 and 40 wt. % of BMIMTf were added into M40, respectively. This was because IL acted as plasticizer by increasing the flexibility of the host polymer which enhanced the transportation of charge carriers (Ye et al., 2013). Incorporation of 50 wt. % BMIMTf into the SPE was prepared and yet to be measured because it was not able to form a free standing thin film.
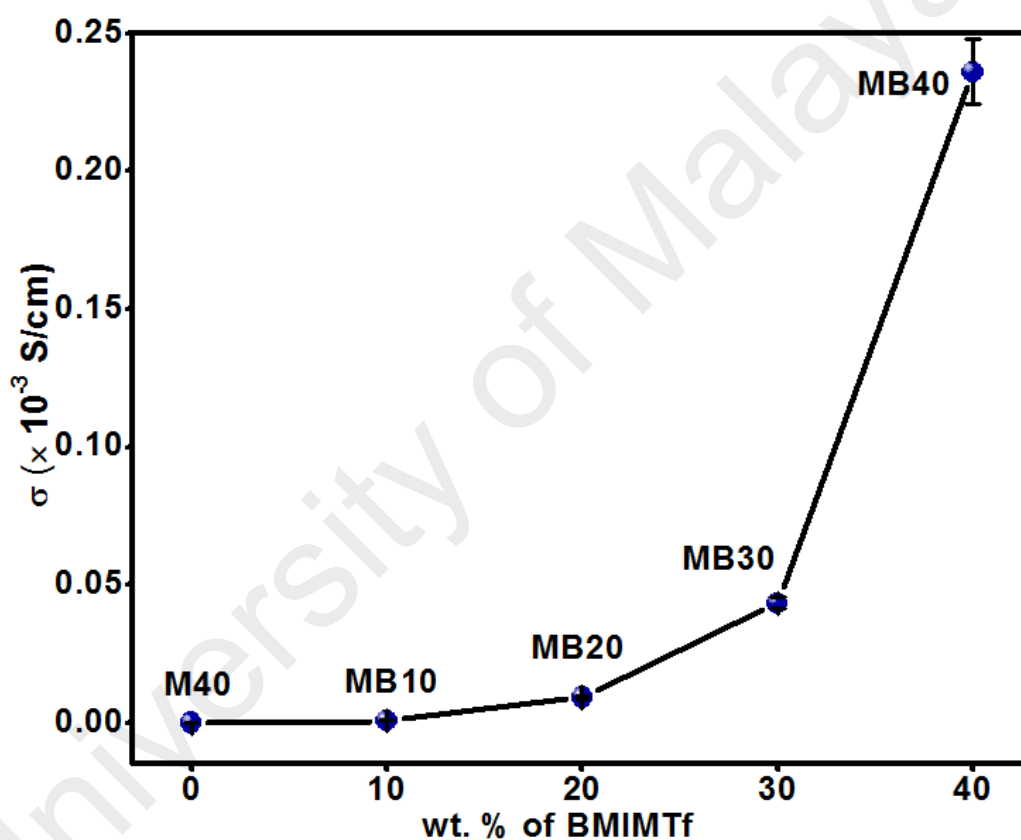
Figure 4.2: Variation of ionic conductivity as a function of BMIMTf contents for HPMC-MgTf$_2$-BMIMTf SPEs at room temperature

4.2.4   HEC-MgTf$_2$ SPEs

The variation of ionic conductivity at room temperature as a function of salt contents for HEC-MgTf$_2$ SPEs is illustrated in Figure 4.3. The ionic conductivity at room temperature rises from 4.76×10^{-7} S/cm to 6.71×10^{-7} S/cm (highest), when MgTf$_2$ was doped from 10 to 20 wt. % into the H0 SPE (1.61×10^{-8} S/cm). The ionic conductivity

was improved gradually with the increase of salt concentration as discussed in Section 4.2.2. However, the ionic conductivity of the SPE complexes dropped to 2.67×10^{-7} S/cm and 2.20×10^{-7} S/cm when 30 and 40 wt. % of MgTf$_2$ salt was doped into H0, respectively. This was because the excessive amount of salt hindered the number and mobility of the charge carriers through the formation of neutral salt aggregation (Seo et al., 2013).
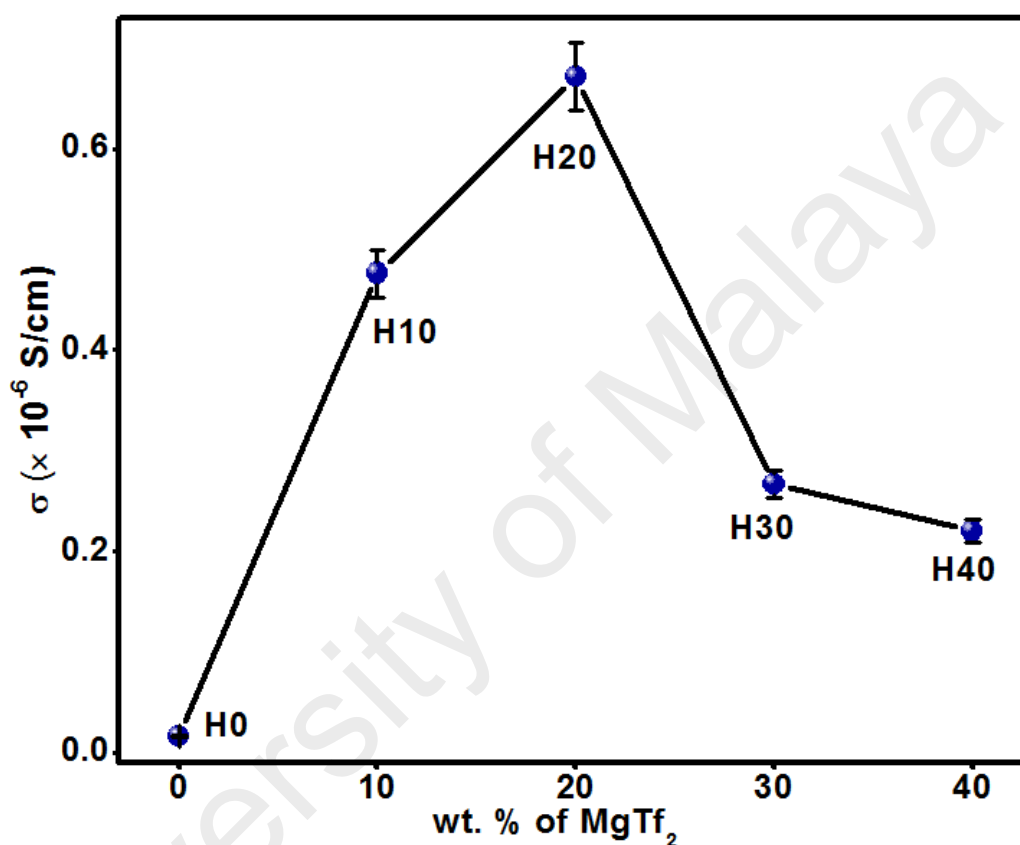
Figure 4.3: Variation of ionic conductivity as a function of salt contents for HEC-MgTf$_2$ SPEs at room temperature

4.2.5   HEC-MgTf$_2$-BMIMTf SPEs

The variation of ionic conductivity at room temperature as a function of BMIMTf contents for HEC-MgTf$_2$-BMIMTf SPEs is shown in Figure 4.4. When the 10, 20 and 30 wt. % of BMIMTf was incorporated into H20 (6.71×10^{-7} S/cm), the ionic conductivity at room temperature increased to 1.60×10^{-6} S/cm, 5.26×10^{-6} S/cm and 1.47×10^{-5} S/cm, respectively. The highest ionic conductivity achieved by SPE upon doping of 40 wt. % of BMIMTf was 3.51×10^{-5} S/cm at room temperature. The ionic conductivity increases

with the increasing wt. % of IL into the SPE as explained in Section 4.2.3. The preparation of free standing thin film upon incorporation of 50 wt. % of BMIMTf into HEC-based SPE was unsuccessful, hence the ionic conductivity of the SPE was not measured. Therefore, SPE containing 40 wt. % of IL was taken as optimized SPE for further experiments.
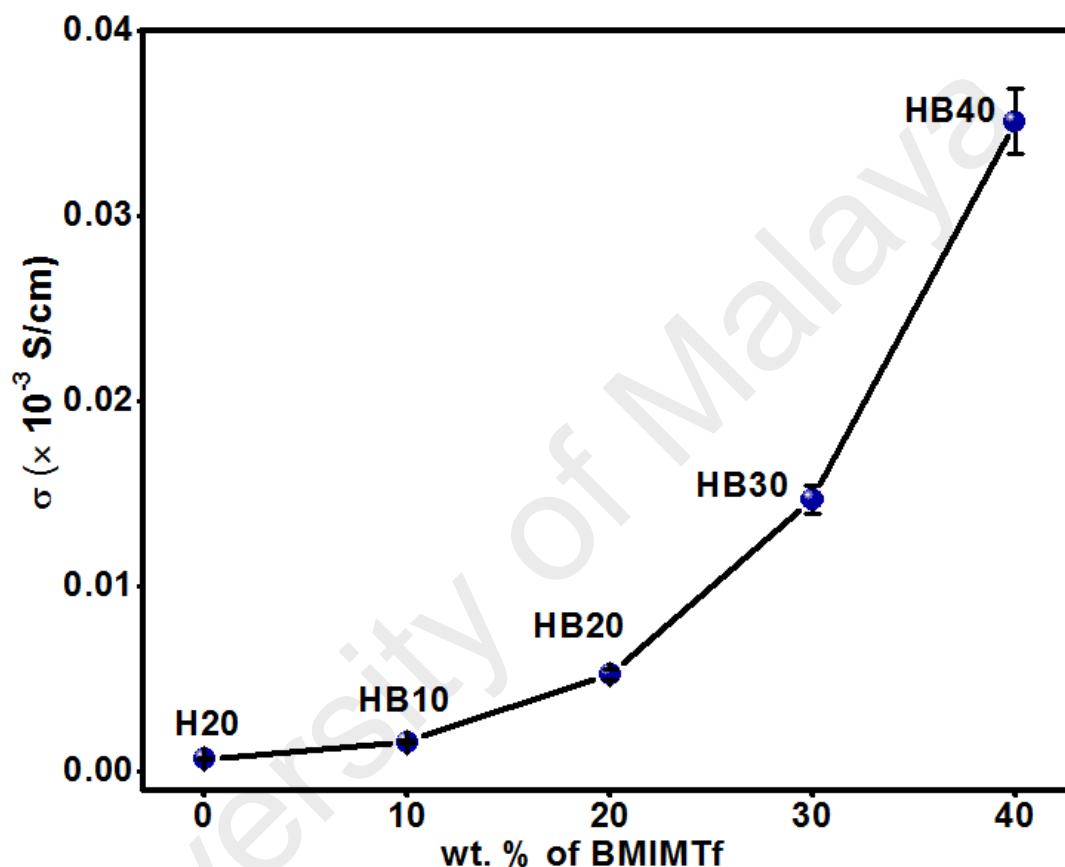
Figure 4.4: Variation of ionic conductivity as a function of BMIMTf contents for HEC-MgTf$_2$-BMIMTf SPEs at room temperature

4.2.6   Summary

Based on the results, SPEs prepared using HPMC and HEC as host polymer required 40 and 20 wt. % of salt, respectively in order to achieve the highest ionic conductivity at room temperature. Hereinafter, H20 and M40 were optimized using BMIMTf and it was found that both SPEs required 40 wt. % of BMIMTf in order to achieve highest ionic conductivity at room temperature. Consequently, MB40 achieved greater ionic conductivity at room temperature compared to HB40 because the bulky residual group

(butyl) in BMIMTf creates dispersion force with HEC polymer easily. Thus, it hindered the adsorption and mobility of the charge carriers on the HEC polymer, which results in retardation of its ionic conductivity (Tafur et al., 2015). In spite of that, still, HEC has been chosen as the host polymer in this study over HPMC because the duration to prepare a SPE based on HPMC is long (5 days) and it is not economically wise due to the use of higher amount of salt which makes it unsuitable for commercialization in future for EDLC. In addition, the preparation of HPMC-based SPE is inconvenient and not environmental friendly because the solvent used is DMSO. On the contrary, the preparation of SPE based on HEC is more convenient and greener because the time taken to prepare the SPE is 2 days, the solvent used is water and it requires lesser amount of salt. Therefore, the ion-conduction, structural studies and interactions of HEC-MgTf$_2$-EMIMTf complex needs to be optimized and it will be discussed in details in Section 4.3.

4.3   Optimization and Characterization of EMIMTf for HEC-MgTf$_2$-EMIMTf SPEs

4.3.1   Introduction

In order to improve the ionic conductivity of HEC-MgTf$_2$-BMIMTf complex, EMIMTf has been chosen to substitute BMIMTf owing to shorter residual group (ethyl) which is believed to be able to suppress the steric hindrance effect in HEC. The ion conduction mechanism, structural studies and interactions between the charge carriers and the host polymer at different wt. % of EMIMTf for the optimized SPE will be discussed using EIS, XRD and FTIR, respectively.

4.3.2   Ionic Conductivity Studies

Electrochemical impedance spectroscopy was performed to investigate the electrical properties of SPE complexes with different weight ratios of EMIMTf. Figure 4.5 depicts the measured Cole-Cole plot for SPE complexes at various wt. % of EMIMTf at room

temperature whereas the inset is the enlarged Cole-Cole plot for HE20, HE30 and HE40 at room temperature.
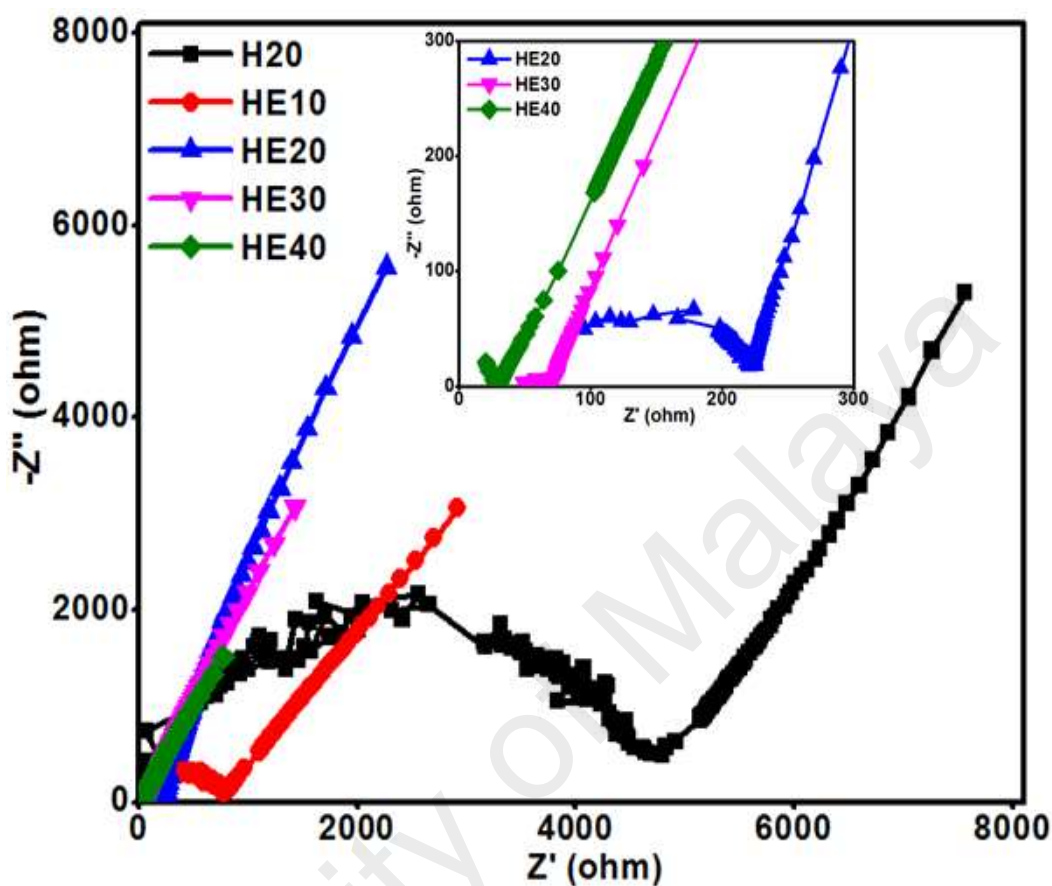
Figure 4.5: Cole-Cole plot for SPE complexes at various wt. % of EMIMTf at room temperature. Inset is the enlarged Cole-Cole plot for HE20, HE30 and HE40 at room temperature

The HE10-based SPE showed a complete semicircle whereas HE20, HE30 and HE40 portray an incomplete semicircle at high frequency region. The diameter of the semicircle at high frequency region is attributed to the R_b resulted from the transportation of charge carriers on the immobile polarized polymer chain. When 10 wt. % of EMIMTf was added into H20, the R_b decreased to 800 Ω from 4790 Ω. The value decreased even more to 225 Ω, 78 Ω and 32 Ω when EMIMTf content increased to 20, 30 and 40 wt. %, respectively. Thus, the R_b values decreased with increased amount of EMIMTf and thereby heightened the rate of transportation of charge carriers (Tang et al., 2016). Nevertheless, all the SPE

complexes were accompanied by an inclined spike at low frequency region owing to the space charge effect formed at the electrolyte/electrode interface. Although, all the SPE complexes suffered an inclined spikes with angle less than 90° to the real axis which may be due to the roughness or non-homogenous surface of electrolyte/electrode interface (Tafur & Romero, 2014).

Analogous to HEC-MgTf$_2$-BMIMTf SPEs, the ionic conductivities of the SPEs at room temperature were also increased at elevated concentrations of EMIMTf. It is worth to mention that the R$_b$ value obtained from Cole-Cole plot was used in calculating the ionic conductivity as in Equation 3.2. The ionic conductivity at room temperature increased consistently to 3.34×10^{-6} S/cm, 1.92×10^{-5} S/cm and 5.64×10^{-5} S/cm when 10, 20 and 30 wt. % of EMIMTf were added into H20, respectively. The highest ionic conductivity obtained by HE40 is 9.28×10^{-5} S/cm at room temperature and it is found to be greater than the ionic conductivity of HB40 by 62.2 % at room temperature.

As a result, EMIMTf is the best choice of IL over BMIMTf in this study due to excellent compatibility between EMIMTf and HEC polymer. It was owing to shorter residual group in EMIM$^+$ ions (lesser steric hindrance) which leads to the enhancement of mobility and amount of charge carriers adsorbed on the host polymer (Liew & Ramesh, 2014). On top of that, the improvement in ionic conductivity is due to better Lewis acid-base interaction between EMIM$^+$ and HEC, since EMIM$^+$ is a stronger Lewis acid compared to BMIM$^+$ (Park et al., 2013). The effects of different wt. % of IL on HEC-MgTf$_2$-EMIMTf complexes were characterized using EIS, XRD and FTIR studies.

The ionic conductivity of all the HEC-MgTf$_2$-EMIMTf SPEs at various wt. % of EMIMTf is directly proportional to the temperature as depicted in Figure 4.6.
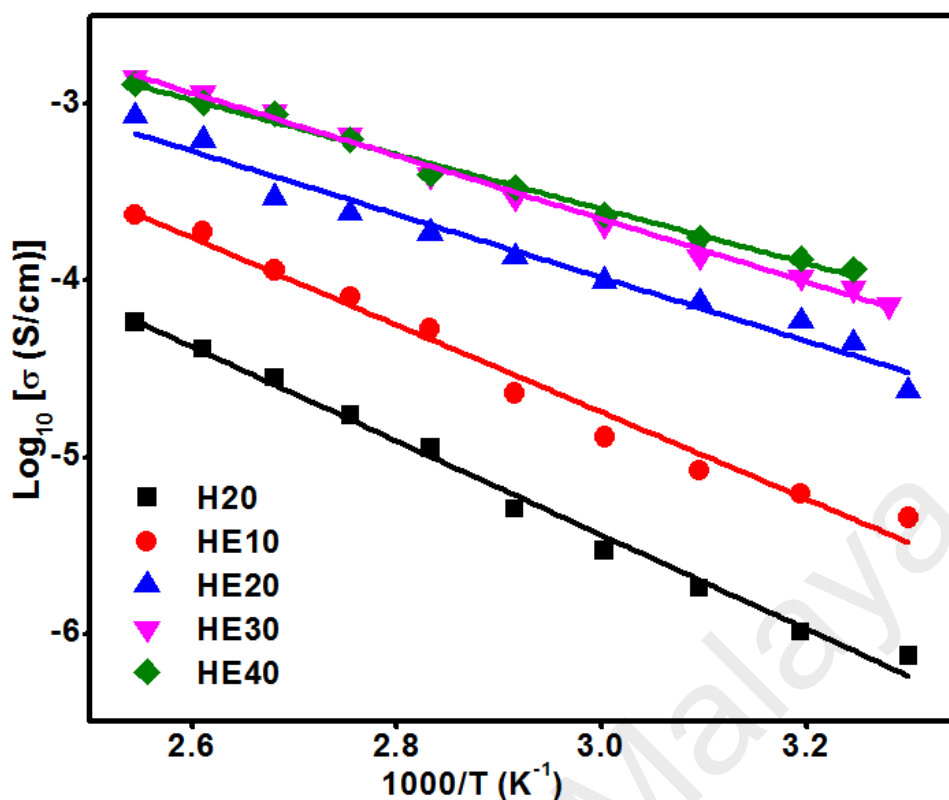
Figure 4.6: Variation of logarithm of ionic conductivity at different wt. % of EMIMTf from 30–120 ˚C

The regression values (R^2) values for HE10, HE20, HE30 and HE40 were 0.98, 0.97, 0.99 and 0.99, respectively indicating that the SPEs obeyed Arrhenius conduction theory. As the temperature increases, the host polymer expands and at the same time, the mobile charge carriers received sufficient energy to overcome the barriers. Hence, these ions hopped to the vacant sites in the complexes. Thus, the ionic conductivity of the SPEs increased at elevated temperature along with depression of activation energy as portrayed in Figure 4.7 (Zebardastan et al., 2016). The activation energy for each SPE complex was calculated using the gradient of the graph based on Equation 3.3. Based on Figure 4.7, it inferred that the highest conducting sample (HE40) possessed the lowest activation energy of 0.306 eV. This was followed by HE30 (0.354 eV), HE20 (0.356 eV) and HE10 (0.489 eV). It shows that the most conducting sample has the highest number of mobile charge carriers which led to higher kinetic energy possessed by these ions. As a consequence, these ions are able to overcome the activation energy easily.
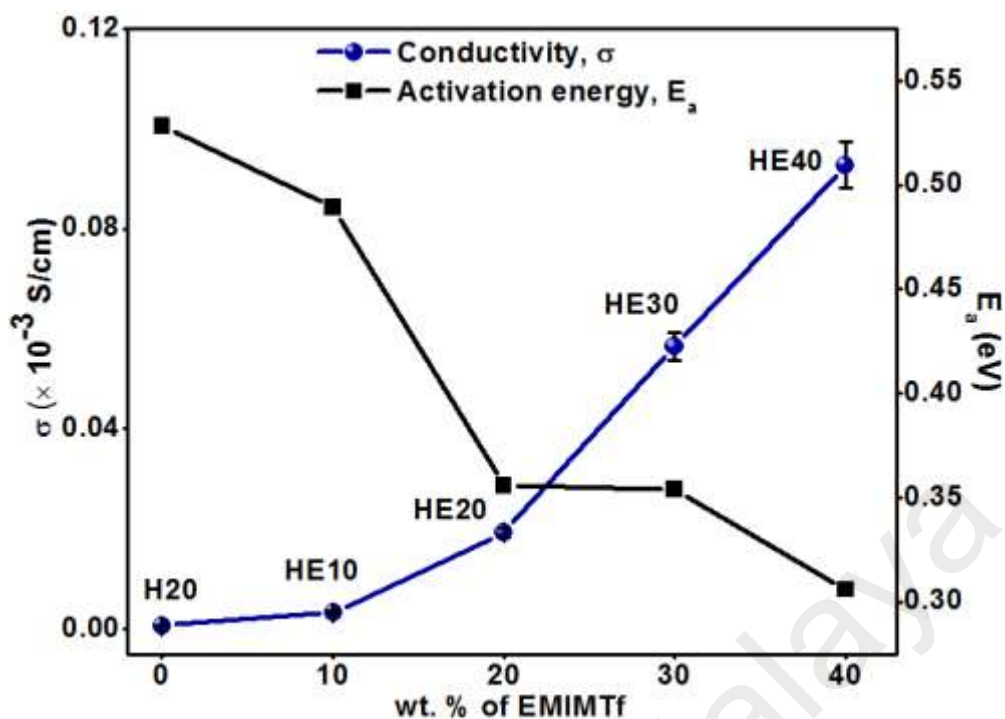
Figure 4.7: Variation of ionic conductivity and activation energy at various wt. % of EMIMTf at room temperature

4.3.3 XRD Studies

Pure HEC displayed diffraction peaks at $2\theta = 9.0°$ and $21.6°$ whereas pure EMIMTf showed diffraction peaks at $2\theta = 16.1°$ (Mukerabigwi et al., 2016). On the other hand, peaks at $2\theta = 13.8°$, $17.2°$, $24.0°$, $29.6°$, $33.9°$ and $42.6°$ were ascribed to pure MgTf$_2$ as shown in Figure 4.8(a)). Based on Figure 4.8(b), complexation between the HEC-MgTf$_2$ complex and various amount of EMIMTf used was indicated by the shift of HEC peak from $2\theta = 21.6°$ to $19.9°$ (Aziz & Abidin, 2013). Also, complete dissolution of salt and host polymer was indicated by the absence of all peaks and diffraction peak at $2\theta = 9.0°$ for MgTf$_2$ and HEC, respectively (Singh et al., 2013). Nonetheless, upon addition of EMIMTf, small diffraction peak at $2\theta = 16.1°$ was observed in HE10, HE20 and HE30. However, when the SPE complex was added with optimized amount of IL (HE40), the diffraction peak of EMIMTf ($2\theta = 16.1°$) was not noticeable. It signified that the transportation of mobile carriers at this stage is attributed to the transportation along the molecular chains in the host polymer only. Hence, the ionic conductivities of the HEC-

MgTf$_2$-EMIMTf complexes were independent from the partial crystallinity of their complexes (Idris et al., 2012).
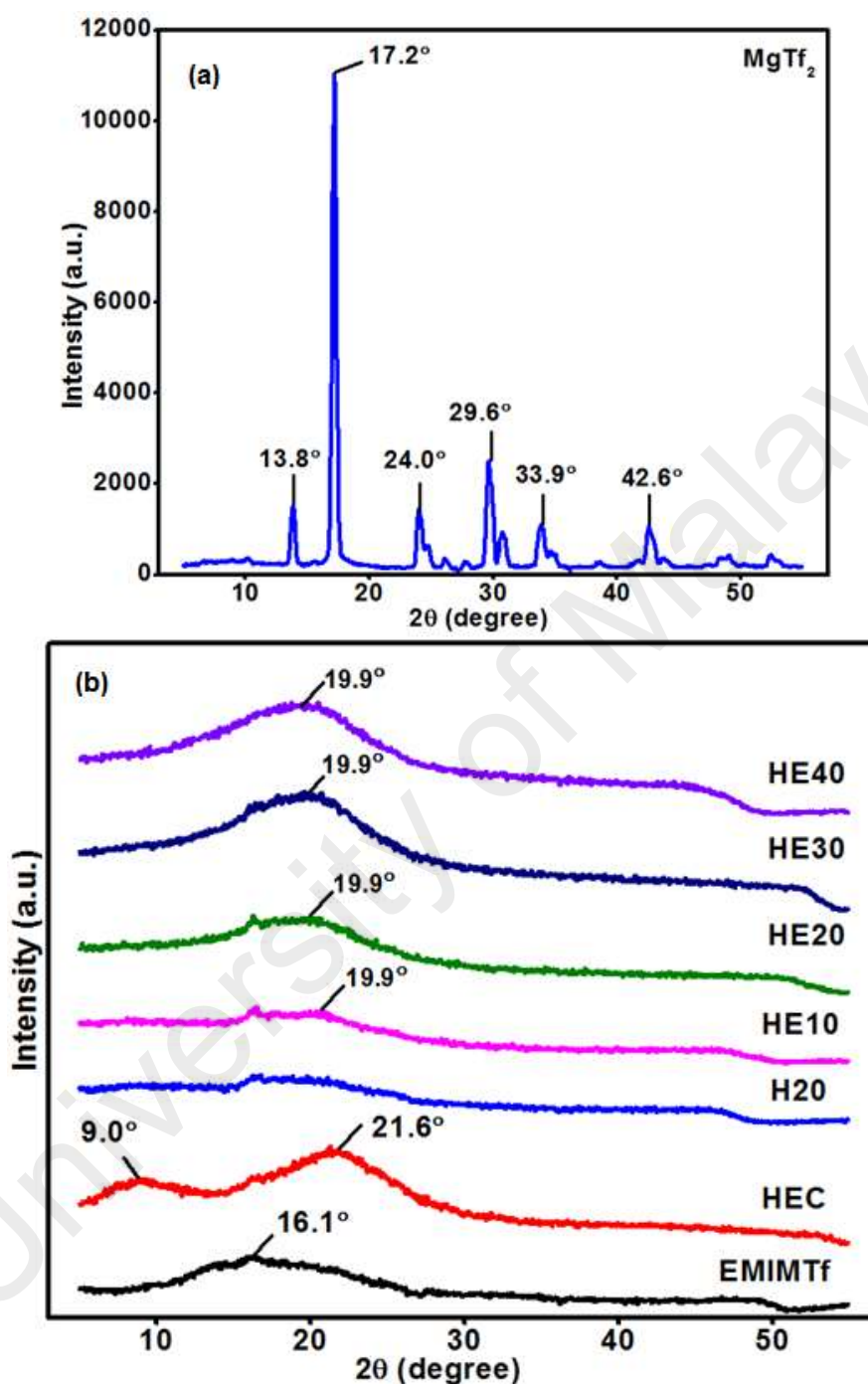
Figure 4.8: XRD patterns of (a) pure MgTf$_2$ (b) pure samples (EMIMTf and HEC) and SPE complexes at various wt. % of EMIMTf

4.3.4   FTIR Studies

Figure 4.9 and Table 4.1 depict the FTIR spectra and the descriptions for each band assignment of pure samples (HEC, MgTf$_2$, EMIMTf) and SPE complexes at various wt.

% of EMIMTf, respectively. Based on Figure 4.10(a), the broadness at 3402 cm^{-1} (–OH stretching) in HEC increased by 66.3 % upon incorporation of MgTf$_2$ due to the intermolecular hydrogen bonding created between the absorbed water in MgTf$_2$ and the hydroxyl group in HEC. The presence of absorbed water in MgTf$_2$ is indicated by the sharp peak at 3490 cm^{-1} (Satyamurthy & Vigneshwaran, 2013). Also, the intermolecular hydrogen bonding was created between the host polymers. However, upon incorporation of 40 wt. % of EMIMTf (most conducting SPE) into H20, it experienced great destruction of intermolecular hydrogen bonding which was resulted from the adsorption of mobile charge carriers on polymer chain. It was supported by the decrease in broadness of HE40 by 30.4 % and 58.2 % compared to HEC and H20, respectively at 3402 cm^{-1} (–OH stretching).

The great adsorption of charge carriers on the host polymer was ascribed to the splitting of asymmetric in-plane C–O–C pyrose ring stretching at 1062 cm^{-1} (in HEC) into two peaks at 1061 cm^{-1} and 1031 cm^{-1} as depicted in Figure 4.10(b) (Winie & Arof, 2006). As a result, HE40 attained the least broadness at 1061 cm^{-1} by 74.9 % and 88.5 % compared to H20 and HEC, respectively. Likewise, HE40 obtained the greatest broadness at 1031 cm^{-1} by 56.5 % and 96.2 % compared to H20 and HEC. This phenomena is due to the highest amount of charge carriers in HE40 which led to great adsorption on the host polymer. Thus, severe rotation and vibration at the –CH$_2$ and –CH$_3$ incurred due to great interaction between the mobile carriers and host polymer. Consequently, the peak intensity at 2912 cm^{-1} (asymmetric stretching of –CH$_2$ and –CH$_3$) and 2875 cm^{-1} (symmetric stretching of –CH$_2$ and –CH$_3$) depressed greatly compared to HEC and H20 as shown in Figure 4.10(c). The FTIR results obtained is in well agreement with the complexation peak observed in XRD patterns discussed in Section 4.3.3.

Figures 4.11(a) – (e) illustrate the interactions between HEC-MgTf$_2$ SPEs and EMIMTf. The successful addition of EMIMTf into the HEC- MgTf$_2$ SPEs was portrayed by consistent increase in peak intensities at 3156 cm^{-1} (ring in-plane symmetric of HCCH), 3117 cm^{-1} (ring NC(H)NCH), 1574 cm^{-1} (ring in-plane asymmetric of (N)CH$_2$ and (N)CH$_3$CN)), 1432 cm^{-1} (ring in-plane asymmetric bending of CH$_3$(N)CN and symmetric bending of CH$_3$(N)HCH)), 756 cm^{-1} (ring HCCH symmetric bending, CF$_3$ symmetric bending, C–O–S bending in –CF$_3$SO$_3^-$) and 702 cm^{-1} (ring in-plane asymmetric bending of CH$_2$(N) and CH$_3$(N)CN)). In addition, none of the characteristic peaks for EMIMTf were present in H20.
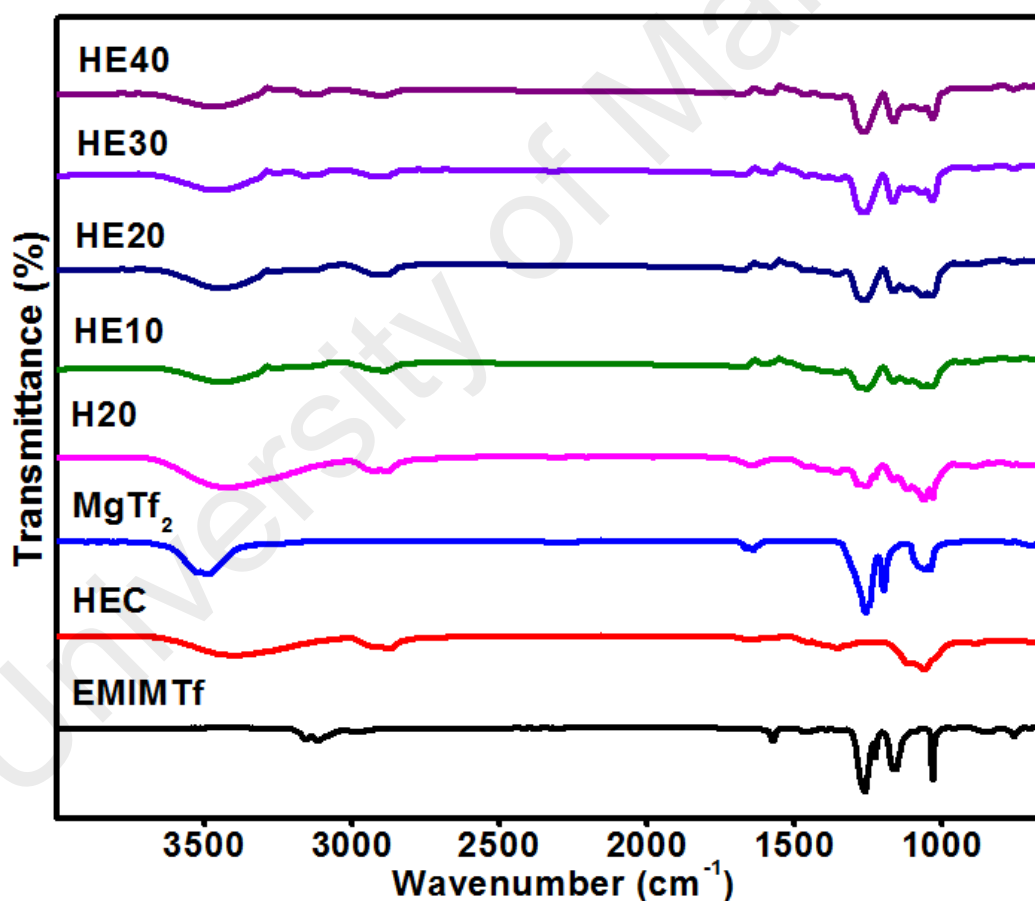
Figure 4.9: FTIR spectra of pure samples (EMIMTf, HEC, MgTf$_2$) and SPE complexes at various wt. % of EMIMTf

Table 4.1: Band assignments of pure samples (EMIMTf, HEC, MgTf$_2$) and SPE complexes at various wt. % of EMIMTf

Band assignments	EMIMTf (cm^{-1})	HEC (cm^{-1})	MgTf$_2$ (cm^{-1})	H20 (cm^{-1})	HE10 (cm^{-1})	HE20 (cm^{-1})	HE30 (cm^{-1})	HE40 (cm^{-1})	Reference
–OH stretching in pure HEC	NIL	3402	NIL	3422	3415	3420	3437	3452	(Chong et al., 2016; Satyamurthy& Vigneshwaran, 2013)
Asymmetric –CH$_2$ and –CH$_3$ stretching in HEC and EMIM$^+$	NIL	2917	NIL	2929	2917	2917	2917	2917	(Abidi et al., 2014; Saroj et al., 2014)
Symmetric –CH$_2$ and –CH$_3$ stretching in HEC and EMIM$^+$	NIL	2875	NIL	2883	2882	2882	2882	2882	(Abidi et al., 2014; Saroj et al., 2014)
Absorbed water	NIL	1652	1644	1648	1678	1674	1674	1674	(Satyamurthy& Vigneshwaran, 2013)
–OH in-plane deformation	NIL	1456	NIL	1457	1456	1456	1456	1456	(Abidi et al., 2014)
C–H bending of –CH$_2$ and –CH$_3$	NIL	1353	NIL	1355	1353	1353	1353	1353	(Abidi et al., 2014)
Asymmetric in-plane C–O–C pyrose ring stretching	NIL	1062	NIL	1061 1031	1055 1027	1055 1029	1058 1027	1061 1031	(Abidi et al., 2014)
Ring in-plane symmetric of HCCH of EMIM$^+$	3156	NIL	NIL	NIL	3155	3155	3155	3155	(Saroj et al., 2014)

Table 4.1 continued……..

Ring NC(H)NCH of EMIM$^+$	3117	NIL	NIL	NIL	3119	3119	3119	3119	(Saroj et al., 2014)
Ring in-plane asymmetric of (N)CH$_2$ and (N)CH$_3$CN in EMIM$^+$	1574	NIL	NIL	NIL	1575	1575	1575	1575	(Heimer et al., 2006)
Ring in-plane asymmetric bending of CH$_3$(N)CN and symmetric bending of CH$_3$(N)HCH in EMIM$^+$	1432	NIL	NIL	NIL	1432	1432	1429	1429	(Kiefer et al., 2007)
SO$_2$ asymmetric stretching with contributions from the CF$_3$ symmetric stretching in –CF$_3$SO$_3^-$	1262	NIL	1258	NIL	1251	1251	1251	1251	(Kiefer et al., 2007)
SO$_2$ symmetric stretching in –CF$_3$SO$_3^-$	1161	NIL	1194	NIL	1161	1161	1161	1161	(Kiefer et al., 2007)
S–O symmetric stretching of SO$_3$ in –CF$_3$SO$_3^-$	1028	NIL	1036	NIL	1028	1028	1028	1028	(Kiefer et al., 2007; Pandey & Hashmi, 2009)
Ring H–C–C–H symmetric bending, CF$_3$ symmetric bending, C–O–S bending in –CF$_3$SO$_3^-$	756	NIL	NIL	NIL	756	756	756	756	(Kiefer et al., 2007)
Ring in-plane asymmetric bending of CH$_2$(N) and CH$_3$(N)CN in EMIM$^+$	702	NIL	NIL	NIL	702	702	702	702	(Kiefer et al., 2007)
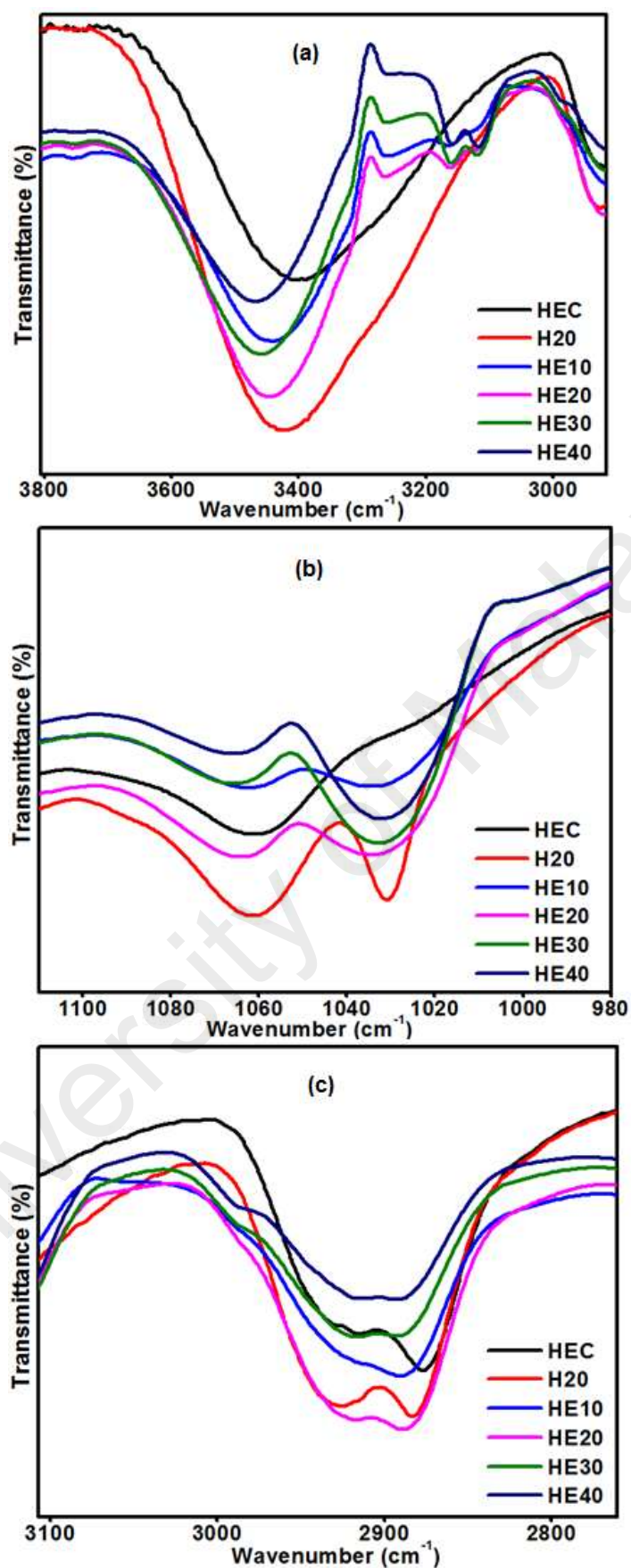
Figure 4.10: The interactions between mobile carriers and host polymer at (a) –OH stretching (3402 cm^{-1}) (b) C–O–C stretching of pyrose ring (1055 and 1026 cm^{-1}) (c) Asymmetric (2912 cm^{-1}) and symmetric (2875 cm^{-1}) stretching of –CH$_2$ and –CH$_3$
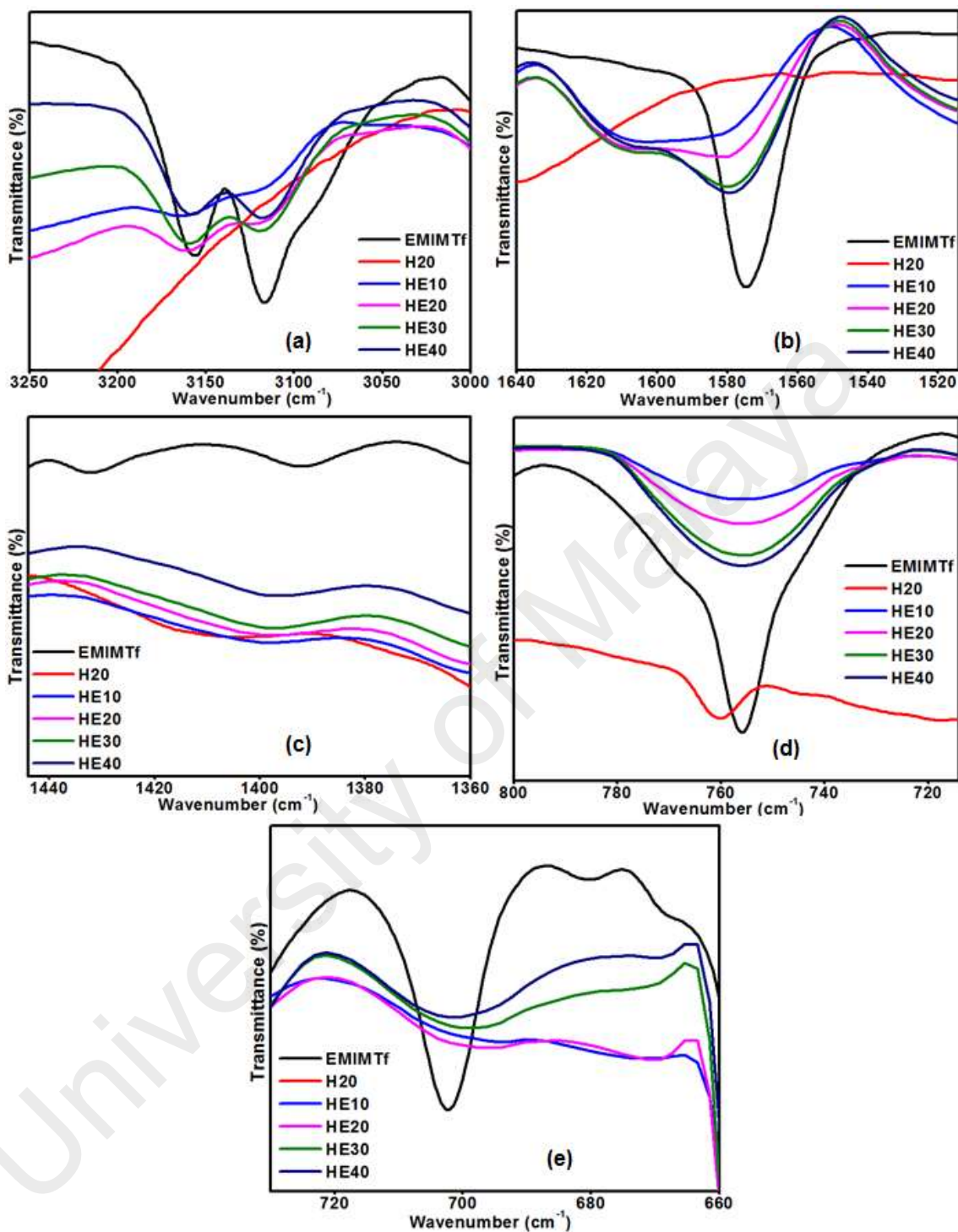
Figure 4.11: The interactions between EMIMTf and HEC-MgTf$_2$ SPEs at (a) Ring in a plane symmetric of HCCH (3157 cm^{-1}) and NC(H)NCH (3119 cm^{-1}) (b) Ring   in-plane asymmetric of (N)CH$_2$ and (N)CH$_3$CN (1576 cm^{-1}) (c) Ring in-plane asymmetric bending of CH$_3$(N)CN and symmetric bending of CH$_3$(N)HCH) (1432 cm^{-1}) (d) Ring HCCH symmetric bending, CF$_3$ symmetric bending, C–O–S bending in –CF$_3$SO$_3^-$ (756 cm^{-1}) (e) Ring in-plane anti-symmetric bending of CH$_2$(N) and CH$_3$(N)CN) (702 cm^{-1})

4.3.5 Summary

In conclusion, EMIMTf was found to be a compatible IL for HEC polymer compared to BMIMTf because EMIM⁺ creates lesser steric hindrance with the host polymer. The EIS, XRD and FTIR were conducted on the HEC-MgTf$_2$-EMIMTf complexes. Based on the EIS findings, the highest ionic conductivity at room temperature (9.28×10^{-5} S/cm) was achieved by HE40. It indicates that more mobile charge carriers in HE40 are capable in overcome its barrier due to its lowest activation energy value of 0.306 eV. All the SPE complexes were thermally activated (obeyed Arrhenius theory). Also, great interaction between host polymer and mobile charge carriers was signified by the splitting of peak at 1062 cm^{-1} into two peaks (1061 cm^{-1} and 1031 cm^{-1}) in the FTIR spectra which is responsible for asymmetric in-plane C–O–C stretching in pyrose ring of HEC. The XRD patterns showed all the SPE complexes at various wt. % of EMIMTf exhibits diffraction peak at $2\theta = 19.9°$ which indicates complete complexation between host polymer and charge carriers. Moreover, it also showed that the ionic conductivity is predominated by the adsorption of ions on the polymer chain.

4.4 Characterization and Optimization of Fumed SiO$_2$ Nanoparticles for HEC-MgTf$_2$-EMIMTf-fumed SiO$_2$ SPEs

4.4.1 Ionic Conductivity Studies

Figure 4.12 shows the impedance plot of HEC-MgTf$_2$-EMIMTf SPEs at various wt. % of fumed SiO$_2$ nanoparticles at room temperature. HS2 attained the lowest R$_b$ value of 14.5 Ω at high frequency region, followed by HS1 (24.1 Ω), HS3 (36 Ω) and HS4 (86.8 Ω). Amongst these R$_b$ values obtained by the SPEs upon inclusion of fumed SiO$_2$ nanoparticles, only HS1 and HS2 experienced smaller values than HE40 whereas both HS3 and HS4 exhibited greater values than HE40. As a consequence, both HS1 and HS2 obtained ionic conductivity of 1.50×10^{-4} S/cm and 2.71×10^{-4} S/cm, respectively at room temperature. On the other hand, both HS3 and HS4 obtained ionic conductivity of

1.07×10^{-4} S/cm and 4.74×10^{-5} S/cm, respectively at room temperature. The HS2-based SPE achieved the highest ionic conductivity at room temperature by of virtue of silanol (Si–OH) group in fumed SiO_2 nanoparticles which served as conjunction site with high affinity of charge carriers (Aziz & Abidin, 2013). On the contrary, both HS3 and HS4 attained a dropped of ionic conductivity by 60.5 % and 82.5 %, respectively compared to HS2 due to the clustering of nanoparticles which retard the flexibility of the polymer chain (Wang & Kim, 2007).
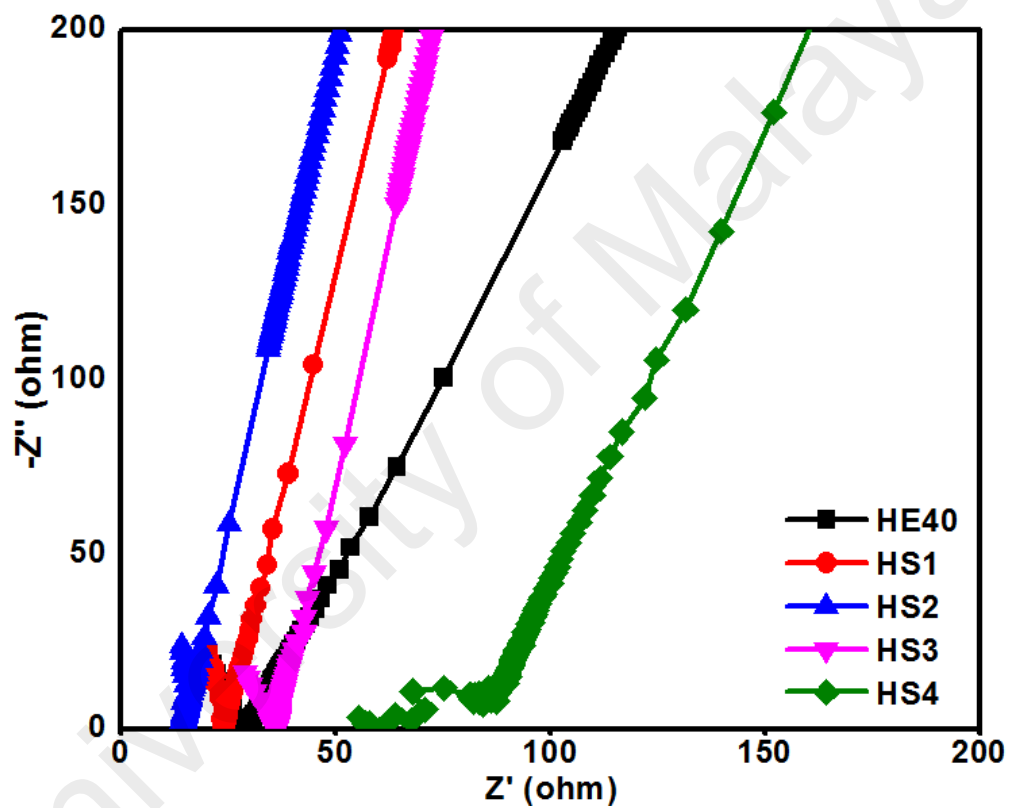
Figure 4.12: Cole-Cole plot for SPE complexes at various wt. % of fumed SiO_2 nanoparticles at room temperature

Figure 4.13 illustrates the relationship between the ionic conductivity and the activation energy at various wt. % of fumed SiO_2 nanoparticles at room temperature. The most conducting SPE (HS2) obtained the lowest activation energy of 0.213 eV due to its easiness to hop to vacant spaces while HS1, HS3 and HS4 obtained activation energies of 0.251 eV, 0.298 eV and 0.309 eV, respectively. Nonetheless, all the SPE complexes experienced fast transportation of charge carriers because incomplete semicircles were

observed (Rajendran et al., 2007). Additionally, HS2 and HS3 complexes suffered less non-homogeneity at the electrode/electrolyte interface compared to HS1 and HS4 and imply more capacitive behavior because the inclined spike of HS2 and HS3 are closer to the vertical axis (Ramya et al., 2008).
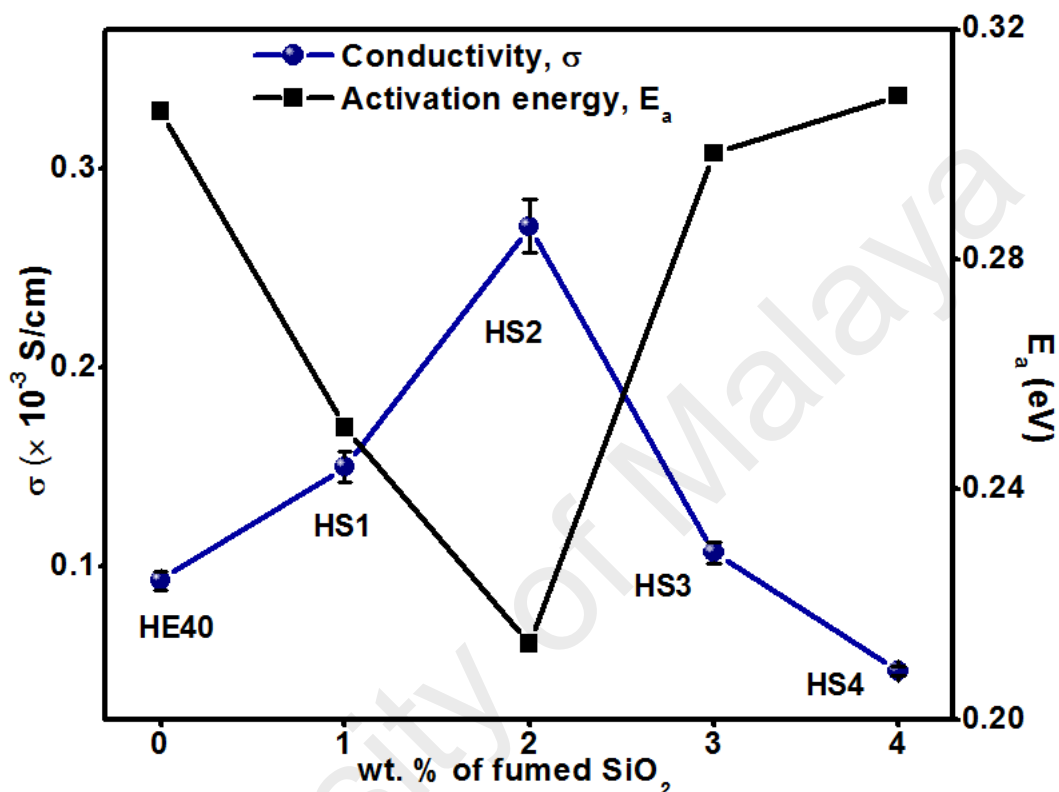
Figure 4.13: Variation of ionic conductivity and activation energy at various wt. % of fumed SiO_2 nanoparticles at room temperature

Figure 4.14 depicts the linear relationship between variations of logarithm of ionic conductivities with 1000/T at various wt. % of fumed SiO_2 nanoparticles. Based on the plot, it indicates the SPE complexes obeyed Arrhenius theory because the R^2 values for all samples were 0.99. According to Idris et al. (2012), all the SPE complexes were thermally activated because the mobility of charge carriers and expansion of polymer were escalated greatly. Hence, the ions have more opportunities to hop to the vacant spaces provided.
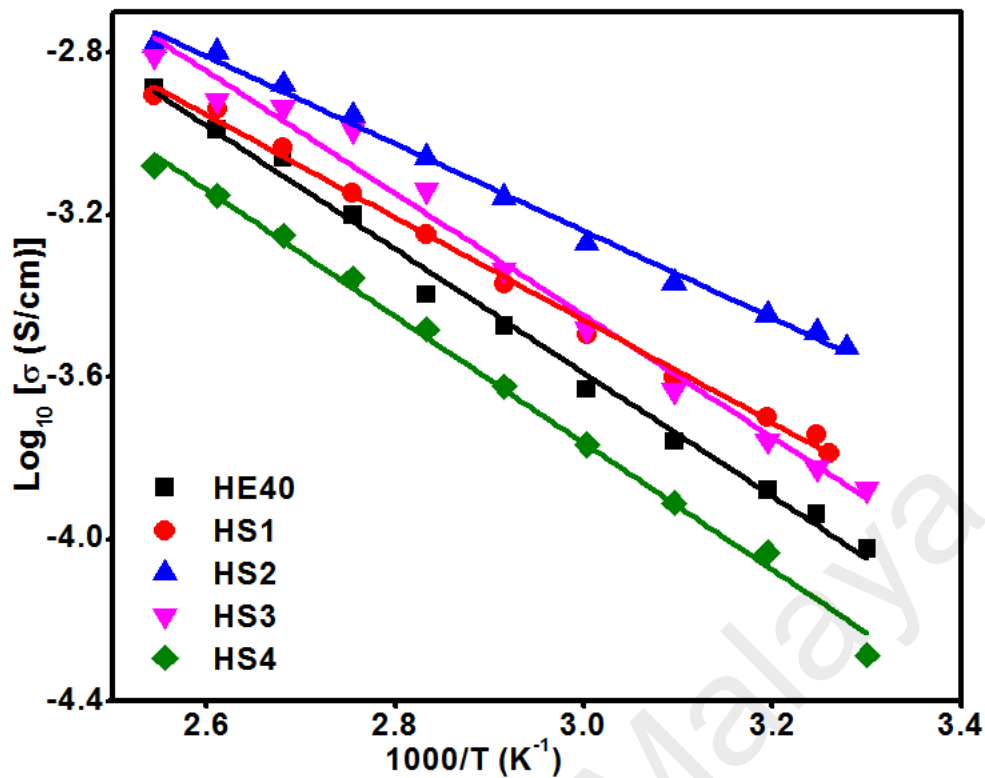
Figure 4.14: Variation of logarithm ionic conductivity from 30–120 ˚C at various wt. % of fumed SiO_2 nanoparticles

4.4.2 Dielectric Studies

Dielectric constant of a material is the ability of a material to hold large quantities of charge for long periods of time. It depends on two factors, namely, dielectric permittivity (real part) and dielectric loss (imaginary part).

4.4.2.1 Dielectric Relaxation Studies

Dielectric permittivity (ε') is a measurement for the electric displacement of the polymer electrolytes with the intensity of the electrical field. Dielectric loss (ε'') quantifies the amount of heat dissipated during ion transportation and dipole polarization (Osman et al., 2012).

Figure 4.15(a) shows the variation of ε' against frequencies at various wt. % of fumed SiO_2 nanoparticles. Generally, the ε' decreases with increasing value of frequencies at various wt. % of fumed SiO_2 nanoparticles. At low frequency, HS2 achieved the highest

ε' (9.0×10^4) because it has the highest number of ions accumulated near the surface of the stainless steel electrodes which is in well agreement with the EIS result discussed in Section 4.4.1 (Mishra & Rao, 1998). Subsequently, at moderate frequency (10^3–$10^{4.5}$ Hz), the charges were stored in the SPE complexes through the realignment of electric dipoles with the electrical field. At high frequency, all the SPE complexes obtained a steady state of dielectric permittivity because the electric dipoles were unable to obey the variation of high electrical field (Tareev, 1975).

Figure 4.15(b) describes the variation of ε'' against frequencies at various wt. % of fumed SiO_2 nanoparticles. HS2 attained the highest ε'' values along with the broadest inflection point from $10^{2.6}$ Hz to 10^6 Hz because it experienced the greatest molecular relaxation (orientation and polarization). Also, the maximum inflection peak of HS2 (the most conducting SPE) has been shifted to the highest frequency of $10^{3.7}$ Hz compared to HS1, HS3, HS4 and HE40 because HS2 has more ions to relax at a higher frequency region (Tamilselvi & Hema, 2014).

4.4.2.2 Modulus Studies

The electric modulus of a material is the ability of a material to relax towards electric field at constant electric displacement. It is the reciprocal of the permittivity which represents real dielectric relaxation process. The electric modulus depends on two factors, one is real part modulus (M') and other is imaginary part modulus (M"). The real part of modulus is used to study long-range ionic conductivity dielectric relaxation, whereas the imaginary part of modulus is to illustrate pure conduction process. The electric modulus measurement is conducted to analyze the dielectric behavior of the polymer electrolytes without involving the effect of electrode polarization.

Figures 4.16(a) and (b) show the variation of M' and M" against frequencies, respectively at various wt. % of fumed SiO_2 nanoparticles. The M' and M" for all SPE

complexes portrayed a "long-tail" pattern from low frequency to $10^{5.5}$ Hz and 10^5 Hz, respectively. The applied electrical field on the long-range ionic conductivity for all SPE complexes were insignificant because this type of conductivity is independent from the nature of electrode materials, the contact between electrode/electrolyte interface, and the impurities adsorbed on the polymer electrolytes. Additionally, all the SPE complexes do not showed maximum peak proving that SPE films are ionic conductor because the experimental frequency window is narrow (Dasari et al., 2011).
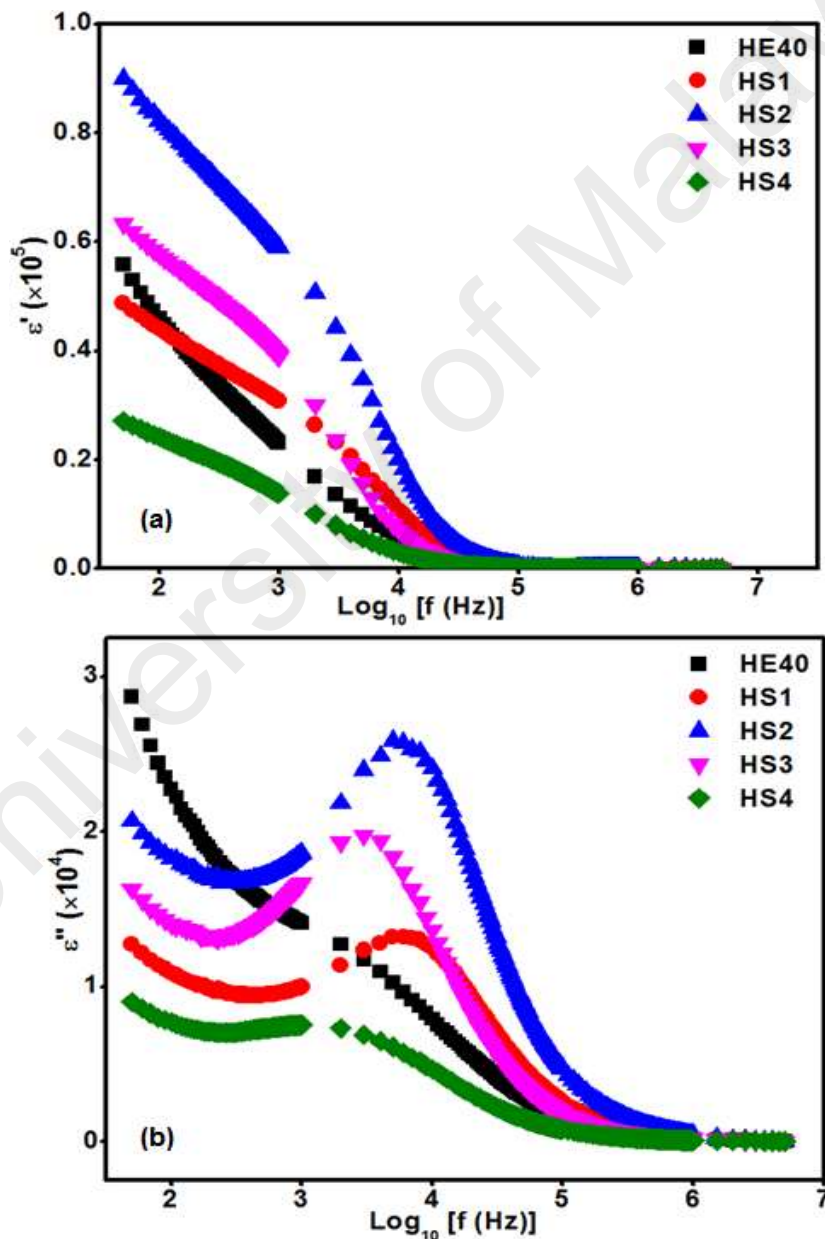
Figure 4.15: Variation of (a) ε' and (b) ε" with frequency at various wt. % of fumed SiO_2 nanoparticles
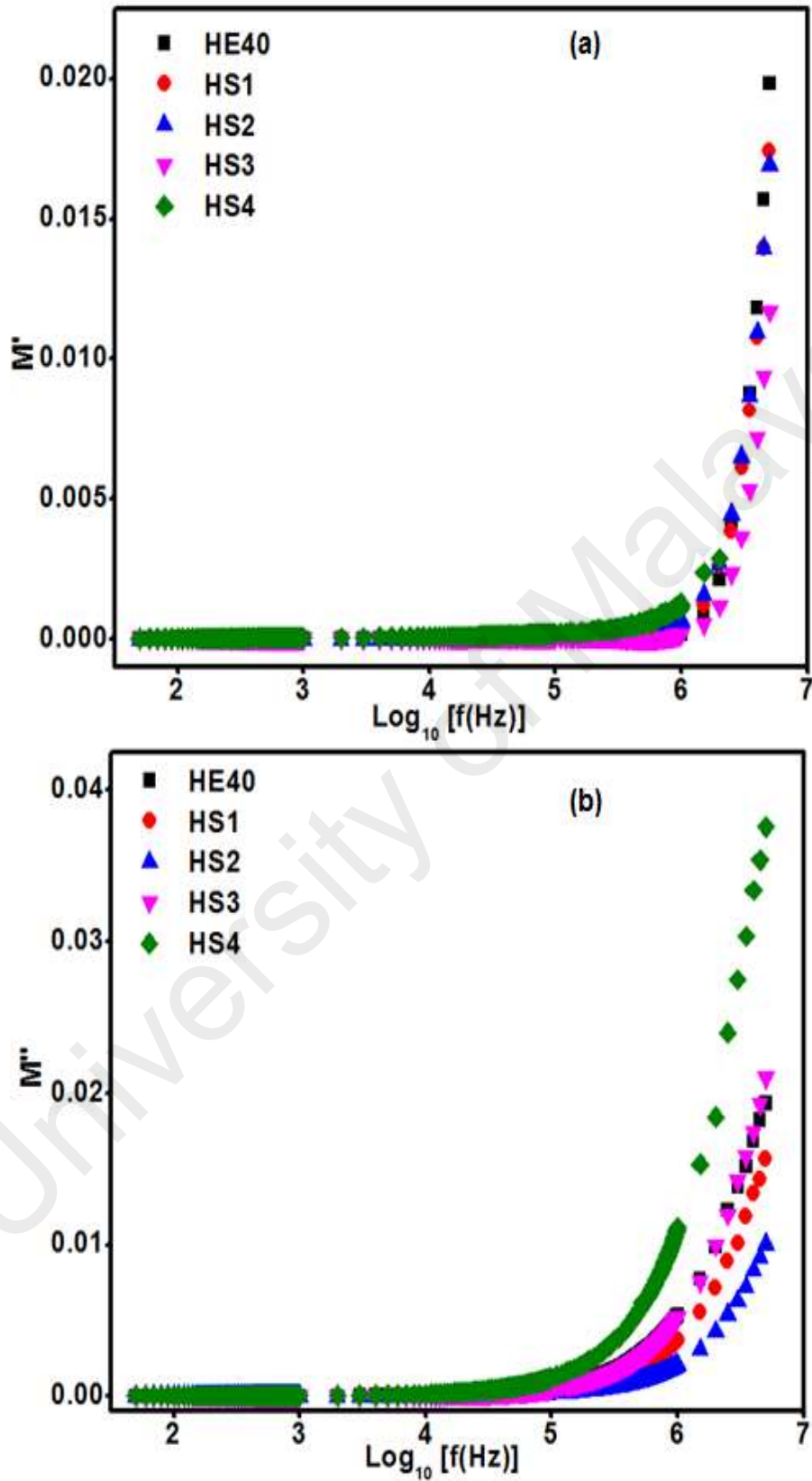
Figure 4.16: Variation of (a) M' and (b) M" with frequency at various wt. % of fumed SiO$_2$ nanoparticles

4.4.3 XRD Studies

Figure 4.17 demonstrates the XRD patterns of pure samples (HEC and fumed SiO_2) and SPE complexes at various wt. % of fumed SiO_2 nanoparticles. According to Burgaz (2011), fumed SiO_2 nanoparticles is amorphous and upon its addition into HE40, only HS2 was partially amorphous whereas the others (HS1, HS3 and HS4) were highly crystalline. Despite, a complexation peak at $2\theta = 20.0°$ was observed disregarding the crystallinity of the SPEs (with and without incorporation of fumed SiO_2 nanoparticles). As a result, HS2 experienced an abrupt decrease in peak broadness at $2\theta = 20.0°$ by 53.4 % compared to HE40. When optimum amount of amorphous nanoparticles was incorporated into the SPE, then it destroyed the crystallinity of the host polymer. Thus, ample spaces for adsorption of charge carriers were provided and led to the escalation of ionic conductivity as discussed in Section 4.4.1 (Capiglia et al., 2002).
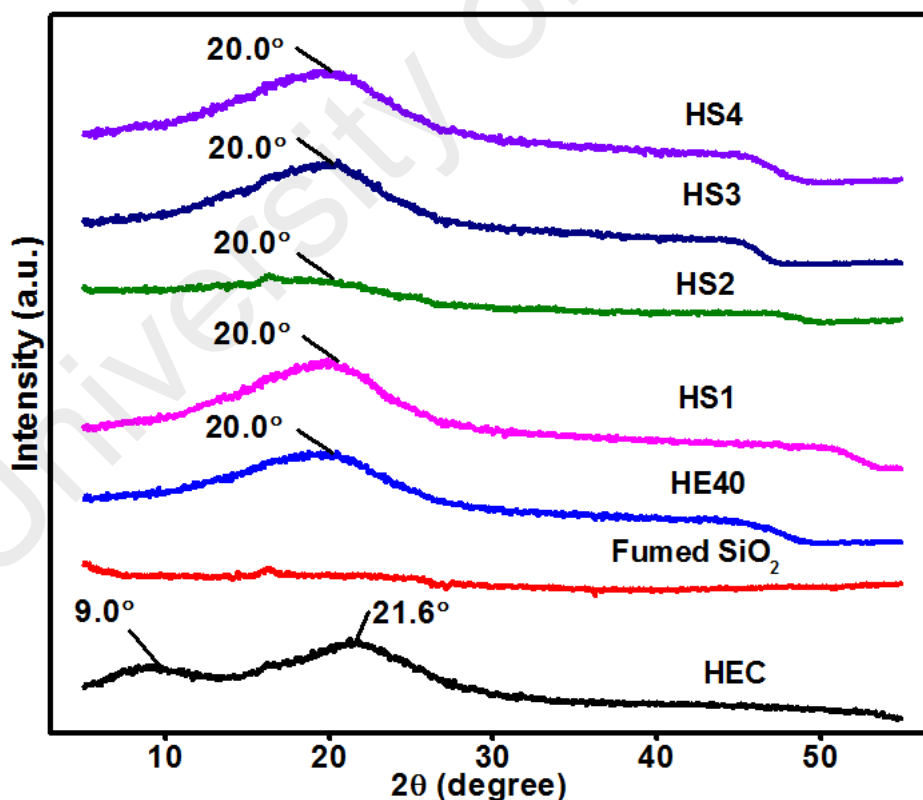
Figure 4.17: XRD patterns of pure samples (HEC and fumed SiO_2) and SPE complexes at various wt. % of fumed SiO_2 nanoparticles

4.4.4 FTIR Studies

Figure 4.18 depicts the FTIR spectra of pure samples (HEC and fumed SiO_2) and SPE complexes at various wt. % of fumed SiO_2 nanoparticles.
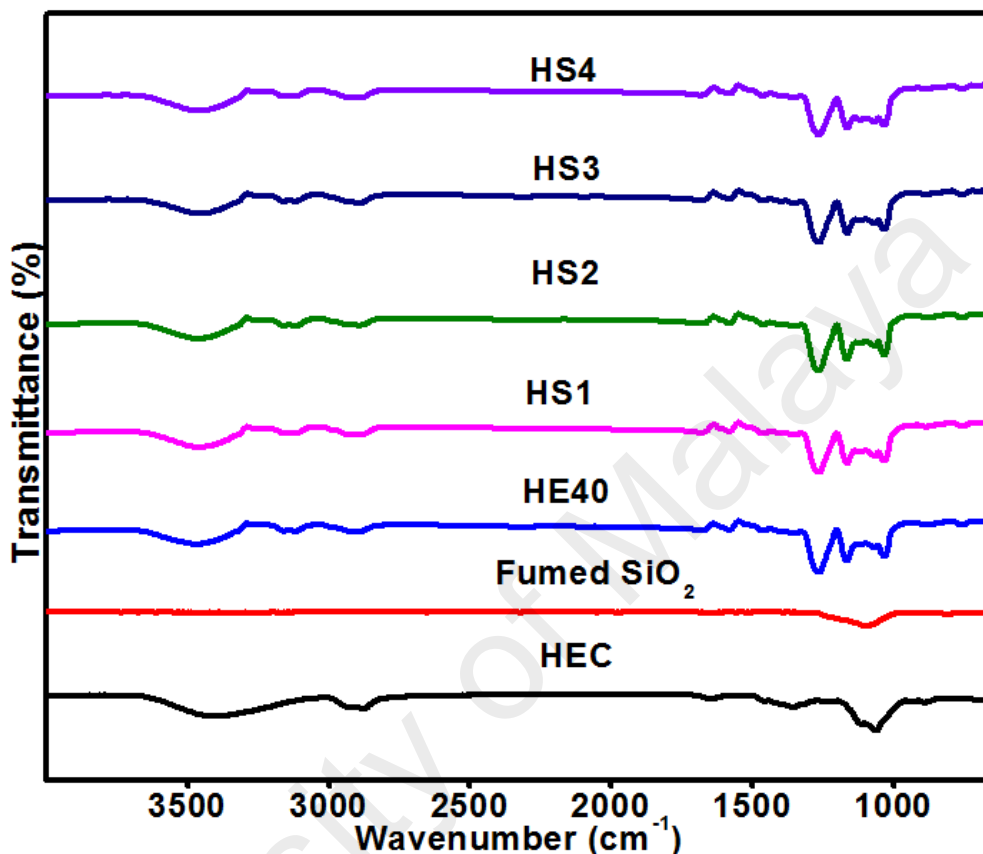
Figure 4.18: FTIR spectra of pure samples (HEC and fumed SiO_2) and SPE complexes at various wt. % of fumed SiO_2 nanoparticles

Fumed SiO_2 has an intense and broad characteristic peaks at 1086 cm^{-1} responsible for asymmetric vibrations of Si–O–Si, respectively (Huang et al., 2016). However, the characteristic peaks of fumed SiO_2 were not noticeable in HS1, HS2, HS3 and HS4 due to too little amount of fumed SiO_2 incorporated into HE40. Although, successful incorporation of fumed SiO_2 nanoparticles into the HEC-MgTf$_2$-EMIMTf complexes was successfully proven from minor decrease in the broadness of –OH stretching (3473 cm^{-1}) by 40.8 % and the shift to a higher wavenumber at peaks 1260 cm^{-1} (–OH in-plane bending) with respect to HE40 as shown in Figure 4.19(a). It can be explained by the destruction of intermolecular hydrogen bonding between silanol group in fumed SiO_2

nanoparticles and host polymer and thereby great reduction in the broadness of –OH stretching peak was apparent (Gupta et al., 2002).

Figure 4.19(b) and (c) demonstrate the SO_2 symmetric stretching in $CF_3SO_3^-$ and in-plane C–O–C pyrose ring stretching at 1165 cm^{-1} and 1030 cm^{-1}, respectively. HS2 exhibited vigorous interaction with charge carriers through the significant increase in peak intensity at wavenumber 1165 cm^{-1} (SO_2 symmetric stretching in $CF_3SO_3^-$) and 1030 cm^{-1} (asymmetric in-plane of C–O–C pyrose ring stretching) by 8.9 % and 34.7 %, respectively compared to HE40. Instead of these changes, prominent change in wavenumber can be observed at peaks 2923 cm^{-1} (asymmetric –CH_2 and –CH_3 stretching), 2881 cm^{-1} (symmetric –CH_2 and –CH_3 stretching), 1357 cm^{-1} (C–H bending of –CH_2 and –CH_3) and 862 cm^{-1} (asymmetric out-of-phase C–O–C pyrose ring stretching) as summarize in Table 4.2.

4.4.5 TGA Studies

Table 4.3 portrays the decomposition temperature of pure samples ($MgTf_2$, EMIMTf and HEC) and SPE complexes at various wt. % of fumed SiO_2 nanoparticles. Figure 4.20(a) shows the thermogram of pure samples ($MgTf_2$, EMIMTf, HEC and fumed SiO_2) whereas Figure 4.20(b) depicts the thermogram of SPE complexes at various wt. % of fumed SiO_2 nanoparticles. Based on figure 4.20(a), fumed SiO_2 does not show any decomposition even when the temperature reached 800 ˚C. This is due to the high decomposition temperature of fumed SiO_2 nanoparticles possess high decomposition temperature which is not able to be measured by the instrument because of its' low detection limit.
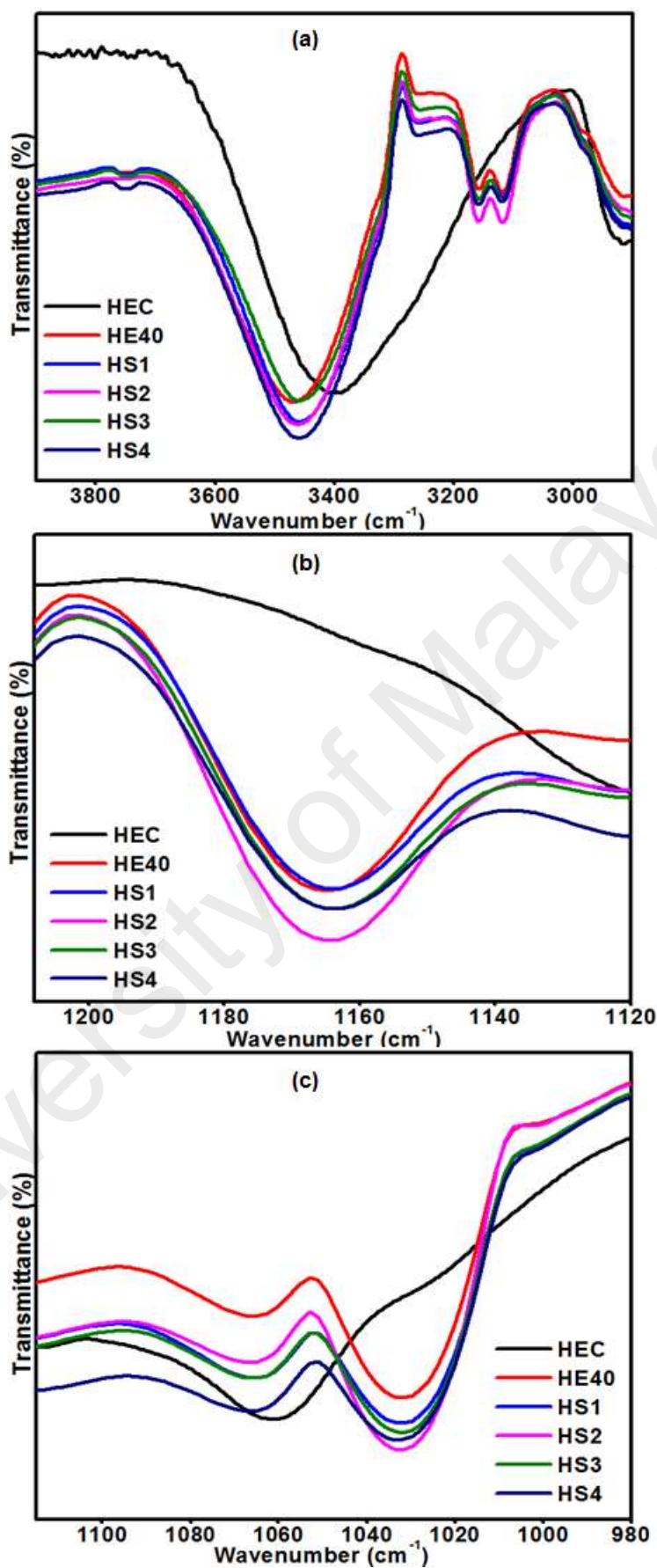
Figure 4.19: (a) –OH stretching (3473 cm^{-1}) (b) SO$_2$ symmetric stretching in CF$_3$SO$_3^-$ (1165 cm^{-1}) and (c) asymmetric in-plane C–O–C pyrose ring stretching (1030 cm^{-1})

Table 4.2: Band assignments of pure samples (HEC and fumed SiO_2) and SPE complexes at various wt. % of fumed SiO_2 nanoparticles

Band assignments	HEC (cm^{-1})	Fumed SiO_2 (cm^{-1})	HE40 (cm^{-1})	HS1 (cm^{-1})	HS2 (cm^{-1})	HS3 (cm^{-1})	HS4 (cm^{-1})	Reference
–OH stretching	3403	NIL	3473	3447	3447	3444	3447	(Chong et al., 2016; Satyamurthy & Vigneshwaran, 2013)
Asymmetric –CH$_2$ and –CH$_3$ stretching	2917	NIL	2923	2923	2926	2923	2917	(Abidi et al., 2014; Saroj et al., 2014)
Symmetric –CH$_2$ and –CH$_3$ stretching	2876	NIL	2881	2887	2887	2884	2884	(Abidi et al., 2014; Saroj et al., 2014)
Absorbed water	1651	NIL	1636	1678	1678	1678	1678	(Chung et al., 2004; Satyamurthy & Vigneshwaran, 2013)
–OH in-plane deformation	1457	NIL	1457	1457	1457	1457	1457	(Abidi et al., 2014)
C–H bending of –CH$_2$ and –CH$_3$	1354	NIL	1357	1357	1357	1354	1354	(Abidi et al., 2014)

Table 4.2 continued………

–OH in-plane bending	1239	NIL	1260	1251	1254	1254	1251	(Chung et al., 2004)
Asymmetric bridge C–O–C stretching	NIL	NIL	1165	1159	1159	1159	1159	(Chung et al., 2004)
SO$_2$ symmetric stretching in –CF$_3$SO$_3^-$	1115	NIL	1118	1115	1115	1115	1112	(Abidi et al., 2014; Chung et al., 2004)
Asymmetric in-plane C–O–C pyrose ring stretching	1062 NIL	NIL	1062 1030	1056 1024	1056 1027	1056 1027	1059 1024	(Abidi et al., 2014; Chung et al., 2004)
Asymmetric out-of-phase C–O–C pyrose ring stretching	889	NIL	862	889	889	889	892	(Chung et al., 2004)
Asymmetric vibrations of Si–O–Si	NIL	1086	NIL	1086	NIL	1086	1114	(Huang et al., 2016)

Generally, the thermal stability of all the SPE complexes improved upon incorporation of fumed SiO_2 nanoparticles which was indicated by the enhancement in decomposition temperature at stage 4. The decomposition temperature at stage 4 (466.0–478.0 °C) was owing to the decomposition of $MgTf_2$ whereas the decomposition temperature at stage 3 (382.0–420.0 °C) and stage 2 (266.0–284.0 °C) were due to the decomposition of EMIMTf and HEC, respectively. However, all the SPE complexes facing shifts of decomposition temperature compared to pure samples due to complexation in the samples as discussed in Section 4.4.3 and 4.4.4 (Fattah et al., 2016). At early stage, HE40 suffered 4.1 % weight loss at decomposition temperature of 54.0 °C due to evaporation of volatile minor impurities and absorbed moisture. Additionally, SPE complexes upon incorporation of fumed SiO_2 nanoparticles exhibit thermal decomposition around 100 °C with weight loss of ~3.0 % which was due to the complete evaporation of water solvent in the SPE complexes (Lewandowska, 2009; Liew et al., 2015).

Table 4.3: The decomposition temperature of pure samples (HEC, $MgTf_2$ and EMIMTf) and SPE complexes at various wt. % of fumed SiO_2 nanoparticles

Samples	Thermal decomposition (°C)			
	Stage 1	Stage 2	Stage 3	Stage 4
HEC	295.9	NIL	NIL	NIL
$MgTf_2$	107.2	460.5	NIL	NIL
EMIMTf	397.5	NIL	NIL	NIL
HE40	51.8	266.6	382.9	466.0
HS1	88.0	282.3	395.3	472.3
HS2	88.0	276.9	414.9	475.9
HS3	88.0	278.7	418.5	475.9
HS4	88.0	284.1	420.3	477.7
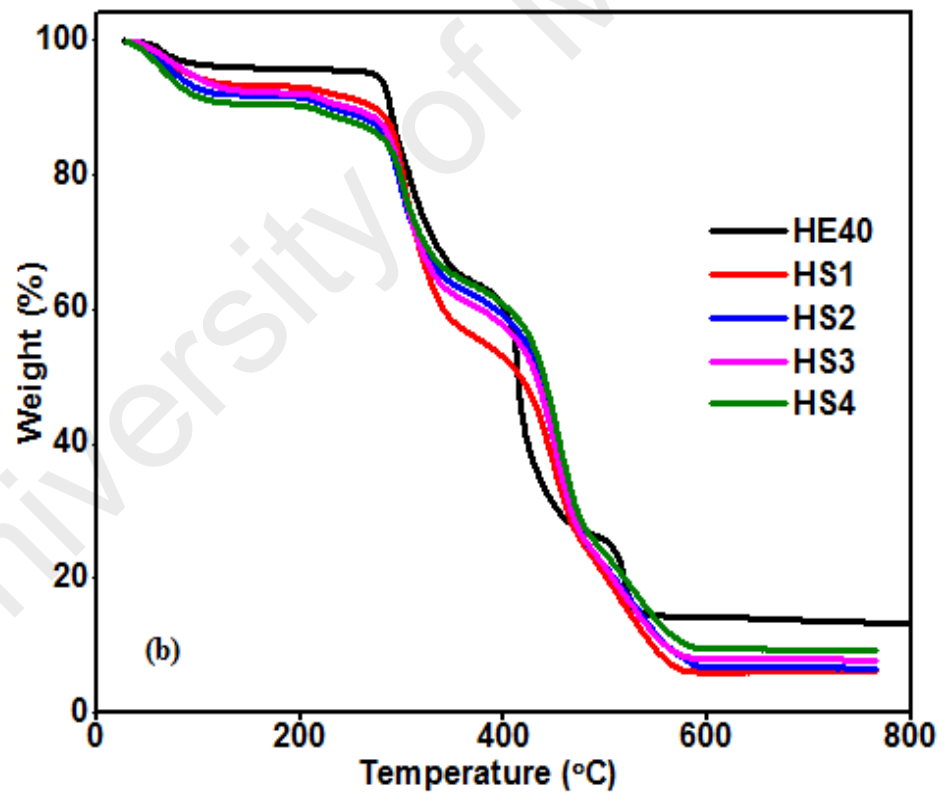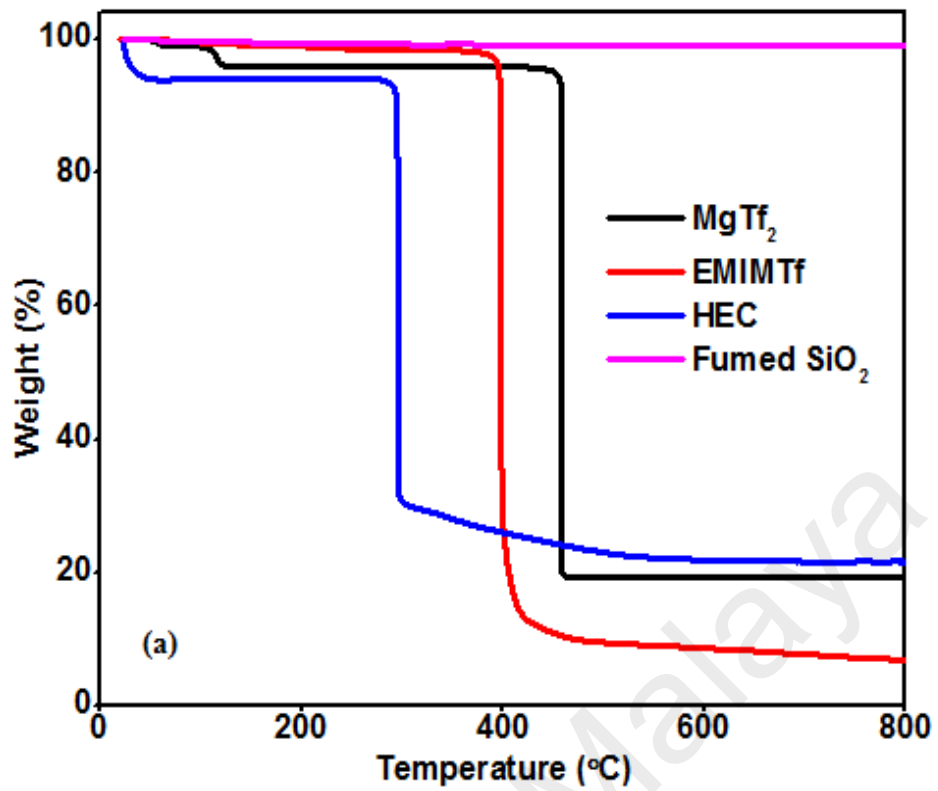
Figure 4.20: Thermograms of (a) pure samples (HEC, MgTf$_2$, EMIMTf and fumed SiO$_2$) and (b) SPE complexes at various wt. % of fumed SiO$_2$ nanoparticles

4.4.6 CV Studies

Figure 4.21 portrays the CV responses for EDLC cells (with and without fumed SiO_2 nanoparticles) at different scan rates over the voltage range from -1 to 1 V.
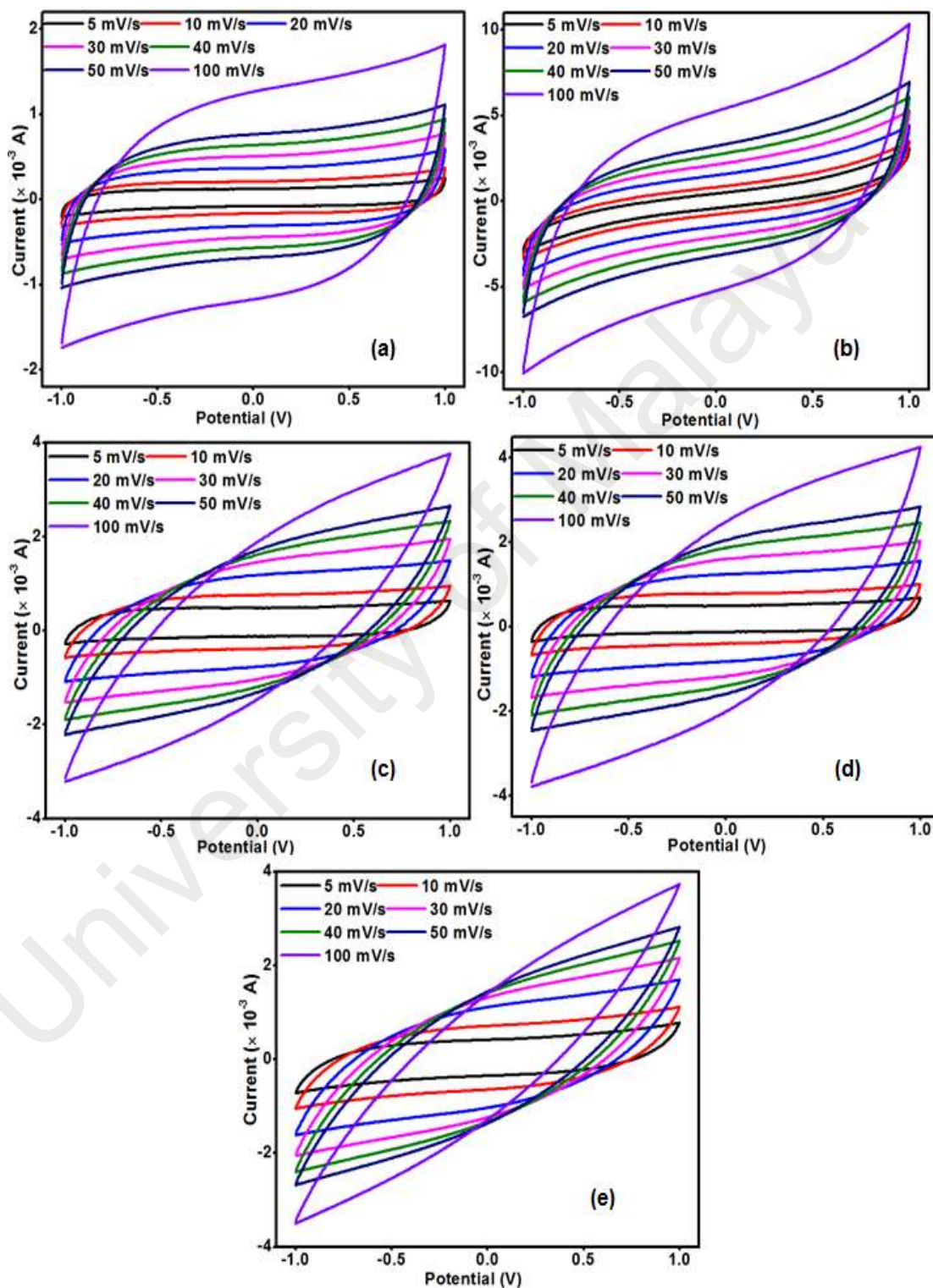
Figure 4.21: CV responses of (a) HE40 (b) HS1 (c) HS2 (d) HS3 and (e) HS4 at different scan rates over the voltage range from -1 to 1 V

Interestingly, all the samples demonstrate an excellent double layer capacitive characteristics below scan rate of 50 mV/s because a rectangular shaped and nearly mirror image symmetry of the current response about the zero line were observed. Additionally, oxidation-reduction peak was not observed in the EDLC cells (with and without incorporation of fumed SiO_2 nanoparticles), revealing that capacitive effective was due to electric double storage of charges.

Figure 4.22(a) depicts the variation of specific capacitance of EDLCs as a function of scan rate. The specific capacitance for all the EDLCs decreased with increasing scan rate due to the delay in reverse adsorption of ions on the electrode/electrolyte interface which is also known as "Electrolyte Starvation Effect" (Mysyk et al., 2009). The phenomena was supported by the ill rectangular shaped of the CV curve obtained by EDLC (with and without fumed SiO_2 nanoparticles) at scan rate of 100 mV/s. Figure 4.22(b) demonstrates the CV responses for EDLCs at scan rate of 5 mV/s. It was found that the maximum specific capacitance calculated based on Equation 3.11 were 23 F/g, 25 F/g, 22 F/g and 19 F/g upon incorporation of 1, 2, 3 and 4 wt. % of fumed SiO_2 nanoparticles into HE40. HS2-based cell attained the greatest increase of specific capacitance at scan rate of 5 mV/s by 127.3 % compared to HE40 cell (11 F/g). It was followed by HS1, HS3 and HS4 with increased in specific capacitance by 108.2 %, 100.0 % and 69.1 %, respectively compared to HE40 cell.

As a result, the performance of the EDLCs with incorporation of fumed SiO_2 nanoparticles were better than HE40 because the charge carriers adsorbed on the fumed SiO_2 nanoparticles (small particle size) permeates faster than the ions adsorbed on the host polymer (bulky molecules) into the carbon electrodes (Chandrasekaran et al., 2008). Amongst the EDLCs incorporated with fumed SiO_2 nanoparticles, HS2-based cell achieved the highest maximum specific capacitance compared to its counterparts because

huge amount of ions penetrated into the carbon electrodes successfully. This was due to HS2-based SPE possessed the highest number of mobile charge carriers which smoothen the penetration of ions into the carbon electrodes (Gryglewicz et al., 2005).
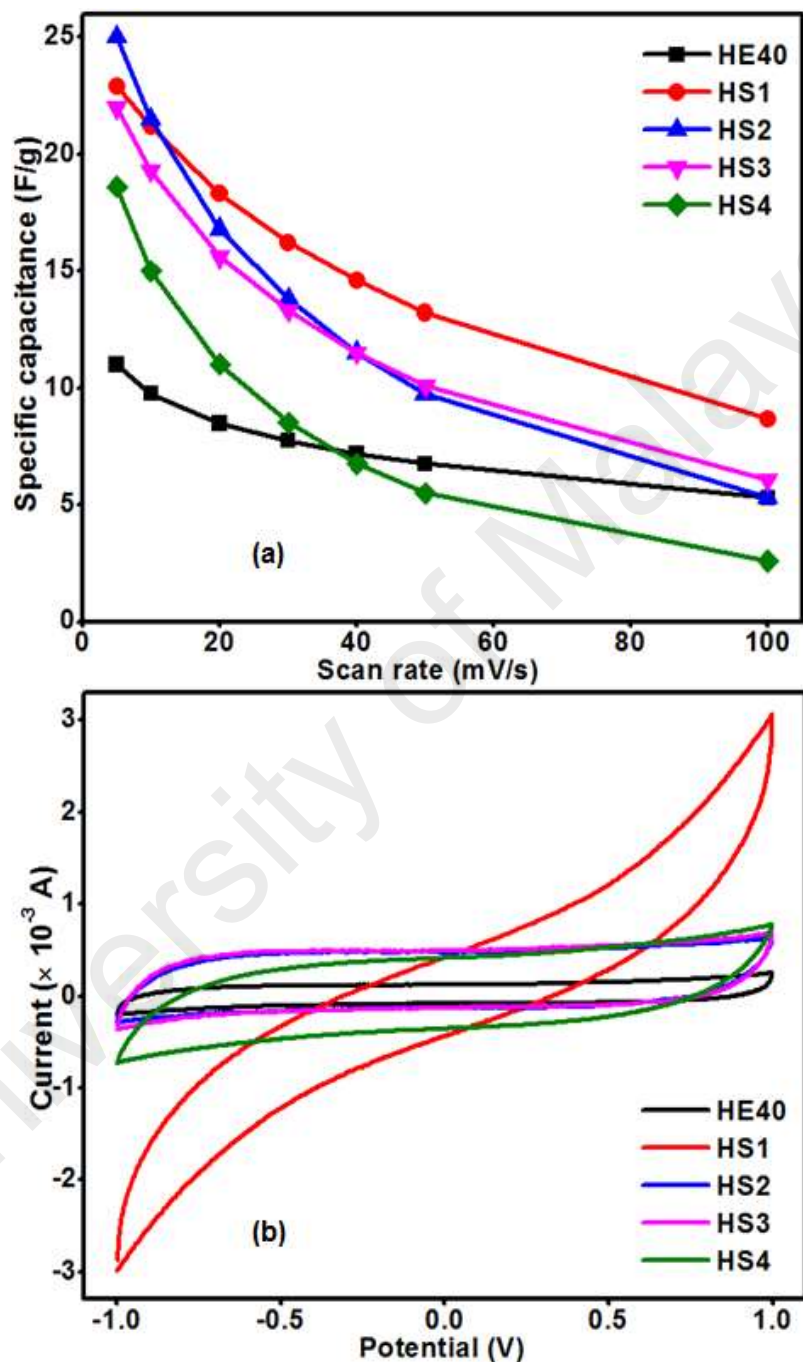
Figure 4.22: (a) Specific capacitance for EDLC cells (with and without incorporation of fumed SiO_2 nanoparticles) as a function of scan rate (b) CV responses at scan rate of 5 mV/s for EDLC cells (with and without incorporation of fumed SiO_2 nanoparticles)

4.4.7 EIS Studies

Table 4.4 demonstrates the R_{ct} values and the deviation from imaginary axis of EDLC cells (with and without incorporation of fumed SiO_2 nanoparticles) whereas Figure 4.23 illustrates the electrochemical impedance spectra of EDLC cells (with and without incorporation of fumed SiO_2 nanoparticles) at room temperature. The HS2-based SPE achieved the highest ionic conductivity at room temperature as well as maximum specific capacitance, thus it attained the lowest R_{ct} value (47.4 Ω). On top of that, the spike deviated the least from the vertical axis (20.7 $^{\circ}$) compared to other EDLCs. This phenomena signified that minimum resistance was created by HS2-based cell due to its thickness along with good transportation of Mg^{2+} ions into the carbon electrodes (Taberna et al., 2003). The results obtained are in well agreement with the maximum specific capacitance calculated at 5 mV/s and the ionic conductivities measured at room temperature which were discussed in Sections 4.4.1 and 4.4.6, respectively. Generally, the charge transfer resistance values for all the EDLC cells after incorporated with fumed SiO_2 nanoparticles were lesser than HE40-based cell.

Table 4.4: R_{ct} values and the deviation from imaginary axis for EDLC cells (with and without incorporation of fumed SiO_2 nanoparticles)

EDLC cell	R_{ct} (Ω)	Deviation from imaginary axis ($^{\circ}$)
HE40	142.0	36.0
HS1	59.8	26.3
HS2	47.4	20.7
HS3	78.8	40.1
HS4	132.3	42.8
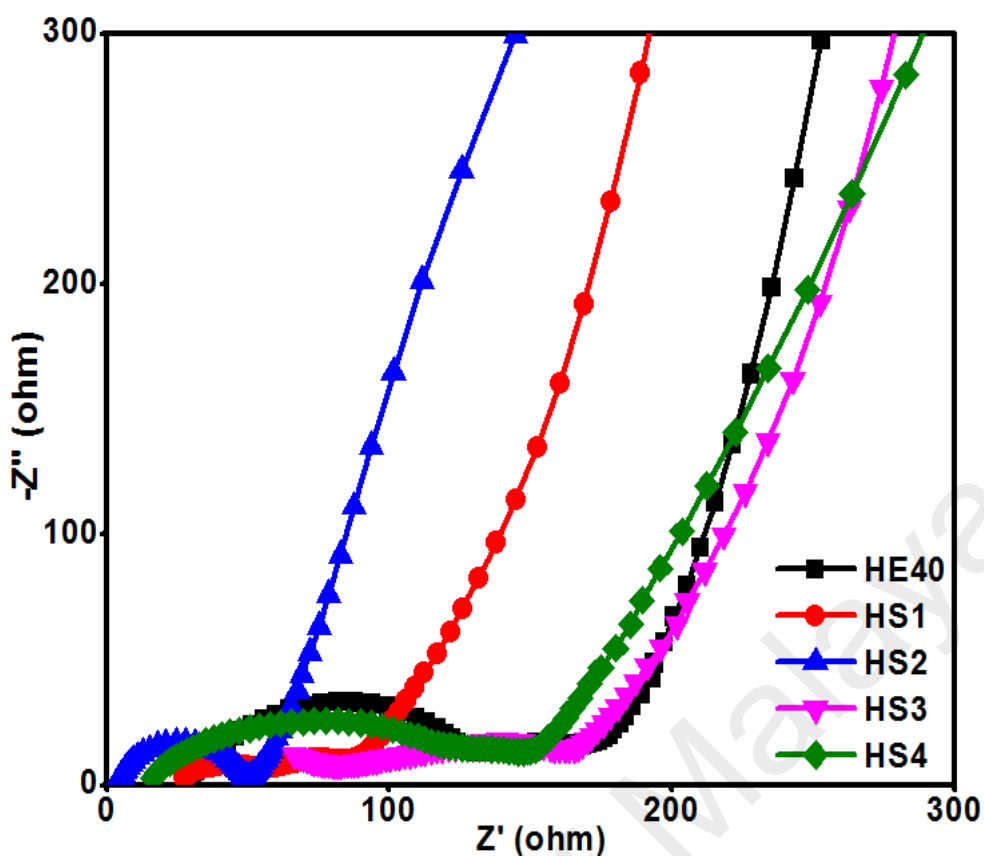
Figure 4.23: Electrochemical impedance spectra of EDLC cells (with and without incorporation of fumed SiO_2 nanoparticles) at room temperature

4.4.8 GCD Studies

Figures 4.24(a) – (e) represent the galvanostatic charge-discharge curves for EDLCs (with and without incorporation of fumed SiO_2 nanoparticles) at different current densities. The EDLCs showed the occurrence of non-Faradaic process because they achieved symmetric triangles of galvanostatic charge-discharge curve in the potential range of 0 to 1 V at different current densities (30, 40, 60, 80 and 100 mA/g) (Luo et al., 2016). Figure 4.24(f) demonstrates the discharge curves of EDLCs at current density of 30 mA/g. Based on the plot, HS1, HS2, HS3 and HS4 based cells achieved longer discharge time of 347.8 s, 389.0 s, 288.6 s, 245.5 s, respectively compared to HE40 cell (136.3 s).
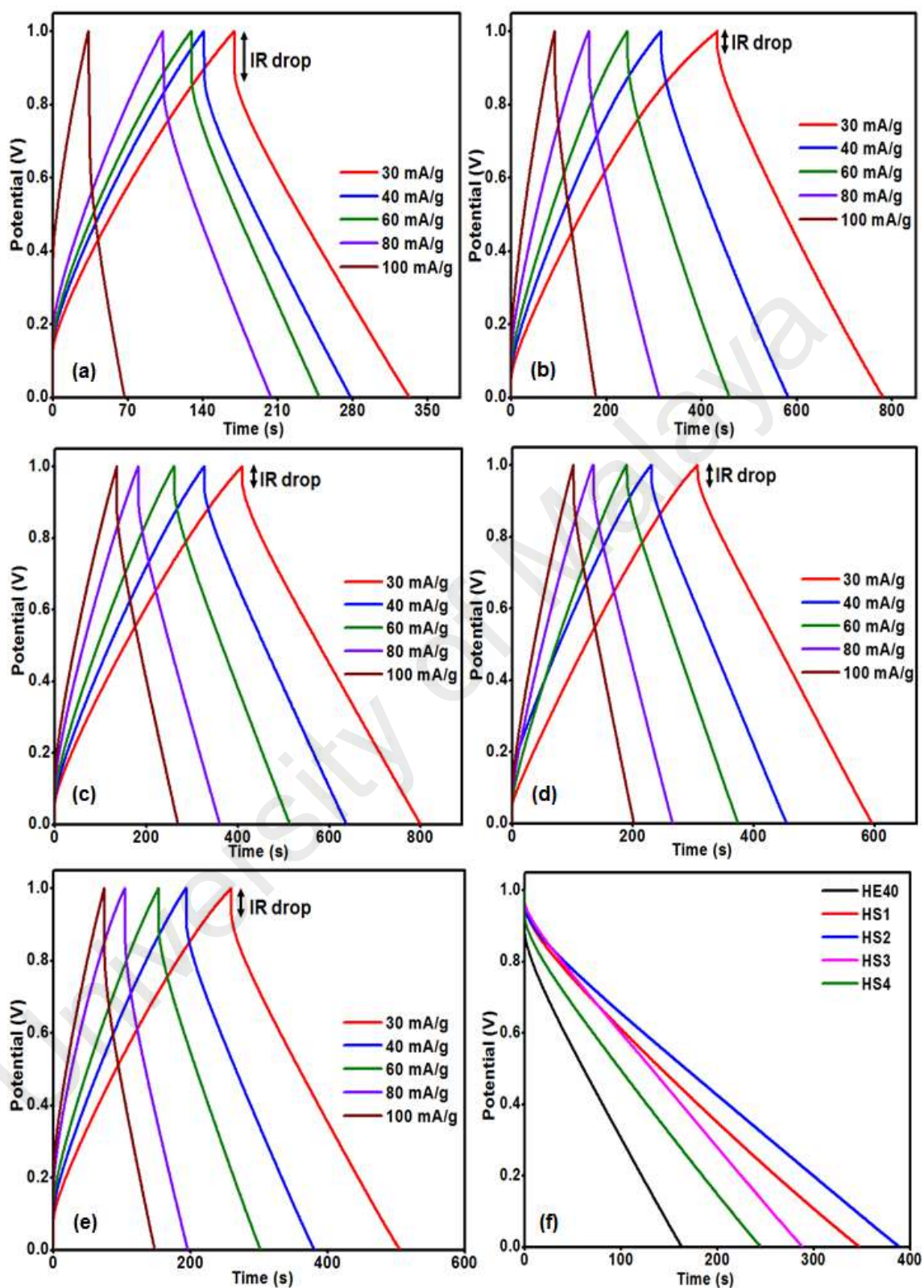
Figure 4.24: Galvanostatic charge-discharge curves of (a) HE40 (b) HS1 (c) HS2 (d) HS3 (e) HS4 at different current densities (f) Discharge curves of EDLC cells (with and without incorporation of fumed SiO_2 nanoparticles) at current density of 30 mA/g

Consequently, HS2 cell exhibits the best discharge property owing to its' longest discharge time by 185.4 % compared to HE40 cell because HS2-based SPE provided more Mg^{2+} ions, which diffused deeply and adsorbed strongly to the carbon electrodes. Likewise, HS2-based cell obtained the highest specific capacitance (24.6 F/g) while HE40, HS1, HS3 and HS4 cells obtained specific capacitance of 9.5 F/g, 22.9 F/g, 22.0 F/g and 18.6 F/g, respectively at current density of 30 mA/g using Equation 3.12. It was found that the EDLCs incorporated with fumed SiO_2 nanoparticles possess higher specific capacitance than HE40 cell and these values resemble the specific capacitance calculated in Section 4.4.6.

Generally, the performance of EDLCs improved greatly upon incorporation of fumed SiO_2 nanoparticles because the diffusion of ions on the electrode/electrolyte interfacial contact was facilitated by small particle size of fumed SiO_2 nanoparticles. Moreover, the internal build-up resistance in the cell depleted upon incorporation of fumed SiO_2 nanoparticles resulted from less ohmic drop (IR drop). Nevertheless, all the EDLCs suffered from depletion of specific capacitance at higher current densities which implies its poor rate performance. Similarly, the IR drop values for all EDLCs elevated at higher current densities because the stability of polymer electrolyte shattered (Qu & Shi, 1998; Xu et al., 2007). Subsequently, HS2-based SPE was selected for the fabrication of EDLC to test its stability at current density of 0.4 A/g. The capacitance of the cell can withstand 67.4 % of its initial capacitance after 2,000 cycles as depicted in Figure 4.25.

4.4.9 Summary

Good performance of EDLCs are predominant after incorporation of fumed SiO_2 nanoparticles and the most performing cell is HS2-based EDLC. The cell experienced a drop by 32.6 % of its initial capacitance over 2,000 cycles at 0.4 A/g. It showed that HS2 cell achieved the requirement of an EDLC, hence the obtained specific capacitance at

scan rate of 5 mV/s, discharge time at 30 mA/g and R_{ct} were 25.0 F/g, 389.0 s and 47.4 Ω, respectively. The ability of HS2 to perform well in EDLC was governed by its improved thermal stability compared to HE40. Additionally, the great reduction of crystallinity at peak $2\theta = 20.0°$ by 53.4 % which led to the highest ionic conductivity at room temperature (2.71×10^{-4} S/cm) and provides more ions to diffuse into the carbon electrodes. The results were well supported by the decrease in –OH stretching (3473 cm^{-1}) by 40.8 % and lowest activation energy (0.213 eV). Nevertheless, the enhancement of adsorption of ions by the nanoparticles and the polymer backbone were equipped with high dielectric permittivity value (9.0×10^{4}) and great interactions at asymmetric in-plane C–O–C pyrose ring stretching (1062 cm^{-1} and 1030 cm^{-1}), asymmetric out-of-phase C–O–C pyrose ring stretching (862 cm^{-1}) and asymmetric –CH$_2$ and –CH$_3$ stretching (2923 cm^{-1}), symmetric –CH$_2$ and –CH$_3$ stretching (2881 cm^{-1}) and C–H bending of –CH$_2$ and –CH$_3$ (1357 cm^{-1}).
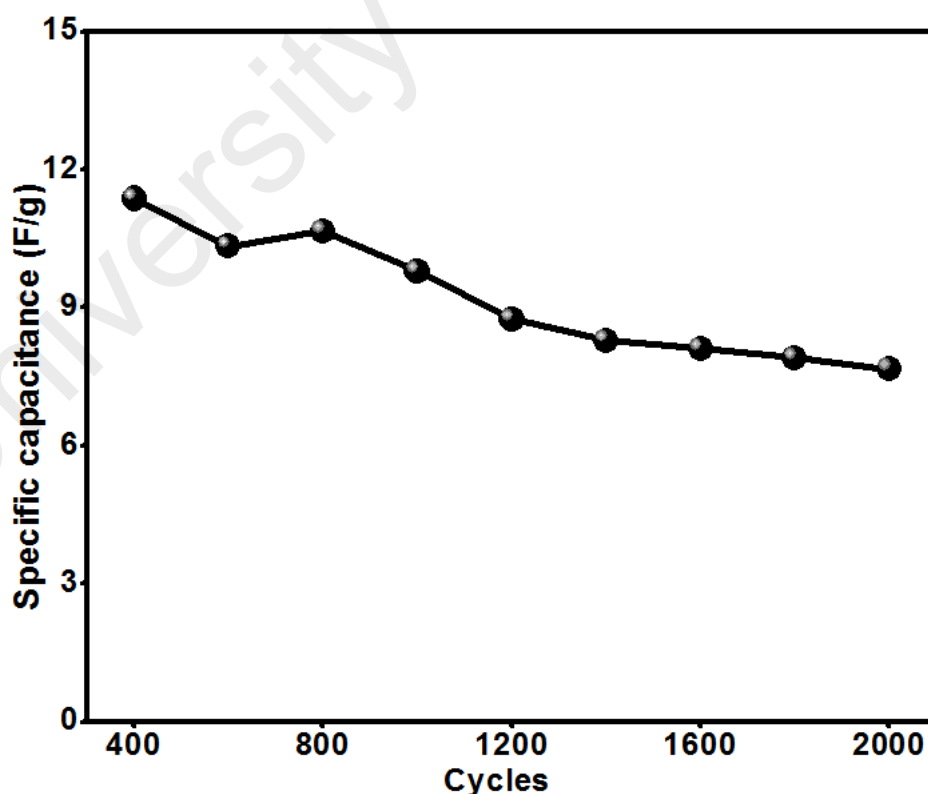
Figure 4.25: Specific capacitance of HS2-based EDLC over 2,000 cycles at current density of 0.4 A/g

4.5 Characterization and Optimization of CuO Nanoparticles for HEC-MgTf$_2$-EMIMTf-CuO SPEs

4.5.1 Ionic Conductivity Studies

Figure 4.26 shows the impedance plot of HEC-MgTf$_2$-EMIMTf SPEs at various wt. % of CuO nanoparticles at room temperature.
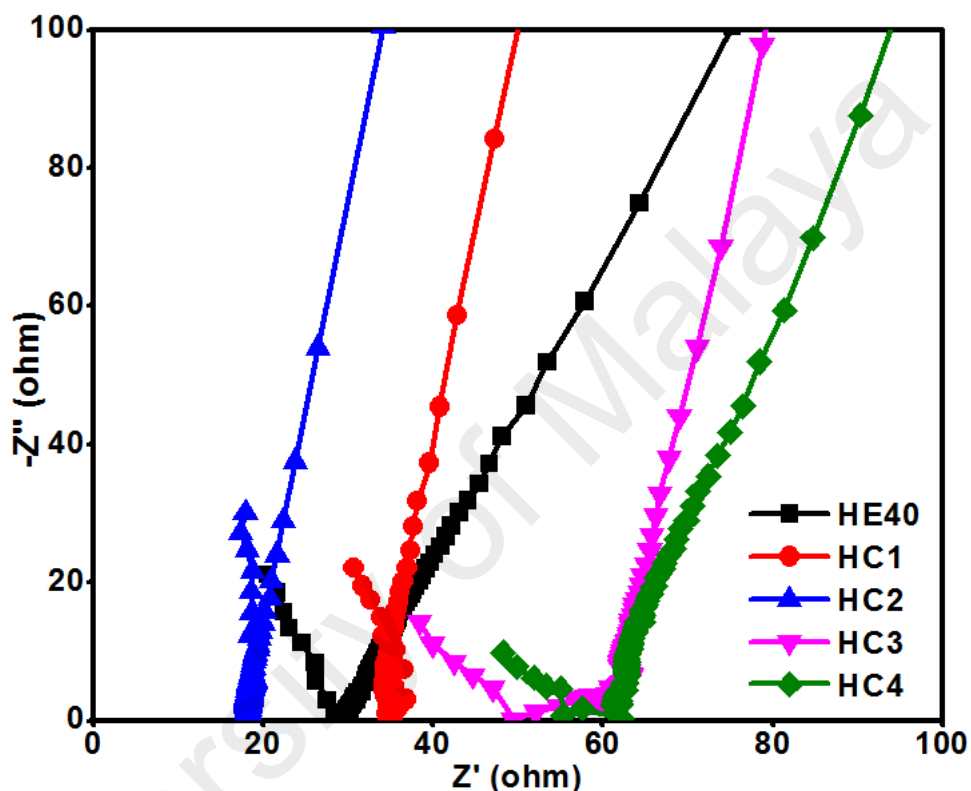
Figure 4.26: Cole-Cole plot for SPE complexes at various wt. % of CuO nanoparticles at room temperature

In general, an incomplete semicircle was observed in all the SPE complexes (before and after incorporation of CuO nanoparticles) due to fast transportation of ions. The R_b values obtained by HC1, HC2, HC3 and HC4 were 34.8 Ω, 18.1 Ω, 49.5 Ω and 61.4 Ω, respectively. Amongst the SPEs, HC2 achieved the lowest R_b compared to HE40 (32.0 Ω). The ionic conductivities at room temperature for the SPEs were calculated based on Equation 3.2. It was found that the ionic conductivity at room temperature increased to 1.37×10^{-4} S/cm and 2.58×10^{-4} S/cm from 9.28×10^{-5} S/cm upon incorporation of 1 and 2 wt. % of CuO nanoparticles, respectively into HE40. When 3 and 4 wt. % of CuO

nanoparticles was incorporated into HE40, the ionic conductivities at room temperature depressed to 8.66×10^{-5} S/cm and 7.67×10^{-5} S/cm, respectively.

Nonetheless, HC2 obtained the highest ionic conductivity at room temperature among all the SPE complexes incorporated with CuO nanoparticles due to less aggregation of nanoparticles unlike HC3 and HC4 which does not hinder the interaction between charge carriers and polymeric chain (Johan et al., 2011). In addition, HC2 has sufficient CuO nanoparticles for transportation of mobile charge carriers unlike HC1. This was due to HC1 has lesser amount of CuO nanoparticles than HC2 and thereby it provides lesser active sites for adsorption of charge carrier. As a consequence, HC1 suffered from lower ionic conductivity at room temperature than HC2.

On top of that, the SPE complexes incorporated with CuO nanoparticles experienced less heterogeneity at the electrode/electrolyte interface because the inclined spike deviated by 8.61˚, 8.94˚, 16.64˚ and 18.29˚ to the y-axis for HC1, HC2, HC3 and HC4, respectively compared to HE40 (27.4˚). All in all, it signifies HC2 achieved improvement in transportation of ions and it is suitable to be used as a conducting SPE. It was supported by the lowest activation energy achieved by HC2-based SPE (0.252 eV) compared to HE40 (0.306 eV), HC1 (0.258 eV), HC3 (0.295 eV) and HC4 (0.295 eV). It indicates that HC2 (the most conducting SPE) exhibits the most impactful hopping of charge carriers to the vacant spaces created by the polymer chain as portrayed in Figure 4.27 (Tuller, 2000). Figure 4.28 depicts the linear relationship between variations of logarithm of ionic conductivities with 1000/T at various wt. % of CuO nanoparticles. All the SPE complexes were thermally activated because the ionic conductivities at any temperature were directly proportional to the swelling of the polymer chain with the regression values (R^2) of 0.99, 0.99, 0.99, 0.97 and 0.99 for HE40, HC1, HC2, HC3 and HC4, respectively.
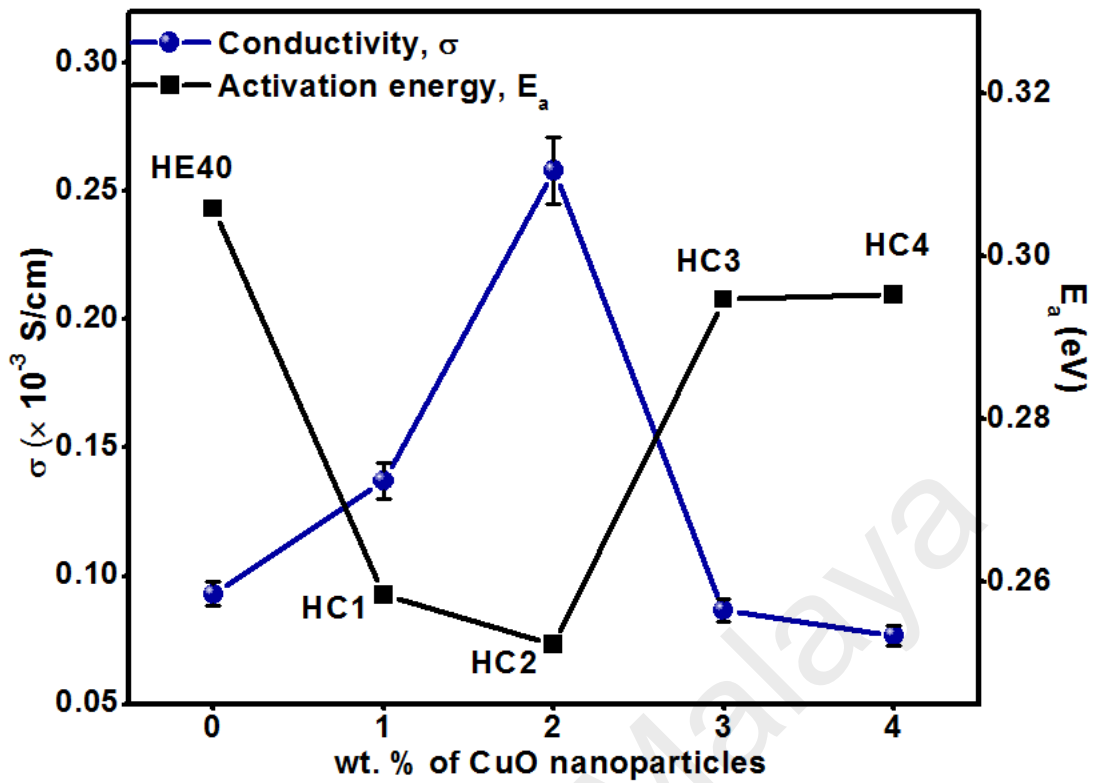
Figure 4.27: Variation of ionic conductivity and activation energy at various wt. % of CuO nanoparticles at room temperature
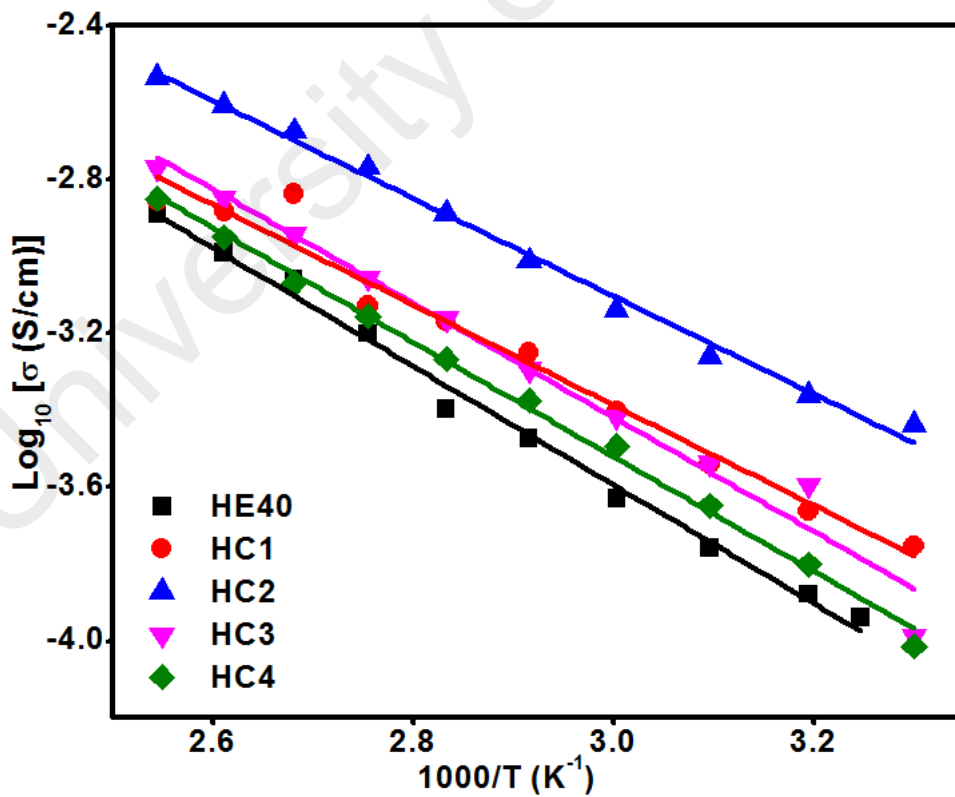
Figure 4.28: Variation of logarithm ionic conductivity from 30–120 ˚C at various wt. % of CuO nanoparticles

4.5.2   Dielectric Studies

4.5.2.1 Dielectric Relaxation Studies

Figure 4.29(a) illustrates the variation of ε' with frequencies at various wt. % of CuO nanoparticles. The ε' values for all the SPE complexes (with and without incorporation of CuO nanoparticles) decreases with increasing frequencies. HC2 has the highest number of accumulated ions near the surface of the stainless steel electrodes owing to its' highest ε' value (1.2×10^5) at low frequency region. At moderate frequency ($10^3 - 10^{4.5}$ Hz), the amount of realigned electric dipoles with the electrical field in the SPE complexes are in well agreement with the ionic conductivity values at room temperature discussed in Section 4.5.1. All the electric dipoles in the SPE complexes were unable to obey the variation of electrical field at high frequency region ($> 10^{4.5}$ Hz) due to the presence of steady state of ε' value close to zero. It shows that the ions in HC2 obeyed non-Debye type of the interactions (Pandey et al., 2010).

Figure 4.29(b) showed the variation of ε'' against frequencies at various wt. % of CuO nanoparticles. A significant molecular relaxation was not observed in HE40 due to the absence of broad inflection peak from $10^{2.6}$–10^6 Hz. The maximum peak for all SPE complexes incorporated with CuO nanoparticles has been shifted to higher frequency than HE40. As a consequence, the maximum peak of ε'' for HC2 has been shifted to the highest frequency of $10^{3.6}$ Hz while the maximum peaks of ε'' for HC1, HC3 and HC4 were shifted to higher frequencies of $10^{3.6}$ Hz, $10^{3.3}$ Hz and $10^{3.3}$ Hz, respectively (Malathi et al., 2010).

4.5.2.2 Modulus Studies

Figures 4.30(a) and (b) show the variation of M' and M" against frequencies at various wt. % of CuO nanoparticles, respectively. All the SPE complexes displayed steady-state of M' and M" from low frequency to 10^6 Hz and 10^5 Hz, respectively. It indicates that the

applied electrical field does not influence the long-range ionic conductivity dielectric relaxation and pure conduction process even after incorporation of CuO nanoparticles into HE40, respectively.
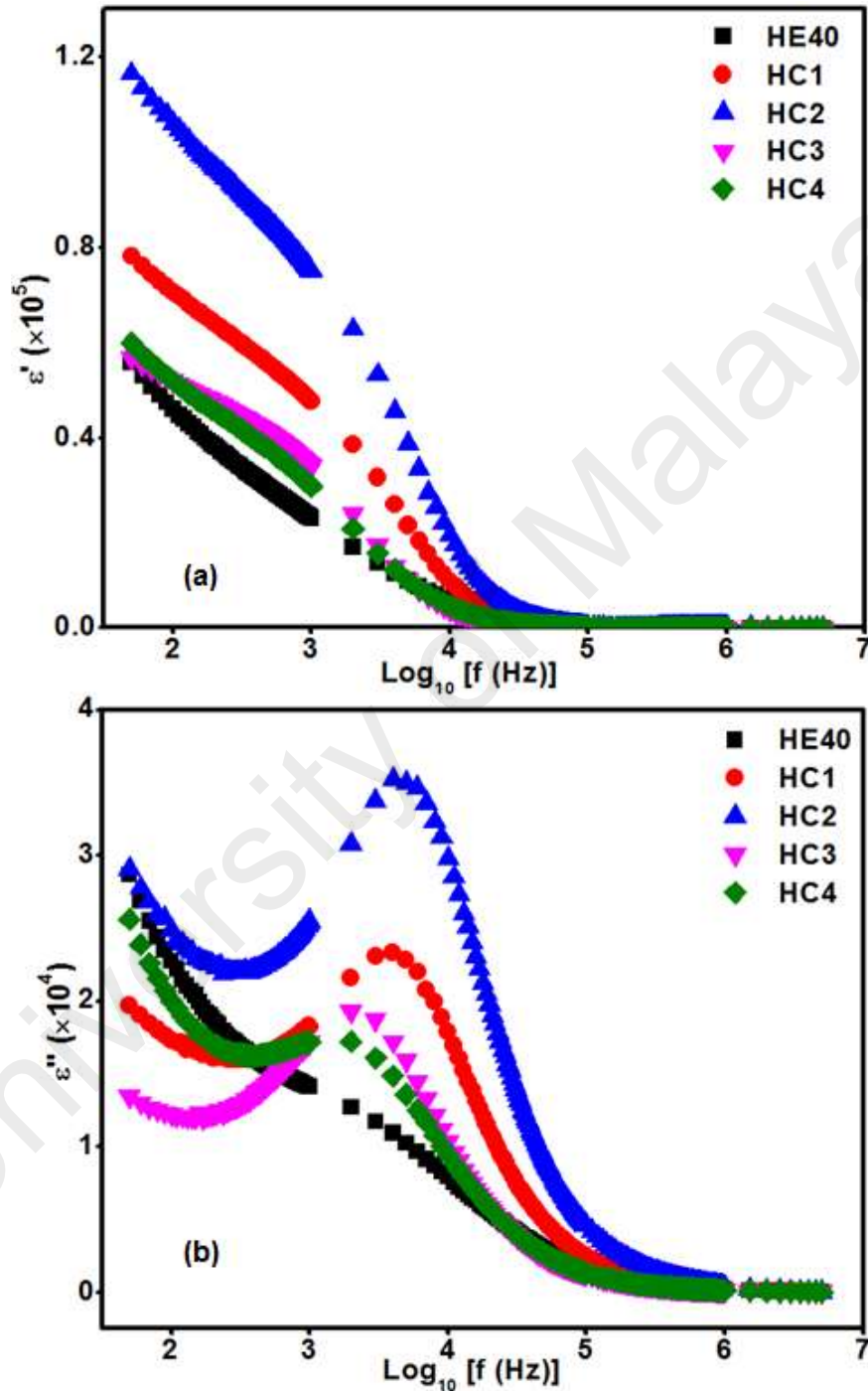
Figure 4.29: Variation of (a) ε' and (b) ε'' with frequency at various wt. % of CuO nanoparticles

The occurrence of long steady-state of M' is independent from nature of electrode materials, the contact between electrode/electrolyte interface, and the impurities adsorbed on the polymer electrolytes. On the other hand, a long steady-state of M" was due to the narrowed of the experimental frequency window (Suthanthiraraj et al., 2009).
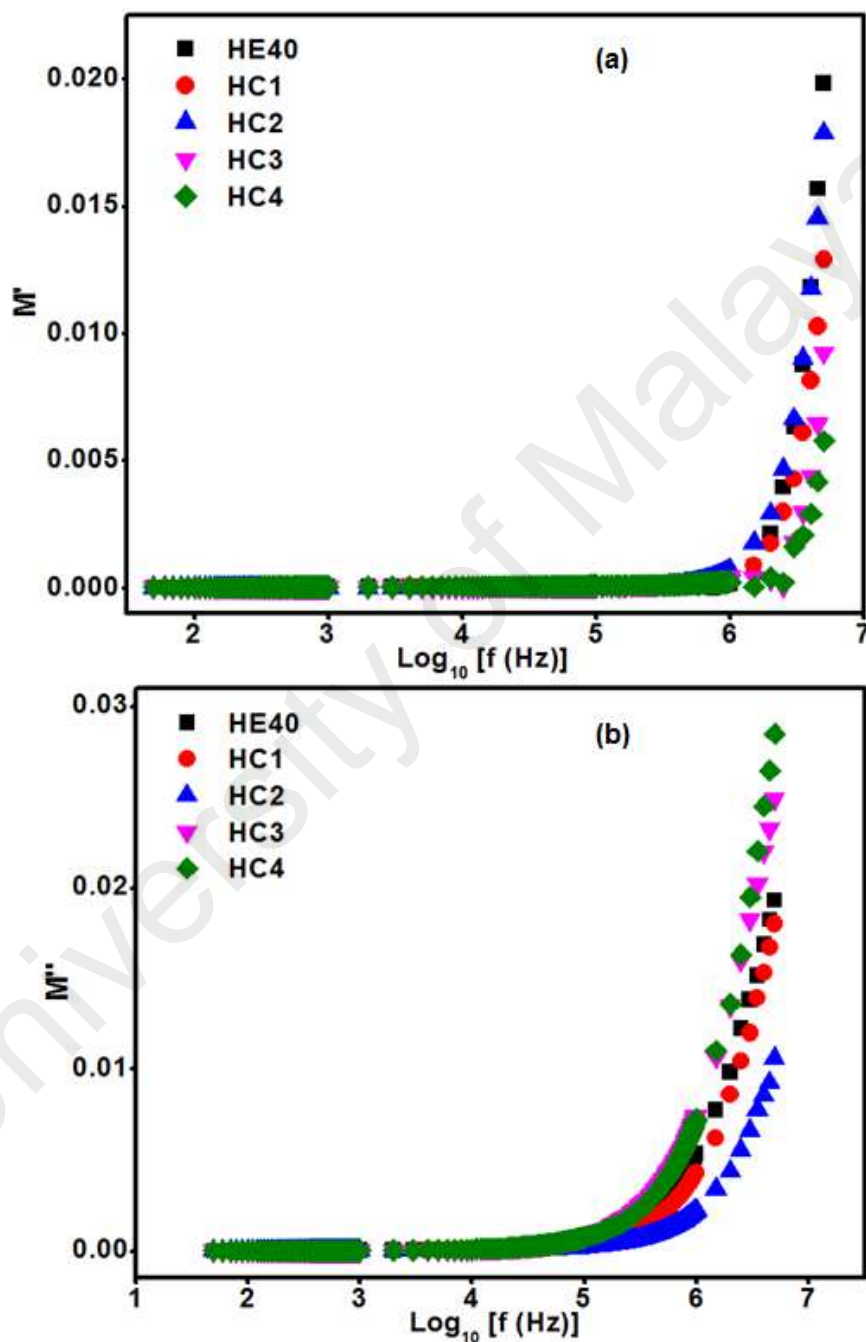
Figure 4.30: Variation of (a) M' and (b) M" with frequency at various wt. % of CuO nanoparticles

4.5.3 XRD Studies

Figure 4.31 demonstrates the XRD patterns of pure samples (HEC and CuO) and SPE complexes at various wt. % of CuO nanoparticles.
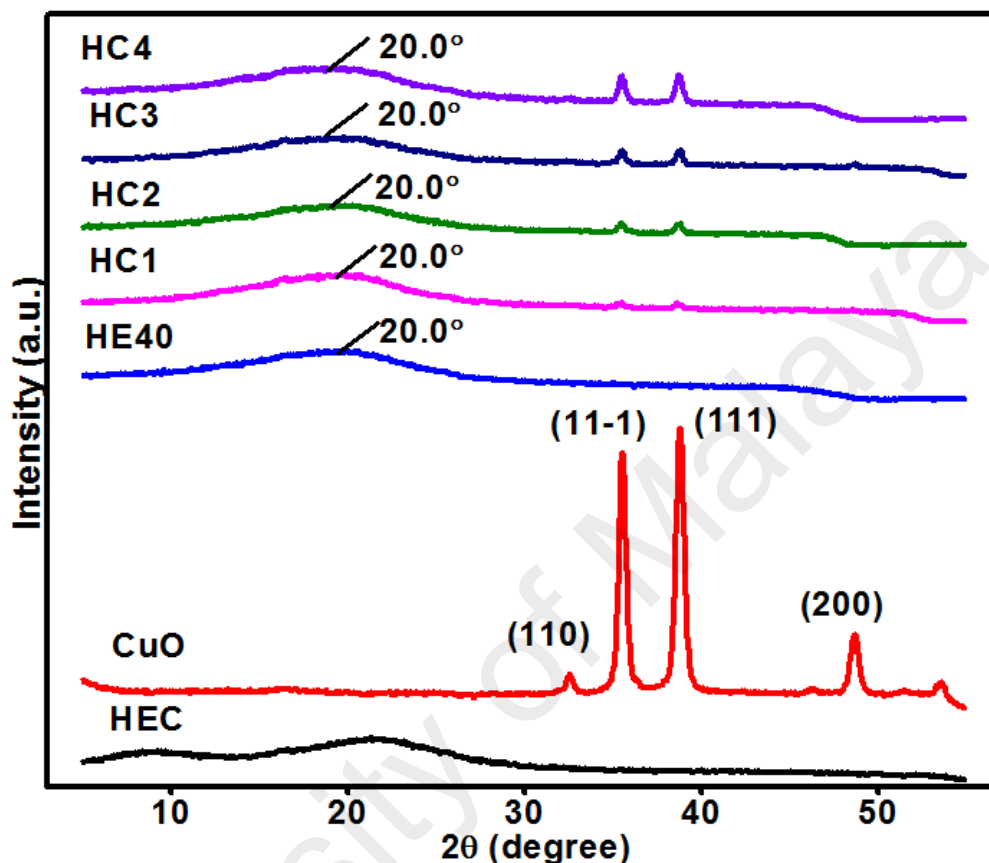
Figure 4.31: XRD patterns of pure samples (HEC and CuO) and SPE complexes at various wt. % of CuO nanoparticles

A pure CuO nanoparticles exhibits the diffraction peaks at 2θ values of $33.6°$, $35.5°$, $38.9°$ and $48.9°$ which are attribute to the (1 1 0), (1 1 -1), (1 1 1) and (2 0 0) crystal planes of monoclinic structured CuO nanoparticles (JCPDS card no. 48-1548). The diffraction peaks of pure CuO at 2θ values of $35.5°$ and $38.9°$ increase steadily in HC1, HC2, HC3 and HC4 which indicates the successful incorporation of CuO nanoparticles into HE40. However, the diffraction peaks of pure CuO at 2θ values of $33.6°$ and $48.9°$ were ruptured in all the SPE complexes (HC1, HC2, HC3 and HC4) due to dissolution of nanoparticles (Aoki et al., 2006).

Additionally, the interaction between charge carriers and host polymer was notified by the shift of pure HEC peak from $2\theta = 21.6°$ to $2\theta = 20.0°$. On top of that, the broadness of pure HEC at $2\theta = 19.8°$ depressed by 1.0 % upon incorporation of 2 wt. % of CuO nanoparticles. The rupturing of the crystallinity in HEC facilitated more room for adsorption and transportation of mobile charge carriers on the host polymer through ion-dipole forces and coordinate bonds. Thus, recrystallization in pure HEC and $MgTf_2$ was prevented by avoiding the formation of intermolecular hydrogen bonding which led to the increase in ionic conductivity (Chung et al., 2001).

4.5.4   FTIR Studies

FTIR spectra of pure samples (HEC and CuO) and SPE complexes at various wt. % of CuO nanoparticles were depicted in Figure 4.32. According to El-Trass et al. (2012), pure CuO has characteristic peak at 532 cm^{-1} which is responsible for the vibrations of Cu–O functional group but the peak was not observed in the all the SPE complexes upon incorporation of CuO nanoparticles owing to addition of small amount of it into HE40. A small hump was observed at 3454 cm^{-1} in pure CuO due to the presence of absorbed water.

Figure 4.33(a), (b) and (c) represent the –OH stretching, SO_2 symmetric stretching in $CF_3SO_3^-$ and in-plane C–O–C stretching of pyrose ring, respectively for pure HEC and SPE complexes (with and without CuO nanoparticles). Generally, the broadness of –OH stretching at 3473 cm^{-1} shrank by 29.6 % compared to HE40. The phenomena was supported by the shift of –OH in-plane deformation (1457 cm^{-1}) and –OH in-plane bending (1260 cm^{-1}) to a higher wavenumber. This was due to the spaces between host polymers were fill up by small size of CuO nanoparticles and thereby ion-dipole forces between Cu^{2+} and lone pair electrons on the oxygen atom of the host polymer become remarkable than intermolecular hydrogen bonding (Tanaka et al., 2004).

Conversely, interactions between charge carriers and the host polymer with the aid of nanoparticles were noticed significantly at wavenumber 1165 cm^{-1} and 1062 cm^{-1} that are responsible for SO$_2$ symmetric stretching in CF$_3$SO$_3^-$ and in-plane C–O–C pyrose ring stretching, respectively. These peaks (1165 cm^{-1} and 1062 cm^{-1}) experienced a drop in their intensities by 5.2 % and 50.0 %, respectively compared to HE40. It indicates that the adsorption of charge carriers on the host polymer was greatly affected by CuO nanoparticles. On top of that, great interactions between host polymer and charge carriers were backed up by the shift of wavenumber for asymmetric –CH$_2$ and –CH$_3$ stretching (2923 cm^{-1}), symmetric –CH$_2$ and –CH$_3$ stretching (2881 cm^{-1}) and C–H bending of –CH$_2$ and –CH$_3$ (1357 cm^{-1}) as summarized in Table 4.5 (Su'ait et al., 2014).
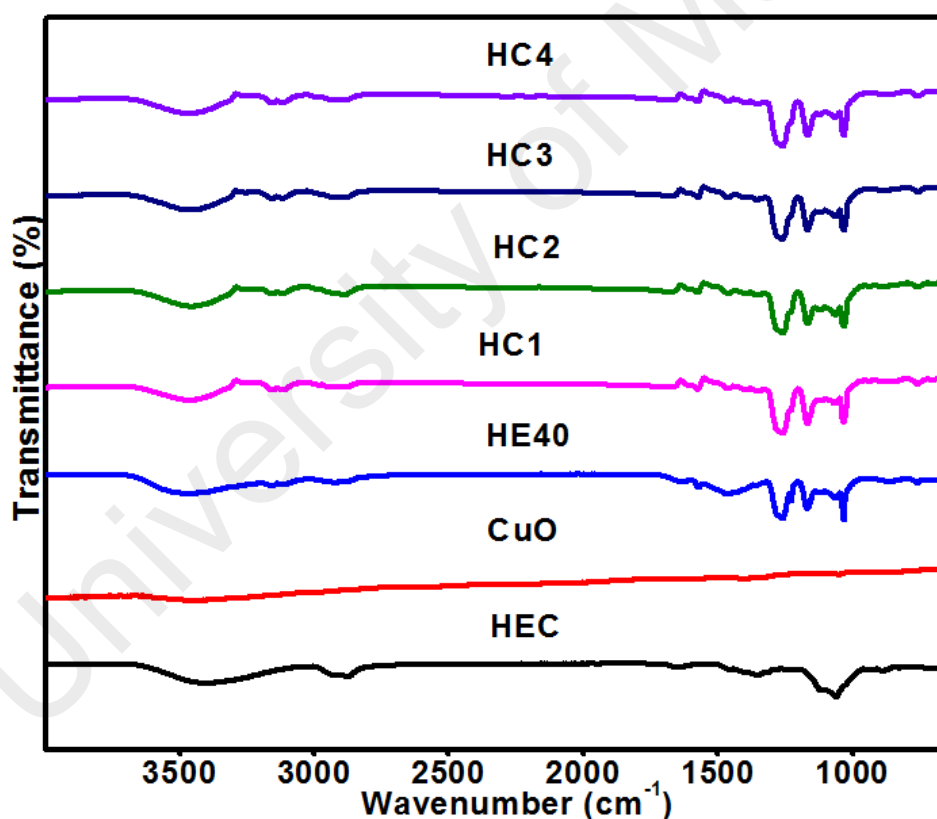
Figure 4.32: FTIR spectra for pure samples (HEC and CuO) and SPE complexes at various wt. % of CuO nanoparticles
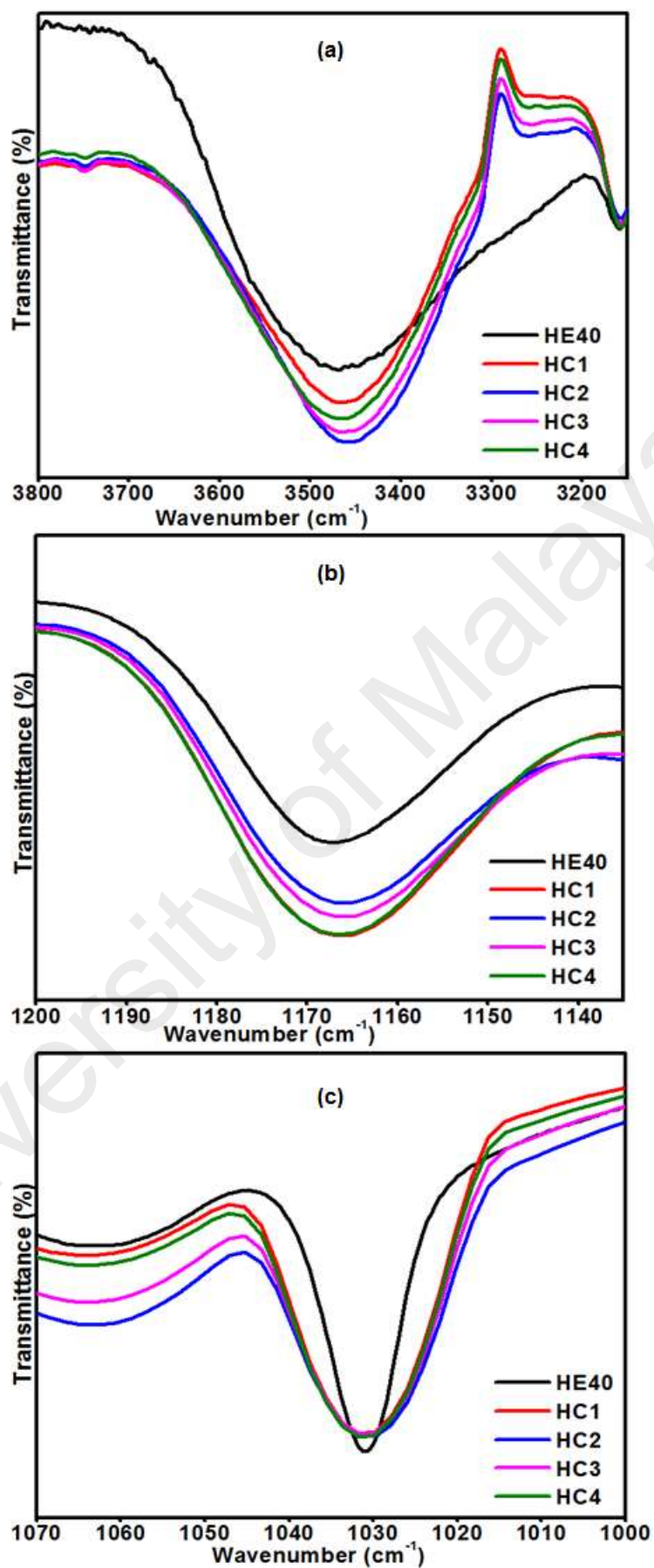
Figure 4.33: (a) –OH stretching (3473 cm^{-1}) (b) SO$_2$ symmetric stretching in CF$_3$SO$_3^-$ (1165 cm^{-1}) (c) Asymmetric in-plane C–O–C pyrose ring (1062 cm^{-1})

Table 4.5: Band assignments of pure HEC and SPE complexes at various wt. % of CuO nanoparticles

Band assignments	HEC (cm⁻¹)	HE40 (cm⁻¹)	HC1 (cm⁻¹)	HC2 (cm⁻¹)	HC3 (cm⁻¹)	HC4 (cm⁻¹)	Reference
$-OH$ stretching	3403	3473	3448	3443	3446	3451	(Chong et al., 2016; Satyamurthy & Vigneshwaran, 2013)
Asymmetric $-CH_2$ and $-CH_3$ stretching	2917	2923	2984	2976	2978	2981	(Abidi et al., 2014; Saroj et al., 2014)
Symmetric $-CH_2$ and $-CH_3$ stretching	2876	2881	2894	2888	2888	2984	(Abidi et al., 2014; Saroj et al., 2014)
Absorbed water	1651	1636	1673	1676	1676	1676	(Chung et al., 2004; Satyamurthy & Vigneshwaran, 2013)
$-OH$ in-plane deformation	1457	1457	1461	1458	1461	1461	(Abidi et al., 2014)
C–H bending of $-CH_2$ and $-CH_3$	1354	1357	1351	1354	1351	1351	(Abidi et al., 2014)
$-OH$ in-plane bending	1239	1260	1252	1252	1252	1252	(Chung et al., 2004)
Asymmetric bridge C–O–C stretching	NIL	1165	1159	1162	1159	1162	(Chung et al., 2004)
SO_2 symmetric stretching in $CF_3SO_3^-$	1115	1118	1116	1116	1116	1116	(Abidi et al., 2014; Chung et al., 2004)
Asymmetric in-plane C–O–C pyrose ring stretching	1062 / NIL	1062 / 1030	1061 / 1026	1061 / 1026	1061 / 1026	1061 / 1026	(Abidi et al., 2014; Chung et al., 2004)
Asymmetric out-of-phase C–O–C pyrose ring stretching	889	862	880	884	884	887	(Chung et al., 2004)

4.5.5 TGA Studies

Table 4.6 depicts the decomposition temperature of SPE complexes at various wt. % of CuO nanoparticles whereas Figure 4.34 represents the thermograms of pure samples (CuO, MgTf$_2$, EMIMTf and HEC) and SPE complexes at various wt. % of CuO nanoparticles. The exact decomposition temperature of a pure CuO was not able to be measured due to the detection limit of the instrument. On the whole, the thermal stability of all the SPE complexes exceeded the performance of HE40 because their decomposition temperature at stage 4 improved by 2.83, 3.78, 4.72 and 2.83 % for HC1, HC2, HC3 and HC4, respectively. The stages of decomposition in all the SPE complexes incorporated with CuO nanoparticles were accountable to the decompositions of MgT$_2$ (466.0–478.0 ˚C), EMIMTf (382.0–425.0 ˚C) and HEC (266.0–282.0 ˚C) as the aforementioned in Section 4.4.5. The interactions in the SPE complexes caused the change of decomposition temperature relatively to the pure samples. Additionally, SPE complexes upon incorporation of CuO nanoparticles exhibit thermal decomposition around 100 ˚C with weight loss of ~3.0 % which was due to the complete evaporation of water solvent in the SPE complexes (Xu et al., 2010).

Table 4.6: The decomposition temperature of SPE complexes at various wt. % of CuO nanoparticles

Samples	Thermal decomposition (˚C)			
	Stage 1	Stage 2	Stage 3	Stage 4
HE40	51.8	266.6	382.9	466.0
HC1	89.0	279.8	426.7	479.2
HC2	89.0	282.0	424.5	483.6
HC3	89.0	279.8	422.3	488.0
HC4	89.0	275.4	424.5	479.2
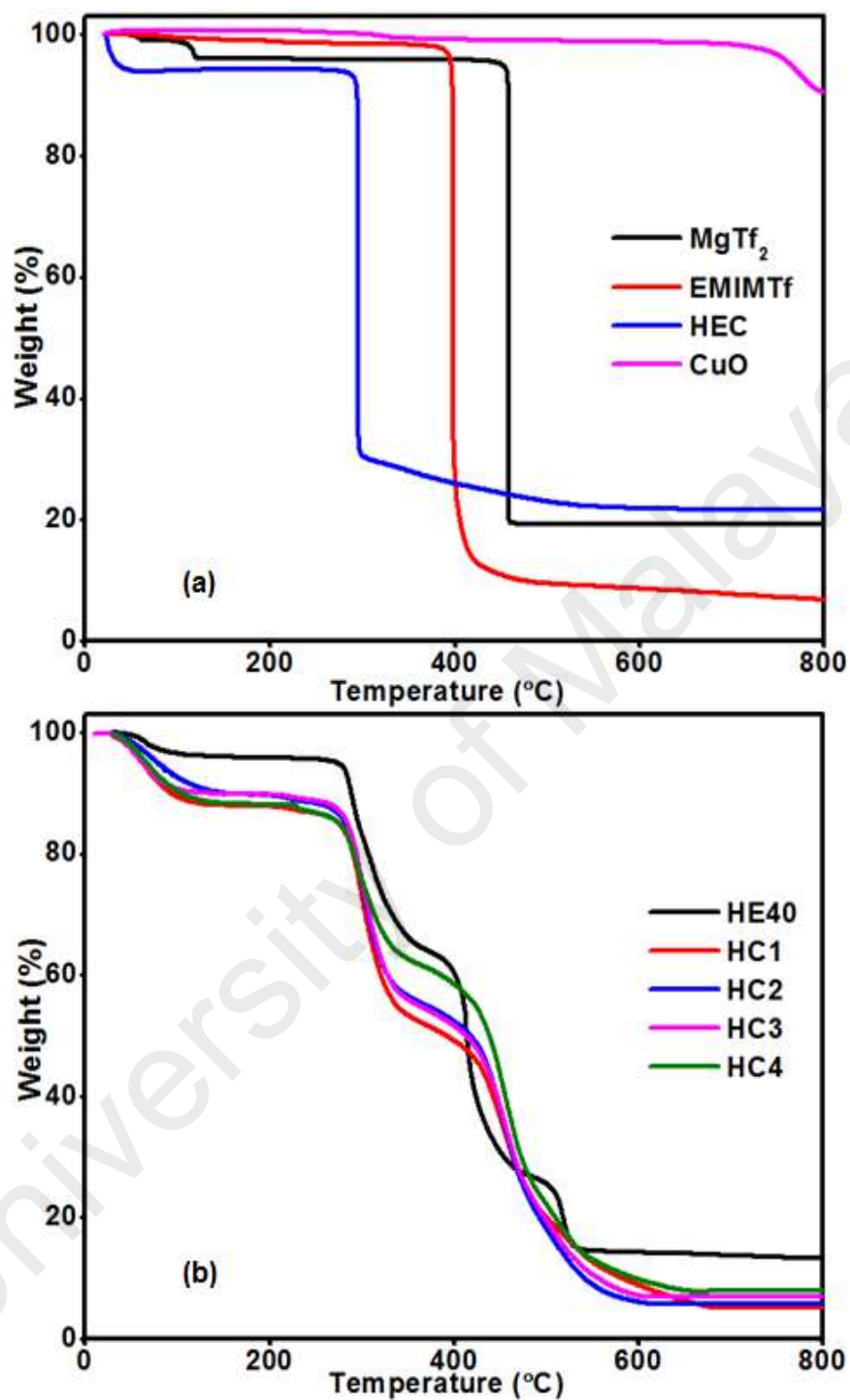
Figure 4.34: Thermograms of (a) pure samples (HEC, MgTf₂, EMIMTf and CuO) and (b) SPE complexes at various wt. % of CuO nanoparticles

4.5.6 CV Studies

All the EDLCs denote a plateau region at constant current from low (5 mV/s) to high scan rate (50 mV/s) without the existence of oxidation-reduction peak which revealed its outstanding double layer capacitive characteristics as depicted in Figure 4.35.
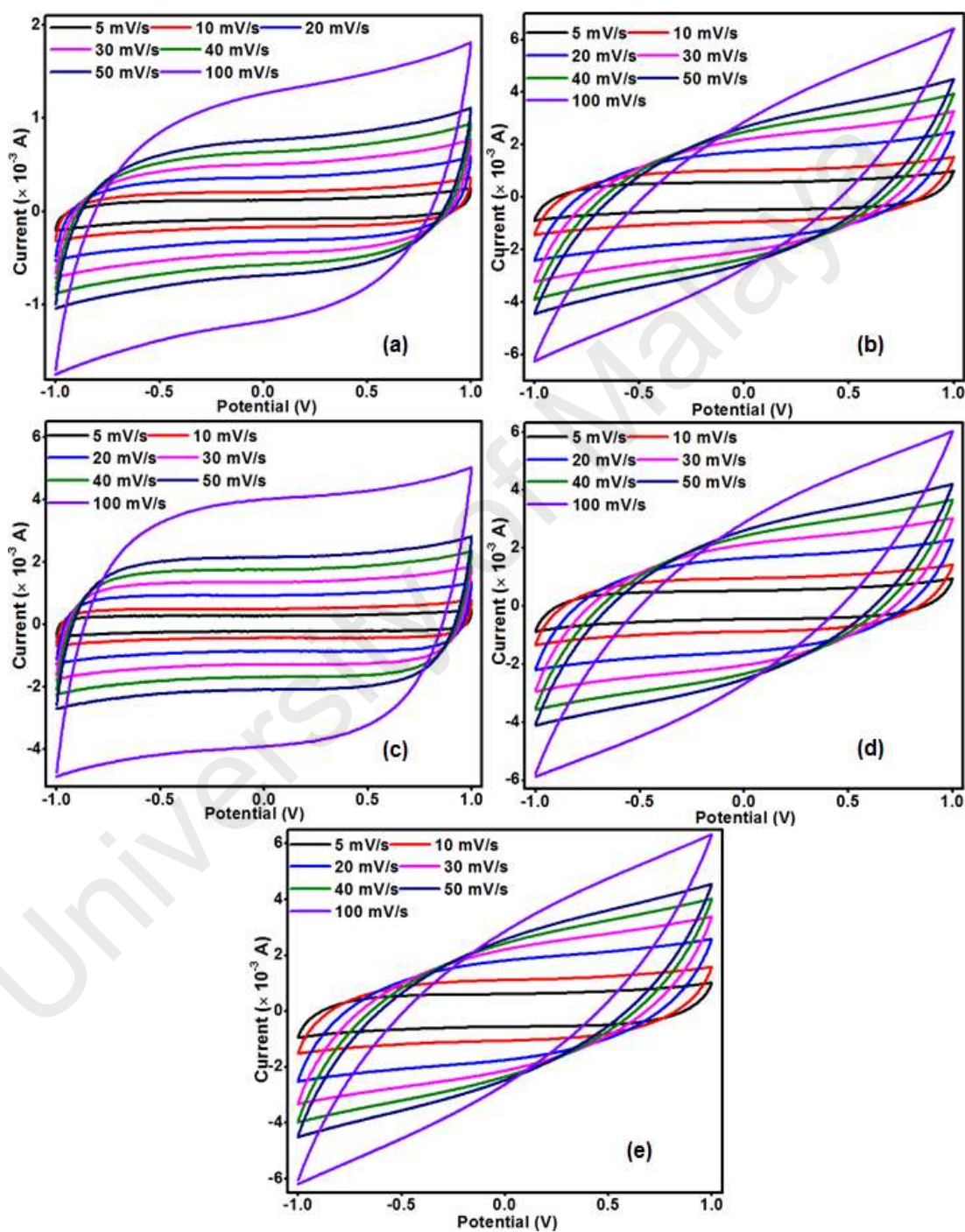
Figure 4.35: CV responses of (a) HE40 (b) HC1 (c) HC2 (d) HC3 (e) HC4 at different scan rates over the voltage range from -1 to 1 V

However, these EDLCs failed to show its outstanding capacitive behavior at scan rate of 100 mV/s. The scenario was fully supported by the variation of specific capacitance with scan rate for all EDLCs as portrayed in Figure 4.36(a) because the ions did not respond well with the applied electric field (Zhang et al., 2011).

Figure 4.36(b) represents the CV responses at scan rate of 5 mV/s for EDLC cells (with and without incorporation of CuO nanoparticles). The maximum specific capacitance of EDLCs incorporated with 1, 2, 3 and 4 wt. % of CuO nanoparticles at scan rate of 5 mV/s were 32.8 F/g, 36.7 F/g, 25.8 F/g and 25.6 F/g, respectively. The values obtained by these EDLCs are greater than HE40 cell (11 F/g) due to efficient permeation of charge carriers by the presence of CuO nanoparticles into the carbon electrodes than the host polymer (Bose et al., 2012). It is worth to mention that the specific capacitance of HC2 cell surpassed the greatest by 233.6 % compared to HE40 cell at scan rate of 5 mV/s because the frequencies and amount of charge carriers to enter the carbon electrode is high. On the contrary, HC3 and HC4 experienced a decrease in specific capacitance although more CuO nanoparticles incorporated because the excess of CuO nanoparticles reduce and block the effective contact surface area between the electrodes and electrolytes (Ketabi & Lian, 2013).

4.5.7   EIS Studies

Figure 4.37 displays the complex impedance spectra of EDLC cells (with and without incorporation of CuO nanoparticles) at room temperature. Table 4.7 represents the R_{ct} values for EDLC cells (with and without incorporation of CuO nanoparticles). The performance of EDLCs upon incorporation of CuO nanoparticles was substantially improved compared to HE40 because all their R_{ct} values and angles to the y-axis were small. Based on Section 4.5.1, HC2 was found to contain the least activation energy of 0.252 eV. Thus, HC2-based cell transporting Mg^{2+} ions into the carbon electrodes with

the least charge transfer resistance (25.0 Ω) and its cell resembles the behavior of a
capacitor owing to its smallest deviation from the y-axis (7.7 °) (Wu et al., 2007).
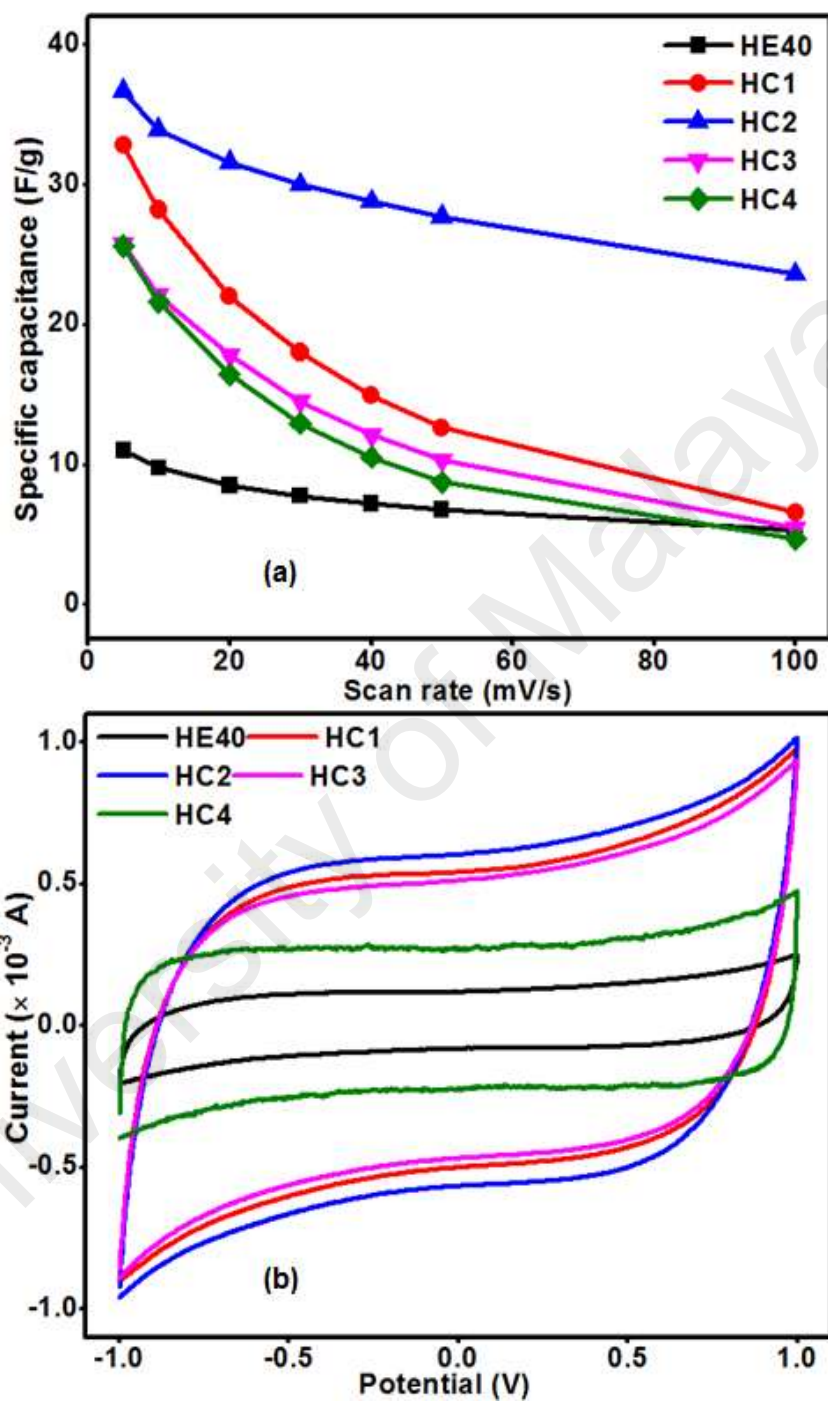
Figure 4.36: (a) Specific capacitance for EDLC cells (with and without incorporation of CuO nanoparticles) as a function of scan rate (b) CV responses at scan rate of 5 mV/s for EDLC cells (with and without incorporation of CuO nanoparticles)
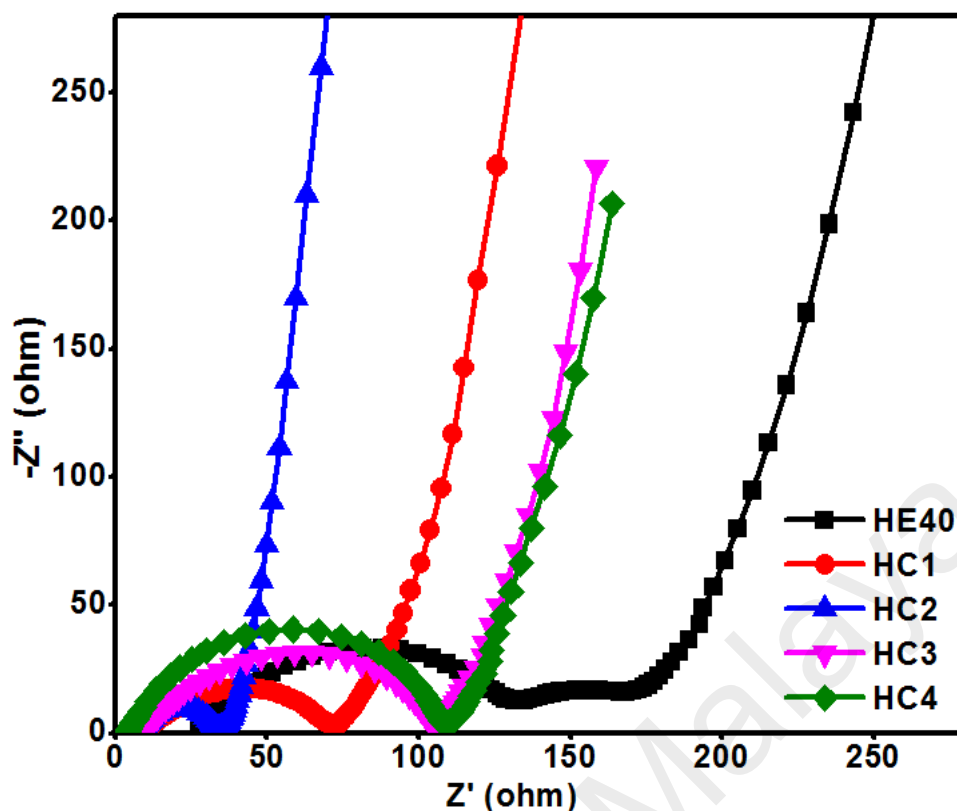
Figure 4.37: Complex impedance spectra of EDLC cells (with and without incorporation of CuO nanoparticles) at room temperature

Table 4.7: R_{ct} values for EDLC cells (with and without incorporation of CuO nanoparticles)

EDLC cell	R_{ct} (Ω)	Deviation from imaginary axis (°)
HE40	142.0	32.7
HC1	60.8	13.8
HC2	25.0	7.7
HC3	97.2	24.3
HC4	104.4	29.8

4.5.8 GCD Studies

Galvanostatic charge-discharge curves for EDLCs (with and without incorporation of CuO nanoparticles) at different current densities were depicted by Figures 4.38(a) – (e). The EDLCs portrayed an excellent behavior of a capacitor due to the perfect isoscele triangular galvanostatic curves. Nevertheless, the EDLCs incorporated with CuO

nanoparticles outperformed HE40 cell (136.3 s) because the time taken to penetrate the carbon electrodes is long as shown in Figure 4.38(f). The discharge time experienced by HC1, HC2, HC3 and HC4 at current density of 30 mA/g were 435.0 s, 438.0 s, 426.6 s and 387.3 s, respectively. As a result, HC2-based cell experienced the longest discharge time by 33.3 % compared to HE40. Also, the values of specific capacitance calculated at current density of 30 mA/g for HC1, HC2, HC3 and HC4-based cells were greater than HE40-based cell (9.5 F/g) by 50.3, 57.0, 42.9 and 22.0 %, respectively. The values obtained were in well agreement with the specific capacitance calculated in Section 4.5.6. This was due to smooth penetration of ions into the carbon electrodes with the help of small particle size of CuO nanoparticles (Zhang et al., 2011). In addition, a more pronounced ohmic drop (IR) at the beginning of the discharge process was observed before addition of CuO nanoparticles which is due to the internal resistance of the electrode. The resistance is associated with the electrical connection, bulk solution, and migration of ions in the electrode materials (Zhang & Zhao, 2009). The IR drop of the EDLCs due to degradation of polymer electrolyte is directly proportionate to the current density and it is inversely proportionate to the specific capacitance (Kötz & Carlen, 2000). Even though the overall performance of all EDLCs incorporated with CuO nanoparticles was improved, still the HC2-based cell exhibited the greatest difference of discharging time compared to HE40-based cell. In addition to this, HC2-based cell portrayed higher specific capacitance than HE40-based cell. This was because HC2-based cell achieved optimum amount of nanoparticles to draw more available charge carriers into the carbon electrodes. The good contact between electrode and electrolyte was tested by conducting the long term cycling test at current density of 0.4 A/g and it was found that HC2-based EDLC has the ability to retain 80.5 % of its capacitance after 3,000 cycles as depicted in Figure 4.39.
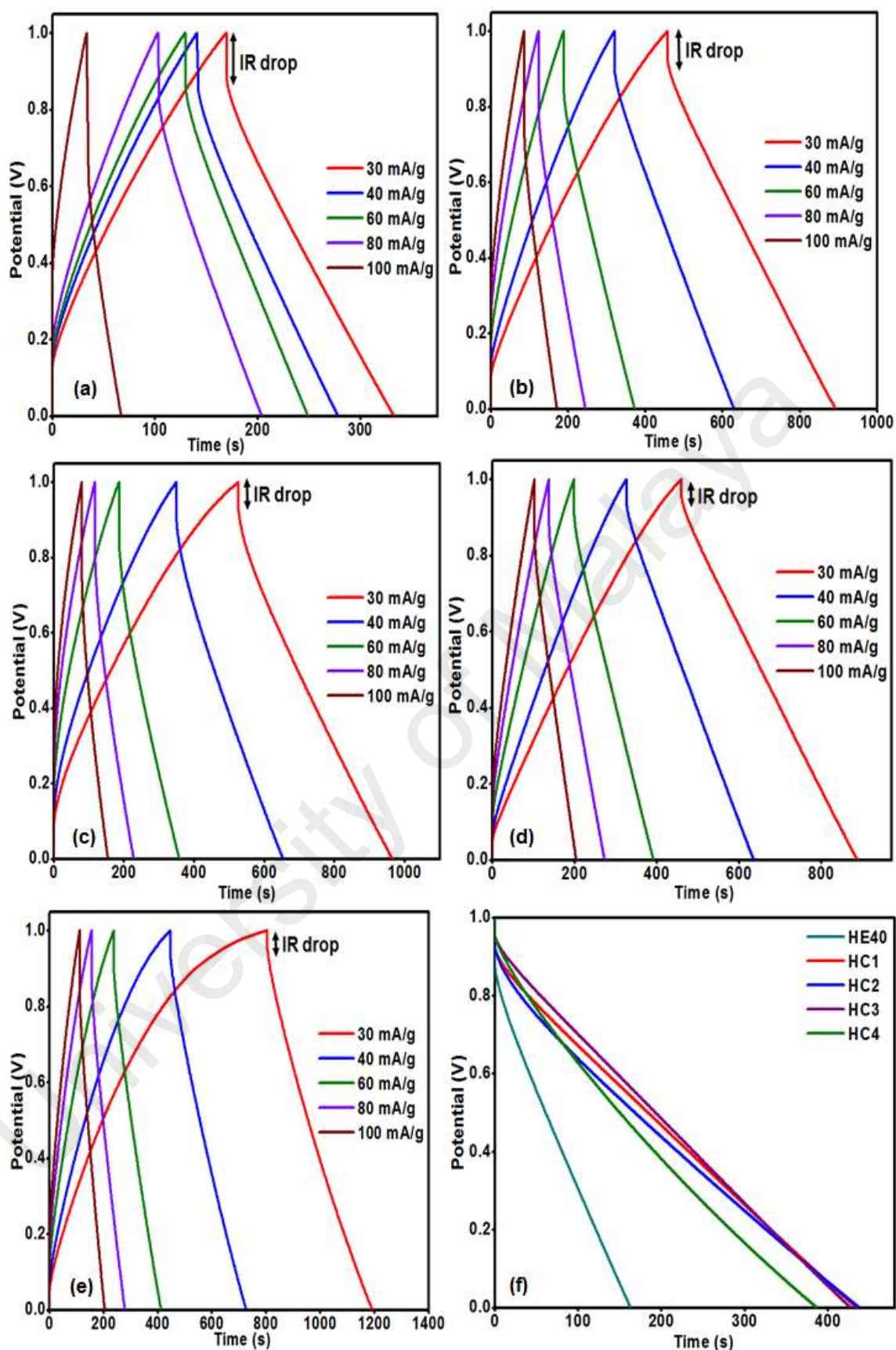
Figure 4.38: Galvanostatic charge-discharge curves of (a) HE40 (b) HC1 (c) HC2 (d) HC3 (e) HC4 at different current densities (f) Discharge curves of EDLC cells (with and without incorporation of CuO nanoparticles) at current density of 30 mA/g
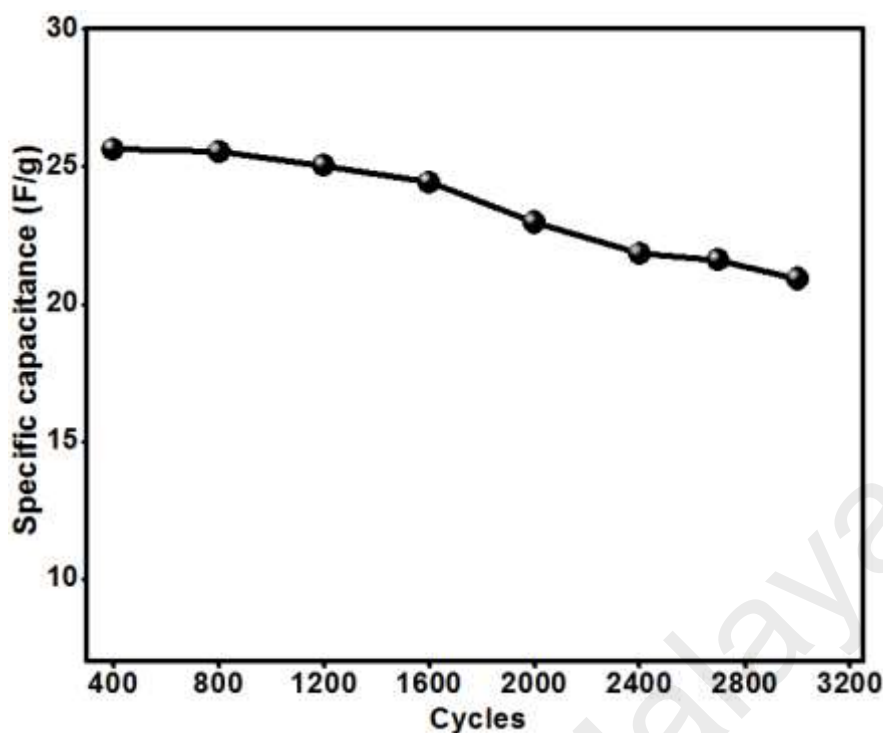
Figure 4.39: Specific capacitance of HC2-based EDLC over 3,000 cycles at current density of 0.4 A/g

4.5.9 Summary

SPEs incorporated with CuO nanoparticles exhibit superior performance as EDLCs owing to its prominent characteristics. Amongst those SPEs, HC2 attained the highest ionic conductivity at room temperature (2.58×10^{-4} S/cm) along with enhanced amorphous region at $2\theta = 20.0°$ in HEC and lowest activation energy (0.252 eV). The results are in well agreement with the interactions occurred at the –OH stretching, SO_2 symmetric stretching in $-CF_3SO_3^-$ and in-plane C–O–C pyrose ring stretching at 3473 cm^{-1}, 1165 cm^{-1} and 1062 cm^{-1}, respectively. The –OH stretching (3473 cm^{-1}) in HC2 reduced its broadness by 29.6 % whereas the SO_2 symmetric stretching in $-CF_3SO_3^-$ and in-plane pyrose ring stretching at 1165 cm^{-1} and 1062 cm^{-1} exhibits a lowering of peak intensities by 5.0 % and 50.0 %, respectively. The effective interaction was due to huge amount of mobile charge carriers which is in accordance to the highest ε' value (1.2×10^5) at low frequency and its maximum ε'' value shifted readily to a higher frequency ($10^{3.6}$ Hz). Also, the SPEs incorporated with CuO nanoparticles has high thermal stability (~470 ˚C)

123

compared to HE40. Following this, HC2 was fabricated for EDLC. As a result, it achieved the highest specific capacitance (36.7 F/g) at 5 mV/s, the least charge transfer resistance (25.0 Ω) and longest discharge time (438.0 s) at 30 mA/g. Hence, HC2-based cell has capacitance retention of 80.5 % after 3,000 cycles at 0.4 A/g owing to less resistance between electrode and electrolyte.

4.6 Characterization and Optimization of Y_2O_3 nanoparticles for HEC-MgTf$_2$-EMIMTf-Y_2O_3 SPEs

4.6.1 Ionic Conductivity Studies

Figure 4.40 depicts the Cole-Cole plot for SPE complexes at various wt. % of Y_2O_3 nanoparticles at room temperature.
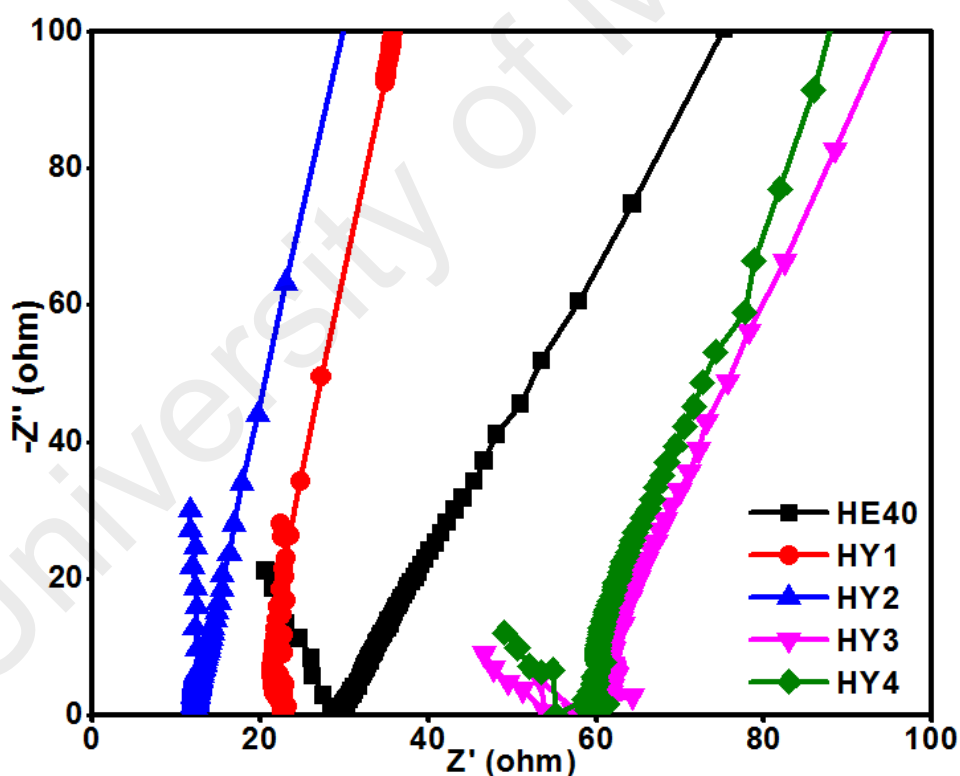
Figure 4.40: Cole-Cole plot for SPE complexes at various wt. % of Y_2O_3 nanoparticles at room temperature

All in all, the arc were absence in all the SPE complexes (with and without Y_2O_3 nanoparticles). Prior to the addition of Y_2O_3 nanoparticles, the R_b value of HE40 was 32 Ω, which was decreased by 29.1 % and 61.9 % to 22.7 Ω and 12.2 Ω upon addition of 1 and 2 wt. % of Y_2O_3 nanoparticles, respectively. The R_b values of HY3 and HY4 were leveled up by 79.1 % and 72.5 % to 57.3 Ω and 55.2 Ω, respectively compared to HE40.

Figure 4.41 shows the relationship between the ionic conductivity at room temperature calculated using Equation 3.2 and the activation energy at various wt. % of Y_2O_3 nanoparticles.
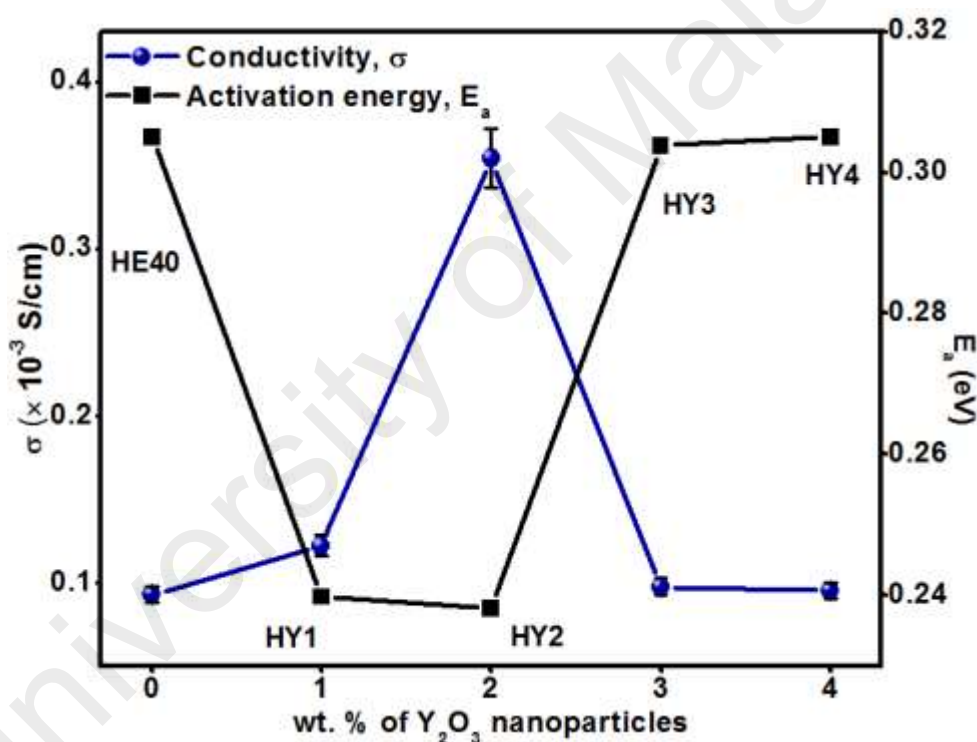
Figure 4.41: Variation of ionic conductivity and activation energy at various wt. % of Y_2O_3 nanoparticles at room temperature

Thence, HY2 attained the highest ionic conductivity of 3.54×10^{-4} S/cm at room temperature along with lowest activation energy of 0.238 eV. This was due to the mobility of charge carriers in HY2 SPE is along the polymer chain and also in the partially amorphous region as discussed in Section 4.6.3 (Ali et al., 2007). When low concentration of Y_2O_3 nanoparticles was added into HE40 (1 wt. %), HY1 achieved ionic conductivity

of 1.22×10^{-4} S/cm at room temperature along with activation energy of 0.240 eV. At this concentration of Y_2O_3 nanoparticles, it provides less active sites for adsorption of charge carriers, hence the ionic conductivity at room temperature is lower than HY2-based SPE. On the other hand, upon incorporation of 3 and 4 wt. % of Y_2O_3 nanoparticles into HE40, the agglomeration of nanoparticles destroyed the conduction pathway in HY3 and HY4. Therefore, more hopping energy are required to overcome the barrier which led to a drop in ionic conductivity at room temperature. As a consequence, both HY3 and HY4 obtained greater activation energies of 0.304 eV and 0.305 eV, respectively than HY2. Likewise, HY3 and HY4 obtained lesser ionic conductivities of 9.76×10^{-5} S/cm and 9.53×10^{-5} S/cm at room temperature than HY2. Nonetheless, all the SPE complexes interact well at the electrode/electrolyte interface due to smaller θ value to the imaginary axis upon incorporation of Y_2O_3 nanoparticles.

Figure 4.42 explains the relationship between ionic conductivity with inverse of absolute temperature at various wt. % of Y_2O_3 nanoparticles.
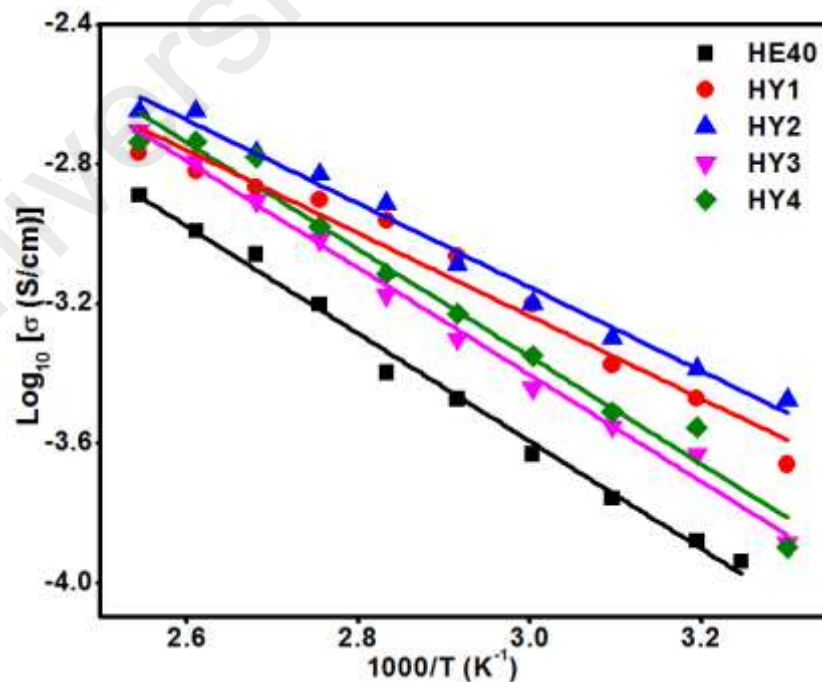
Figure 4.42: Variation of logarithm ionic conductivity from 30–120 ˚C at various wt. % of Y_2O_3 nanoparticles

The R^2 values of HE40, HY1, HY2, HY3 and HY4 are 0.99, 0.97, 0.99, 0.99 and 0.98, respectively. It indicates that the conductivity and temperature values for all the SPE complexes fit into Arrhenius equation. Additionally, it signifies that the amount of spaces provided by the expansion of polymer chain at increasing temperature are comparable to the rate of charge hopping (Ramesh & Arof, 2001).

4.6.2 Dielectric Studies

4.6.2.1 Dielectric Relaxation studies

Figures 4.43(a) and (b) illustrate the variation of ε' and ε'', respectively, with frequencies at various wt. % of Y_2O_3 nanoparticles. According to Section 4.6.1, HY2 is the most conducting SPE and has the highest number of ions gathered on the surface of the stainless steel electrodes at low frequency. This was proven from the highest ε' value (9.4×10^4) and its non-Debye interactions (Awadhia et al., 2006). The other SPE complexes portrayed a similar trend of increasing ε' value at low frequency.

When the mobile ions receive moderate amount of electric field, the number of realigned electric dipoles for all the SPE complexes is similar to the ionic conductivity pattern at room temperature as depicted in Figure 4.41. Once, these SPE complexes received excessive amount of electric field, the electric dipole went haywire and were not able to obey the direction of its current, thus a steady state of ε' value approaching zero was observed. Generally, the charged electric dipoles in all SPE complexes undergo both orientation and polarization relaxation at moderate frequencies. Amongst the SPEs, HY2-based SPE possess the greatest ability to relax at the highest frequency of $10^{3.9}$ Hz compared to its counterpart. On the other hand, HY1, HY3 and HY4 relaxed at frequencies of $10^{3.6}$ Hz, $10^{3.3}$ Hz and $10^{3.5}$ Hz, respectively. The ability for the SPEs to relax depends on the amount of charge carriers adsorbed on the host polymer because it is in accordance to their ionic conductivities values at room temperature.
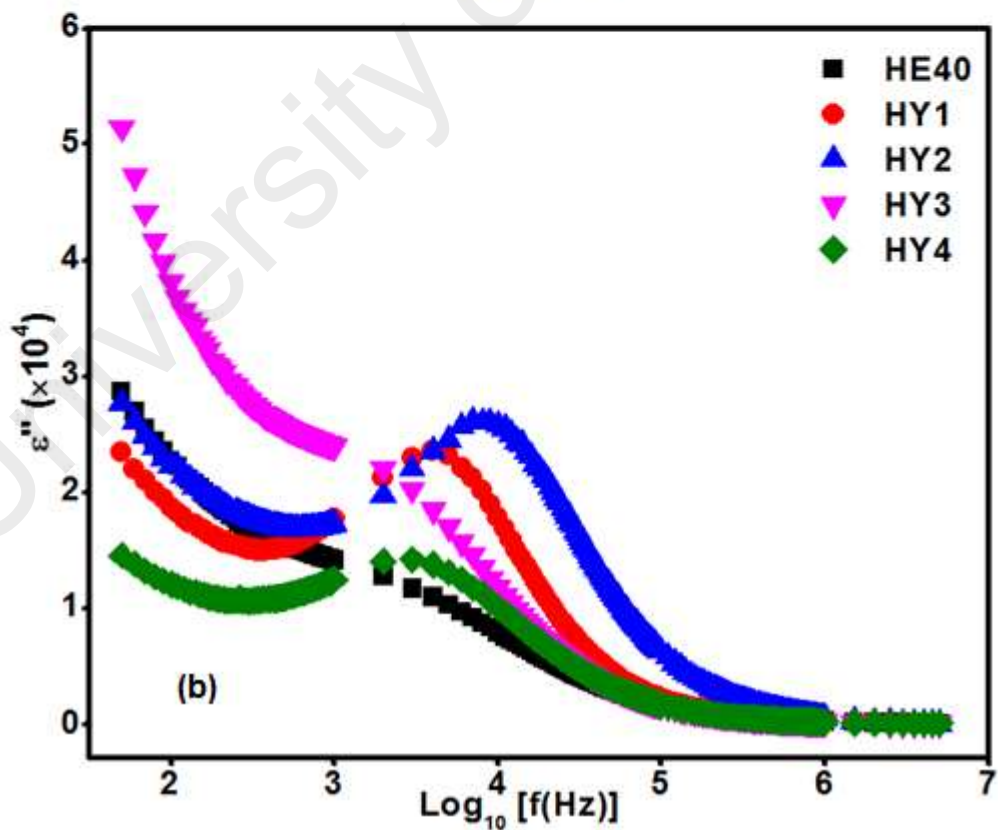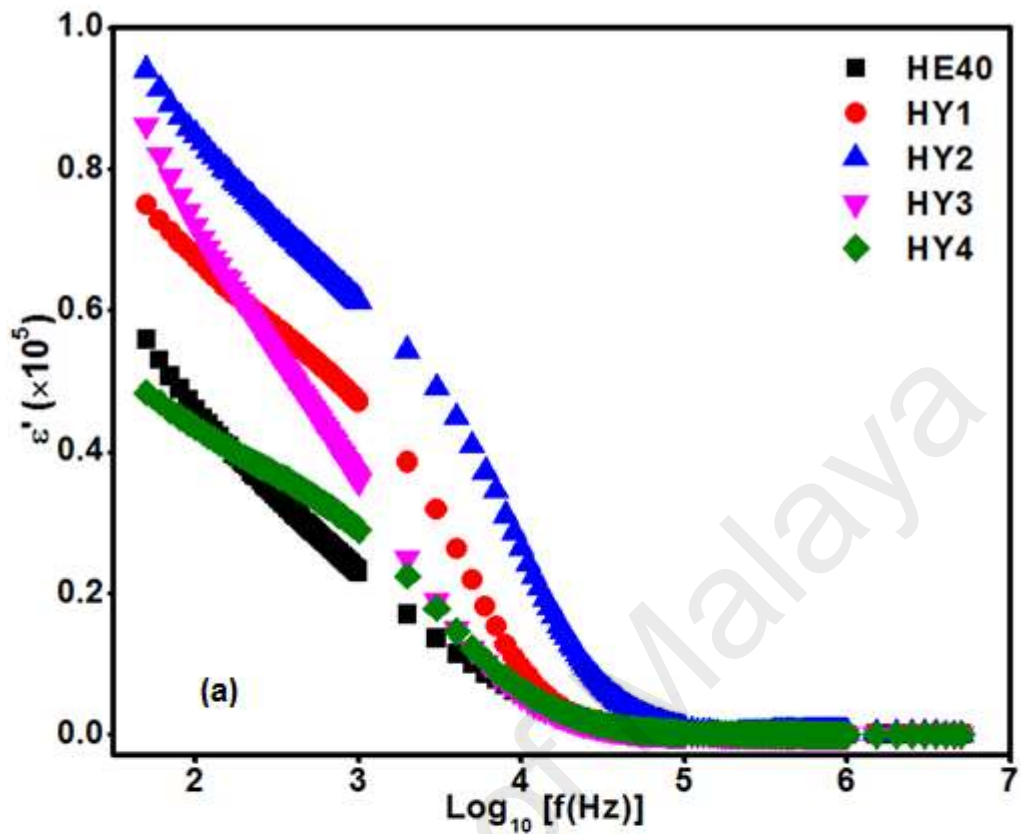
Figure 4.43: Variation of (a) ε' and (b) ε'' with frequency at various wt. % of Y_2O_3 nanoparticles

4.6.2.2 Modulus studies

The variation of M' and M" against frequency at various wt. % of Y_2O_3 nanoparticles were presented in Figures 4.44(a) and (b), respectively.
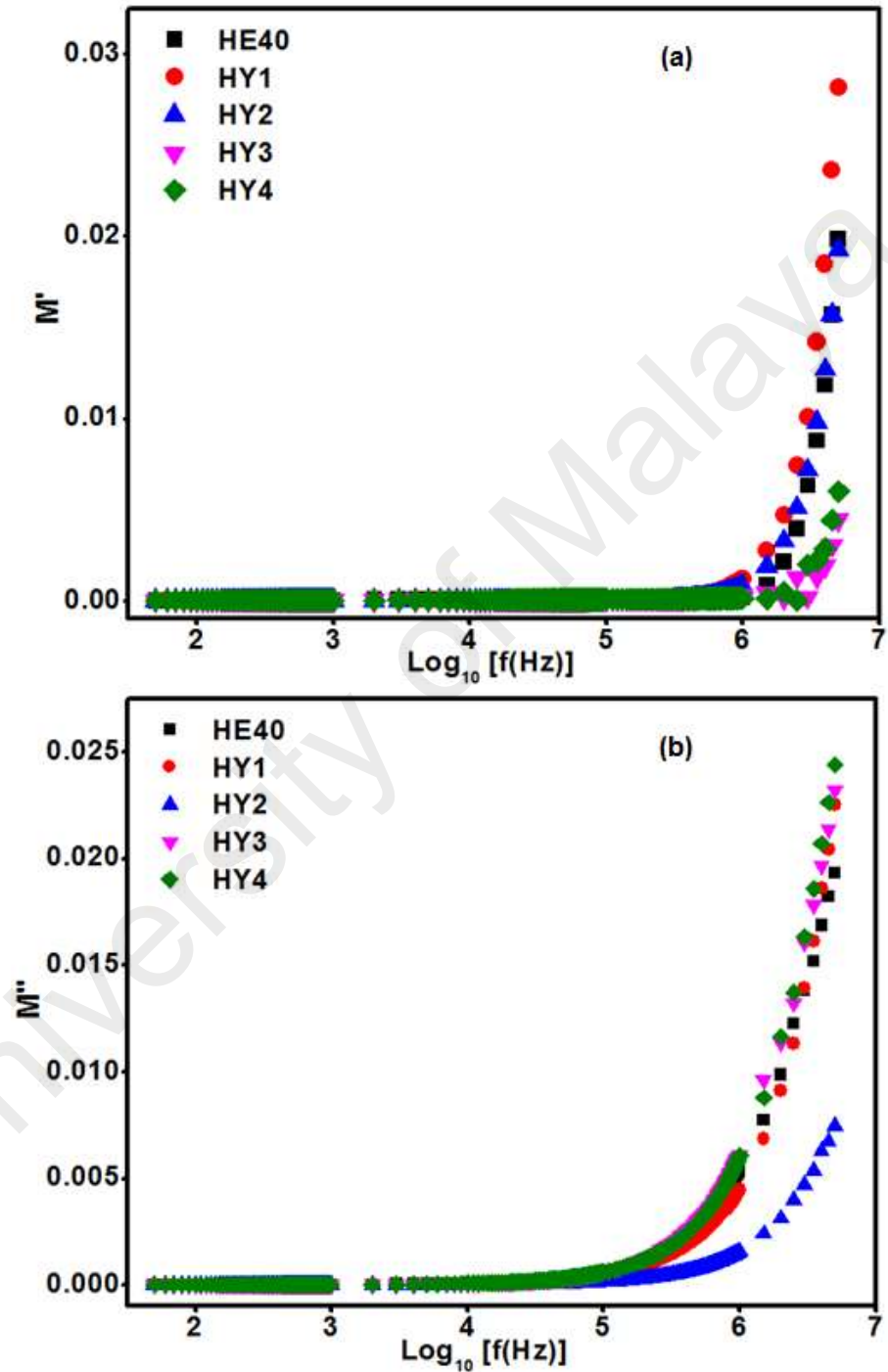
Figure 4.44: Variation of (a) M' and (b) M" with frequency at various wt. % of Y_2O_3 nanoparticles

As usual, constant values of M' and M" approaching zero were observed at low and moderate frequency regions for all SPE complexes. Although, rare-earth metal oxide nanoparticles has been incorporated into HE40, and yet, the long-range ionic conductivity and pure conduction mechanism of these SPEs were not disrupted by the electric field. In fact, an immense inflection peak which disclose the ionic conductivity of the SPE complexes at high frequency region was supposed to be seen but it was shattered by virtue of the limited experimental frequency window (Ramesh & Ling, 2010).

4.6.3   XRD studies

The diffractogram of pure samples (HEC and Y_2O_3) and SPE complexes at various wt. % of Y_2O_3 nanoparticles were depicted in Figure 4.45.
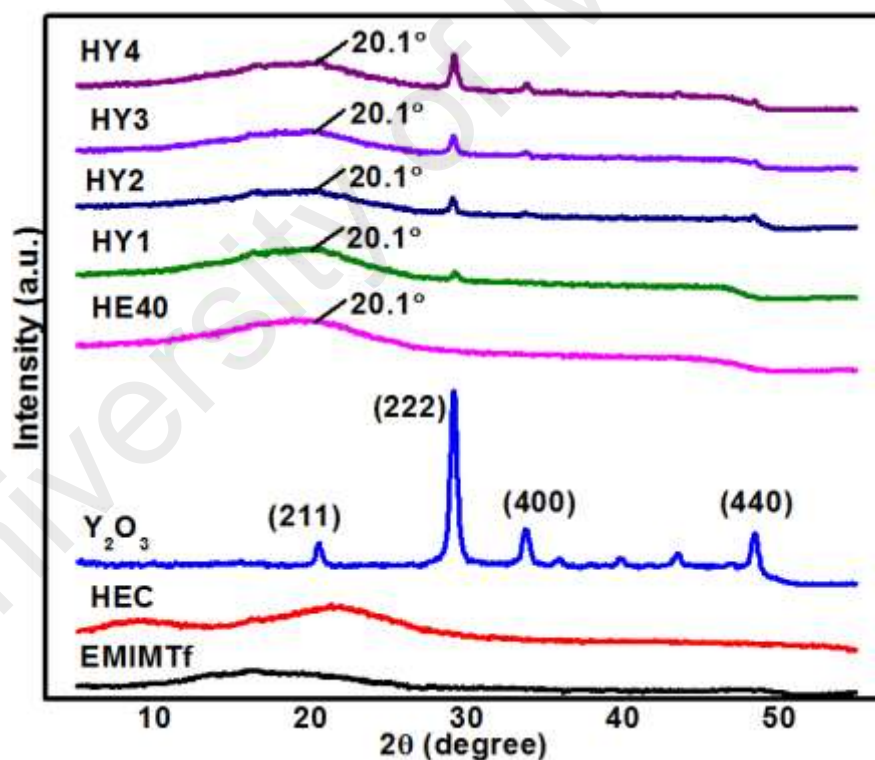
Figure 4.45: XRD patterns of pure samples (HEC and Y_2O_3) and SPE complexes at various wt. % of Y_2O_3 nanoparticles

The relationship between charge carriers and other materials (i.e. host polymer and nanoparticles) in all the SPE complexes were attributed to the presence of the peak at $2\theta = 20.1°$ (Ravi et al., 2011). The amorphorcity region of HEC increases upon

incorporation of 2 wt. % of Y_2O_3 nanoparticles because the broadness of HY2 decreased the most by 19.8 %. Subsequently, the partially amorphous region provides a smoother pathway for the mobility of charge carriers. On the other hand, Y_2O_3 nanoparticles was incorporated into HE40 successfully due to the presence of (2 2 2) peak at $2\theta = 29.2°$ in HY1, HY2, HY3 and HY4. Also, peak responsible for (4 0 0) at $2\theta = 33.9°$ can only be seen in HY2, HY3 and HY4 but not in HY1 because the SPE complex has very small amount of Y_2O_3 nanoparticles. Instead of peaks at $2\theta = 29.2°$ and 33.9°, pure cubic phase structure Y_2O_3 nanoparticles displayed characteristic peaks at 2θ of 21.0° and 48.6°, which are accountable to (2 1 1) and (4 4 0) planes, respectively (JCPDS card no. 86-1326).

4.6.4   FTIR studies

FTIR spectra of pure samples (Y_2O_3 and HEC) and SPE complexes at various wt. % of Y_2O_3 nanoparticles were depicted in Figure 4.46.
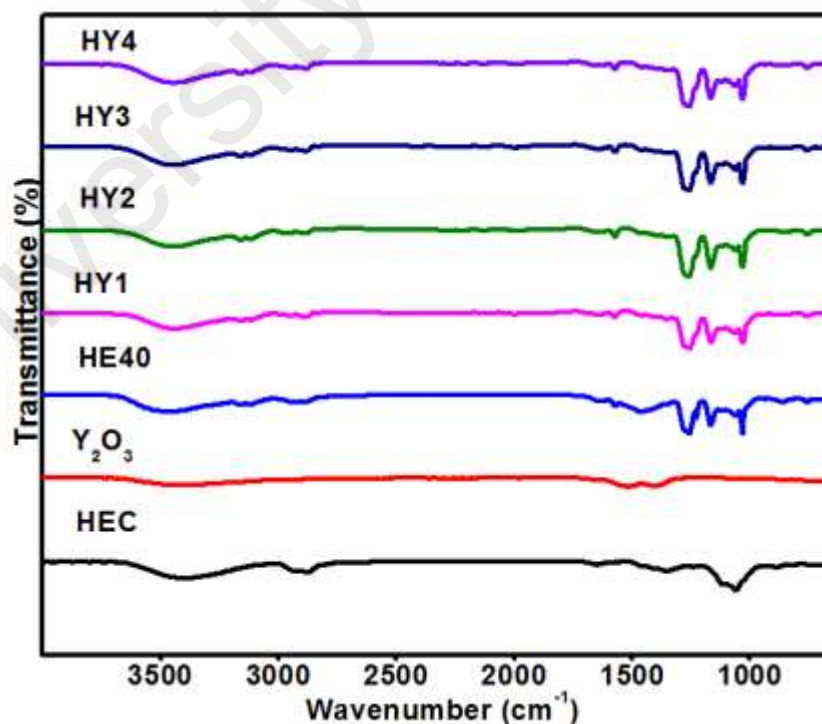
Figure 4.46: FTIR spectra for pure samples (HEC and Y_2O_3) and SPE complexes at various wt. % of Y_2O_3 nanoparticles

A pure Y_2O_3 nanoparticles exhibits characteristic peak at 415.0 cm^{-1} responsible for Y–O bond. However, the peak was not observed in the SPEs (HY1, HY2, HY3 and HY4) and in order for the peak to be noticeable, incorporation of at least 30 wt. % of Y_2O_3 nanoparticles is required as reported (Vishnuvardhan et al., 2006). Although, the main peaks of Y_2O_3 nanoparticles were invisible, yet it affects the absorption of Mg^{2+} ions on the host polymer as aforementioned in Section 4.5.4.

The interactions between the charge carriers and polymer chain were notified by the shift of wavenumber at 1026 cm^{-1} that are responsible for asymmetric in-plane C–O–C pyrose ring stretching. Also, the peak at wavenumber of 862 cm^{-1} which belongs to the asymmetric out-of-plane C–O–C pyrose ring stretching has been shifted to a higher wavenumber. Similarly, the peak intensity at 1159 cm^{-1} (SO_2 symmetric stretching in $CF_3SO_3^-$) was heightened by 40.3 % compared to HE40 owing to its most conducting SPE as shown in Figure 4.47(a). Therefore, it causes the asymmetric and symmetric stretching of $-CH_2$ and $-CH_3$ for pure HEC moved from 2917 cm^{-1} and 2873 cm^{-1}, respectively to a higher wavenumber. In addition, C–H bending of $-CH_2$ and $-CH_3$ (1357 cm^{-1}) has been shifted to lower wavenumber due to the interaction between charge carriers and the oxygen atom in the pyrose ring as displayed in Table 4.8 (Ramana & Singh, 1988).

Additionally, incorporation of Y_2O_3 nanoparticles produce fruitful yield of ionic conductivity at room temperature because it destroyed the crystallinity of HEC hinder by the formation of intermolecular hydrogen bonding between them. It was proven through the reduction in the broadness of –OH stretching peak (3382 cm^{-1}) by 49.9 % as depicted in Figure 4.47(b). On top of that, it was accompanied by the shift of –OH in-plane deformation (1457 cm^{-1}) to a higher wavenumber (Belfer et al., 2000).
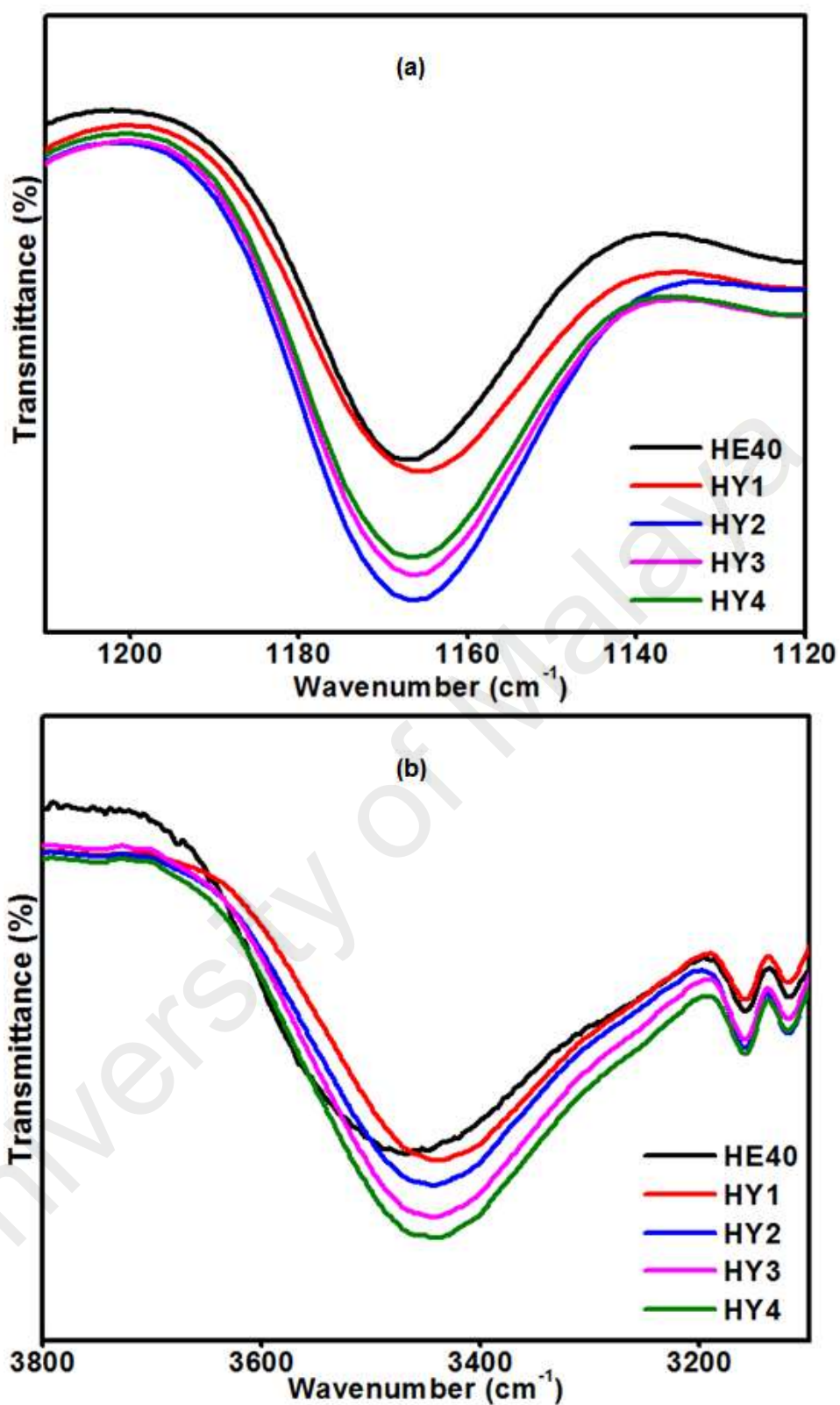
Figure 4.47: (a) SO$_2$ symmetric stretching in CF$_3$SO$_3^-$ (1167 cm^{-1}) and (b) –OH stretching (3473 cm^{-1}) SPE complexes (with and without Y$_2$O$_3$ nanoparticles)

Table 4.8: Band assignments of pure HEC and SPE complexes at various wt. % of Y_2O_3 nanoparticles

Band assignments	HEC (cm^{-1})	HE40 (cm^{-1})	HY1 (cm^{-1})	HY2 (cm^{-1})	HY3 (cm^{-1})	HY4 (cm^{-1})	Reference
−OH stretching	3403	3473	3426	3435	3429	3423	(Chong et al., 2016; Satyamurthy & Vigneshwaran, 2013)
Asymmetric −CH$_2$ and −CH$_3$ stretching	2917	2923	2946	2952	2946	2946	(Abidi et al., 2014; Saroj et al., 2014)
Symmetric −CH$_2$ and −CH$_3$ stretching	2876	2881	2884	2887	2887	2887	(Abidi et al., 2014; Saroj et al., 2014)
Absorbed water	1651	1636	1645	1642	1645	1639	(Chung et al., 2004; Satyamurthy & Vigneshwaran, 2013)
−OH in-plane deformation	1457	1457	1463	1463	1460	1463	(Abidi et al., 2014)
C−H bending of −CH$_2$ and −CH$_3$	1354	1357	1351	1345	1348	1348	(Abidi et al., 2014)
−OH in-plane bending	1239	1260	1254	1254	1251	1254	(Chung et al., 2004)
Asymmetric bridge C−O−C stretching	NIL	1167	1166	1166	1166	1166	(Chung et al., 2004)
SO$_2$ symmetric stretching in CF$_3$SO$_3^-$	1115	1118	1118	1118	1118	1115	(Abidi et al., 2014; Chung et al., 2004)
Asymmetric in-plane C−O−C pyrose ring stretching	1062 NIL	1062 1030	1062 1024	1062 1024	1062 1024	1062 1024	(Abidi et al., 2014; Chung et al., 2004)
Asymmetric out-of-phase C−O−C pyrose ring stretching	889	862	883	886	886	880	(Chung et al., 2004)

4.6.5   TGA studies

Table 4.9 depicts the decomposition temperature for SPE complexes at various wt. % of Y_2O_3 nanoparticles. The thermograms of pure samples (HEC, $MgTf_2$, EMIMTf and Y_2O_3) and SPE complexes at various wt. % of Y_2O_3 nanoparticles are shown in Figure 4.48. In general, all the SPE complexes exhibited four stages of decomposition. At the first stage, HE40 faced decomposition temperature at 51.7 ˚C whereas SPEs incorporated with Y_2O_3 nanoparticles exhibited decomposition temperature around 100 ˚C which was due to the evaporation of minor impurities and absorbed moisture (Liu et al., 2008). Conversely, the SPE complexes incorporated with Y_2O_3 nanoparticles encounter a decomposition around 90.0 ˚C, which was responsible for the complete evaporation of water solvent from the SPE complexes. At the second stage, the decomposition of host polymer was observed because all the complexes decomposed at the range of temperature from 266–284.1 ˚C. Subsequently, at the third and last stage, all the SPE complexes experienced decomposition of EMIMTf and $MgTf_2$ which occurred at temperature range from 382–418.5 ˚C and 466–479.5 ˚C, respectively. In conclusion, the thermal stability of the SPEs incorporated with Y_2O_3 nanoparticles was better than HE40.

Table 4.9: The decomposition temperature of SPE complexes (with and without incorporation of Y_2O_3 nanoparticles

Samples	Thermal decomposition (˚C)			
	Stage 1	Stage 2	Stage 3	Stage 4
HE40	51.8	266.6	382.9	466.0
HY1	90.3	284.1	418.5	479.4
HY2	89.5	280.5	409.5	474.1
HY3	90.5	276.9	409.5	474.1
HY4	90.3	284.1	411.3	474.1
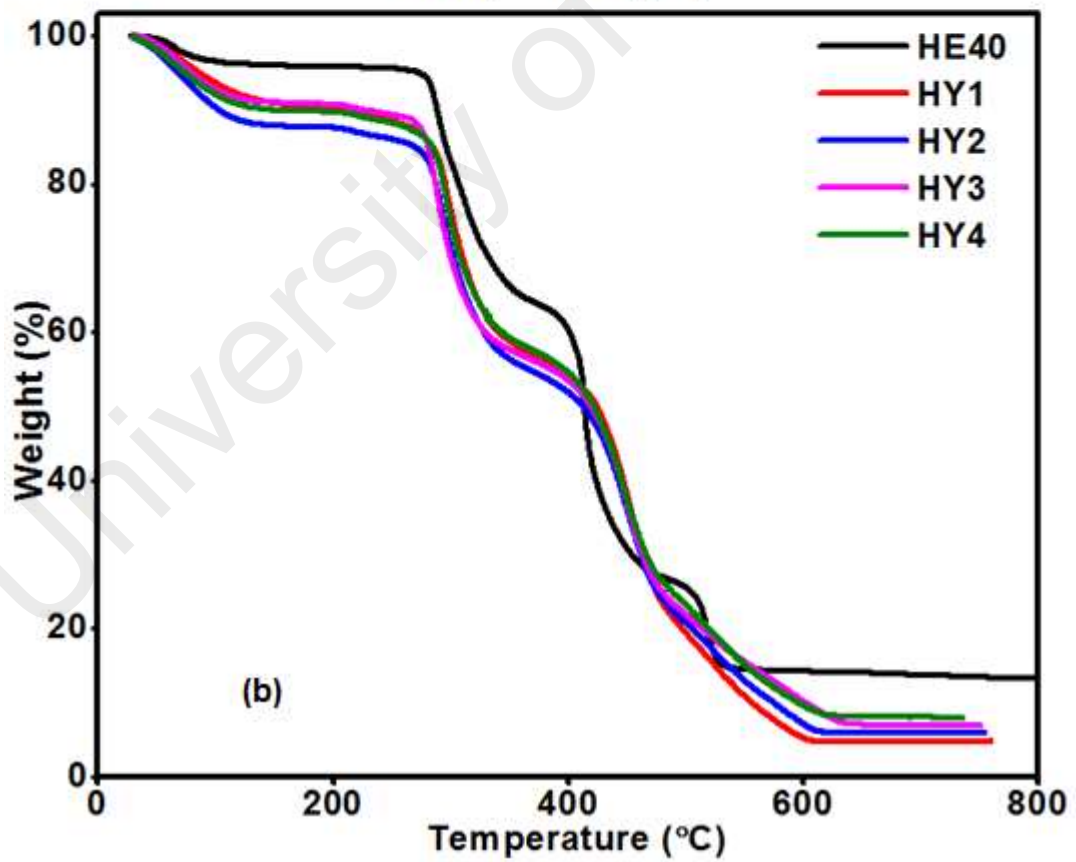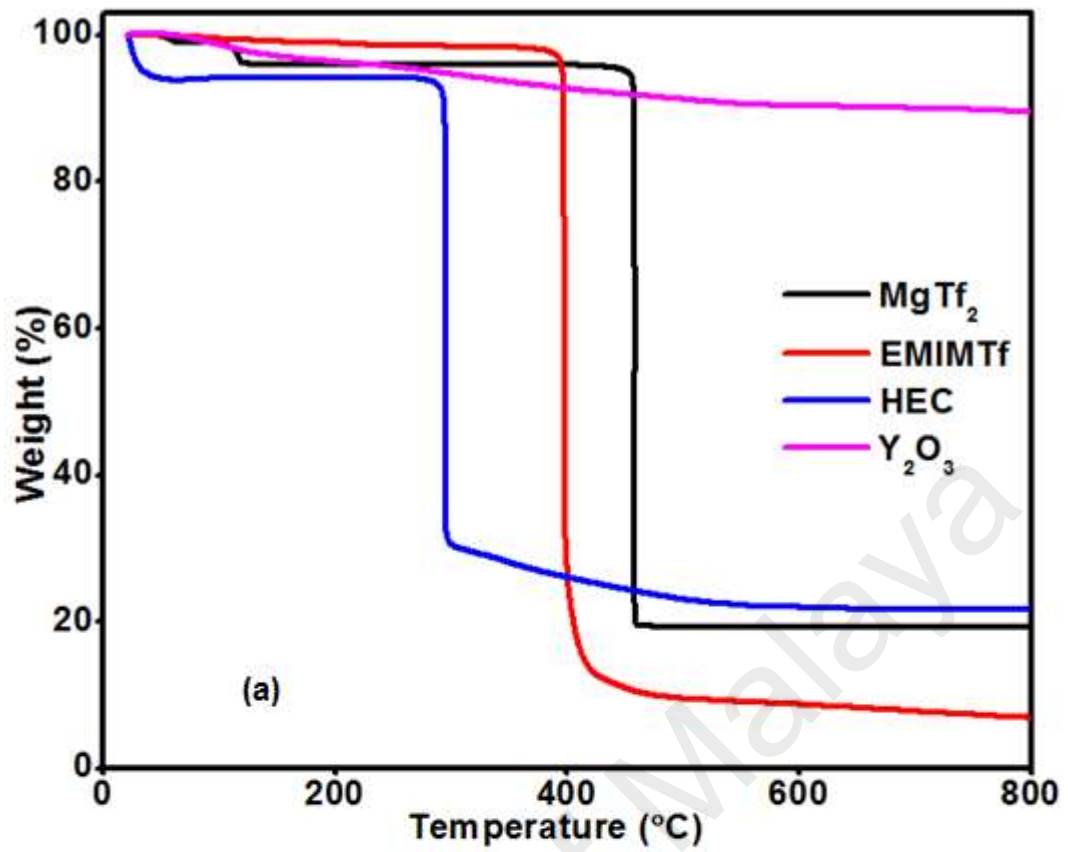
Figure 4.48: Thermograms of (a) pure (HEC, $MgTf_2$, EMIMTf and Y_2O_3) and (b) SPE complexes at various wt. %of Y_2O_3 nanoparticles

4.6.6   CV Studies

Figure 4.49 illustrates the voltammograms from -1 to 1 V at various scan rate for EDLCs (with and without Y_2O_3 nanoparticles).
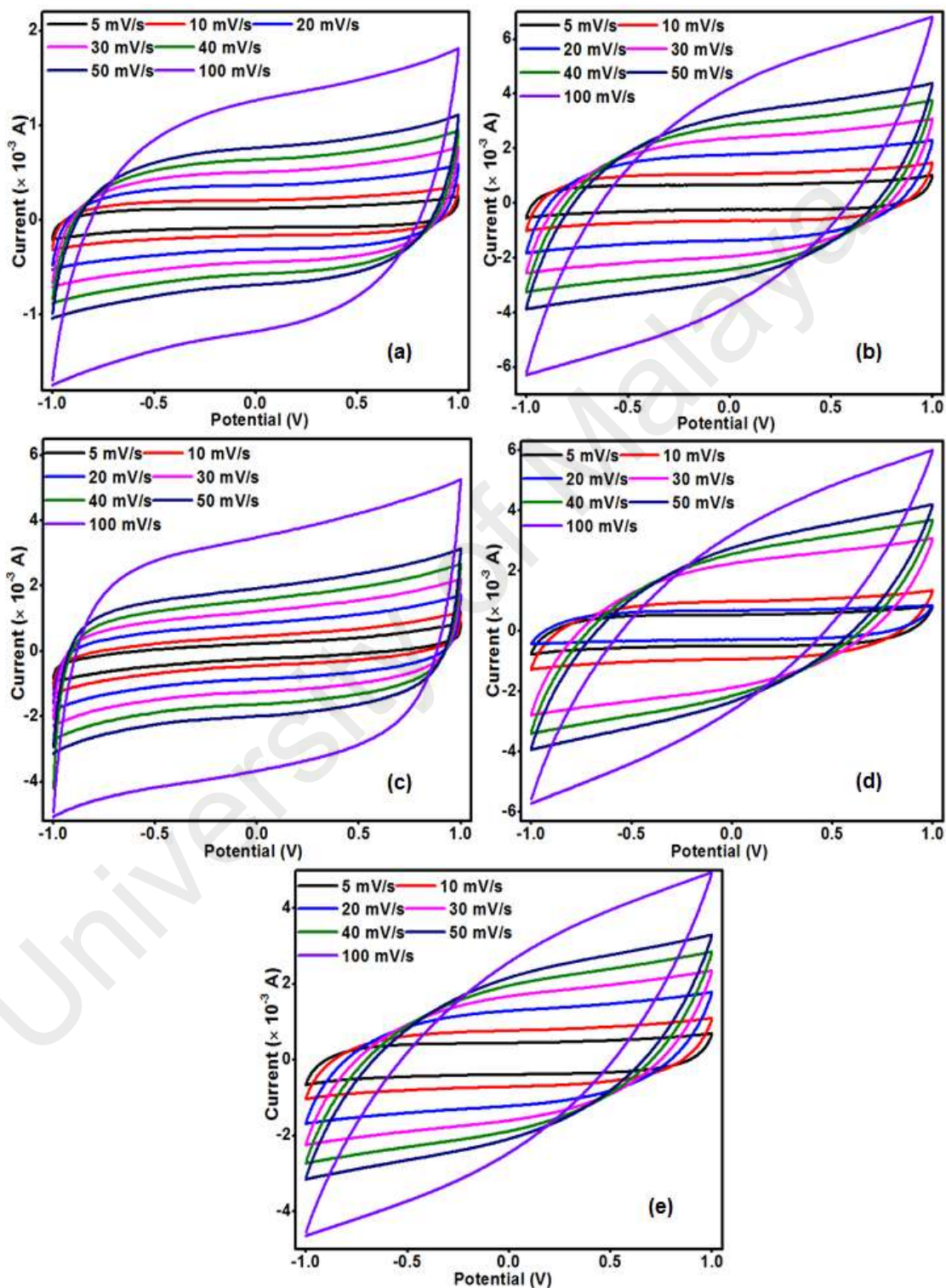
Figure 4.49: CV responses of (a) HE40 (b) HY1 (c) HY2 (d) HY3 (e) HY4 at different scan rates over the voltage range from -1 to 1 V

Figure 4.50(a) and (b) represent the voltammogram at scan rate of 5 mV/s and the correlation between the specific capacitance and scan rate applied, respectively for EDLCs (with and without Y_2O_3 nanoparticles).
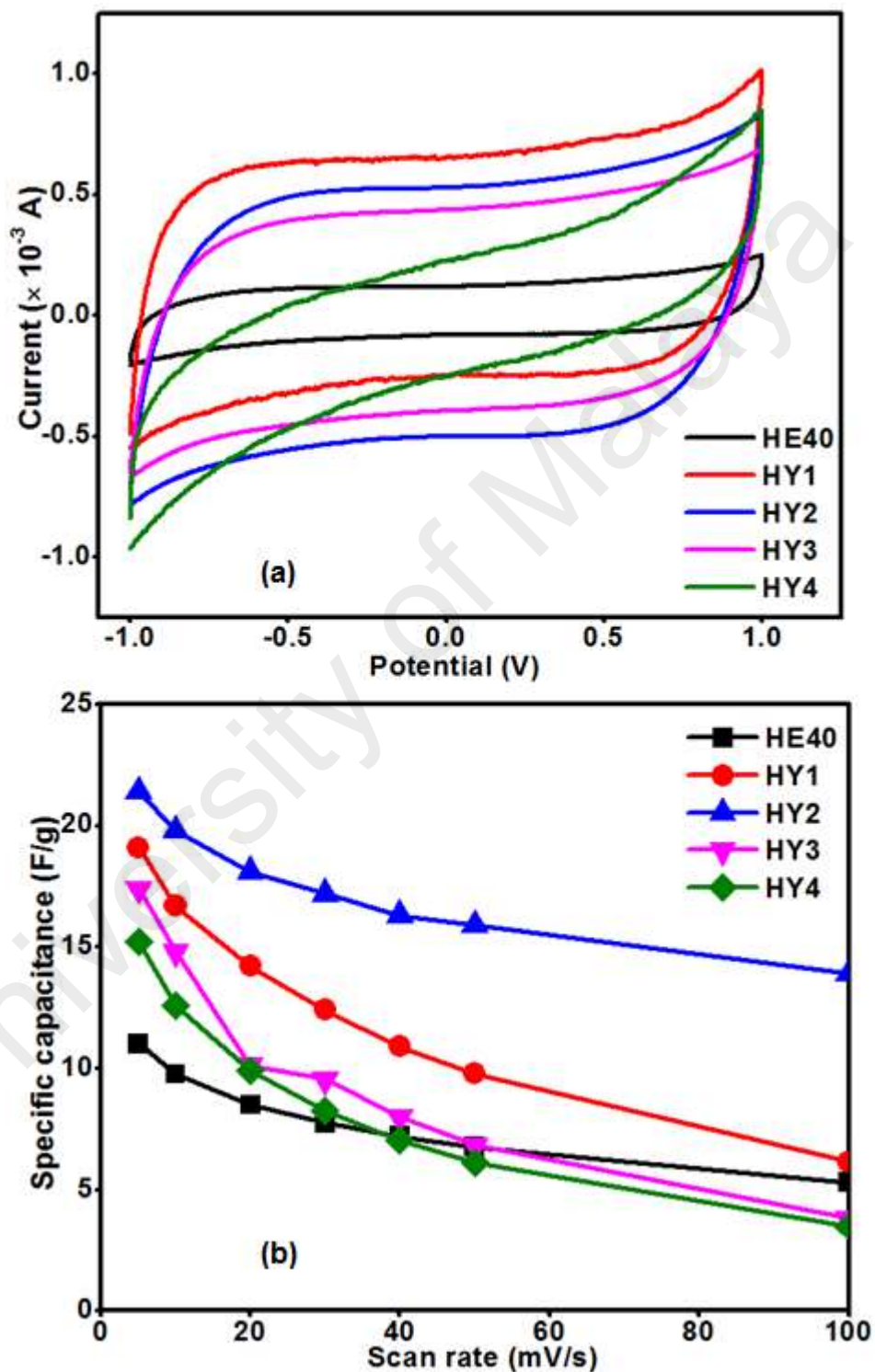
Figure 4.50: (a) CV responses at scan rate of 5 mV/s for EDLC cells (with and without incorporation of Y_2O_3 nanoparticles) (b) Specific capacitance for EDLC cells (with and without incorporation Y_2O_3 nanoparticles) as a function of scan rate

All the EDLCs maintain their double layer capacitive property at scan rate below 50 mV/s. It was indicated by the well-defined rectangular shape of the CV curve. When the scan rate reaches 100 mV/s, the CV curves of the EDLCs became leaf shape signifies that the electric dipoles failed to obey the rhythm of the electric field applied. In another words, most EDLCs will suffer decrease in specific capacitance as the scan rate increases (Arulepp et al., 2004).

Generally, the performance of the EDLCs after incorporated with Y_2O_3 nanoparticles was boosted because the nanoparticles provide more active sites to transport charge carriers into the carbon electrodes. Hence, the specific capacitance calculated for HY1-based cell is 19.1 F/g, which is followed by HY2 (21.4 F/g,), HY3 (17.4 F/g) and HY4 (15.2 F/g). The EDLC fabricated by HY2 attained the greatest difference by 94.5 % in terms of specific capacitance at scan rate of 5 mV/s compared to HE40 cell.

4.6.7   EIS Studies

Figure 4.51 describes the complex impedance spectra of EDLCs (with and without Y_2O_3 nanoparticles). The EDLCs incorporated with Y_2O_3 nanoparticles achieved smaller semicircle at high frequency region compared to HE40 cell because the nanoparticles are capable to enhance the rate of diffusion of charge carriers into the carbon electrodes (Singh et al., 2014). Based on the results, the R_{ct} values of HE40, HY1, HY2, HY3 and HY4 cells were 142.0 Ω, 51.8 Ω, 27.9 Ω, 54.6 Ω and 68.6 Ω, respectively. In addition, the capacitive behavior improved drastically upon incorporation of nanoparticles owing to smaller arc tangent values to the imaginary axis at low frequency region compared to HE40 cell as reported in Table 4.10. Above all the descriptions, HY2-based cell obtained the smallest R_{ct} and least deviation from the vertical axis because the ions in HY2-based SPE diffuses into the carbon electrodes easily owing to its lowest activation energy of 0.238 eV.
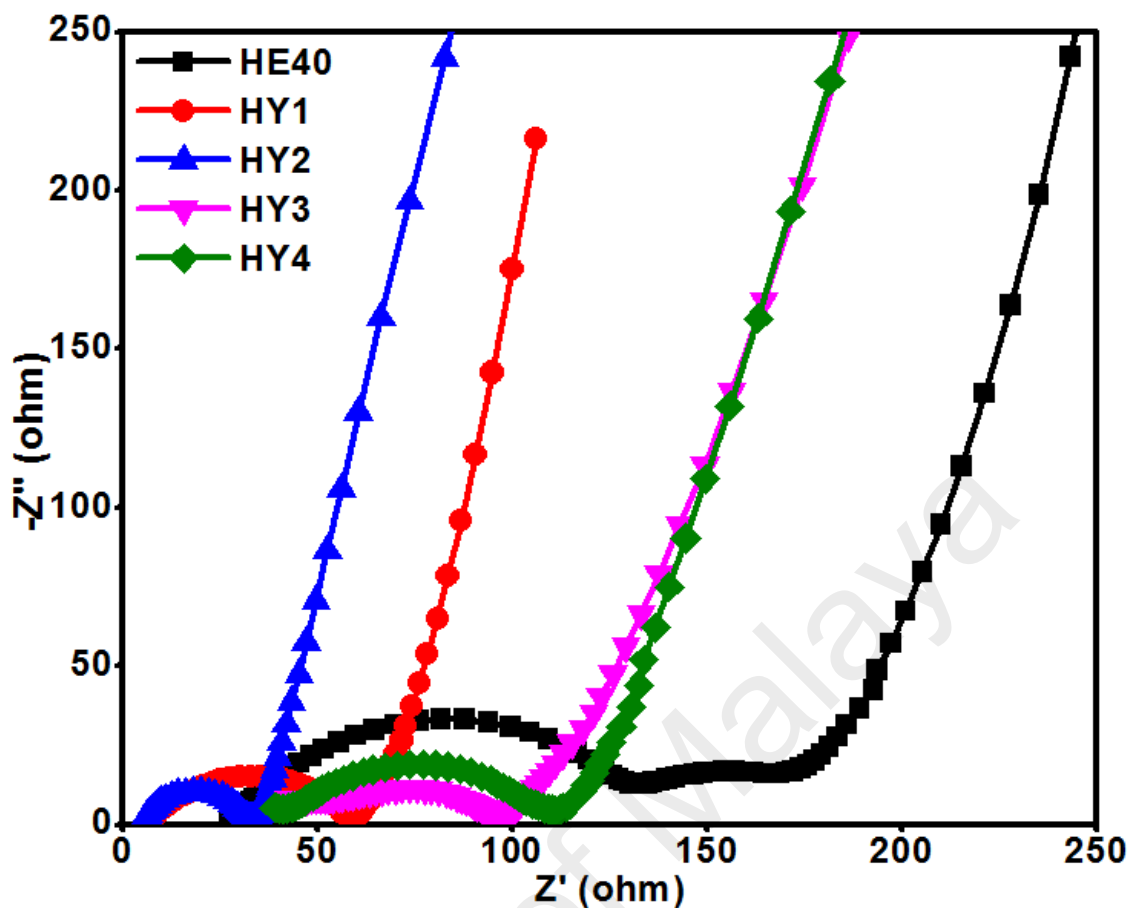
Figure 4.51: Complex impedance spectra of EDLC cells (with and without incorporation of Y_2O_3 nanoparticles) at room temperature

Table 4.10: R_{ct} values for EDLC cells (with and without incorporation of Y_2O_3 nanoparticles)

EDLC cell	R_{ct} (Ω)	Deviation from imaginary axis ($^\circ$)
HE40	142.0	32.7
HY1	51.8	15.9
HY2	27.9	12.3
HY3	54.6	21.0
HY4	68.6	17.2

4.6.8   GCD Studies

Figures 4.52(a) – (e) represents the variation of potential with time of EDLCs (with and without incorporation of Y_2O_3 nanoparticles) at different current densities. Generally, as the current density increased, only a handful amount of charge carriers were able to

penetrate into the electrodes due to slow diffusion, hence the charging and discharge time decreases (El-Kady et al., 2012). Also, the ohmic potential (IR) drop increases with the increment in current densities due to internal resistances (i.e. internal resistance between electrode and electrolyte, between current collector and active material and between electrode and connector) of the cell (Stoller & Ruoff, 2010; Zheng, 2004). However, all the EDLCs showed a symmetrical triangle shape which is in lieu to its highly reversible charging and discharging process between charge carriers and electrode (Liu et al., 2008).

Figure 4.52(f) displays the discharge curves of EDLCs at current density of 30 mA/g. The discharge time obtained by HE40, HY1, HY2, HY3 and HY4 cells were 136.3 s, 284.9 s, 355.2 s, 280.7 s and 193.3 s, respectively. It was found out that HY2 cell obtained the longest discharge time by 160.6 % compared to HE40 because the penetration of charge carriers were smooth with the presence of optimum amount of Y_2O_3 nanoparticles.. On the other hand, the specific capacitance for HE40, HY1, HY2, HY3 and HY4 at current density of 30 mA/g were 9.5 F/g, 17.9 F/g, 17.6 F/g, 12.7 F/g and 18.4 F/g, respectively. The specific capacitance values calculated based on Equation 3.12 resembles the values discussed in Section 4.6.6.

Figure 4.53 depicts the cyclic charge-discharge test. Based on the plot, the specific capacitance of the most outstanding EDLC (HY2 cell) dropped by 8.7 % after 3,000 cycles at current density of 0.4 A/g. The result shows better diffusion and entrapment of ions by HY2-based SPE into the bulk electrodes.
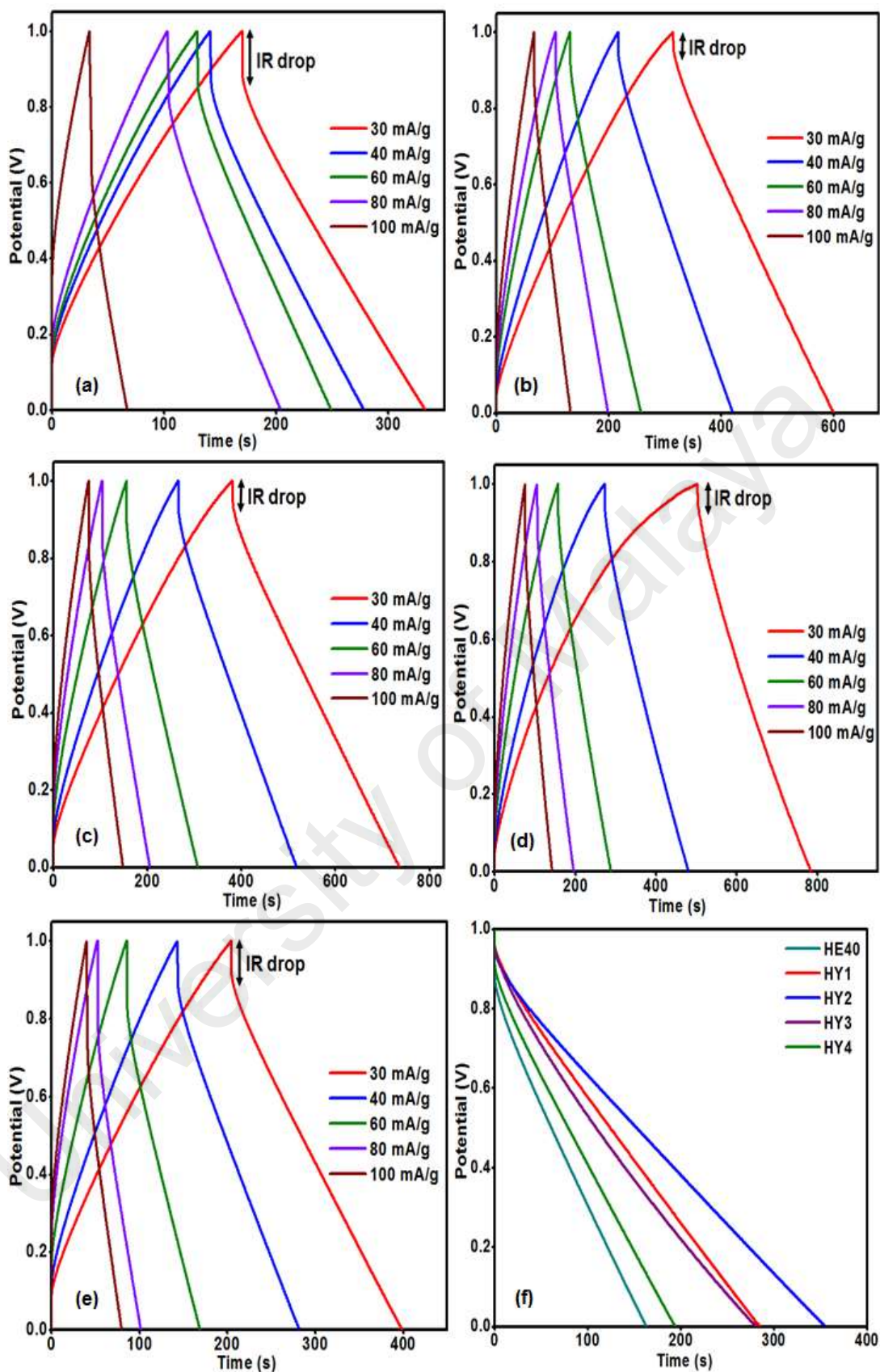
Figure 4.52: Galvanostatic charge-discharge curves of (a) HE40 (b) HY1 (c) HY2 (d) HY3 (e) HY4 at different current densities (f) Discharge curves of EDLC cells (with and without incorporation of Y_2O_3 nanoparticles) at current density of 30 mA/g
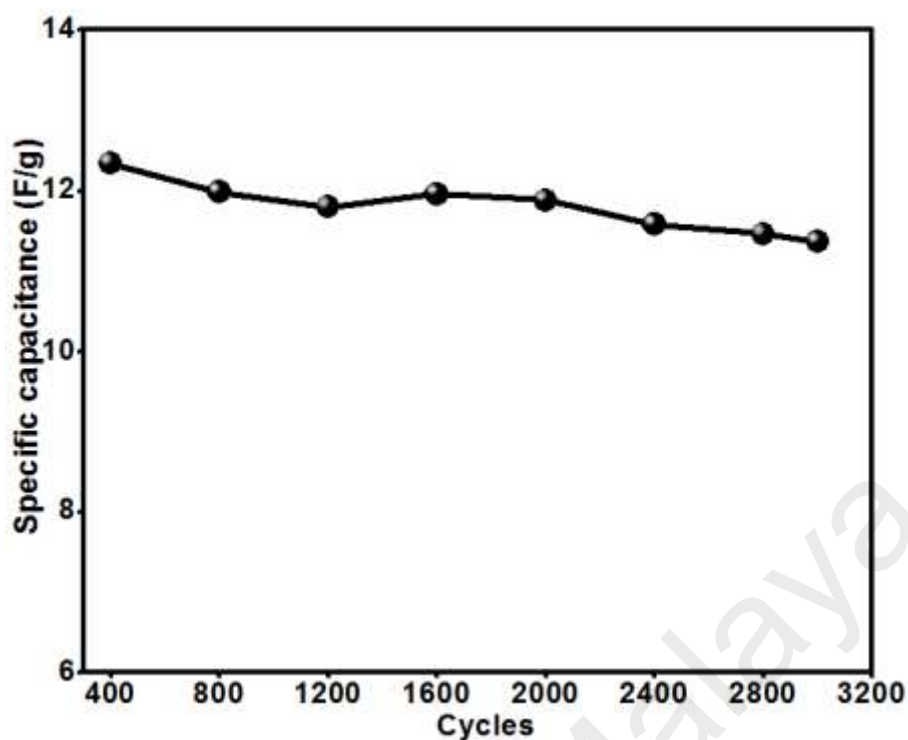
Figure 4.53: Specific capacitance of HY2-based EDLC over 3,000 cycles at current density of 0.4 A/g

4.6.9 Summary

In conclusion, the performance of the EDLCs based on SPE incorporated with Y_2O_3 nanoparticles are better than HE40. Among the SPEs, HY2 obtained the highest ionic conductivity at room temperature (3.54×10^{-4} S/cm) along with the smallest R_b value (12.1 Ω) from the Cole-Cole impedance plot. In addition, it achieved the smallest activation energy (0.238 eV) among the thermally activated SPEs. This was due to more number of available mobile charge carriers that can be transported easily through the partially amorphous region when 2 wt. % of nanoparticles has been incorporated into HE40. The phenomena is well supported by the decrease in crystallinity of the peak at $2\theta = 20.1°$ by 19.8 %. Moreover, it was endorsed by the depression in the broadness of –OH stretching (3435 cm^{-1}) by 49.4 % compared to HE40. Moreover, HY2 achieved the highest ε' (9.4×10^4) and it is capable to relax at higher frequency of $10^{3.8}$ Hz. The results indicated that HY2-based SPE has the most number of mobile charge carriers adsorbed to the host polymer. In general, the thermal stability of the SPEs improved upon addition

143

of nanoparticles (~470.0 ˚C) and thereby HY1, HY2, HY3 and HY4 are suitable for energy storage devices. Amongst all the EDLCs, HY2 cell possesses the highest specific capacitance at 5 mV/s, lowest R_{ct} and longest discharging time at 30 mA/g of 21.4 F/g, 27.9 Ω and 355.2 s, respectively because it has the best interfacial contact with the carbon electrode. The result is in accordance to the cycling stability test for HY2 cell in which it obtained 91.3 % capacitance retention after 3,000 cycles at 0.4 A/g.

CHAPTER 5: DISCUSSIONS

Based on HEC-MgTf$_2$-EMIMTf-fumed SiO$_2$, HEC-MgTf$_2$-EMIMTf-CuO and HEC-MgTf$_2$-EMIMTf-Y$_2$O$_3$ systems, HS2, HC2 and HY2 cells were the most outperformed EDLC.

The highest specific capacitance at 5 mV/s was attributed to HC2 cell (36.7 F/g) in which the value calculated resembles the specific capacitance calculated from the discharge curve (30.0 F/g) at 20 mA/g. Also, the specific capacitance of HC2 cell decreased steadily on elevated scan rate even though all the EDLCs showed good behavior of a capacitor through a well-defined rectangular shape of voltammogram until 50 mV/s. This is due to the stickier appearance of HC2 SPE compared to HY2 and HS2. As a result, it improves the diffusion of ions into the carbon electrode with minimum charge transfer resistance of 25.0 Ω (Latifatu et al., 2012; Li et al., 2013).

Similarly, EDLC based on HC2 experienced the longest discharge time at 30 mA/g compared to HS2 and HY2 although all exhibit symmetrical triangle of charge-discharge curve. The phenomena was governed by excellent penetration and adsorption of charge carriers to the carbon electrodes by the small particle size of CuO nanoparticles (Ren et al., 2013). The CuO nanoparticles has smaller particle size (~ 25 nm) than Y$_2$O$_3$ nanoparticles (~ 50 nm) but larger particle size than fumed SiO$_2$ nanoparticles (~ 12 nm). Even though, fumed SiO$_2$ nanoparticles has small particle size, yet it exhibits shorter discharge time than CuO-based cell due to its high charge density. The high charge density on fumed SiO$_2$ nanoparticles cause solvation of ions, aggregations of nanoparticles and neutralization of the charge carriers. Hence, EDLC based on fumed SiO$_2$ nanoparticles will block the ions pathway into the pore of the electrodes (Hu et al., 2005).

In sharp contrast, HY2-based cell gives the best cycling stability by retaining its initial specific capacitance at 91.3 % over 3,000 cycles at 0.4 A/g even though it obtained the lowest specific capacitance of 21.4 F/g at 5 mV/s compared to HC2 cell. It was proven that the specific capacitance independent from its cycling stability (Kumar et al., 2012). Based on Kumar et al. (2012), the GPE prepared by PVdF-HFP, LiTf and EMIMTf exhibits 32 F/g with 100 % capacitance retention over 50,000 cycles using multi-walled carbon nanotubes whereas a GPE prepared by PVdF-HFP, LiTf, EMIMTf and EC/PC plasticizers exhibit 157 F/g with 100 % capacitance retention over 4,000–5,000 cycles. It indicates that the cycling stability of a cell is independent of its specific capacitance.

On the other hand, HY2-based device has longer service compared to HC2-based cell because the SPE formed by incorporation of Y_2O_3 nanoparticles creates a strong polymer backbone owing to its higher Young's modulus (55.0 MPa) than HC2 SPE (15.6 MPa) (Croce et al., 1998). Consequently, HY2 cell has better mechanical strength (less sticky appearance) than HC2 in which it is highly durable to the absorption-desorption of ions at the electrode/electrolyte interface (Aygün et al., 2003; Chen et al., 2009).

It is worth to mention that HS2, HC2 and HY2 cells are highly suitable for green EDLC because their SPEs exhibits superior thermal stability (~470 ˚C) and high ionic conductivity at ambient temperature (~10^{-4} S/cm).

146

6.1 Conclusions

There were four objectives in this research. The first objective was to optimize and characterize the most suitable host polymer and IL to prepare the SPE.

Based on the results, HEC is found to be more suitable as host polymer for EDLC compared to HPMC because it is cheap, easy to process and environmentally friendly (as less amount of salt is used), shorter time (2 days) to prepare a thin film and the usage of green solvent (water). HEC has more bulky residual group, hence EMIMTf (shorter alkyl chain) IL is found to be more compatible than BMIMTf (longer alkyl chain) because it can minimize the steric hindrance between the host polymer and IL. As a result, HEC-$MgTf_2$ system achieved the lowest R_b (32.0 Ω) and highest ionic conductivity (9.28×10^{-5} S/cm) at room temperature upon incorporation of 40 wt. % EMIMTf. The interactions between the polymer chain and charge carriers are well supported by the splitting of asymmetric in-plane C–O–C stretching in pyrose ring (1062 cm^{-1}) revealed in the IR spectra and shift of HEC peak at $2\theta = 19.9°$ in the XRD pattern. The SPE obeyed Arrhenius theory with a low activation energy of 0.306 eV.

Subsequently, HEC-$MgTf_2$-EMIMTf system has been incorporated with three types of nanoparticles (fumed SiO_2, CuO and Y_2O_3) and these three new systems have been characterized and fabricated for EDLC.

Based on the first system (HEC-$MgTf_2$-EMIMTf-fumed SiO_2), SPE incorporated with 2 wt. % of fumed SiO_2 nanoparticles (HS2) has the maximum number of conducting ions. The presence of large number of conducting ions is well supported by the smallest R_b (14.5 Ω), lowest activation energy (0.213 eV), highest ionic conductivity at room

temperature (2.71×10^{-4} S/cm), highest dielectric permittivity (9.0×10^4) and maximum dielectric loss that was shifted to the highest frequency ($10^{3.7}$ Hz) based on EIS results. On top of that, the rupture of crystallinity in HEC at $2\theta = 20.0$ ˚ by 53.4 % indicated that the transportation of ions in the entire system were easy. The transportation of ions led to great interactions between the ions and nanoparticles along the polymer chain. It is well endorsed by the shift of wavenumber at peaks 2923 cm^{-1} (asymmetric $–CH_2$ and $–CH_3$ stretching), 2881 cm^{-1} (symmetric $–CH_2$ and $–CH_3$ stretching), 1357 cm^{-1} (C–H bending of $–CH_2$ and $–CH_3$) and 862 cm^{-1} (asymmetric out-of-phase C–O–C pyrose ring stretching). Also, the FTIR results showed a decrease in peak intensity at wavenumber 1165 cm^{-1} (SO_2 symmetric stretching in $CF_3SO_3^-$) and 1030 cm^{-1} (asymmetric in-plane of C–O–C pyrose ring stretching) by 8.9 % and 34.7 %, respectively. HS2-based SPE responded well with the change of temperature because it is stable at high temperature (~470 ˚C) and the ions in it obeyed Arrhenius theory, which mean it is suitable for EDLC. The EDLC based on the first system (HS2 cell) has good interfacial contact with the carbon electrodes because it achieves the highest specific capacitance (24.6 F/g) at scan rate of 5 mV/s and the shape CV curve remain rectangular until 50 mV/s. On top of that, it achieves longest discharge time (389.0 s) at current density of 30 mA/g, capacitance retention of 67.4 % over 2,000 cycles at 0.4 A/g and minimum R_{ct} (47.4 Ω).

For the second system (HEC-$MgTf_2$-EMIMTf-CuO), the EIS results showed that the ions in the SPE are thermally activated with lowest R_b (18.1 Ω), highest ionic conductivity value at room temperature (2.58×10^{-4} S/cm), lowest activation energy (0.252 eV), highest ε' (1.2×10^5) at low frequency region and the maximum value of ε'' shifted to a higher frequency ($10^{3.6}$ Hz) upon incorporation of 2 wt. % of CuO nanoparticles. At this optimum wt. % of CuO nanoparticles, the adsorption and transportation of charge carriers along the polymer chain were the highest compared to the other SPEs. The result obtained were compatible with slight reduction in crystallinity at $2\theta = 20.0°$ in HEC by 1.0 % in

148

the XRD pattern along with the decrease in the broadness of –OH stretching at 3473 cm^{-1} by 29.6 % compared to HE40. In addition, based on the FTIR spectra, the peak intensities at 1165 cm^{-1} (SO$_2$ symmetric stretching in CF$_3$SO$_3^-$) and 1062 cm^{-1} (asymmetric in-plane C–O–C pyrose ring stretching) dropped by 5.2 % and 50.0 %, respectively compare to HE40 whereas shifts of wavenumber were seen at 2923 cm^{-1} (asymmetric –CH$_2$ and –CH$_3$ stretching), 2881 cm^{-1} (symmetric –CH$_2$ and –CH$_3$ stretching) and 1357 cm^{-1} (C–H bending of –CH$_2$ and –CH$_3$) owing to the interactions between charge carriers and host polymer. HC2-based EDLC are safe to be fabricated by virtue of its high thermal decomposition temperature at ~470 ˚C based on the thermogram. It obtained 36.7 F/g, 25.0 Ω, 438.0 s and 80.5 % of specific capacitance at 5 mV/s, R$_{ct}$, discharge time at 30 mA/g and capacitance retention over 3,000 cycles at 0.4 A/g current density, respectively.

In the last system (HEC-MgTf$_2$-EMIMTf-Y$_2$O$_3$), the SPE incorporated with 2 wt. % of Y$_2$O$_3$ nanoparticles (HY2) attained the smallest R$_b$ (12.1 Ω), lowest activation energy (0.238 eV), highest ionic conductivity at room temperature (3.54 × 10^{-4} S/cm), highest dielectric permittivity (9.4 × 10^4) and maximum dielectric loss that was shifted to the highest frequency (10$^{3.9}$ Hz). The results obtained are due to the huge amount of charge carriers in the SPE that led to fast facilitation on the polymer chain. It can be explained by the highly disordered crystallinity in HEC at 2θ = 20.1 ˚ by 19.8 % and the collapse of the –OH stretching (3382 cm^{-1}) by 49.9 % with respect to HE40. The attachment and detachment of ions on the polymer chain and the surface of the nanoparticles can be observed through the vigorous twisting and rotation of the bands at 862 cm^{-1}, 1062 cm^{-1}, 2917 cm^{-1} and 2873 cm^{-1} that are responsible for asymmetric out-of-plane and in-plane of C–O–C pyrose ring stretching, asymmetric and symmetric stretching of –CH$_2$ and –CH$_3$, respectively. Nevertheless, the most abrupt change was highlighted by the increase in peak intensity at 1159 cm^{-1} (SO$_2$ symmetric stretching in CF$_3$SO$_3^-$) by 40.3 % compared

to HE40. The HY2 SPE was thermally stable and has good non-Faradaic process at the electrode/electrolyte interface. Thus, it achieved specific capacitance of 21.4 F/g at scan rate of 5 mV/s, R_{ct} value of 27.9 Ω, moderate discharge time (355.2 s) at current density of 30 mA/g and capacitance retention of 91.3 % over 3,000 cycles at 0.4 A/g.

As a conclusion, all the SPEs prepared were applicable for EDLC due to their improved results that are comparable with other works. It is worth to mention, that HC2 and HY2 SPEs are more suitable for EDLC due to their unique characteristic such as high specific capacitance and excellent cycling stability, respectively compared to HS2 cell.

6.2   Future Work

There is many room for improvement in this research work because it has the ability to mitigate the severe environmental problems caused by disposal of harmful materials by utilization of electronic gadgets. The proposed future works to improve the performance of biodegradable EDLC are:

a) Fabrication of magnesium battery using the HC2, HY2 and HS2 SPEs as an alternative to lithium ion batteries. This is due to magnesium metal is not reactive in air, easy to handle and it gives similar chemical and atomic size as lithium due to its diagonal position in the periodic table.

b) Prepare blend polymer of HEC and other polymer (either biodegradable or non-biodegradable) that is a good network for better entrapment of mobile carriers.

c) Synthesis and preparation of activated carbon from leaves, wood, fungi, etc. that contains high percentage of calcium as reported by Wang et al. (2014) for better diffusion of ions into the pore of the carbon electrode for better performance of EDLC.

REFERENCES

Abidi, N., Cabrales, L., & Haigler, C. H. (2014). Changes in the cell wall and cellulose content of developing cotton fibers investigated by FTIR spectroscopy. *Carbohydrate Polymers, 100*, 9-16.

Adebahr, J., Byrne, N., Forsyth, M., MacFarlane, D., & Jacobsson, P. (2003). Enhancement of ion dynamics in PMMA-based gels with addition of TiO_2 nano-particles. *Electrochimica Acta, 48*(14), 2099-2103.

Adhyapak, P., Maddanimath, T., Pethkar, S., Chandwadkar, A., Negi, Y., & Vijayamohanan, K. (2002). Application of electrochemically prepared carbon nanofibers in supercapacitors. *Journal of Power Sources, 109*(1), 105-110.

Aghazadeh, M., Hosseinifard, M., Peyrovi, M. H., & Sabour, B. (2013). Electrochemical preparation and characterization of brain-like nanostructures of Y_2O_3. *Journal of Rare Earths, 31*(3), 281-288.

Agrawal, R., & Pandey, G. (2008). Solid polymer electrolytes: Materials designing and all-solid-state battery applications: An overview. *Journal of Physics D: Applied Physics, 41*(22), 223001-223018.

Ali, A., Yahya, M., Bahron, H., Subban, R., Harun, M., & Atan, I. (2007). Impedance studies on plasticized PMMA-LiX [X: $CF_3SO_3^-$, $N(CF_3SO_2)_2-$] polymer electrolytes. *Materials Letters, 61*(10), 2026-2029.

AlKhatib, H. S., Aiedeh, K. M., Bustanji, Y., Hamed, S., Mohammad, M., AlKhalidi, B., & Najjar, S. (2008). Modulation of buspirone HCl release from hypromellose matrices using chitosan succinate: implications for pH-independent release. *European Journal of Pharmaceutics and Biopharmaceutics, 70*(3), 804-812.

Aoki, T., Ohta, T., & Fujinami, T. (2006). Lithium ion conductivity of gel polymer electrolytes containing insoluble lithium tetrakis (pentafluorobenzenethiolato) borate. *Journal of Power Sources, 156*(2), 589-593.

Armand, M., Endres, F., MacFarlane, D. R., Ohno, H., & Scrosati, B. (2009). Ionic-liquid materials for the electrochemical challenges of the future. *Nature Materials, 8*(8), 621-629.

Arof, A., Shuhaimi, N., Alias, N., Kufian, M., & Majid, S. (2010). Application of chitosan/iota-carrageenan polymer electrolytes in electrical double layer capacitor (EDLC). *Journal of Solid State Electrochemistry, 14*(12), 2145-2152.

Arulepp, M., Permann, L., Leis, J., Perkson, A., Rumma, K., Jänes, A., & Lust, E. (2004). Influence of the solvent properties on the characteristics of a double layer capacitor. *Journal of Power Sources, 133*(2), 320-328.

Asmara, S., Kufian, M., Majid, S., & Arof, A. (2011). Preparation and characterization of magnesium ion gel polymer electrolytes for application in electrical double layer capacitors. *Electrochimica Acta, 57*, 91-97.

Awadhia, A., Patel, S., & Agrawal, S. (2006). Dielectric investigations in PVA based gel electrolytes. *Progress in Crystal Growth and Characterization of Materials, 52*(1), 61-68.

Aygün, A., Yenisoy-Karakaş, S., & Duman, I. (2003). Production of granular activated carbon from fruit stones and nutshells and evaluation of their physical, chemical and adsorption properties. *Microporous and Mesoporous Materials, 66*(2), 189-195.

Aziz, S. B., & Abidin, Z. H. Z. (2013). Electrical conduction mechanism in solid polymer electrolytes: New concepts to arrhenius equation. *Journal of Soft Matter, 2013*, 1-8.

Baskaran, R., Selvasekarapandian, S., Kuwata, N., Kawamura, J., & Hattori, T. (2006). Conductivity and thermal studies of blend polymer electrolytes based on PVAc–PMMA. *Solid State Ionics, 177*(26), 2679-2682.

Belfer, S., Fainchtain, R., Purinson, Y., & Kedem, O. (2000). Surface characterization by FTIR-ATR spectroscopy of polyethersulfone membranes-unmodified, modified and protein fouled. *Journal of Membrane Science, 172*(1), 113-124.

Bittner, A., Zhu, M., Yang, Y., Waibel, H., Konuma, M., Starke, U., & Weber, C. (2012). Ageing of electrochemical double layer capacitors. *Journal of Power Sources, 203*, 262-273.

Bondarenko, O., Juganson, K., Ivask, A., Kasemets, K., Mortimer, M., & Kahru, A. (2013). Toxicity of Ag, CuO and ZnO nanoparticles to selected environmentally relevant test organisms and mammalian cells in vitro: A critical review. *Archives of Toxicology, 87*(7), 1181-1200.

Bose, S., Kuila, T., Mishra, A. K., Rajasekar, R., Kim, N. H., & Lee, J. H. (2012). Carbon-based nanostructured materials and their composites as supercapacitor electrodes. *Journal of Materials Chemistry, 22*(3), 767-784.

Burgaz, E. (2011). Poly(ethylene-oxide)/clay/silica nanocomposites: Morphology and thermomechanical properties. *Polymer, 52*(22), 5118-5126.

Calebrese, C., Hui, L., Schadler, L. S., & Nelson, J. K. (2011). A review on the importance of nanocomposite processing to enhance electrical insulation. *IEEE Transactions on Dielectrics and Electrical Insulation, 18*(4), 938-945.

Capiglia, C., Yang, J., Imanishi, N., Hirano, A., Takeda, Y., & Yamamoto, O. (2002). Composite polymer electrolyte: The role of filler grain size. *Solid State Ionics, 154*, 7-14.

Carnes, C. L., & Klabunde, K. J. (2003). The catalytic methanol synthesis over nanoparticle metal oxide catalysts. *Journal of Molecular Catalysis A: Chemical, 194*(1), 227-236.

Cespi, M., Bonacucina, G., Mencarelli, G., Casettari, L., & Palmieri, G. F. (2011). Dynamic mechanical thermal analysis of hypromellose 2910 free films. *European Journal of Pharmaceutics and Biopharmaceutics, 79*(2), 458-463.

Chandrasekaran, R., Soneda, Y., Yamashita, J., Kodama, M., & Hatori, H. (2008). Preparation and electrochemical performance of activated carbon thin films with polyethylene oxide-salt addition for electrochemical capacitor applications. *Journal of Solid State Electrochemistry, 12*(10), 1349-1355.

Chen, H.-H., Lin, C.-H., & Kang, H.-Y. (2009). Maturation effects in fish gelatin and HPMC composite gels. *Food Hydrocolloids, 23*(7), 1756-1761.

Chen, S., Zou, Y., Yan, Z., Shen, W., Shi, S., Zhang, X., & Wang, H. (2009). Carboxymethylated-bacterial cellulose for copper and lead ion removal. *Journal of Hazardous Materials, 161*(2), 1355-1359.

Cheng, Q., Pavlinek, V., Li, C., Lengalova, A., He, Y., & Saha, P. (2006). Synthesis and structural properties of polypyrrole/nano-Y_2O_3 conducting composite. *Applied Surface Science, 253*(4), 1736-1740.

Chong, M. Y., Liew, C.-W., Numan, A., Yugal, K., Ramesh, K., Ng, H., Chong, T., & Ramesh, S. (2016). Effects of ionic liquid on the hydroxylpropylmethyl cellulose (HPMC) solid polymer electrolyte. *Ionics*, 1-10.

Chung, C., Lee, M., & Choe, E. K. (2004). Characterization of cotton fabric scouring by FT-IR ATR spectroscopy. *Carbohydrate Polymers, 58*(4), 417-420.

Chung, S., Wang, Y., Persi, L., Croce, F., Greenbaum, S., Scrosati, B., & Plichta, E. (2001). Enhancement of ion transport in polymer electrolytes by addition of nanoscale inorganic oxides. *Journal of Power Sources, 97*, 644-648.

Chupp, J., Shellikeri, A., Palui, G., & Chatterjee, J. (2015). Chitosan‐based gel film electrolytes containing ionic liquid and lithium salt for energy storage applications. *Journal of Applied Polymer Science, 132*(26), 42143-42150.

Croce, F., Appetecchi, G., Persi, L., & Scrosati, B. (1998). Nanocomposite polymer electrolytes for lithium batteries. *Nature, 394*(6692), 456-458.

Croce, F., Curini, R., Martinelli, A., Persi, L., Ronci, F., Scrosati, B., & Caminiti, R. (1999). Physical and chemical properties of nanocomposite polymer electrolytes. *The Journal of Physical Chemistry B, 103*(48), 10632-10638.

Croce, F., Settimi, L., & Scrosati, B. (2006). Superacid ZrO_2-added, composite polymer electrolytes with improved transport properties. *Electrochemistry Communications, 8*(2), 364-368.

D' Arcy Research Lab. Retrieved February 20, 2017, from https://pages.wustl.edu/darcylab/research.

Dasari, M., Rao, K. S., Krishna, P. M., & Krishna, G. G. (2011). Barium strontium bismuth niobate layered perovskites: Dielectric, impedance and electrical modulus characteristics. *Acta Physica Polonica A, 119*(3), 387-394.

Deyab, M. (2015). Hydroxyethyl cellulose as efficient organic inhibitor of zinc–carbon battery corrosion in ammonium chloride solution: Electrochemical and surface morphology studies. *Journal of Power Sources, 280*, 190-194.

El-Kady, M. F., Strong, V., Dubin, S., & Kaner, R. B. (2012). Laser scribing of high-performance and flexible graphene-based electrochemical capacitors. *Science, 335*(6074), 1326-1330.

El-Trass, A., ElShamy, H., El-Mehasseb, I., & El-Kemary, M. (2012). CuO nanoparticles: Synthesis, characterization, optical properties and interaction with amino acids. *Applied Surface Science, 258*(7), 2997-3001.

Fan, L.-Q., Zhong, J., Wu, J.-H., Lin, J.-M., & Huang, Y.-F. (2014). Improving the energy density of quasi-solid-state electric double-layer capacitors by introducing redox additives into gel polymer electrolytes. *Journal of Materials Chemistry A, 2*(24), 9011-9014.

Fattah, N., Ng, H., Mahipal, Y., Numan, A., Ramesh, S., & Ramesh, K. (2016). An approach to solid-state electrical double layer capacitors fabricated with graphene oxide-doped ionic liquid-based solid copolymer electrolytes. *Materials, 9*(6), 450-464.

Feng, W., Sun, L.-D., Zhang, Y.-W., & Yan, C.-H. (2010). Synthesis and assembly of rare earth nanostructures directed by the principle of coordination chemistry in solution-based process. *Coordination Chemistry Reviews, 254*(9), 1038-1053.

Feuillade, G., & Perche, P. (1975). Ion-conductive macromolecular gels and membranes for solid lithium cells. *Journal of Applied Electrochemistry, 5*(1), 63-69.

Frackowiak, E., & Beguin, F. (2001). Carbon materials for the electrochemical storage of energy in capacitors. *Carbon, 39*(6), 937-950.

Frietsch, M., Zudock, F., Goschnick, J., & Bruns, M. (2000). CuO catalytic membrane as selectivity trimmer for metal oxide gas sensors. *Sensors and Actuators B: Chemical, 65*(1), 379-381.

Ghosh, A., & Lee, Y. H. (2012). Carbon‐based electrochemical capacitors. *ChemSusChem, 5*(3), 480-499.

Goodwin, D., Picout, D., Ross-Murphy, S., Holland, S., Martini, L., & Lawrence, M. (2011). Ultrasonic degradation for molecular weight reduction of pharmaceutical cellulose ethers. *Carbohydrate Polymers, 83*(2), 843-851.

Gray, F. (1997). *Polymer Electrolytes*. RSC Materials Monographs, Cambridge. Royal Society Chemistry.

Gray, F. M., MacCallum, J. R., & Vincent, C. A. (1986). Poly (ethylene oxide)-LiCF$_3$SO$_3$-polystyrene electrolyte systems. *Solid State Ionics, 18*, 282-286.

Gryglewicz, G., Machnikowski, J., Lorenc-Grabowska, E., Lota, G., & Frackowiak, E. (2005). Effect of pore size distribution of coal-based activated carbons on double layer capacitance. *Electrochimica Acta, 50*(5), 1197-1206.

Gupta, M. K., Tseng, Y.-C., Goldman, D., & Bogner, R. H. (2002). Hydrogen bonding with adsorbent during storage governs drug dissolution from solid-dispersion granules. *Pharmaceutical Research, 19*(11), 1663-1672.

Hager, A.-S., & Arendt, E. K. (2013). Influence of hydroxypropylmethylcellulose (HPMC), xanthan gum and their combination on loaf specific volume, crumb hardness and crumb grain characteristics of gluten-free breads based on rice, maize, teff and buckwheat. *Food Hydrocolloids, 32*(1), 195-203.

Hall, P. J., Mirzaeian, M., Fletcher, S. I., Sillars, F. B., Rennie, A. J., Shitta-Bey, G. O., Wilson, G., Cruden, Andrew., & Carter, R. (2010). Energy storage in electrochemical capacitors: Designing functional materials to improve performance. *Energy & Environmental Science, 3*(9), 1238-1251.

Hallinan Jr, D. T., & Balsara, N. P. (2013). Polymer electrolytes. *Annual Review of Materials Research, 43*, 503-525.

Heacock, M., Kelly, C. B., & Suk, W. A. (2016). E-waste: The growing global problem and next steps. *Reviews on Environmental Health, 31*(1), 131-135.

Heimer, N. E., Del Sesto, R. E., Meng, Z., Wilkes, J. S., & Carper, W. R. (2006). Vibrational spectra of imidazolium tetrafluoroborate ionic liquids. *Journal of Molecular Liquids, 124*(1), 84-95.

Herat, S., & Agamuthu, P. (2012). E-waste: a problem or an opportunity? Review of issues, challenges and solutions in Asian countries. *Waste Management & Research, 30*(11), 1113-1129.

Hu, J. S., Ren, L. L., Guo, Y. G., Liang, H. P., Cao, A. M., Wan, L. J., & Bai, C. L. (2005). Mass production and high photocatalytic activity of ZnS nanoporous nanoparticles. *Angewandte Chemie, 117*(8), 1295-1299.

Huang, C. W., Wu, C. A., Hou, S. S., Kuo, P. L., Hsieh, C. T., & Teng, H. (2012). Gel electrolyte derived from poly(ethylene glycol) blending poly(acrylonitrile) applicable to roll‑to‑roll assembly of electric double layer capacitors. *Advanced Functional Materials, 22*(22), 4677-4685.

Huang, Y.-D., Gao, X.-D., Gu, Z.-Y., & Li, X.-M. (2016). Amino-terminated SiO_2 aerogel towards highly-effective lead (II) adsorbent via the ambient drying process. *Journal of Non-Crystalline Solids, 443*, 39-46.

Huang, Y.-F., Wu, P.-F., Zhang, M.-Q., Ruan, W.-H., & Giannelis, E. P. (2014). Boron cross-linked graphene oxide/polyvinyl alcohol nanocomposite gel electrolyte for flexible solid-state electric double layer capacitor with high performance. *Electrochimica Acta, 132*, 103-111.

Hyperphysics, Department of Physics and Astronomy, Georgia State University. Retrieved from February 20, 2017 from http://hyperphysics.phy-astr.gsu.edu/hbase/quantum/bragg.html

Idris, N. H., Rahman, M. M., Wang, J.-Z., & Liu, H.-K. (2012). Microporous gel polymer electrolytes for lithium rechargeable battery application. *Journal of Power Sources, 201*, 294-300.

Inagaki, M., Konno, H., & Tanaike, O. (2010). Carbon materials for electrochemical capacitors. *Journal of Power Sources, 195*(24), 7880-7903.

Ingle, A. P., Duran, N., & Rai, M. (2014). Bioactivity, mechanism of action, and cytotoxicity of copper-based nanoparticles: A review. *Applied Microbiology and Biotechnology, 98*(3), 1001-1009.

Jayalakshmi, M., & Balasubramanian, K. (2008). Simple capacitors to supercapacitors-An overview. *International Journal of Electrochemical Science, 3*(11), 1196-1217.

Jia, G., Zheng, Y., Liu, K., Song, Y., You, H., & Zhang, H. (2008). Facile surfactant-and template-free synthesis and luminescent properties of one-dimensional Lu_2O_3: Eu^{3+} phosphors. *The Journal of Physical Chemistry C, 113*(1), 153-158.

Jian-hua, T., Peng-fei, G., Zhi-yuan, Z., Wen-hui, L., & Zhong-qiang, S. (2008). Preparation and performance evaluation of a Nafion-TiO_2 composite membrane for PEMFCs. *International Journal of Hydrogen Energy, 33*(20), 5686-5690.

Jiang, M., Zhu, J., Chen, C., Lu, Y., Ge, Y., & Zhang, X. (2016). Poly(vinyl alcohol) borate gel polymer electrolytes prepared by electrodeposition and their application in electrochemical supercapacitors. *ACS Applied Materials & Interfaces, 8*(5), 3473-3481.

Jiménez, A., Fabra, M., Talens, P., & Chiralt, A. (2010). Effect of lipid self-association on the microstructure and physical properties of hydroxypropyl-methylcellulose edible films containing fatty acids. *Carbohydrate Polymers, 82*(3), 585-593.

Johan, M. R., Shy, O. H., Ibrahim, S., Yassin, S. M. M., & Hui, T. Y. (2011). Effects of Al_2O_3 nanofiller and EC plasticizer on the ionic conductivity enhancement of solid PEO–$LiCF_3SO_3$ solid polymer electrolyte. *Solid State Ionics, 196*(1), 41-47.

Juying, T., Qiang, G., Xiaolin, T., Xia, L., Dan, L., & Yunfeng, D. (2011). Characterization of SPEEK/Y_2O_3 proton exchange membrane treated with high magnetic field. *Journal of Rare Earths, 29*(6), 604-608.

Kadir, M., & Arof, A. (2011). Application of PVA–chitosan blend polymer electrolyte membrane in electrical double layer capacitor. *Materials Research Innovations, 15*(sup2), s217-s220.

Karan, N., Pradhan, D., Thomas, R., Natesan, B., & Katiyar, R. (2008). Solid polymer electrolytes based on polyethylene oxide and lithium trifluoromethane sulfonate (PEO–$LiCF_3SO_3$): Ionic conductivity and dielectric relaxation. *Solid State Ionics, 179*(19), 689-696.

Ketabi, S., & Lian, K. (2013). Effect of SiO_2 on conductivity and structural properties of PEO–$EMIHSO_4$ polymer electrolyte and enabled solid electrochemical capacitors. *Electrochimica Acta, 103*, 174-178.

Kido, R., Ueno, K., Iwata, K., Kitazawa, Y., Imaizumi, S., Mandai, T., Dokko, Kaoru & Watanabe, M. (2015). Li^+ ion transport in polymer electrolytes based on a glyme-Li salt solvate ionic liquid. *Electrochimica Acta, 175*, 5-12.

Kiefer, J., Fries, J., & Leipertz, A. (2007). Experimental vibrational study of imidazolium-based ionic liquids: Raman and infrared spectra of 1-ethyl-3-methylimidazolium

bis(trifluoromethylsulfonyl) imide and 1-ethyl-3-methylimidazolium ethylsulfate. *Applied Spectroscopy, 61*(12), 1306-1311.

Kim, D. J., Jo, M. J., & Nam, S. Y. (2015). A review of polymer–nanocomposite electrolyte membranes for fuel cell application. *Journal of Industrial and Engineering Chemistry, 21*, 36-52.

Kim, H.-S., Kum, K.-S., Cho, W.-I., Cho, B.-W., & Rhee, H.-W. (2003). Electrochemical and physical properties of composite polymer electrolyte of poly (methyl methacrylate) and poly (ethylene glycol diacrylate). *Journal of Power Sources, 124*(1), 221-224.

Kim, J.-K., Cheruvally, G., Li, X., Ahn, J.-H., Kim, K.-W., & Ahn, H.-J. (2008). Preparation and electrochemical characterization of electrospun, microporous membrane-based composite polymer electrolytes for lithium batteries. *Journal of Power Sources, 178*(2), 815-820.

Kim, K. M., Park, N.-G., Ryu, K. S., & Chang, S. H. (2002). Characterization of poly (vinylidenefluoride-co-hexafluoropropylene)-based polymer electrolyte filled with TiO_2 nanoparticles. *Polymer, 43*(14), 3951-3957.

Klongkan, S., & Pumchusak, J. (2015). Effects of nano alumina and plasticizers on morphology, ionic conductivity, thermal and mechanical properties of PEO-$LiCF_3SO_3$ solid polymer electrolyte. *Electrochimica Acta, 161*, 171-176.

Kötz, R., & Carlen, M. (2000). Principles and applications of electrochemical capacitors. *Electrochimica Acta, 45*(15), 2483-2498.

Krawiec, W., Scanlon, L., Fellner, J., Vaia, R., Vasudevan, S., & Giannelis, E. (1995). Polymer nanocomposites: A new strategy for synthesizing solid electrolytes for rechargeable lithium batteries. *Journal of Power Sources, 54*(2), 310-315.

Kuilla, T., Bhadra, S., Yao, D., Kim, N. H., Bose, S., & Lee, J. H. (2010). Recent advances in graphene based polymer composites. *Progress in Polymer Science, 35*(11), 1350-1375.

Kumar, B., & Rodrigues, S. J. (2001). Poly(ethylene oxide)-based composite electrolytes: Crystalline ⇌ amorphous transition. *Journal of The Electrochemical Society, 148*(12), A1336-A1340.

Kumar, M. S., & Bhat, D. K. (2009a). $LiClO_4$‐doped plasticized chitosan as biodegradable polymer gel electrolyte for supercapacitors. *Journal of Applied Polymer Science, 114*(4), 2445-2454.

Kumar, M. S., & Bhat, D. K. (2009b). Polyvinyl alcohol–polystyrene sulphonic acid blend electrolyte for supercapacitor application. *Physica B: Condensed Matter, 404*(8), 1143-1147.

Kumar, Y., Pandey, G., & Hashmi, S. (2012). Gel polymer electrolyte based electrical double layer capacitors: comparative study with multiwalled carbon nanotubes and activated carbon electrodes. *The Journal of Physical Chemistry C, 116*(50), 26118-26127.

157

Langjahr, P. A., Oberacker, R., & Hoffmann, M. J. (2001). Long‑term behavior and application limits of plasma‑sprayed zirconia thermal barrier coatings. *Journal of the American Ceramic Society, 84*(6), 1301-1308.

Latifatu, M., Kim, K. M., Kim, Y. J., & Ko, J. M. (2012). Electrochemical properties of activated carbon capacitor adopting a proton-conducting hydrogel polymer electrolyte. *Elastomers and Composites, 47*(4), 292-296.

Łatoszyńska, A. A., Żukowska, G. Z., Rutkowska, I. A., Taberna, P.-L., Simon, P., Kulesza, P. J., & Wieczorek, W. (2015). Non-aqueous gel polymer electrolyte with phosphoric acid ester and its application for quasi solid-state supercapacitors. *Journal of Power Sources, 274*, 1147-1154.

Lewandowska, K. (2009). Miscibility and thermal stability of poly(vinyl alcohol)/ chitosan mixtures. *Thermochimica Acta, 493*(1), 42-48.

Li, F., Wang, W., Wang, X., & Yu, J. (2014). Changes of structure and property of alkali soluble hydroxyethyl celluloses (HECs) and their regenerated films with the molar substitution. *Carbohydrate Polymers, 114*, 206-212.

Li, X., Wang, G., Wang, X., Li, X., & Ji, J. (2013). Flexible supercapacitor based on MnO_2 nanoparticles via electrospinning. *Journal of Materials Chemistry A, 1*(35), 10103-10106.

Liew, C.-W., & Ramesh, S. (2014). Comparing triflate and hexafluorophosphate anions of ionic liquids in polymer electrolytes for supercapacitor applications. *Materials, 7*(5), 4019-4033.

Liew, C.-W., & Ramesh, S. (2015). Electrical, structural, thermal and electrochemical properties of corn starch-based biopolymer electrolytes. *Carbohydrate Polymers, 124*, 222-228.

Liew, C.-W., Ramesh, S., & Arof, A. (2014). Good prospect of ionic liquid based-poly (vinyl alcohol) polymer electrolytes for supercapacitors with excellent electrical, electrochemical and thermal properties. *International Journal of Hydrogen Energy, 39*(6), 2953-2963.

Liew, C.-W., Ramesh, S., & Arof, A. (2015). Characterization of ionic liquid added poly (vinyl alcohol)-based proton conducting polymer electrolytes and electrochemical studies on the supercapacitors. *International Journal of Hydrogen Energy, 40*(1), 852-862.

Liew, C.-W., Ramesh, S., & Arof, A. (2016). Investigation of ionic liquid-doped ion conducting polymer electrolytes for carbon-based electric double layer capacitors (EDLCs). *Materials & Design, 92*, 829-835.

Lim, C.-S., Teoh, K., Liew, C.-W., & Ramesh, S. (2014a). Capacitive behavior studies on electrical double layer capacitor using poly(vinyl alcohol)–lithium perchlorate based polymer electrolyte incorporated with TiO_2. *Materials Chemistry and Physics, 143*(2), 661-667.

Lim, C.-S., Teoh, K., Liew, C.-W., & Ramesh, S. (2014b). Electric double layer capacitor based on activated carbon electrode and biodegradable composite polymer electrolyte. *Ionics, 20*(2), 251-258.

Liu, R., Cho, S. I., & Lee, S. B. (2008). Poly(3, 4-ethylenedioxythiophene) nanotubes as electrode materials for a high-powered supercapacitor. *Nanotechnology, 19*(21), 215710.

Liu, X., Yu, L., Liu, H., Chen, L., & Li, L. (2008). In situ thermal decomposition of starch with constant moisture in a sealed system. *Polymer Degradation and Stability, 93*(1), 260-262.

Lokman, A., Arof, H., & Harun, S. (2015). Tapered fiber coated with hydroxyethyl cellulose/polyvinylidene fluoride composite for relative humidity sensor. *Sensors and Actuators A: Physical, 225*, 128-132.

Luo, G., Huang, H., Lei, C., Cheng, Z., Wu, X., Tang, S., & Du, Y. (2016). Facile synthesis of porous graphene as binder-free electrode for supercapacitor application. *Applied Surface Science, 366*, 46-52.

Ma, Y., Li, L., Gao, G., Yang, X., You, J., & Yang, P. (2016). Ionic conductivity enhancement in gel polymer electrolyte membrane with N-methyl-N-butyl-piperidine-bis (trifluoromethylsulfonyl) imide ionic liquid for lithium ion battery. *Colloids and Surfaces A: Physicochemical and Engineering Aspects, 502*, 130-138.

Malathi, J., Kumaravadivel, M., Brahmanandhan, G., Hema, M., Baskaran, R., & Selvasekarapandian, S. (2010). Structural, thermal and electrical properties of PVA–LiCF$_3$SO$_3$ polymer electrolyte. *Journal of Non-Crystalline Solids, 356*(43), 2277-2281.

Masuda, S. N., Masuko, N., & Mochizuki, T. (1986). Study of rapidly quenched Al–Ti alloys for electrolytic capacitor electrodes. *Keikinzoku/Journal of the Japan Institute of Light Metals, 36*(10), 633-639.

Matsui, I. (2005). Nanoparticles for electronic device applications: A brief review. *Journal of Chemical Engineering of Japan, 38*(8), 535-546.

Mayo, F. R., & Walling, C. (1950). Copolymerization. *Chemical Reviews, 46*(2), 191-287.

Merget, R., Bauer, T., Küpper, H., Philippou, S., Bauer, H., Breitstadt, R., & Bruening, T. (2002). Health hazards due to the inhalation of amorphous silica. *Archives of Toxicology, 75*(11-12), 625-634.

Miller, J. (2007). A Brief History of Supercapacitors. Battery and Energy Storage Technology. *History of Technology Series Autumn*. 61-70

Mishra, K., Hashmi, S., & Rai, D. (2013). Nanocomposite blend gel polymer electrolyte for proton battery application. *Journal of Solid State Electrochemistry, 17*(3), 785-793.

Mishra, R., & Rao, K. (1998). Electrical conductivity studies of poly(ethyleneoxide)-poly (vinylalcohol) blends. *Solid State Ionics, 106*(1), 113-127.

Mollart, T., & Lewis, K. (2001). Transition metal oxide anti-reflection coatings for airborne diamond optics. *Diamond and Related Materials, 10*(3), 536-541.

Monta, M., & Matsuda, Y. (1996). Ethylene carbonate-based organic electrolytes for high performance aluminium electrolytic capacitors. *Journal of Power Sources, 60*(2), 179-183.

Moon, W. G., Kim, G.-P., Lee, M., Song, H. D., & Yi, J. (2015). A biodegradable gel electrolyte for use in high-performance flexible supercapacitors. *ACS Applied Materials & Interfaces, 7*(6), 3503-3511.

Morita, M., Fujisaki, T., Yoshimoto, N., & Ishikawa, M. (2001). Ionic conductance behavior of polymeric composite solid electrolytes containing lithium aluminate. *Electrochimica Acta, 46*(10), 1565-1569.

Mukerabigwi, J. F., Lei, S., Fan, L., Wang, H., Luo, S., Ma, X., Qin, J., Huang, X., & Cao, Y. (2016). Eco-friendly nano-hybrid superabsorbent composite from hydroxyethyl cellulose and diatomite. *RSC Advances, 6*(38), 31607-31618.

Murata, K., Izuchi, S., & Yoshihisa, Y. (2000). An overview of the research and development of solid polymer electrolyte batteries. *Electrochimica Acta, 45*(8), 1501-1508.

Mysyk, R., Raymundo-Pinero, E., & Béguin, F. (2009). Saturation of subnanometer pores in an electric double-layer capacitor. *Electrochemistry Communications, 11*(3), 554-556.

Nagata, I. (1983). *Aluminum Dry Electrolytic Capacitors*. Japan Capacitor Industry, Tokyo.

Namisnyk, A. M. (2003). *A survey of electrochemical supercapacitor technology.* Australian Universities Power Engineering Conference. University of Canterbury, New Zealand, 1-6.

Nawaz, A., Sharif, R., Rhee, H.-W., & Singh, P. K. (2016). Efficient dye sensitized solar cell and supercapacitor using 1-ethyl 3-methyl imidazolium dicyanamide incorporated PVDF–HFP polymer matrix. *Journal of Industrial and Engineering Chemistry, 33*, 381-384.

Ng, L. Y., Mohammad, A. W., Leo, C. P., & Hilal, N. (2013). Polymeric membranes incorporated with metal/metal oxide nanoparticles: A comprehensive review. *Desalination, 308*, 15-33.

Ngah, W. W., Teong, L., & Hanafiah, M. (2011). Adsorption of dyes and heavy metal ions by chitosan composites: A review. *Carbohydrate Polymers, 83*(4), 1446-1456.

Nicotera, I., Coppola, L., Oliviero, C., Castriota, M., & Cazzanelli, E. (2006). Investigation of ionic conduction and mechanical properties of PMMA–PVdF blend-based polymer electrolytes. *Solid State Ionics, 177*(5), 581-588.

Nishino, A. (1996). Capacitors: Operating principles, current market and technical trends. *Journal of Power Sources, 60*(2), 137-147.

Nithya, V., & Arul, N. S. (2016). Progress and development of Fe_3O_4 electrodes for supercapacitors. *Journal of Materials Chemistry A, 4*(28), 10767-10778.

Nnorom, I. C., & Osibanjo, O. (2009). Toxicity characterization of waste mobile phone plastics. *Journal of Hazardous Materials, 161*(1), 183-188.

Orlins, S., & Guan, D. (2016). China's toxic informal e-waste recycling: Local approaches to a global environmental problem. *Journal of Cleaner Production, 114*, 71-80.

Osada, I., de Vries, H., Scrosati, B., & Passerini, S. (2016). Ionic‐liquid‐based polymer electrolytes for battery applications. *Angewandte Chemie International Edition, 55*(2), 500-513.

Osińska, M., Walkowiak, M., Zalewska, A., & Jesionowski, T. (2009). Study of the role of ceramic filler in composite gel electrolytes based on microporous polymer membranes. *Journal of Membrane Science, 326*(2), 582-588.

Osman, Z., Ghazali, M. M., Othman, L., & Isa, K. M. (2012). AC ionic conductivity and DC polarization method of lithium ion transport in $PMMA–LiBF_4$ gel polymer electrolytes. *Results in Physics, 2*, 1-4.

Pandey, G., & Hashmi, S. (2009). Experimental investigations of an ionic-liquid-based, magnesium ion conducting, polymer gel electrolyte. *Journal of Power Sources, 187*(2), 627-634.

Pandey, G., & Hashmi, S. (2013a). Ionic liquid 1-ethyl-3-methylimidazolium tetracyanoborate-based gel polymer electrolyte for electrochemical capacitors. *Journal of Materials Chemistry A, 1*(10), 3372-3378.

Pandey, G., & Hashmi, S. (2013b). Performance of solid-state supercapacitors with ionic liquid 1-ethyl-3-methylimidazolium tris (pentafluoroethyl) trifluorophosphate based gel polymer electrolyte and modified MWCNT electrodes. *Electrochimica Acta, 105*, 333-341.

Pandey, G., Hashmi, S., & Agrawal, R. (2008). Hot-press synthesized polyethylene oxide based proton conducting nanocomposite polymer electrolyte dispersed with SiO_2 nanoparticles. *Solid State Ionics, 179*(15), 543-549.

Pandey, G., Hashmi, S., & Kumar, Y. (2010a). Multiwalled carbon nanotube electrodes for electrical double layer capacitors with ionic liquid based gel polymer electrolytes. *Journal of The Electrochemical Society, 157*(1), A105-A114.

Pandey, G., Hashmi, S., & Kumar, Y. (2010b). Performance studies of activated charcoal based electrical double layer capacitors with ionic liquid gel polymer electrolytes. *Energy & Fuels, 24*(12), 6644-6652.

Pandey, G., Kumar, Y., & Hashmi, S. (2011). Ionic liquid incorporated PEO based polymer electrolyte for electrical double layer capacitors: A comparative study with lithium and magnesium systems. *Solid State Ionics, 190*(1), 93-98.

Pandey, K., Dwivedi, M. M., Singh, M., & Agrawal, S. (2010). Studies of dielectric relaxation and ac conductivity in [(100− x)PEO+ xNH₄SCN]: Al-Zn ferrite nano composite polymer electrolyte. *Journal of Polymer Research, 17*(1), 127-133.

Pandolfo, A., & Hollenkamp, A. (2006). Carbon properties and their role in supercapacitors. *Journal of Power Sources, 157*(1), 11-27.

Pani, N. R., & Nath, L. K. (2014). Development of controlled release tablet by optimizing HPMC: Consideration of theoretical release and RSM. *Carbohydrate Polymers, 104*, 238-245.

Parameswaranpillai, J., Thomas, S., & Grohens, Y. (2014). Polymer Blends: State of the Art, New Challenges, and Opportunities. *Characterization of Polymer Blends: Miscibility, Morphology and Interfaces*, 1-6. Wiley, Germany.

Park, J.-W., Ueno, K., Tachikawa, N., Dokko, K., & Watanabe, M. (2013). Ionic liquid electrolytes for lithium–sulfur batteries. *The Journal of Physical Chemistry C, 117*(40), 20531-20541.

Park, S.-S., & Lee, B.-T. (2004). Anodizing properties of high dielectric oxide films coated on aluminum by sol-gel method. *Journal of Electroceramics, 13*(1-3), 111-116.

Patel, D. D., & Lee, J. M. (2012). Applications of ionic liquids. *The Chemical Record, 12*(3), 329-355.

Pawlicka, A., Sabadini, A. C., Raphael, E., & Dragunski, D. C. (2008). Ionic conductivity thermogravimetry measurements of starch-based polymeric electrolytes. *Molecular Crystals and Liquid Crystals, 485*(1), 804-816.

Pell, W. G., & Conway, B. E. (2004). Peculiarities and requirements of asymmetric capacitor devices based on combination of capacitor and battery-type electrodes. *Journal of Power Sources, 136*(2), 334-345.

Peng, C., Zhang, S., Jewell, D., & Chen, G. Z. (2008). Carbon nanotube and conducting polymer composites for supercapacitors. *Progress in Natural Science, 18*(7), 777-788.

Qu, D., & Shi, H. (1998). Studies of activated carbons used in double-layer capacitors. *Journal of Power Sources, 74*(1), 99-107.

Quartarone, E., & Mustarelli, P. (2011). Electrolytes for solid-state lithium rechargeable batteries: recent advances and perspectives. *Chemical Society Reviews, 40*(5), 2525-2540.

Raghavan, P., Zhao, X., Shin, C., Baek, D.-H., Choi, J.-W., Manuel, J., Heo, M., Ahn, J., & Nah, C. (2010). Preparation and electrochemical characterization of polymer electrolytes based on electrospun poly(vinylidene fluoride-co-hexafluoroprop-

ylene)/polyacrylonitrile blend/composite membranes for lithium batteries. *Journal of Power Sources, 195*(18), 6088-6094.

Rahman, I. A., & Padavettan, V. (2012). Synthesis of silica nanoparticles by sol-gel: Size-dependent properties, surface modification, and applications in silica-polymer nanocomposites—A review. *Journal of Nanomaterials, 2012*, 1-15.

Rajendran, S., Babu, R. S., & Sivakumar, P. (2007). Effect of salt concentration on poly(vinyl chloride)/poly(acrylonitrile) based hybrid polymer electrolytes. *Journal of Power Sources, 170*(2), 460-464.

Ramana, K. V., & Singh, S. (1988). Raman spectral studies on solutions of lithium bromide in binary mixtures of water and acetonitrile in the C-H and C-N stretching regions. *Spectrochimica Acta Part A: Molecular Spectroscopy, 44*(3), 277-282.

Ramesh, S., & Arof, A. (2001). Ionic conductivity studies of plasticized poly(vinyl chloride) polymer electrolytes. *Materials Science and Engineering: B, 85*(1), 11-15.

Ramesh, S., Leen, K. H., Kumutha, K., & Arof, A. (2007). FTIR studies of PVC/PMMA blend based polymer electrolytes. *Spectrochimica Acta Part A: Molecular and Biomolecular Spectroscopy, 66*(4), 1237-1242.

Ramesh, S., & Liew, C.-W. (2012). Exploration on nano-composite fumed silica-based composite polymer electrolytes with doping of ionic liquid. *Journal of Non-Crystalline Solids, 358*(5), 931-940.

Ramesh, S., & Ling, O. P. (2010). Effect of ethylene carbonate on the ionic conduction in poly(vinylidenefluoride-hexafluoropropylene) based solid polymer electrolytes. *Polymer Chemistry, 1*(5), 702-707.

Ramesh, S., & Lu, S. C. (2012). Enhancement of ionic conductivity and structural properties by 1‐butyl‐3‐methylimidazolium trifluoromethanesulfonate ionic liquid in poly(vinylidene fluoride–hexafluoropropylene)‐based polymer electrolytes. *Journal of Applied Polymer Science, 126*(S2), E484-E492.

Ramesh, S., Ramesh, K., & Arof, A. (2013). Fumed silica-doped poly(vinyl chloride)-poly(ethylene oxide)(PVC/PEO)-based polymer electrolyte for lithium ion battery. *International Journal Electrochemistry Science, 8*, 8348-8355.

Ramesh, S., Shanti, R., & Morris, E. (2012). Discussion on the influence of DES content in CA-based polymer electrolytes. *Journal of Materials Science, 47*(4), 1787-1793.

Ramesh, S., Shanti, R., & Morris, E. (2013). Characterization of conducting cellulose acetate based polymer electrolytes doped with "green" ionic mixture. *Carbohydrate Polymers, 91*(1), 14-21.

Ramesh, S., Winie, T., & Arof, A. (2007). Investigation of mechanical properties of polyvinyl chloride–polyethylene oxide (PVC–PEO) based polymer electrolytes for lithium polymer cells. *European Polymer Journal, 43*(5), 1963-1968.

Ramya, C., Selvasekarapandian, S., Hirankumar, G., Savitha, T., & Angelo, P. (2008). Investigation on dielectric relaxations of PVP–NH$_4$SCN polymer electrolyte. *Journal of Non-Crystalline Solids, 354*(14), 1494-1502.

Ravi, M., Pavani, Y., Kumar, K. K., Bhavani, S., Sharma, A., & Rao, V. N. (2011). Studies on electrical and dielectric properties of PVP: KBrO$_4$ complexed polymer electrolyte films. *Materials Chemistry and Physics, 130*(1), 442-448.

Ren, J., Bai, W., Guan, G., Zhang, Y., & Peng, H. (2013). Flexible and weaveable capacitor wire based on a carbon nanocomposite fiber. *Advanced Materials, 25*(41), 5965-5970.

Research and Development Indian Institute of Technology Kanpur. Retrieved from February 20, 2017 from http://www.iitk.ac.in/dordold/index.php?option=com_content&view=categorylayout=blog&id=221&Itemid=240)

Ring, W., Mita, I., Jenkins, A., & Bikales, N. (1985). Source-based nomenclature for copolymers (Recommendations 1985). *Pure and Applied Chemistry, 57*(10), 1427-1440.

Rodríguez, J., Navarrete, E., Dalchiele, E. A., Sánchez, L., Ramos-Barrado, J. R., & Martín, F. (2013). Polyvinylpyrrolidone–LiClO$_4$ solid polymer electrolyte and its application in transparent thin film supercapacitors. *Journal of Power Sources, 237*, 270-276.

Rozali, M., Samsudin, A., & Isa, M. (2012). Ion conducting mechanism of carboxy methylcellulose doped with ionic dopant salicylic acid based solid polymer electrolytes. *International Journal of Applied Science and Technology, 2*(4), 113-121.

Sa'adun, N. N., Subramaniam, R., & Kasi, R. (2014). Development and characterization of poly(1-vinylpyrrolidone-co-vinyl acetate) copolymer based polymer electrolytes. *The Scientific World Journal, 2014,* 1-7.

Sakabe, Y. (1997). Multilayer ceramic capacitors. *Current Opinion in Solid State and Materials Science, 2*(5), 584-587.

Salleh, N., Aziz, S. B., Aspanut, Z., & Kadir, M. (2016). Electrical impedance and conduction mechanism analysis of biopolymer electrolytes based on methyl cellulose doped with ammonium iodide. *Ionics*, 1-11.

Saroj, A., Singh, R., & Chandra, S. (2014). Thermal, vibrational, and dielectric studies on PVP/LiBF$_4$ + ionic liquid [EMIM][BF$_4$]-based polymer electrolyte films. *Journal of Physics and Chemistry of Solids, 75*(7), 849-857.

Satyamurthy, P., & Vigneshwaran, N. (2013). A novel process for synthesis of spherical nanocellulose by controlled hydrolysis of microcrystalline cellulose using anaerobic microbial consortium. *Enzyme and Microbial Technology, 52*(1), 20-25.

Sau, T. K., Rogach, A. L., Jäckel, F., Klar, T. A., & Feldmann, J. (2010). Properties and applications of colloidal nonspherical noble metal nanoparticles. *Advanced Materials, 22*(16), 1805-1825.

Schneuwly, A., & Gallay, R. (2000). *Properties and applications of supercapacitors: From the state-of-the-art to future trends*. Proceedings PCIM 2000, Rossens, Switzerland.

Scrosati, B. (1993). *Applications of electroactive polymers (Vol. 75)*: Springer, Netherlands.

Selvakumar, M., & Bhat, D. K. (2008). $LiClO_4$ doped cellulose acetate as biodegradable polymer electrolyte for supercapacitors. *Journal of Applied Polymer Science, 110*(1), 594-602.

Seo, D. M., Borodin, O., Balogh, D., O'Connell, M., Ly, Q., Han, S.-D., Passerini, S., & Henderson, W. A. (2013). Electrolyte solvation and ionic association III. Acetonitrile-lithium salt mixtures–transport properties. *Journal of The Electrochemical Society, 160*(8), A1061-A1070.

Seyedlar, R. M., Nodehi, A., Atai, M., & Imani, M. (2014). Gelation behavior of in situ forming gels based on HPMC and biphasic calcium phosphate nanoparticles. *Carbohydrate Polymers, 99*, 257-263.

Sharma, P., & Bhatti, T. (2010). A review on electrochemical double-layer capacitors. *Energy Conversion and Management, 51*(12), 2901-2912.

Shin, J., & Passerini, S. (2004). PEO $LiN(SO_2CF_2CF_3)_2$ Polymer electrolytes V. effect of fillers on ionic transport properties. *Journal of The Electrochemical Society, 151*(2), A238-A245.

Shon, B.-y., Hong, T.-W., & Jung, M. (2012). Hydrogen permeation of Y_2O_3–CuO–CeO_2/Ni composite membrane. *Solid State Ionics, 225*, 695-698.

Shuhaimi, N., Alias, N., Majid, S., & Arof, A. (2008). Electrical double layer capacitor with proton conducting κ-carrageenan–chitosan electrolytes. *Functional Materials Letters, 1*(03), 195-201.

Shuhaimi, N., Teo, L., Woo, H., Majid, S., & Arof, A. (2012). Electrical double-layer capacitors with plasticized polymer electrolyte based on methyl cellulose. *Polymer Bulletin, 69*(7), 807-826.

Shukur, M., Ithnin, R., Illias, H., & Kadir, M. (2013). Proton conducting polymer electrolyte based on plasticized chitosan–PEO blend and application in electrochemical devices. *Optical Materials, 35*(10), 1834-1841.

Shukur, M., & Kadir, M. (2015). Hydrogen ion conducting starch-chitosan blend based electrolyte for application in electrochemical devices. *Electrochimica Acta, 158*, 152-165.

Sim, L., Yahya, R., & Arof, A. (2016). Blend polymer electrolyte films based on poly(ethyl methacrylate / poly(vinylidenefluoride-co-hexafluoropropylene)

incorporated with 1-butyl-3-methyl imidazolium iodide ionic liquid. *Solid State Ionics, 291*, 26-32.

Simon, P., & Gogotsi, Y. (2008). Materials for electrochemical capacitors. *Nature Materials, 7*(11), 845-854.

Simon, P., & Gogotsi, Y. (2012). Capacitive energy storage in nanostructured carbon–electrolyte systems. *Accounts of Chemical research, 46*(5), 1094-1103.

Singh, A., Roberts, A. J., Slade, R. C., & Chandra, A. (2014). High electrochemical performance in asymmetric supercapacitors using MWCNT/nickel sulfide composite and graphene nanoplatelets as electrodes. *Journal of Materials Chemistry A, 2*(39), 16723-16730.

Singh, M. K., Suleman, M., Kumar, Y., & Hashmi, S. (2015). A novel configuration of electrical double layer capacitor with plastic crystal based gel polymer electrolyte and graphene nano-platelets as electrodes: A high rate performance. *Energy, 80*, 465-473.

Singh, R., Jadhav, N. A., Majumder, S., Bhattacharya, B., & Singh, P. K. (2013). Novel biopolymer gel electrolyte for dye-sensitized solar cell application. *Carbohydrate Polymers, 91*(2), 682-685.

Song, J., Xu, L., Zhou, C., Xing, R., Dai, Q., Liu, D., & Song, H. (2013). Synthesis of graphene oxide based CuO nanoparticles composite electrode for highly enhanced nonenzymatic glucose detection. *ACS Applied Materials & Interfaces, 5*(24), 12928-12934.

Stepniak, I., & Ciszewski, A. (2011). Electrochemical characteristics of a new electric double layer capacitor with acidic polymer hydrogel electrolyte. *Electrochimica Acta, 56*(5), 2477-2482.

Stepniak, I., Galinski, M., Nowacki, K., Wysokowski, M., Jakubowska, P., Bazhenov, V., Leisegang, T., Ehrlich, H., & Jesionowski, T. (2016). A novel chitosan/sponge chitin origin material as a membrane for supercapacitors–preparation and characterization. *RSC Advances, 6*(5), 4007-4013.

Sthiannopkao, S., & Wong, M. H. (2013). Handling e-waste in developed and developing countries: Initiatives, practices, and consequences. *Science of the Total Environment, 463*, 1147-1153.

Stoller, M. D., & Ruoff, R. S. (2010). Best practice methods for determining an electrode material's performance for ultracapacitors. *Energy & Environmental Science, 3*(9), 1294-1301.

Su'ait, M. S., Ahmad, A., Badri, K., Mohamed, N., Rahman, M. Y. A., Ricardo, C. A., & Scardi, P. (2014). The potential of polyurethane bio-based solid polymer electrolyte for photoelectrochemical cell application. *International Journal of Hydrogen Energy, 39*(6), 3005-3017.

166

Subramaniam, C., Ramya, C., & Ramya, K. (2011). Performance of EDLCs using Nafion and Nafion composites as electrolyte. *Journal of Applied Electrochemistry, 41*(2), 197-206.

Sudhakar, Y., & Selvakumar, M. (2012). Lithium perchlorate doped plasticized chitosan and starch blend as biodegradable polymer electrolyte for supercapacitors. *Electrochimica Acta, 78*, 398-405.

Sudhakar, Y., Selvakumar, M., & Bhat, D. K. (2015a). Lithium salts doped biodegradable gel polymer electrolytes for supercapacitor application. *Journal of Materials and Environmental Science, 6*(5), 1218-1227.

Sudhakar, Y., Selvakumar, M., & Bhat, D. K. (2015b). Preparation and characterization of phosphoric acid-doped hydroxyethyl cellulose electrolyte for use in supercapacitor. *Materials for Renewable and Sustainable Energy, 4*(3), 1-9.

Suja, F., Abdul Rahman, R., Yusof, A., & Masdar, M. S. (2014). e-Waste management scenarios in Malaysia. *Journal of Waste Management, 2014*.

Sun, H., Takeda, Y., Imanishi, N., Yamamoto, O., & Sohn, H. J. (2000). Ferroelectric materials as a ceramic filler in solid composite polyethylene oxide‐based electrolytes. *Journal of The Electrochemical Society, 147*(7), 2462-2467.

Sun, H. Y., Sohn, H. J., Yamamoto, O., Takeda, Y., & Imanishi, N. (1999). Enhanced lithium‐ion transport in PEO‐based composite polymer electrolytes with ferroelectric BaTiO$_3$. *Journal of The Electrochemical Society, 146*(5), 1672-1676.

Sun, Z., Xiao, Y., Sietsma, J., Agterhuis, H., Visser, G., & Yang, Y. (2015). Characterisation of metals in the electronic waste of complex mixtures of end-of-life ICT products for development of cleaner recovery technology. *Waste Management, 35*, 227-235.

Sun, Z., Xiao, Y., Sietsma, J., Agterhuis, H., & Yang, Y. (2015). A cleaner process for selective recovery of valuable metals from electronic waste of complex mixtures of end-of-life electronic products. *Environmental Science & Technology, 49*(13), 7981-7988.

Suo, L., Hu, Y.-S., Li, H., Armand, M., & Chen, L. (2013). A new class of solvent-in-salt electrolyte for high-energy rechargeable metallic lithium batteries. *Nature Communications, 4*, 1481-1489.

Susan, M. A. B. H., Kaneko, T., Noda, A., & Watanabe, M. (2005). Ion gels prepared by in situ radical polymerization of vinyl monomers in an ionic liquid and their characterization as polymer electrolytes. *Journal of the American Chemical Society, 127*(13), 4976-4983.

Suthanthiraraj, S. A., Sheeba, D. J., & Paul, B. J. (2009). Impact of ethylene carbonate on ion transport characteristics of PVdF–AgCF$_3$SO$_3$ polymer electrolyte system. *Materials Research Bulletin, 44*(7), 1534-1539.

Swift, G. (1993). Directions for environmentally biodegradable polymer research. *Accounts of Chemical Research, 26*(3), 105-110.

Syahidah, S. N., & Majid, S. (2013). Super-capacitive electro-chemical performance of polymer blend gel polymer electrolyte (GPE) in carbon-based electrical double-layer capacitors. *Electrochimica Acta, 112*, 678-685.

Taberna, P., Simon, P., & Fauvarque, J.-F. (2003). Electrochemical characteristics and impedance spectroscopy studies of carbon-carbon supercapacitors. *Journal of The Electrochemical Society, 150*(3), A292-A300.

Tafur, J. P., & Romero, A. J. F. (2014). Electrical and spectroscopic characterization of PVdF-HFP and TFSI—Ionic liquids-based gel polymer electrolyte membranes. Influence of ZnTf$_2$ salt. *Journal of Membrane Science, 469*, 499-506.

Tafur, J. P., Santos, F., & Romero, A. J. F. (2015). Influence of the ionic liquid type on the gel polymer electrolytes properties. *Membranes, 5*(4), 752-771.

Taghizadeh, M. T., & Seifi-Aghjekohal, P. (2015). Sonocatalytic degradation of 2-hydroxyethyl cellulose in the presence of some nanoparticles. *Ultrasonics Sonochemistry, 26*, 265-272.

Tamilselvi, P., & Hema, M. (2014). Conductivity studies of LiCF$_3$SO$_3$ doped PVA: PVdF blend polymer electrolyte. *Physica B: Condensed Matter, 437*, 53-57.

Tanahashi, I., Yoshida, A., & Nishino, A. (1990). Comparison of the electrochemical properties of electric double-layer capacitors with an aqueous electrolyte and with a nonaqueous electrolyte. *Bulletin of the Chemical Society of Japan, 63*(12), 3611-3614.

Tanaka, T., Montanari, G., & Mulhaupt, R. (2004). Polymer nanocomposites as dielectrics and electrical insulation-perspectives for processing technologies, material characterization and future applications. *IEEE Transactions on Dielectrics and Electrical Insulation, 11*(5), 763-784.

Tang, C., Hackenberg, K., Fu, Q., Ajayan, P. M., & Ardebili, H. (2012). High ion conducting polymer nanocomposite electrolytes using hybrid nanofillers. *Nano Letters, 12*(3), 1152-1156.

Tang, D., Yuan, R., & Chai, Y. (2007). Magnetic control of an electrochemical microfluidic device with an arrayed immunosensor for simultaneous multiple immunoassays. *Clinical Chemistry, 53*(7), 1323-1329.

Tang, J., Muchakayala, R., Song, S., Wang, M., & Kumar, K. N. (2016). Effect of EMIMBF$_4$ ionic liquid addition on the structure and ionic conductivity of LiBF$_4$-complexed PVdF-HFP polymer electrolyte films. *Polymer Testing, 50*, 247-254.

Tareev, B. M. (1975). *Physics of Dielectric Materials*. Mir publishers, Moscow.

Teoh, K., Lim, C.-S., Liew, C.-W., & Ramesh, S. (2015). Electric double-layer capacitors with corn starch-based biopolymer electrolytes incorporating silica as filler. *Ionics, 21*(7), 2061-2068.

Tõnurist, K., Thomberg, T., Jänes, A., Kink, I., & Lust, E. (2012). Specific performance of electrical double layer capacitors based on different separator materials in room temperature ionic liquid. *Electrochemistry Communications, 22*, 77-80.

Trasatti, S., & Buzzanca, G. (1971). Ruthenium dioxide: a new interesting electrode material. Solid state structure and electrochemical behaviour. *Journal of Electroanalytical Chemistry and Interfacial Electrochemistry, 29*(2), A1-A5.

Tuller, H. L. (2000). Ionic conduction in nanocrystalline materials. *Solid State Ionics, 131*(1), 143-157.

Ue, M., Takeda, M., Suzuki, Y., & Mori, S. (1996). Chemical stability of γ-butyrolactone-based electrolytes for aluminum electrolytic capacitors. *Journal of Power Sources, 60*(2), 185-190.

Utracki, L. A., & Wilkie, C. A. (2002). *Polymer blends handbook (Vol. 1):* Springer, Netherlands.

Verma, M. L., Minakshi, M., & Singh, N. K. (2014). Synthesis and characterization of solid polymer electrolyte based on activated carbon for solid state capacitor. *Electrochimica Acta, 137*, 497-503.

Vila, J., Varela, L., & Cabeza, O. (2007). Cation and anion sizes influence in the temperature dependence of the electrical conductivity in nine imidazolium based ionic liquids. *Electrochimica Acta, 52*(26), 7413-7417.

Vishnuvardhan, T., Kulkarni, V., Basavaraja, C., & Raghavendra, S. (2006). Synthesis, characterization and ac conductivity of polypyrrole/Y_2O_3 composites. *Bulletin of Materials Science, 29*(1), 77-83.

Wang, J., Senkovska, I., Kaskel, S., & Liu, Q. (2014). Chemically activated fungi-based porous carbons for hydrogen storage. *Carbon, 75*, 372-380.

Wang, Y.-J., & Kim, D. (2007). Crystallinity, morphology, mechanical properties and conductivity study of in situ formed $PVdF/LiClO_4/TiO_2$ nanocomposite polymer electrolytes. *Electrochimica Acta, 52*(9), 3181-3189.

Wang, Y. (2009). Recent research progress on polymer electrolytes for dye-sensitized solar cells. *Solar Energy Materials and Solar Cells, 93*(8), 1167-1175.

Watanabe, K., Sakairi, M., Takahashi, H., Hirai, S., & Yamaguchi, S. (1999). Formation of Al–Zr composite oxide films on aluminum by sol–gel coating and anodizing. *Journal of Electroanalytical Chemistry, 473*(1), 250-255.

Winie, T., & Arof, A. (2006). FT-IR studies on interactions among components in hexanoyl chitosan-based polymer electrolytes. *Spectrochimica Acta Part A: Molecular and Biomolecular Spectroscopy, 63*(3), 677-684.

Winter, M., & Brodd, R. J. (2004). What are batteries, fuel cells, and supercapacitors? *Chemical Reviews, 104*(10), 4245-4270.

Wu, C.-L., & Chen, Y. (2015). Hydroxyethyl cellulose filled with M^{2+} chelate complexes with ethylenediaminetetraacetic acid (EDTA) as an effective electron-injection layer for polymer light-emitting diodes. *Organic Electronics, 25*, 156-164.

Wu, Q.-F., He, K.-X., Mi, H.-Y., & Zhang, X.-G. (2007). Electrochemical capacitance of polypyrrole nanowire prepared by using cetyltrimethylammonium bromide (CTAB) as soft template. *Materials Chemistry and Physics, 101*(2), 367-371.

Xu, B., Wu, F., Chen, S., Zhang, C., Cao, G., & Yang, Y. (2007). Activated carbon fiber cloths as electrodes for high performance electric double layer capacitors. *Electrochimica Acta, 52*(13), 4595-4598.

Xu, H., Fang, J., Guo, M., Lu, X., Wei, X., & Tu, S. (2010). Novel anion exchange membrane based on copolymer of methyl methacrylate, vinylbenzyl chloride and ethyl acrylate for alkaline fuel cells. *Journal of Membrane Science, 354*(1), 206-211.

Xu, K. (2004). Nonaqueous liquid electrolytes for lithium-based rechargeable batteries. *Chemical Reviews, 104*(10), 4303-4418.

Xu, Y. (2004). $Al_2O_3-(Ba_{0.5}Sr_{0.5})TiO_3$ composite oxide films on etched aluminum foil by sol–gel coating and anodizing. *Ceramics International, 30*(7), 1741-1743.

Yamagata, M., Soeda, K., Ikebe, S., Yamazaki, S., & Ishikawa, M. (2013). Chitosan-based gel electrolyte containing an ionic liquid for high-performance nonaqueous supercapacitors. *Electrochimica Acta, 100*, 275-280.

Yamamoto, H., Oshima, M., Fukuda, M., Isa, I., & Yoshino, K. (1996). Characteristics of aluminium solid electrolytic capacitors using a conducting polymer. *Journal of Power Sources, 60*(2), 173-177.

Yamamoto, H., Oshima, M., Hosaka, T., & Isa, I. (1999). Solid electrolytic capacitors using an aluminum alloy electrode and conducting polymers. *Synthetic Metals, 104*(1), 33-38.

Yang, C.-M., Cho, W. I., Lee, J. K., Rhee, H.-W., & Cho, B. W. (2005). EDLC with UV-cured composite polymer electrolyte based on poly[(ethylene glycol) diacrylate] /poly(vinylidene fluoride) /poly(methyl methacrylate) blends. *Electrochemical and Solid-State Letters, 8*(2), A91-A95.

Yang, L., Hu, J., Lei, G., & Liu, H. (2014). Ionic liquid-gelled polyvinylidene fluoride/polyvinyl acetate polymer electrolyte for solid supercapacitor. *Chemical Engineering Journal, 258*, 320-326.

Yang, P., Liu, L., Li, L., Hou, J., Xu, Y., Ren, X., An, M., & Li, N. (2014). Gel polymer electrolyte based on polyvinylidenefluoride-co-hexafluoropropylene and ionic liquid for lithium ion battery. *Electrochimica Acta, 115*, 454-460.

Ye, Y.-S., Rick, J., & Hwang, B.-J. (2013). Ionic liquid polymer electrolytes. *Journal of Materials Chemistry A, 1*(8), 2719-2743.

Yu, W., & Xie, H. (2012). A review on nanofluids: preparation, stability mechanisms, and applications. *Journal of Nanomaterials, 2012*, 1.

Yusof, Y., Majid, N., Kasmani, R., Illias, H., & Kadir, M. (2014). The effect of plasticization on conductivity and other properties of starch/chitosan blend biopolymer electrolyte incorporated with ammonium iodide. *Molecular Crystals and Liquid Crystals, 603*(1), 73-88.

Zebardastan, N., Khanmirzaei, M., Ramesh, S., & Ramesh, K. (2016). Novel poly (vinylidene fluoride-co-hexafluoro propylene)/polyethylene oxide based gel polymer electrolyte containing fumed silica (SiO_2) nanofiller for high performance dye-sensitized solar cell. *Electrochimica Acta, 220*, 573-580.

Zhang, D., Zhang, X., Chen, Y., Yu, P., Wang, C., & Ma, Y. (2011). Enhanced capacitance and rate capability of graphene/polypyrrole composite as electrode material for supercapacitors. *Journal of Power Sources, 196*(14), 5990-5996.

Zhang, H. H., Maitra, P., & Wunder, S. L. (2008). Preparation and characterization of composite electrolytes based on PEO(375)-grafted fumed silica. *Solid State Ionics, 178*(39), 1975-1983.

Zhang, L. L., & Zhao, X. (2009). Carbon-based materials as supercapacitor electrodes. *Chemical Society Reviews, 38*(9), 2520-2531.

Zhang, P., Yang, L., Li, L., Ding, M., Wu, Y., & Holze, R. (2011). Enhanced electrochemical and mechanical properties of P(VDF-HFP)-based composite polymer electrolytes with SiO_2 nanowires. *Journal of Membrane Science, 379*(1), 80-85.

Zhang, T., Xue, J., Gao, C.-z., Qiu, R.-l., Li, Y.-x., Li, X., Huang, M-z., & Kannan, K. (2016). Urinary Concentrations of bisphenols and their association with biomarkers of oxidative stress in people living near e-waste recycling facilities in china. *Environmental Science & Technology, 50*(7), 4045-4053.

Zhang, Y., Feng, H., Wu, X., Wang, L., Zhang, A., Xia, T., Dong, H., Li, X., & Zhang, L. (2009). Progress of electrochemical capacitor electrode materials: A review. *International Journal of Hydrogen Energy, 34*(11), 4889-4899.

Zheng, J. P. (2004). Resistance distribution in electrochemical capacitors with a bipolar structure. *Journal of Power Sources, 137*(1), 158-162.

Zhong, C., Deng, Y., Hu, W., Qiao, J., Zhang, L., & Zhang, J. (2015). A review of electrolyte materials and compositions for electrochemical supercapacitors. *Chemical Society Reviews, 44*(21), 7484-7539.

Zulkifli, F. H., Shahitha, F., Yusuff, M. M., Hamidon, N. N., & Chahal, S. (2013). Cross-linking effect on electrospun hydroxyethyl cellulose/poly(vinyl alcohol) nanofibrous scaffolds. *Procedia Engineering, 53*, 689-695.

LIST OF PUBLICATIONS AND PAPERS PRESENTED

List of Publications:

1.   **Chong, M. Y.**, Liew, C. W., Numan, A., Yugal, K., Ramesh, K., Ng, H. M., Chong, T. V., & Ramesh, S. (2016). Effects of ionic liquid on the hydroxylpropylmethyl cellulose (HPMC) solid polymer electrolyte. *Ionics*, *22(12)*: 2421-2430.

2.   **Chong, M. Y.**, Numan, A., Liew, C. W., Ramesh, K., & Ramesh, S. (2017). Comparison of the performance of copper oxide and yttrium oxide nanoparticle based hydroxylethyl cellulose electrolytes for supercapacitors. *Journal of Applied Polymer Science*, *134*(13).

Paper presented in international conference:

1.   **Chong, M. Y.,** Numan, A., Ramesh, K., & Ramesh, S. "The effect of different weight percentages of lead(II) oxide nanoparticles based solid polymer electrolyte towards ionic conductivity." in *ISER-50th International Conference on Chemical and Environmental Science (ICCES),* 11-12 August 2016, Putrajaya, Malaysia. **(Oral presentation).**